

SANDIA REPORT

SAND2009-6327

Unlimited Release

Printed October 2009

Discovery, Integration, and Interrogation of Biotic/Abiotic Materials and Systems

Eric C. Carnes, Carlee E. Ashley, Helen K. Baca, DeAnna M. Lopez, Darren R. Dunphy,
and C. Jeffrey Brinker

Prepared by
Sandia National Laboratories
Albuquerque, New Mexico 87185 and Livermore, California 94550

Sandia is a multiprogram laboratory operated by Sandia Corporation,
a Lockheed Martin Company, for the United States Department of Energy's
National Nuclear Security Administration under Contract DE-AC04-94AL85000.

Approved for public release; further dissemination unlimited.



Issued by Sandia National Laboratories, operated for the United States Department of Energy by Sandia Corporation.

NOTICE: This report was prepared as an account of work sponsored by an agency of the United States Government. Neither the United States Government, nor any agency thereof, nor any of their employees, nor any of their contractors, subcontractors, or their employees, make any warranty, express or implied, or assume any legal liability or responsibility for the accuracy, completeness, or usefulness of any information, apparatus, product, or process disclosed, or represent that its use would not infringe privately owned rights. Reference herein to any specific commercial product, process, or service by trade name, trademark, manufacturer, or otherwise, does not necessarily constitute or imply its endorsement, recommendation, or favoring by the United States Government, any agency thereof, or any of their contractors or subcontractors. The views and opinions expressed herein do not necessarily state or reflect those of the United States Government, any agency thereof, or any of their contractors.

Printed in the United States of America. This report has been reproduced directly from the best available copy.

Available to DOE and DOE contractors from
U.S. Department of Energy
Office of Scientific and Technical Information
P.O. Box 62
Oak Ridge, TN 37831

Telephone: (865) 576-8401
Facsimile: (865) 576-5728
E-Mail: reports@adonis.osti.gov
Online ordering: <http://www.osti.gov/bridge>

Available to the public from
U.S. Department of Commerce
National Technical Information Service
5285 Port Royal Rd.
Springfield, VA 22161

Telephone: (800) 553-6847
Facsimile: (703) 605-6900
E-Mail: orders@ntis.fedworld.gov
Online order: <http://www.ntis.gov/help/ordermethods.asp?loc=7-4-0#online>



SAND2009-6327
Unlimited Release
Printed October 2009

Discovery, Integration, and Interrogation of Biotic/Abiotic Materials and Systems

Eric C. Carnes^a, Carlee E. Ashley^a, Helen K. Baca^a, DeAnna M. Lopez^a, Darren R. Dunphy^a, and
C. Jeffrey Brinker^{a,b}

^aChemical and Nuclear Engineering Department, Center for Micro-Engineered Materials, University of
New Mexico, Albuquerque, NM 87106

^bSelf-Assembled Materials Department
Sandia National Laboratory, P.O. 5800, Albuquerque, NM 87185-1349

Executive Summary

Immobilization of individual cells and collections of cells in well-defined, reproducible, nano-to-microscale structures that allow structural and functional manipulation and interrogation is important for developing new classes of biotic/abiotic materials, for establishing the relationship between genotype and phenotype, and for elucidating responses to disease, injury/stress, or therapy – primary goals of biomedical research. Although there has been considerable recent progress in investigating the response of cells to chemical or topological patterns defined lithographically on 2D surfaces, it is time to advance from two-dimensional adhesion on dishes/fluidic devices to three-dimensional architectures that better represent the nanoporous, 3-D extracellular matrix (ECM). 3D immobilization in nanostructured hosts enables cells to be surrounded by other cells, maintains fluidic connectivity/accessibility, and allows development of 3-D molecular or chemical gradients that provide an instructive background to guide cellular behavior. Although 3-D cell immobilization in polymers, hydrogels, and inorganic gels has been practiced for decades, these approaches do not provide for bio/nano interfaces with 3D spatial control of topology and composition important to both *the maintenance of natural cellular behavior patterns and the development of new non-native behaviors and functions*.

This LDRD project exploited our discovery of the ability of living cells to organize extended nanostructures and nano-objects in a manner that creates a unique, highly biocompatible bio/nano interface, mimicking the ECM, and maintaining cell viability, accessibility, and functionality (Baca *et al. Science*, 2006). Briefly, we found that, using short chain phospholipids to direct the formation of thin film silica mesophases during evaporation-induced self-assembly (EISA, Lu, Brinker *et al. Nature* 1997), the introduction of cells (yeast, Gram negative and positive bacteria, and several mammalian cells) alters profoundly the inorganic self-assembly pathway. Cells actively organize around themselves an ordered, multilayered lipid-membrane that interfaces coherently with a lipid-templated silica nanostructure. This bio/nano interface is unique in that it withstands drying (even evacuation) without cracking or the development of tensile stresses – yet it maintains accessibility to molecules, proteins/antibodies, plasmids, etc - introduced into the 3D silica host. Additionally cell viability is preserved for weeks to months in the absence of buffer or a fluidic architecture, making these constructs useful as standalone cell-based sensors. (On this basis, our sensors were launched to the space station for viability studies after exposure to vacuum and UV)

The bio/nano interfaces we describe do not form ‘passively’ – rather they are a consequence of the cell’s ability to sense and actively respond to external stimuli. During EISA, solvent evaporation concentrates the extracellular environment in osmolytes. In response to this hyperosmotic stress, the cells release water, creating a gradient in pH (and presumably other molecular components), which is maintained within the adjoining nanostructured host and serves to localize lipids, proteins, plasmids, lipidized nanocrystals, and a variety of other components at the cellular surface. This active organization of the bio/nano interface, which we refer to as *cell directed assembly* (CDA) can be accomplished during ink-jet printing or selective wetting – processes allowing patterning of cellular arrays – what’s more we find that cells printed onto preformed, fluid lipid/silica mesophases integrate themselves within the silica nanostructure, creating a 3D environment essentially indistinguishable from that in CDA. We refer to this latter process as *cell-directed integration* (CDI).

The synthetic constructs we have developed have allowed us to explore several fundamental questions concerning the mechanisms by which cells actively control nanostructure formation and function and conversely the mechanisms by which nanostructured interfaces, matrices, and patterns can control cellular behavior. Highlights of our findings are summarized below and described in detail in the following chapters.

- We showed that lipid localization at the cellular interface can be used to co-localize foreign transmembrane proteins and confer to the cellular system new behaviors. Importantly we demonstrated that long-chained lipids added as protein containing liposomes selectively partition to the immediate cell surface during CDA, thereby localizing foreign transmembrane proteins in their native/functional conformations in close proximity to the cell surface.
- We developed several strategies enabling simple, efficient, in situ cell transformation. Patterned deposition of cells plus plasmids on a pre-formed lipid/silica film results in cellular integration, plasmid localization, and efficient transformation, providing a means for spatial patterning of cellular behavior.
- We have used CDA to incorporate model mammalian cells, such as adherent human embryonic kidney (HEK) cells, into our lipid-templated nanostructures and have found that mammalian cells localize phospholipids and create bio/nano interfaces similar to, yet distinct from, single-celled eukaryotes and prokaryotes. HEK cells immobilized within lipid/silica nanostructures had viability comparable to HEK in buffer.
- We developed a new optically and metabolically controlled lithography process *cell directed integration* (CDI) to enable the patterned integration of arbitrary cell lines into solidstate devices.
- We quantified the control parameters of the CDI process.
- We developed a nanostructured platform enabling interrogation of cellular behavior at the individual cell level.
- We observed that confinement of individual bacterial cells induces so-called quorum sensing pathways and genetic reprogramming important to understanding bacterial survival, virulence, and evolution and now recognized as potentially relevant to a spectrum of diseases including cancer.

Acknowledgements

This work was partially supported by Sandia National Laboratory's Laboratory Directed R&D program, Air Force Office of Scientific Research grant FA 9550-07-1-0054, DOE Basic Energy Sciences grant DE-FG02-02-ER15368, NSF IGERT Fellowship grant DGE-0504276, the Defense Threat Reduction Agency grant B0844671, the NIH/Roadmap for Medical Research under grant PHS 2 PN2 EY016570B, and NIH grants R01 AI-064926, AI-081090, AI-037142, and AI-047441. Some images were generated in the University of New Mexico Cancer Center Fluorescence Microscopy Facility, supported as detailed at: <http://hsc.unm.edu/crtc/microscopy/Facility.html>. Sandia is a multiprogram laboratory operated by Sandia Corporation, a Lockheed Martin Company, for the U.S. Department of Energy's National Nuclear Security Administration under contract DE-AC04-94AL85000.

Contents

Executive Summary	4
Acknowledgements	6
I. Biotic/Abiotic Materials and Interfaces Made by Cell-Directed Assembly and Cell-Directed Integration	8
II. Confinement-Induced Quorum Sensing of Individual <i>Staphylococcus aureus</i> Bacteria	146
III. Cell-Directed Localization and Orientation of a Functional Foreign Transmembrane Protein within a Silica Nanostructure	157
IV. Characterization of Lipid-Templated Silica and Hybrid Thin Film Mesophases by Grazing Incidence Small-Angle X-ray Scattering	160
Appendix A. Publications and Presentations	170
Distribution list	175

Biotic/Abiotic Materials and Interfaces Made by Cell-Directed Assembly and Cell-Directed Integration

Immobilization of individual cells and collections of cells in well-defined, reproducible, nano-to-microscale structures that allow structural and functional manipulation and interrogation is important for developing new classes of biotic/abiotic materials, for establishing the relationship between genotype and phenotype, and for elucidating responses to disease, injury/stress, or therapy – primary goals of biomedical research. Although there has been considerable recent progress in investigating the response of cells to chemical or topological patterns defined lithographically on two-dimensional (2D) surfaces, it is time to advance from 2D adhesion on dishes/fluidic devices to three-dimensional (3D) architectures that better represent the natural nanoporous and 3D extracellular matrix (ECM). 3D immobilization in nanostructured hosts enables cells to be surrounded by other cells, maintains fluidic connectivity/accessibility, and allows development of 3D molecular or chemical gradients that provide an instructive background to guide cellular behavior. Although 3D cell immobilization in polymers, hydrogels, and inorganic gels has been practiced for decades, these approaches do not provide for bio/nano interfaces with 3D spatial control of topology and composition important to both the maintenance of natural cellular behavior patterns and the development of new non-native behaviors and functions. In particular, for all previously reported approaches there was neither an apparent effect of the cell on the surrounding host nor any apparent means to purposefully use the

nanostructured host to develop new cellular behaviors. Here we show two novel encapsulation strategies, cell-directed assembly (CDA) and cell-directed integration (CDI), to be unique, distinguished approaches to prepare new bio/nano interfaces and to develop new cellular behaviors as shown below in Figure 0-1.

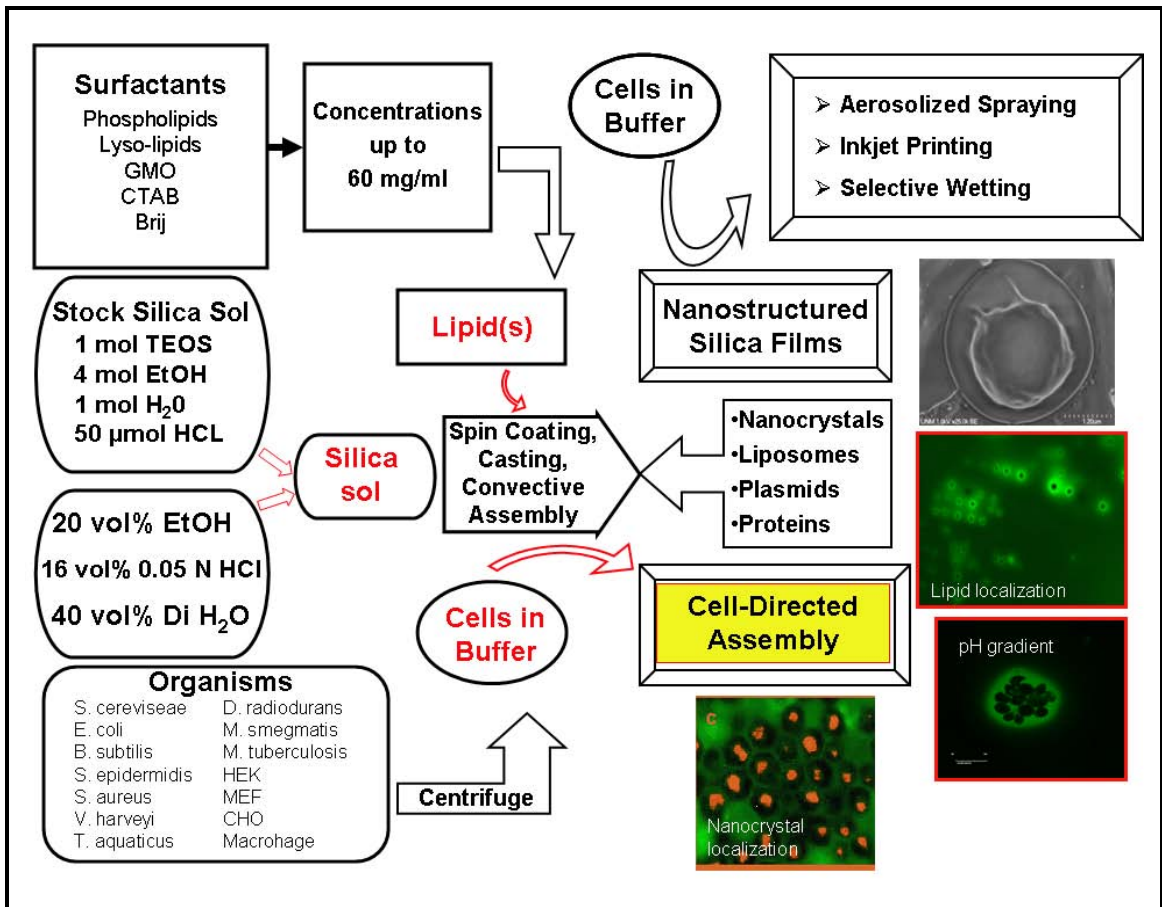


Figure 0-1. Overview of CDA process highlighting pertinent features that can be varied and investigated.

1.1 Characterization and Extension of Cell-Directed Assembly

1.1.1 Process Overview

Cell-directed assembly (CDA) is characterized by the ability of a living cell to intervene during traditional self-assembly, resulting in an active, as opposed to passive, assembly process. This modified evaporation-induced self-assembly (EISA) process begins with a single-batch mixture of cells, surfactant, solvent, and aqueous silica precursors (and other nanomaterials of interest if desired) as shown below in Figure 0-2. Since the reagents are mixed prior to application via spincoating, etc., it is necessary to maintain the viability of the cells by minimizing the amount of solvent present and by carefully choosing a biocompatible surfactant. This, however, greatly reduces the potential control over the material properties. A compromise has been found that consists of water soluble, short chain phospholipids along with a low-solvent concentration sol, referred to throughout as sol E (see experimental section). While this approach proves adequate for a wide variety of single-cell organisms, it does not afford long-term viability to more fragile mammalian cells. Additionally, due to the chemical constraints of the system, the ability to prescribe and develop a specific nanostructure via EISA approaches we have developed in inorganic systems are reduced and the methods by which patterned localization of cells could be achieved are few. My research began with solidifying the preliminary characterization of the CDA process, then progressed to extending the process to different cell lines and foreign nanocomponents, applying the process to

investigate a fundamental question in cell biology, and then to extending CDA to allow for patterning as well as immobilization of mammalian cell lines using a new lithography technique referred to as cell-directed integration (CDI).

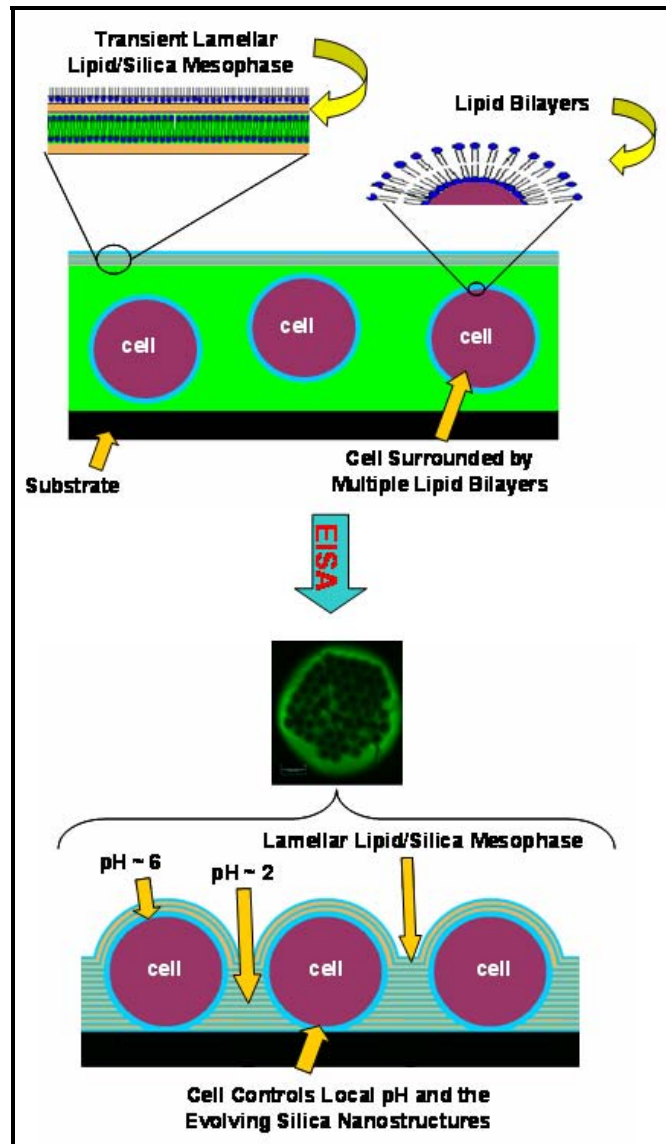


Figure 0-2. Schematic representation of Cell-Directed Assembly. In this process, live cells are added to a mixture of biocompatible surfactants and aqueous silica precursors. During an evaporation-induced self-assembly process, the cells exert control over their environment and, as a result, alter the developing material by localizing an amount of surfactant and altering the local pH.

1.1.2 Background

Previous research in our group identified the ability of yeast to localize an amount of diC_6PC when introduced to a mixture of lipid and aqueous silica precursors during EISA. Despite our experience in creating nanostructured inorganic films through EISA, initial observations of x-ray scattering data were not consistent with the anticipated nanostructure. Following observation using electron microscopy, it was discovered that the region around the cell appeared to be dramatically enriched in lipid compared to the bulk (Figure 0-3B). This lipid-rich region surrounding the cell was confirmed using confocal microscopy and a fluorescently-labeled lipid analogue (panel A). This lipid-rich local region serves to maintain a coherent interface with the bulk material (panels B and D). This coherent interface does not form when no lipid template is present, resulting in a desiccating silica environment (panel C). The remainder of the lipid is available to self-assemble and template silica host, resulting in an unanticipated, yet ordered nanostructure (panel E).

This discovery initiated several interesting investigations. The nature of this lipid layer needed to be elucidated (extent of localization, fluidity, etc.), along with other mechanisms by which cells interact with their environment (osmosis, etc.). The effect of different lipid types on the cells and the system also needed to be investigated to develop systems that could be more naturally mimetic. Eventually, it would also be desired to investigate this phenomenon in the presence of other cells in the hopes of extending CDA to a generalized cell-immobilization process.

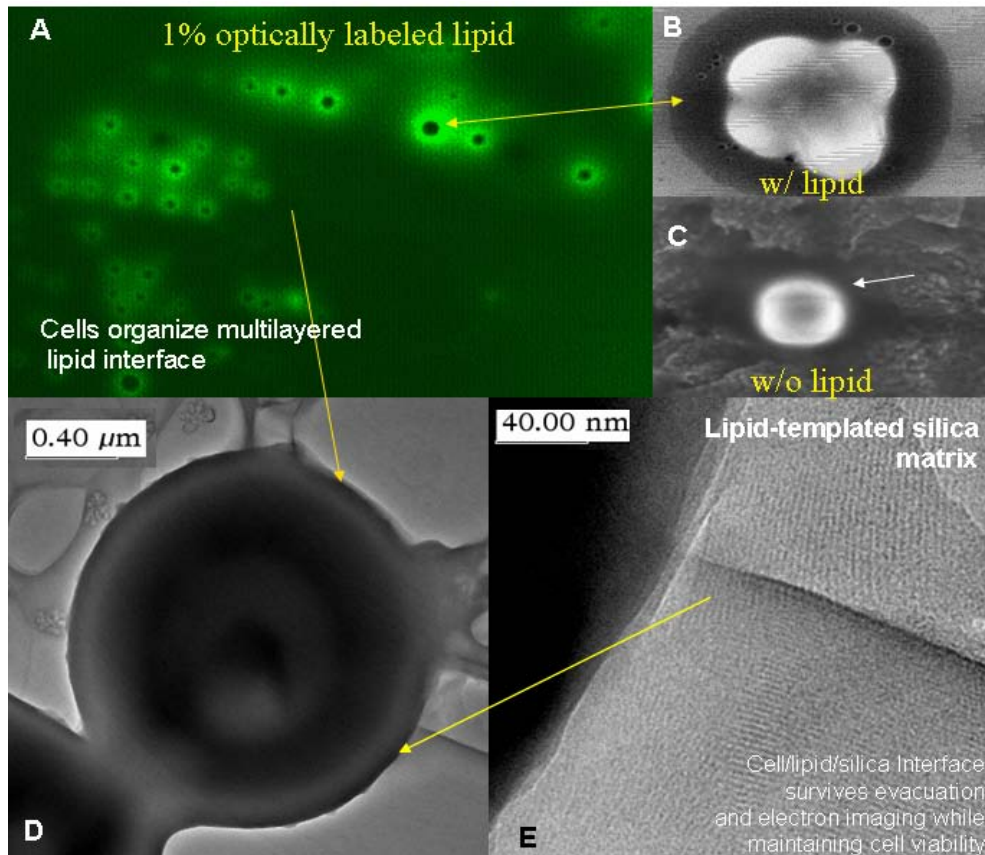


Figure 0-3. Yeast cells localize an amount of lipid to create a coherent interface with the surrounding lipid-templated silica matrix. (A) Confocal fluorescence image of NBD-tagged lipid localized around yeast cells, (B) SEM image of lipid layer around yeast showing coherence with the surrounding bulk, (C) without lipid, there is no observable coherent interface observed in the SEM, (D) TEM of yeast cell also indicates lipid accumulation, (E) TEM at increased magnitude confirms that bulk material is nanostructured lipid-templated silica.

1.1.3 Initial Characterization of Cell-Directed Assembly

The discovery of the ability of a living yeast cell to localize the lipid *diC₆PC* and control the developing nanostructure during CDA is intriguing, establishing the concept

that cells direct the formation of inorganic materials in their environment. Although it may seem intuitive now, this would turn out to be the outstanding feature that separated CDA from all other cell encapsulation schemes. To this day, researchers are investigating the effects of the cell on their materials, only the effects of the materials on the viability of the cells. Thus it was essential that we determined the characteristic ways in which a cell would interact with the lipid/silica system.

Initial research in this area focused on investigating the cell-specific localization of *diC₆PC* lipid surrounding the immobilized yeast cells and elucidating possible mechanisms for this phenomenon. This pursuit led to the discovery of the ability of cells to buffer the pH of their local microenvironment and thereby establish a pH gradient within the film. These effects were then verified using different cell-surrogate systems. The effect of other short-chain phospholipids and the corresponding impact on pH was determined. The surface accessibility of immobilized cells was also confirmed. Finally, the viability of yeast immobilized via CDA with various biocompatible surfactants was assessed.

1.1.3.1 Cells localize *diC₆PC* into fluid multi-layer region

Previous observations by fluorescence microscopy established the ability of live yeast to localize an amount of *diC₆PC* during the CDA process. The nature of this aggregated lipid was suspected to be a key feature in the coherence of the system and

corresponding increased cell viability. First, it is found that the cells always localize a certain amount of lipid, regardless of the total amount of lipid present. As shown in Figure 0-4, for the 2 orders of magnitude of lipid concentration over which a high-quality film can be assembled (300 $\mu\text{g/mL}$ to 30 mg/mL), yeast cells localize *diC₆PC* over a range of approximately 3-5 microns, indicating that the active lipid assembly by the cells dominates the passive self-assembly in the bulk film, demonstrating the power of the cells to alter their environment in an attempt to establish survivable conditions. Corresponding confocal stacks confirm the 3D nature of this lipid localization.

It was also desired to understand the fluidic nature of the localized lipid in the system. Fluorescence recovery after photobleaching (FRAP) is a traditional technique in biological and material science that allows the translational diffusion coefficients of lipid assemblies to be determined. If the lipid region is fluid, a photobleached spot will recover in time as the bleached molecules diffuse out and unbleached molecules diffuse in. The fluorescence of an initial area of interest is recorded and the spot is then rapidly photobleached using a high-intensity argon laser. The fluorescence recovery is then monitored in the area of interest and the rate of recovery is used to determine the translational diffusion coefficients of the lipids. Although diffusion is happening in three dimensions, many approximate calculations are available for determining the diffusion coefficients in the pseudo-2D confocal slice.

To determine the diffusion coefficient for the localized lipid layer surrounding the yeast, a thin-cast film of cells with NBD-tagged lipid and sol E was allowed to dry for one hour and then monitored for FRAP. The region of interest and results are shown below in Figure 0-5. The 100 μm^2 area of interest was completely bleached with 10

seconds of 40 mW argon laser intensity and was then able to recover 90% of the initial fluorescence within 30 minutes, indicating that the lipid region remained fluid although the film was visibly dry. An approximate diffusion coefficient of 1×10^{-10} cm²/sec is calculated from the FRAP data, indicating that this lipid region has a diffusivity between that of lipid in a fluid phase (4×10^{-8} cm²/sec) and that of lipid in a gel phase (10^{-9} to 10^{-14} cm²/sec). Diffusion data was calculated based on homogeneous 2D diffusion, so the actual diffusion coefficient could vary due to unaccounted diffusion in and out of the focal plane, as well as inhomogeneous nature of the cell-lipid-silica interface.

Additional FRAP experiments performed on lamellar ordered regions away from the cells and films containing hexagonally ordered lipid micelles in silica without cells show no measurable recovery over comparable time periods in which the available system could accurately measure, indicating that the diffusion constant is at least 1-2 orders of magnitude lower than that found when using cells. Thus, the ability of the cells to localize a fluid, multi-layer structure of the exogenous short-chain lipid is recognized as a key feature of the CDA process that contributes to the extended viability of immobilized cells, as well as other interesting features such as increased membrane permeability which are described in further detail below.

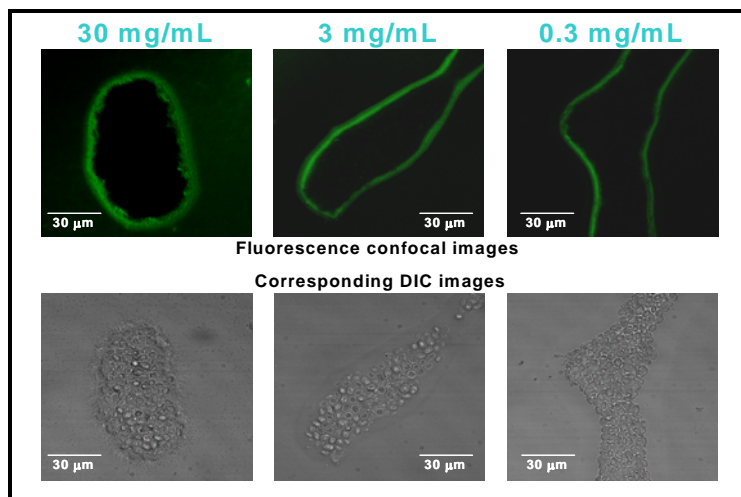


Figure 0-4. The extent of *diC6PC* localization by yeast remains constant over a range of concentrations during CDA. The top row of confocal images show localization of NBD-tagged lipid over 2 orders of magnitude, with the corresponding DIC images below.

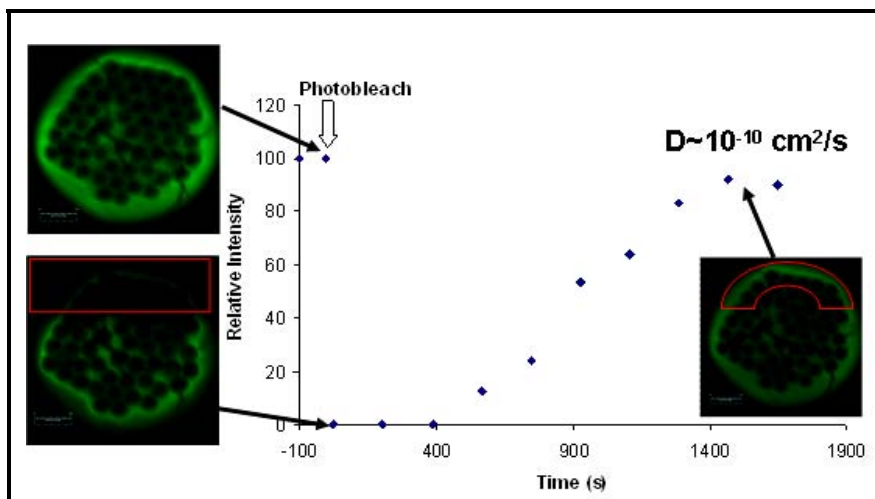


Figure 0-5. Fluidity of *diC6PC* localized by yeast in a nanostructured silica film via CDA is verified by fluorescence recovery after photobleaching (FRAP). Top left confocal image shows the initial confocal image of NBD-tagged lipid around cell. The bottom left image shows the photobleached region of interest after 30 seconds of exposure. Right-hand image shows 90% recovery of initial fluorescence after 1500 seconds. The fluorescence intensity was measured in time and plotted to determine an approximate diffusion coefficient that is one order of magnitude slower than free diffusion, indicating that the localized lipid is interacting with the cell and the bulk material.

1.1.3.2 Cell surrogates do not organize fluid lipid layer

Following the realization that live yeast cells will intervene in the self-assembly pathway of *diC₆PC*, it was essential to determine the nature of interaction between the lipid and cell. Possible factors contributing to the lipid localization included both inactive and active functions of the cell. To investigate the effect of cell size and surface electrostatics, latex beads with controlled surface charges were used as cell surrogates and the localization of NBD-tagged lipid during CDA was monitored via confocal microscopy. Additionally, heat-induced apoptotic (programmed cell death cycle) yeast cells and yeast spheroplasts (cell wall starches enzymatically removed, leaving only cell membrane) were used to investigate the effects of the cell metabolic state and cell wall composition. Volume fractions of surrogates and modified cells, comparable to volume used in initial stationary-phase yeast experiments, were introduced during CDA, with the results shown below in Figure 0-6.

We find that the uncharged latex bead surrogates do not have any effect on the assembly of *diC₆PC*, indicating that the cells are not simply serving as a heterogeneous nucleation site for lipid assembly. However, both the negatively-charged latex beads (carboxylate-modified) and the positively-charged latex beads (lysine-modified) do show localization of lipid. While the surface of the stationary phase yeast used for normal CDA does have an overall negative surface charge, the surface itself is highly crowded with both positively- and negatively-charged protein residues. Lipid aggregation around charged beads, although not fluid (from FRAP data) and less homogeneous than around live yeast cells, implies that electrostatic interactions are responsible in part for forming

the lipid-rich interface in cell-containing systems. This localization, however, does not direct a change in nanostructure development, as seen in CDA with live yeast.

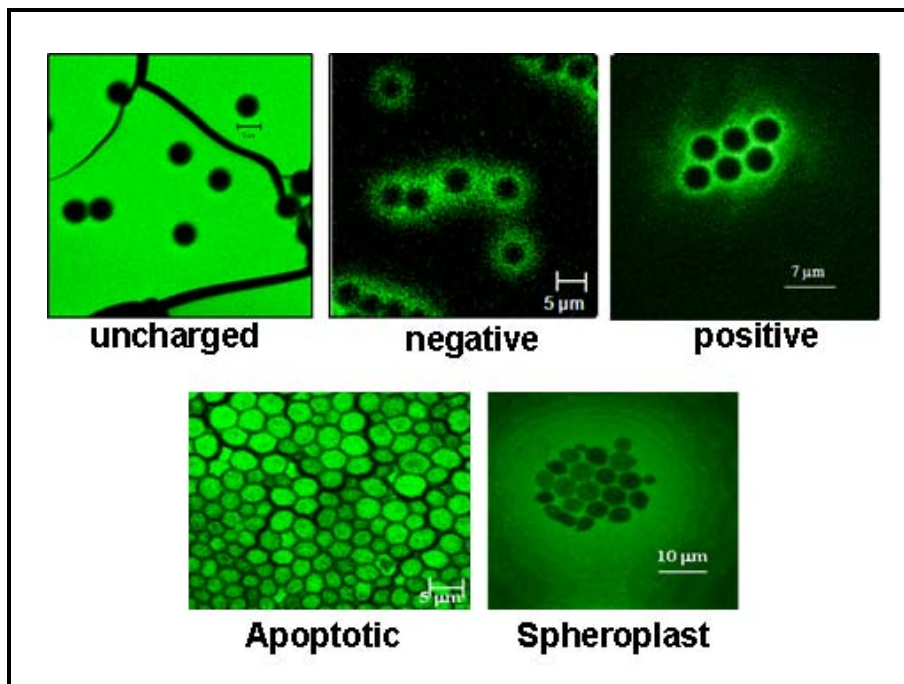


Figure 0-6. Interaction of *diC₆PC* with cell surrogates during CDA. Confocal images show uncharged latex beads have no localization of NBD-tagged lipid, though negative and positive surface charge beads do show some non-coherent localization. Apoptotic cells show rapid localization and internalization of lipid, while spheroplasts show slight localization and internalization of the lipid.

When using apoptotic yeast during CDA, we find that, although the *diC₆PC* is localized to the cell surface, it is quickly internalized by the cell due to the many changes in metabolism induced by apoptosis. This clearly demonstrates the necessity of live cells, performing normal metabolic functions, to fully participate in CDA. Also, when spheroplasts are used, there is no concentrated lipid localization, as seen with the

uncharged latex beads, although there is lipid internalization due to the lack of a cell wall. Due to the nature of the short chain diC_6PC , there is rapid exchange of the lipid through the exposed cell membrane resulting in an equilibrium like-distribution of lipid throughout the film and the cell. This is in stark contrast to the apoptotic cells, which, although they do rapidly internalize the lipid, they do localize it from the bulk material first. The spheroplasts do not show any active organization of the lipid, demonstrating the importance of the interaction between the cell surface and the bulk material. Additionally, it is found that none of these surrogate systems direct development of the nanostructure in a manner similar to yeast, as seen below in Figure 0-7.

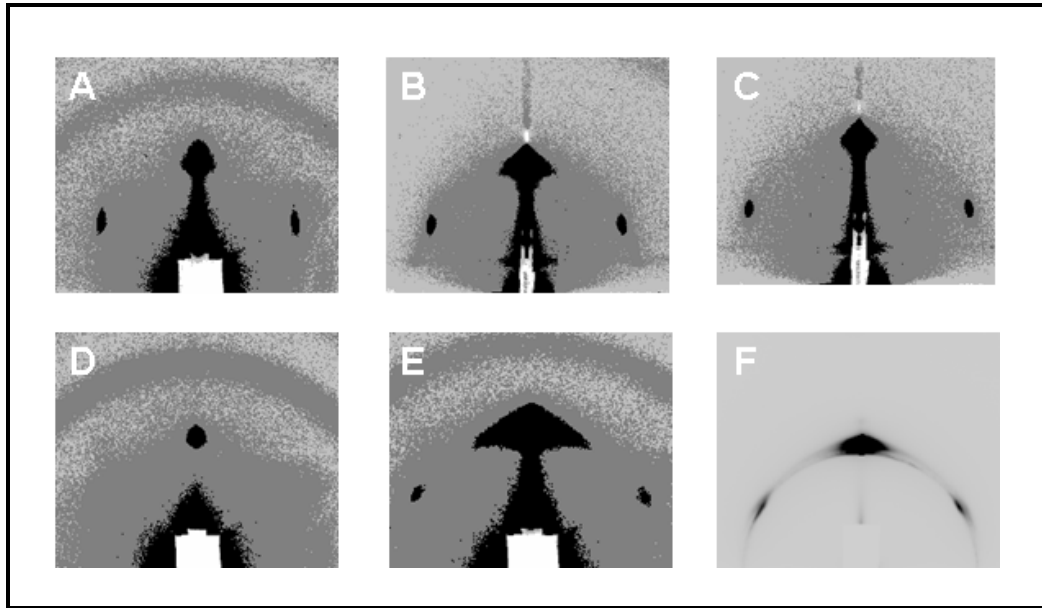


Figure 0-7. GISAXS images of yeast/lipid/silica and surrogate systems. (A) diC_6PC in sol E, (B) diC_6PC with uncharged latex beads in sol E, (C) diC_6PC with negatively-charged latex beads in sol E, (D) diC_6PC with live yeast in sol E, (E) diC_6PC with apoptotic yeast in sol E, (F) diC_6PC with spheroplasts in sol E

1.1.3.3 Different lipids lead to different bio/nano interfaces

In order to understand the influence of the lipid on CDA and explore the ability to develop more complex and functional interfaces and matrices (mimicking on some level the extra-cellular matrix), we have employed a series of water soluble diC6 lipids as structure directing agents and have monitored the evolving structure with fluorescence microscopy and GISAXS. Figure 0-8, shows confocal images of yeast immobilized within silica matrices where we included 1% of the corresponding optically labeled lipid analog. We observe that different lipid headgroups result in quite different bio/nano interfaces. Most dramatically switching from phosphotidyl-choline (PC) to phosphotidyl-ethanolamine (PE) results in an interface where there is no apparent preferential lipid localization. In that the pKa of these headgroups is similar within half a unit, these results indicate that the cell/lipid interaction (and resulting interface) cannot be explained strictly by electrostatics. GISAXS studies of this system showed that the PE headgroup also did not 'switch' the nanostructure from 2D hexagonal to lamellar as observed for PC. To fundamentally understand the lipid headgroup/cell interaction, it will be necessary to conduct AFM studies of the effective interaction potential between cells and model supported lipid bilayer systems, lipid bilayer coated beads or supported lipid bilayers, respectively.

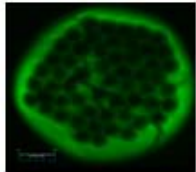
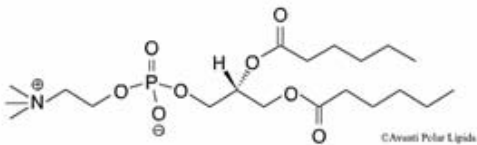
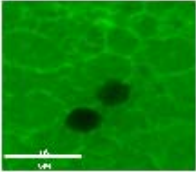
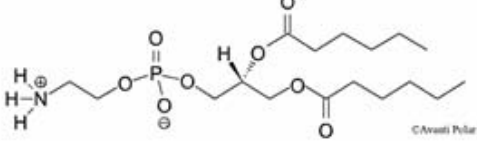
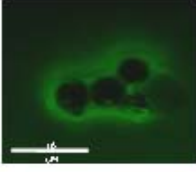
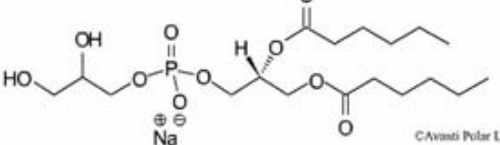
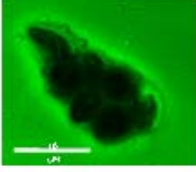
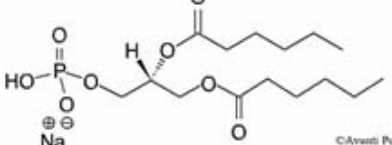
			<u>pKa</u>
PC Phosphotidyl Choline			1.0
PE Phosphotidyl Ethanolamine			1.7, 9.8
PG Phosphotidyl Glycerol			0.0
PA Phosphotidic Acid			3.0

Figure 0-8. Effect of lipid headgroup on development of bio/nano interface via CDA. Confocal images of NBD-tagged lipids show the previously mentioned localization of PC. However, no localization is observed for a similar lipid, PE. PG shows a small amount of localization, while PA also shows no localization.

To introduce other non-soluble, biologically relevant lipids for CDA, we have prepared water-soluble liposomes that were then introduced during the standard CDA process. Figure 0-9 shows confocal slices of a system prepared with 1% NBD-labeled *diC₆PC* plus palmitoyl-oleyl-phosphatidyl-choline (POPC) liposomes optically labeled with 1% of Texas-Red labeled dihexanoyl-phosphatidyl-ethanolamine (DHPE). We observe that both the short chain *diC₆PC* structure directing lipid and the longer chained POPC lipids are localized at the cellular surface. The merged image, however, suggests that the longer chain lipid is preferentially localized at the cellular interface as well as the

interface with the surrounding silica nanostructure. This agrees with the notion that the POPC would interact more readily with the cell surface due to its more natural curvature¹.

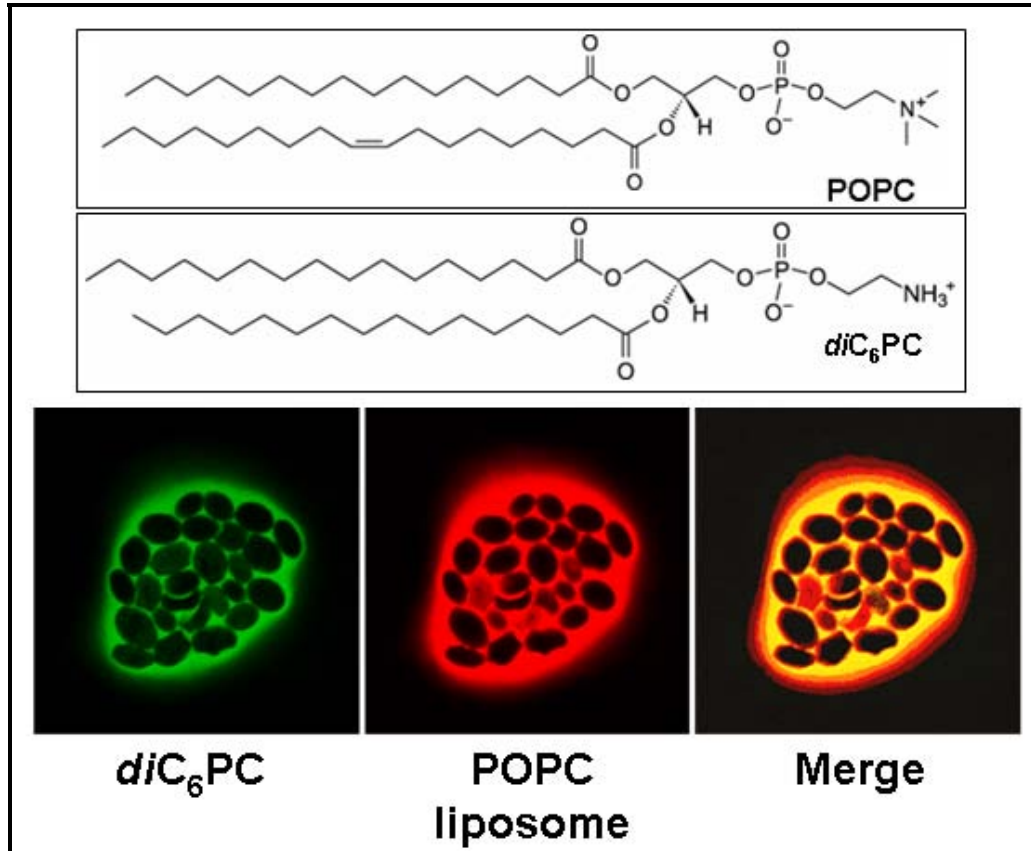


Figure 0-9. POPC lipids are preferentially organized around yeast during CDA compared to short-chain PC. Confocal images show different spectral channels of same image of sample containing equivalent amounts of NBD-tagged *diC₆PC* (left) and Texas Red-tagged POPC (middle). Overlapping of the images (right) shows that the POPC is localized closer to the cell surface.

1.1.3.4 Live cells effect their environment by establishing pH gradients

This surfactant localization by cellular influences on inorganic self-assembly are unprecedented, as it is well recognized that the addition of spherical colloidal particles to surfactant/silica systems has no influence on self-assembly. This emphasizes that, unlike latex beads, cells are active colloids, where the cell wall represents a dynamic structure actively maintained by the living cell and capable of sensing and responding to its environment. Although lipid localization by bead surrogates shares some similarities with live yeast in CDA, more pronounced distinctions are noted when probing local chemical effects. Specifically of interest is the effect of cells on system pH, as cells have multiple redundant pathways dedicated to the establishment and maintenance of ionic gradients and balancing of osmotic stresses. In Figure 0-10, confocal fluorescence imaging of systems containing uncharged or negatively charged beads and an impermeable pH-sensitive dye shows the film has a uniform pH of ~ 3 , attributed to the acidity of the silanol-terminated silica surface. In striking contrast, with cell-containing films we observe a local pH of 5-6 at the cell surface that decreases to about 3-4, corresponding to the nanostructured silica matrix, at a distance of several micrometers. Corresponding confocal stacks confirm the 3D nature of this lipid localization. Additional, time resolved studies indicate that these very different pH conditions are maintained throughout the course of EISA. To ensure that the observed pH gradients were not a function of dye concentration, all samples were washed with base following imaging to verify homogeneous distribution of the pH probe.

Importantly, and perhaps uniquely, our assembly methods create a localized microenvironment in which chemical gradients can be established and maintained. Three-dimensional chemical gradients are thermodynamically required for life, as they provide

the instructive background needed to guide cell behavior^{2,3}. To date, cell differentiation, quorum sensing, biofilm formation, and many other important cellular functions have been shown to be dependent on the development of spatio-temporal gradients of signaling molecule to activate response pathways^{4,5}.

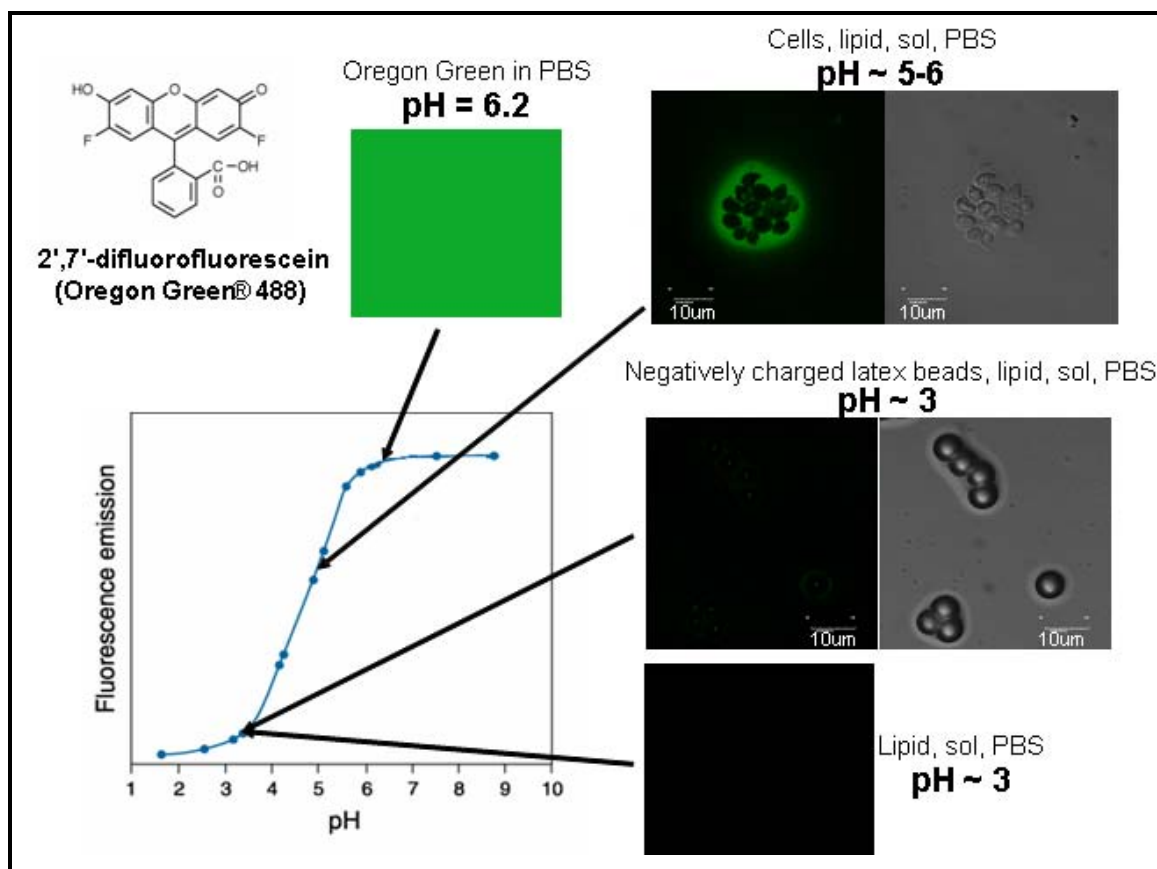


Figure 0-10. Live cells will alter local pH while surrogate systems do not show any pH effect. Fluorescent pH probe, Oregon Green (left), was incorporated within lipid/silica films along with either live yeast cells or bead surrogates. Values of pH were then evaluated using confocal microscopy and the fluorescence emission was quantified to determine pH value. Live yeast are able to establish a pH gradient ranging from values of ~2 in the bulk to ~7 near the cell surface (top right). Bead surrogates do not show any effect on pH (middle) and are similar to a lipid templated silica film (bottom right). Ubiquitous presence of pH probe was confirmed following experiments by a base wash.

1.1.3.5 Cell response to osmotic stress effects development of pH gradient

Previous gravimetric analyses had confirmed the yeast's ability to rapidly respond to osmotic stresses by regulating transmembrane water and ion fluxes. In combination with the cell's ability to establish and maintain a pH gradient throughout CDA, this suggests the cells are invoking complicated metabolic pathways used for osmoregulation. One of the most studied osmotic stress responses in yeast is the high-osmolarity glycerol (HOG) pathway⁶. When placed under significant osmotic stress, as during CDA, the yeast will immediately initiate production of glycerol to slow transport of water through channels in the cell membrane in order to maintain turgor. The total cell response time is on the order of minutes, which corresponds to the rates we observe during CDA. To validate this idea, we obtained several strains of mutant yeast cells that have various genes deleted from the HOG pathway and investigated the pH development using the same pH-sensitive fluorescent probe as above⁷. In Figure 0-11, we see confocal projections of the pH gradients developed by each of the cell mutants during CDA. Due to the difference in established pH gradients around the different cell mutants, it is highly likely that this HOG pathway is being invoked and is at least partly responsible for the cell's ability to buffer the local pH and maintain this chemical gradient.

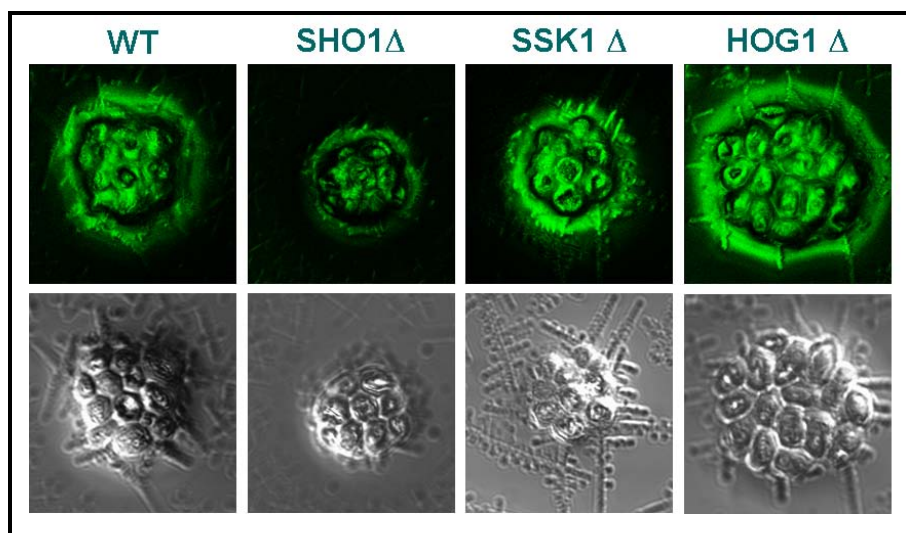


Figure 0-11. HOG pathway in yeast is invoked during CDA. Values of pH were determined by confocal microscopy using a fluorescent pH probe. Topographical confocal projections (top row) and DIC images (bottom row) show the standard yeast pH response for the wild-type cells (WT), while various gene deletions result in different extents of pH control as noted by the varying green intensity (SHO1 Δ , SSK1 Δ , and HOG1 Δ).

1.1.3.6 Ability of cell to localize lipid and control pH are dependent on each other

Although it was initially believed that the ability of the cell to establish a pH gradient served as a driving force for lipid localization, further evidence using confocal microscopy and a fluorescent pH probe indicate that the two phenomena are not directly related but remain intimately entwined. Figure 0-12 shows the change in pH of the local environment of yeast cells during CDA. We find that, as mentioned previously, normal cells will organize *diC₆PC* during CDA to create a lipid-rich local region that extends approximately 2-3 microns from the cell surface while maintaining a pH gradient over a similar distance, ranging from pH~7 at the cell surface to pH~3 in the bulk silica matrix. However, if we remove the *diC₆PC* from the system, we find that the cell is no longer

able to maintain a pH gradient, ultimately leading to low viability. This indicates that, although establishment of a pH gradient may initiate lipid localization, the presence of some lipid (and the corresponding coherent, fluid interface with a nanostructured matrix) may be required for the pH gradient to be maintained. Additionally, we find that apoptotic cells, which are able to localize lipid which then is rapidly internalized, are able to establish and maintain a more internal pH gradient, indicating that the cell walls of the yeast have been permeabilized. This suggests that a functional cell with an intact wall will attempt to react to osmotic stress by establishing a pH gradient which initiates localization of *diC₆PC*, thus creating a physical system that helps to maintain the physiological pH of the cell's local environment.

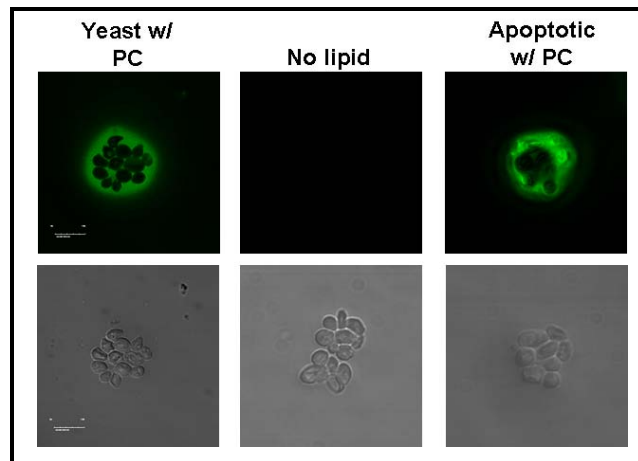


Figure 0-12. Live cells and lipid are required to maintain pH gradient. Using confocal microscopy with a fluorescent pH probe (top row) and DIC images (bottom row) we find that the cells can not maintain a pH gradient when in silica containing no lipid (middle). Apoptotic cells with lipid are able to affect pH (right), although not as extensively as live yeast (left).

1.1.3.7 Differences in lipid headgroup localization dramatically alter pH development

Although the majority of preliminary work on cell-directed assembly established the ability of yeast to localize *diC₆PC* while establishing and maintaining a pH gradient around the cell, we found above that the lipid, the metabolic state of the cell, and the ability to control pH are all connected. To further understand this relationship between pH gradients and lipid localization, the fluorescent pH probe Oregon Green was again employed along with confocal microscopy. In Figure 0-13 below, we find that the cells ability to maintain a pH gradient in its local environment is heavily dependent on the type of lipid headgroup and the corresponding localization of that lipid. Using various lipids of similar size differing only in headgroup type, we find that lipid localization and a maintained pH gradient are not necessarily causal. Again, homogeneous distribution of the probe was confirmed following the addition of base as mentioned earlier.

When performing CDA with yeast and dihexanoyl-phosphatidyl-glycerol (*diC₆PG*), we find that these lipids are localized around the cell and a pH gradient is maintained over a distance similar to that of the localized lipid region as observed in the yeast/ *diC₆PC* system. However, when we use *diC₆PE*, we find that the cell is able to establish and maintain a similar pH gradient to that of the *diC₆PC* system despite the fact that *diC₆PE* is not localized to the cell surface. This would seem to indicate that the ability of the lipid to create a nanostructured host matrix is the key factor in maintaining a pH gradient during CDA. A pH gradient is not necessarily the result of the localization of the lipid around the cell, since it is seen above that without any lipid to direct the

development of a nanostructure, no coherent interface with the bulk material forms and the cell is unable to maintain any pH gradient.

The interaction of the lipid type with the cell wall and the corresponding effects on the integrity of the cell wall also contribute significantly to the establishment of pH gradients. Although we showed previously that *diC₆PC* is localized and a pH gradient is established when the yeast are healthy, induction of apoptosis in the cells results in rapid internalization of the lipid and a dramatically reduced ability to maintain a pH gradient. Similar lipid localization and reduced pH effects were also observed in a completely different system comprised of normal yeast and dihexanoyl-phosphatidyl-phosphatidic acid (*diC₆PA*) in silica. In this system, no localization of the lipid is noted along with a very restricted pH gradient and leaking of the impermeant pH probe into the cell. Both of these systems result in the internalization of impermeable pH dye, indicating that the cell wall has been permeabilized. Although with the apoptotic cells, the permeabilization of the cell wall is a result of metabolic changes⁸, in the *diC₆PA* system, the permeabilization results from the interaction of the lipid with the cell wall components. In both systems, though, the permeabilization does not result in total compromisation, as indicated by the ability of the impermeant dye to remain in the cell once it has crossed the cell membrane. The similarities between these two extremely different systems demonstrate the importance of an intact cell wall to the cells' ability to control pH and interact with the various lipid types used in CDA.

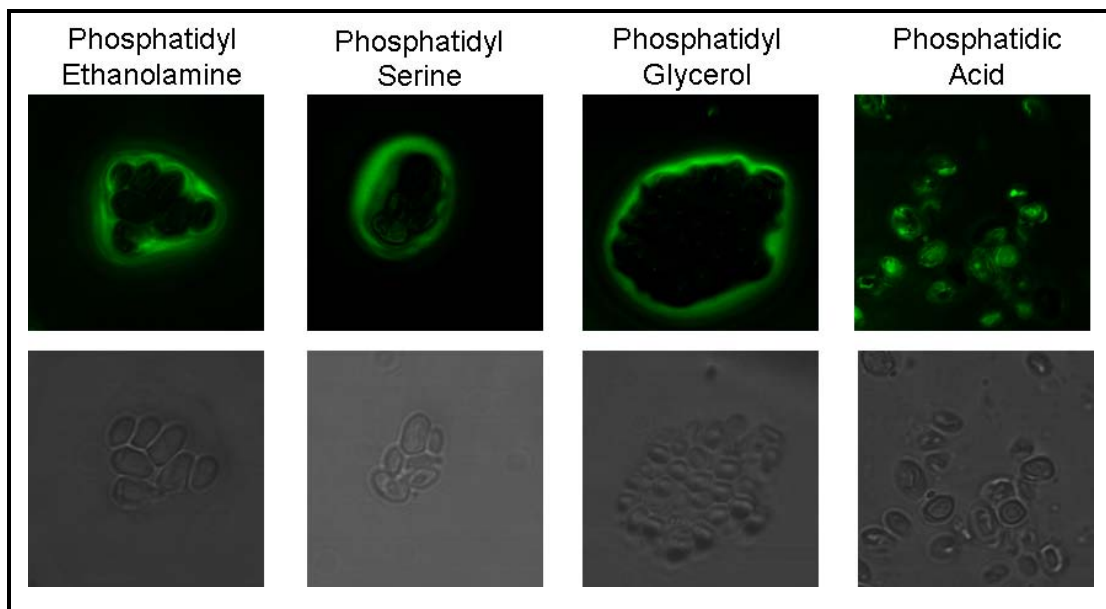


Figure 0-13. CDA with different lipids can result in different pH gradients. Confocal microscopy with pH probe (top row) and DIC images (bottom) show that the PE (far left), PS (near left), and PG (near right) systems have similar pH gradients to the standard PC system. The PA appears to permeabilize the cell wall, allowing for uptake of the cell-impermeant pH probe (far right).

The resulting interactions during CDA between live yeast cells and various headgroup types of short-chain phospholipids differ in regards to the extent of lipid localization and the maintenance of established pH gradients. However, the key unifying feature appears to be the ability of the lipid to create a coherent, nanostructured host matrix while also interacting with the wall of the cell to create slightly-altered cell function without resulting in cell wall compromise and inevitable cell death that results from the use of traditional surfactants. This feature allows CDA to be extended to include biologically-relevant, water-soluble lipids that enable us to more closely mimic the complicated extra-cellular matrix. The complex interaction between lipid, the

evolving nanostructured silica host, cell wall, and pH changes within the system combine to create a unique system for immobilizing yeast cells.

1.1.3.8 CDA provides a unique route to viable yeast encapsulation

Although an interesting phenomenon at least, in order for CDA to be considered a fully-useful procedure for cell encapsulation, the cells must remain viable following immobilization. We assessed the viability of yeast cells encapsulated in lipid-templated, nanostructured silica matrices using the cell-directed assembly process with various short-chain phospholipids by using the standard, two-color, fluorescent yeast viability probe kit from Invitrogen. The data was collected on a fluorescence microscope with a filter set designed especially for imaging this viability probe and the results are shown below in Figure 0-14.

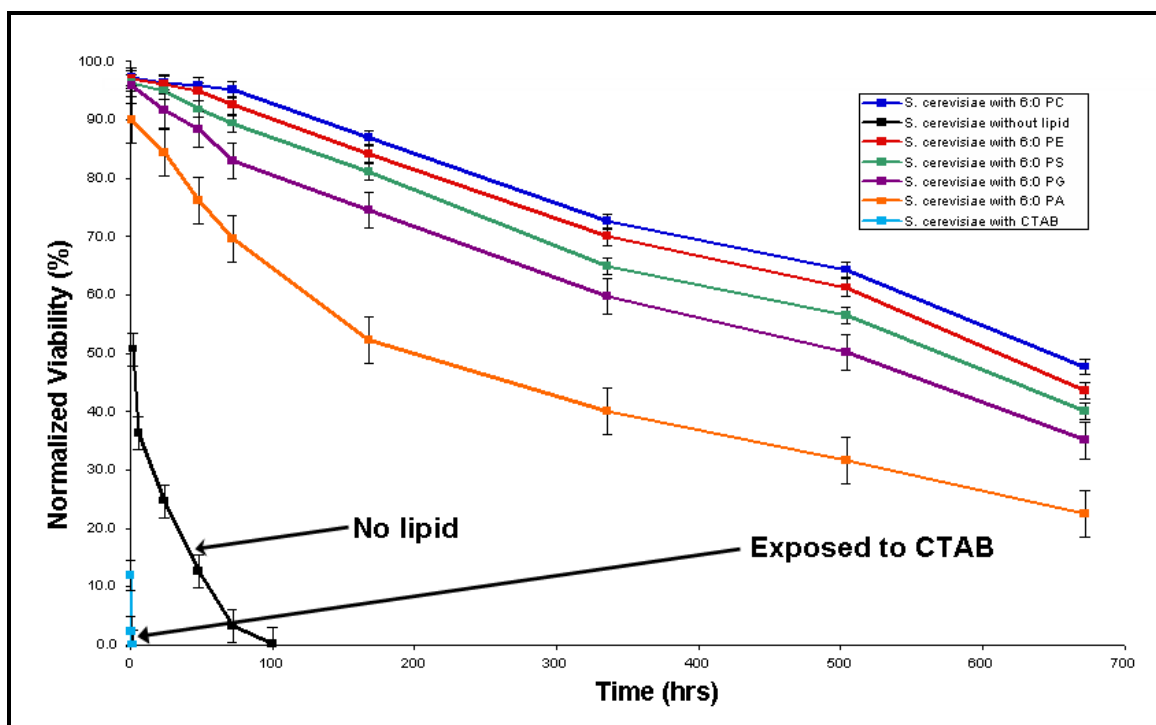


Figure 0-14. The use of different surfactants drastically alters yeast viability in CDA. Viability was assessed using the standard two-color fluorescent probe for yeast with various or no surfactants. Viability directly correlates with the ability to form a localized lipid layer and maintain a buffered pH gradient. We also find that traditional surfactants (CTAB) are not compatible with cells in CDA. At all times $p < 0.05$ when comparing cells immobilized with lipid versus those without, according to ANOVA Dunn Post-Test. Error bars represent 95% confidence interval.

We find that encapsulation of yeast using CDA with any of the various lipid headgroups creates a system allowing the cells to remain viable on the benchtop without exogenous buffers or media for at least 4 weeks. This clearly demonstrates the usefulness of CDA as an encapsulation technique for live-cell based studies and devices. The prolonged viability without the need for external fluids establishes CDA as the premiere technique for incorporating cells within solid-state devices, as no other technique has provided viability in a solid medium on the order of weeks.

The major advantage of the cell-directed assembly approach is the introduction of short-chain phospholipids as biocompatible surfactants. The fluidic lipid interface formed during CDA protects the cell from both mechanical and chemical stresses. Cells immobilized by CDA have markedly improved viability compared to cells immobilized in traditional sol-gel silica films. When cells are immobilized in silica matrices without lipid, 50% of the cells are dead within 2 hours and less than 10% are alive at 3 days. Attempts to use a traditional surfactant, such as CTAB, to create a silica host matrix results in only 10% of cells remaining viable after one hour. Immobilizing cells through CDA with *diC₆PC*, however, preserves cell viability at more than 93% at 3 days, with over 50% of the cells remaining viable for several weeks. Weight loss measurements and spectroscopic analysis of the lipid/silica/cell system during CDA show that the hygroscopic nature of the lipids and their organization into a uniform nanostructure serve to suppress the overall water loss, allowing the cell to be maintained in a fluid, water-rich microenvironment, even upon evacuation and electron imaging in a SEM.

Closer examination of the data demonstrates the essential dual nature of the lipids as bio-compatible surfactants. While the introduction of the lipids dramatically extends the viability of the cells, the viability is also clearly dependent on the type of lipid and resulting physical system that is developed. We find that the highest viability is obtained when cells are surrounded by localized lipid-rich region that allows for a coherent, fluid interface with the nanostructured silica host leading to maintenance of an established pH gradient without dramatically perturbing normal cell functions, i.e. CDA using *diC₆PC*. However, viability decreases when any of these key features are compromised. For example, lower viability is observed when the extent of lipid localization is not high

(*diC₆PE*) or when the cell does not establish a large pH gradient (*diC₆PG*). Viability is even lower when the system does not feature lipid localization or pH gradient maintenance due to excessive cell wall permeabilization (*diC₆PA*). However, the clear viability advantage obtained through use of the short-chain phospholipids over traditional or no surfactants demonstrates the importance of encapsulating cells in a nanostructured host matrix that prevents excessive drying of water while also interacting with the cell through the use of biocompatible surfactants without causing excessive damage to the cell.

1.1.3.9 Surface proteins of encapsulated cells remain accessible and functional

In order to create any useful, cell-based system, it is essential that the cell remains not only viable but also retains normal cell functions and is accessible to the environment for probing and waste exchange. Measuring viability of cells immobilized via CDA by using fluorescent probe molecules not only gave an indication of cell viability, but also elucidated the accessibility of the immobilized cells to the environment. Additional work with GFP-modified yeast immobilized via CDA confirmed accessibility of the cell to liquid media as well as the ability of the cell to participate in normal cellular functions like transcription and translation. To confirm that immobilization of cell-directed assembly did not damage receptors on the cell surface, important to almost all applications of any cell-based system, fluorescent anti-bodies were introduced both during CDA and following encapsulation. The ability of the antibodies to recognize and

bind their surface receptors was monitored with confocal microscopy, and the results are shown below in Figure 0-15.

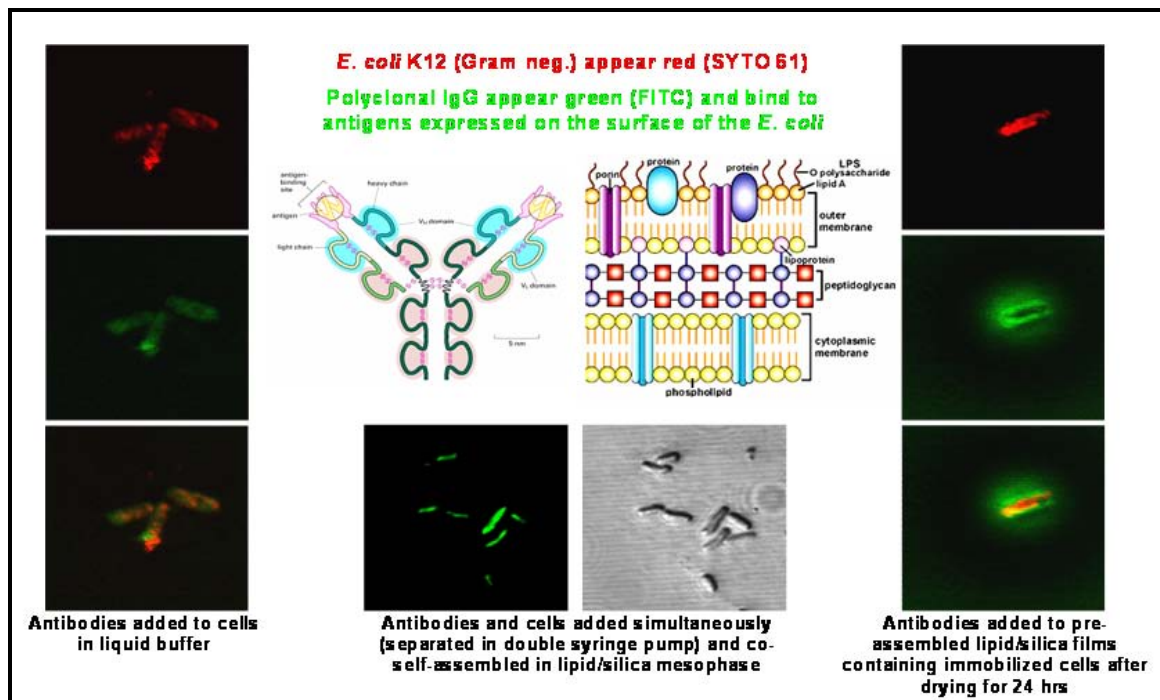


Figure 0-15. Antibodies are used to confirm that cell surface proteins remain intact and accessible throughout CDA. Cells were stained red and antibodies were labeled green prior to visualization using confocal microscopy. Antibodies added to cells in liquid buffer bind in the expected manner (left). Antibodies added in liquid during the CDA process also bind in a similar manner (middle) indicating that the exposure to silica and solvents does not destroy surface proteins. Antibodies added following immobilization (right) are also able to bind the cell surface, indicating that the cell surface is accessible and that the drying process does not dramatically alter the cell surface.

Although discussion of immobilization of various cell types using CDA will follow, to demonstrate cell surface accessibility *E. coli* bacteria (fluorescently stained red) were immobilized using CDA with *diC*₆PC. FITC-tagged anti-*E. coli* IgG antibodies (green) were added either before, during, or after encapsulation in order to determine

ability to access and bind surface proteins. The images show that antibodies added during CDA have identical binding characteristics as those added to cells in buffer. This indicates that the cell surface remains accessible during the assembly process, which is not surprising considering that the cells and antibodies are added together in a liquid solution. This also indicates, though, that the assembly process, with the surfactants, solvents, and acid, does not damage the cell surface to the point of denaturing the cell surface proteins and does not dramatically effect the fluidity of the cell surface.

To confirm accessibility and functionality of cell surface proteins following encapsulation, cells were first immobilized in a nanostructured thin film via CDA and then allowed to dry on the benchtop for 24 hours. When films were then exposed to a liquid solution of antibodies, we find that the antibodies are still able to recognize and bind cell surface proteins. This demonstrates that, even following immobilization and drying, the surface of the cell remains functional and accessible. Interestingly, a noticeable gradient of antibodies can be seen disseminating from the surface of the immobilized cells, confirming that although the cell surface is accessible, there are transport limitations when attempting to access the encapsulated cells that would not be present in a well-mixed liquid system. This ability to maintain molecular gradients within the film could have several applications for biological investigations, as the importance of chemical gradients in numerous cell signaling pathways are becoming more evident in biological and biomedical systems.

1.1.4 Increased functionality through the addition of foreign nanocomponents

To increase the functionality of the system and investigate new bio/nano interfaces, various nanoscale components have been added to the system. We find that hybrid materials can be obtained that retain the ability to create localized lipid layers around the cell and an ordered nanostructure while also introducing various nanoparticles, proteins, and DNA, as seen in Figure 0-16. These additions allow us to not only impart new properties to the material, but also to impart new properties to the cells themselves.

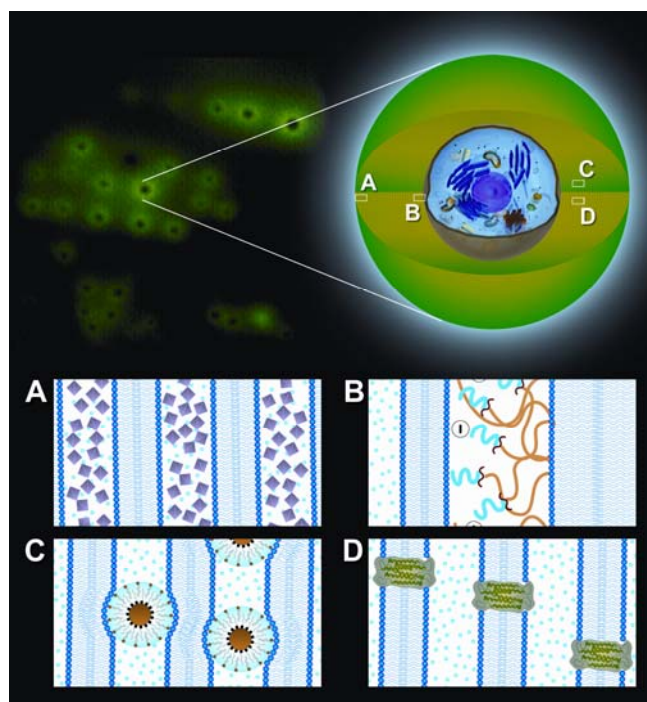


Figure 0-16. Novel bio/nano interfaces are obtainable using CDA. During CDA, living cells are encapsulated in a nanostructured silica host (A) and protected by a lipid interface (B). Added nanocomponents [nanocrystals (C) and proteins (D)] are localized in the fluid lipid interface.

1.1.4.1 Nanoparticles can be organized by cells during assembly

Over the past several years, synthesis of a wide variety of nanoparticles has become prevalent. The ability to control particle size and shape has been elucidated, and a variety of nanoparticles with novel functionalities have been produced^{9,10}. One major drawback of most synthesis methods is the lack of nanoparticle biocompatibility, as the particles are either soluble only in organic solvents, which are lethal to living cells, or are stabilized by surfactants that disrupt cell membrane integrity and lead to cell lysis. Our group has previously demonstrated the synthesis of biocompatible nanoparticles via phospholipid encapsulation¹¹, and we find that the addition of these particles, which would be toxic to cells using standard preparation techniques, do not substantially affect viability when combined with living cells during CDA and is described in more detail below. A schematic of the CDA process with the addition of nanoparticles is shown below in Figure 0-17. In addition, cells are able to actively organize these biocompatible nanoparticles at the cell surface, which has been confirmed using TEM and confocal microscopy.

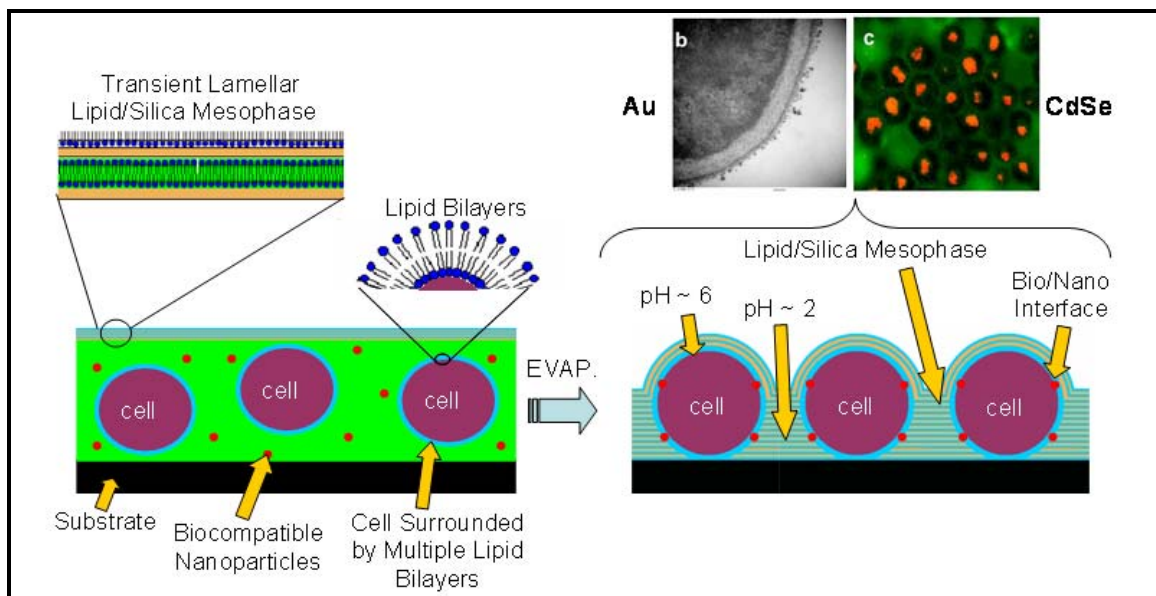


Figure 0-17. Schematic representation of the addition of functional nanocomponents during CDA. Components are added to mixture of cells, lipid, and aqueous silica precursors (left). Following evaporation, compenents can be localized by the cell and organized in the ordered nanostructured host (left).

SEM, EDS, and Grazing Incidence Small Angle X-Ray Scattering (GISAXS) have also been used to investigate the localization of biocompatible gold nanoparticles at the surface of yeast cells during CDA, with results shown below in Figure 0-18. We find in SEM images that with large amounts of gold particles (~1 wt %) the cells will actually organize the particles into what resembles an semi-cohesive shell whose composition was confirmed by EDS. Further investigation into the organization of these particles reveals that they are actually arranged in a manner that is not predicted by normal, passive assembly. Instead, the particles are actively arranged by the cell to form an unanticipated, yet ordered, nanostructure around the cell, in a manner similar to that of the cell organization of lipids resulting in unanticipated nanostructures.

To further extend the CDA process and investigate several other possible bio/nano interfaces of interest, a range of different functional nanoparticles have been introduced with yeast via CDA and the corresponding viability of cells following encapsulation was monitored. We see from Figure 0-19 below that the viability of cells changes when different types of nanoparticles are introduced in similar concentrations. Biocompatible gold nanoparticles, of interest in electronic devices and as infra-red heat transmitters, have the smallest effect on cell viability. This is not surprising, as colloidal gold has long been used as a homeopathic supplement and is not known to be toxic except in exceedingly high doses. Magnetic iron oxide particles, which have been coated with an identical lipid coating as the previously mentioned gold particles, also have a minimal impact on viability as expected. These magnetic particles would be especially interesting for targeted delivery of materials, cell sorting, and ablation of cells with oscillating magnetic fields. Fluorescent cadmium selenide nanoparticles, of interest as stable optical markers, have the largest negative impact on cell viability. This is also not surprising, as cadmium is known to be toxic as it accumulates in cells. Most importantly, this data serves as evidence that CDA can be used to create many new bio/nano interfaces featuring living cells and inorganic particles of interest for continuing development of cell-based systems, most notably the Surface-Enhanced Raman Spectroscopy (SERS)-based cell discovery platform currently in development through a collaboration between our group, Northwestern University, and the University of Washington.

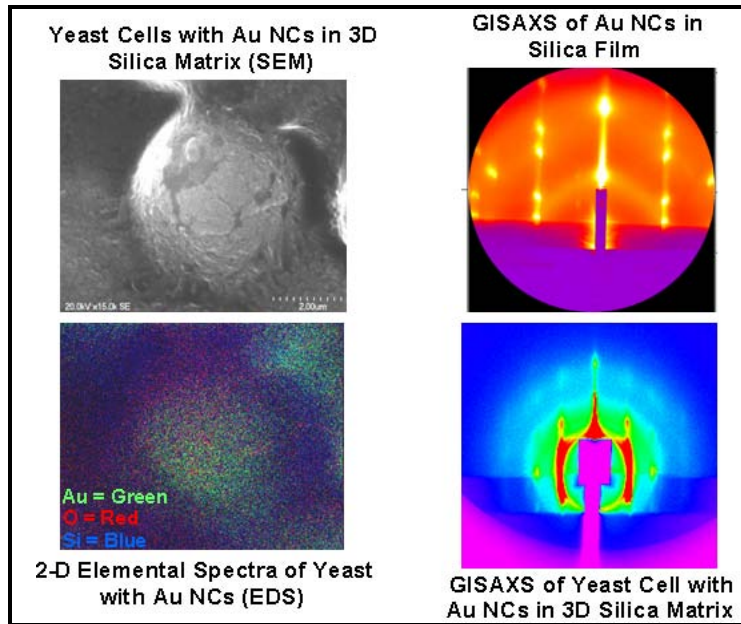


Figure 0-18. Cells will localize and organize lipid-coated Au nanoparticles during CDA. SEM (top left) and EDS (bottom left) confirm the presence of localized Au. Additionally, GISAXS was used to find that the nanoparticles are organized by the cell (bottom right) differently than the particles would normally self-assemble (top right).

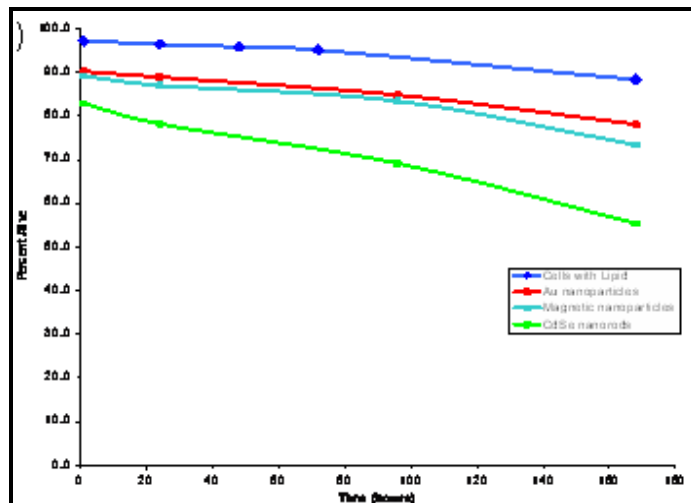


Figure 0-19. Viable yeast can be immobilized with various nanoparticles using CDA. Viability was determined using the standard two-color probe kit. Although having lower viability than the standard lipid/silica system (blue), viable cells remain in systems following the addition of Au nanoparticles (red), FeO nanoparticles (aqua) and CdSe quantum dots (green).

1.1.4.2 Functional foreign proteins can be introduced during CDA

Attempts to physically modify the cell surface and introduce new functionality through the integration of non-native proteins have seldom been successful due to the complexity associated with proteins and cells. Therefore, cell modification is usually accomplished via labor intensive, time consuming and expensive genetic modifications. Genetic engineering techniques require extensive specialization, and although considerable progress has been made in genomics and proteomics, there are still numerous physical barriers to overcome when attempting to introduce foreign functionality across cell species and kingdoms. Recently, we have demonstrated a novel technique that utilizes our CDA process to physically introduce functional bacterial proteins at the surface of yeast cells. Bacteriorhodopsin (BR) is a transmembrane photochromic protein isolated from the purple membrane of the salt marsh halophile, *Halobacterium salinarum*. It acts as an energy transducer, absorbing and converting light into chemical energy. We have introduced BR to yeast via CDA using two approaches: addition of the purified protein directly, as described above for nanoparticle introduction, or incorporation of the BR into a DMPC liposome as depicted below in Figure 0-20 prior to addition during CDA.

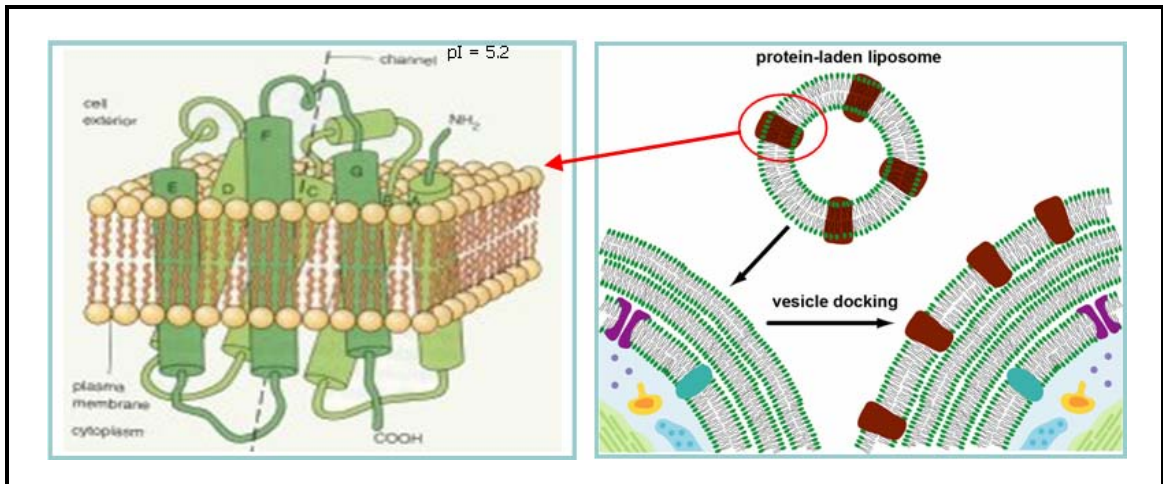


Figure 0-20. Introduction of bacteriorhodopsin (BR) during CDA via liposome stabilization. Left shows representation of membrane stabilized BR protein. Right shows a mechanism for introduction to cell surface using vesicle docking of liposome stabilized BR.

The top row of confocal images in Figure 0-21 shows that adding the protein (fluorescently labeled red) directly results in BR localization in a somewhat diffuse region that corresponds closely to the region of *diC₆PC* lipid localization (fluorescently labeled green). As seen in the lower row of images, the introduction of BR in a liposome results in a more conformal region of BR localization and that the longer chain DMPC (fluorescently labeled green) preferentially localizes at the cellular surface. Because BR functionality, like all transmembrane proteins, requires incorporation in a lipid bilayer with the structure/dimension needed to accommodate the hydrophilic and hydrophobic domains, we hypothesized that, to function as a protein pump, BR would have to be incorporated in a longer chain lipid bilayer. This is suggested by the large increase in the fluorescence output of the protein when added in the stabilized liposomes¹².

Figure 0-22 shows pH gradient development for these two approaches as measured by a fluorescent pH probe and confocal microscopy. We find that BR introduced in a liposome dramatically changes the pH gradient normally developed by the cell during CDA. This suggests the BR is functional and preferentially oriented at the cellular surface. These results point out a completely new approach in which proteins with unusual properties can be isolated from one organism and physically introduced at the surface of another organism via CDA to provide new, non-native functionalities without the need for genetic modification.

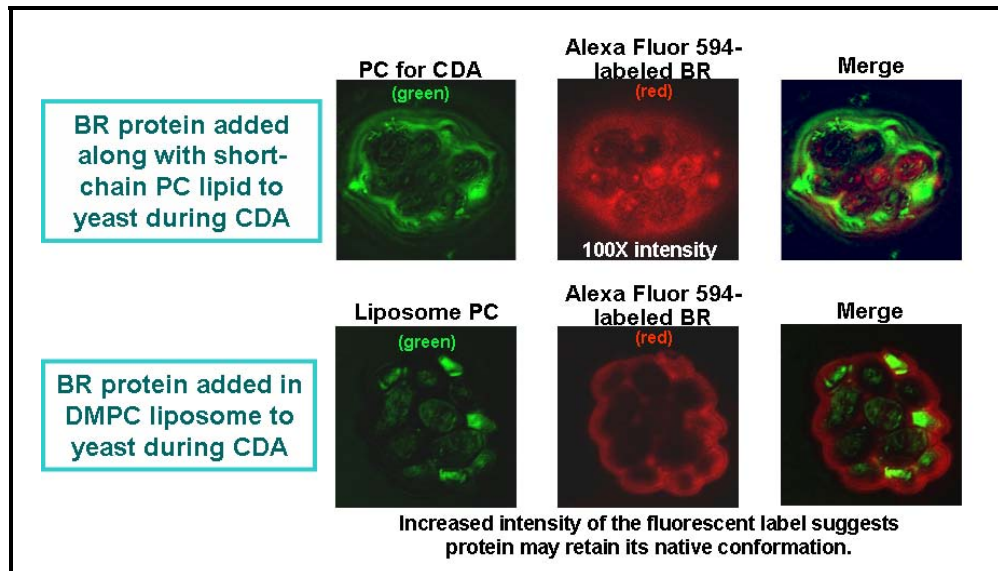


Figure 0-21. Localization of *diC₆PC*, DMPC, and bacteriorhodopsin during CDA. (Top) BR (red) can be localized to the cell surface when added in bulk during CDA with yeast and *diC₆PC* (green), although it does not form a very homogeneous region. (Bottom) BR (red) introduced in DMPC liposomes (green) show uniform localization and highly increased fluorescence.

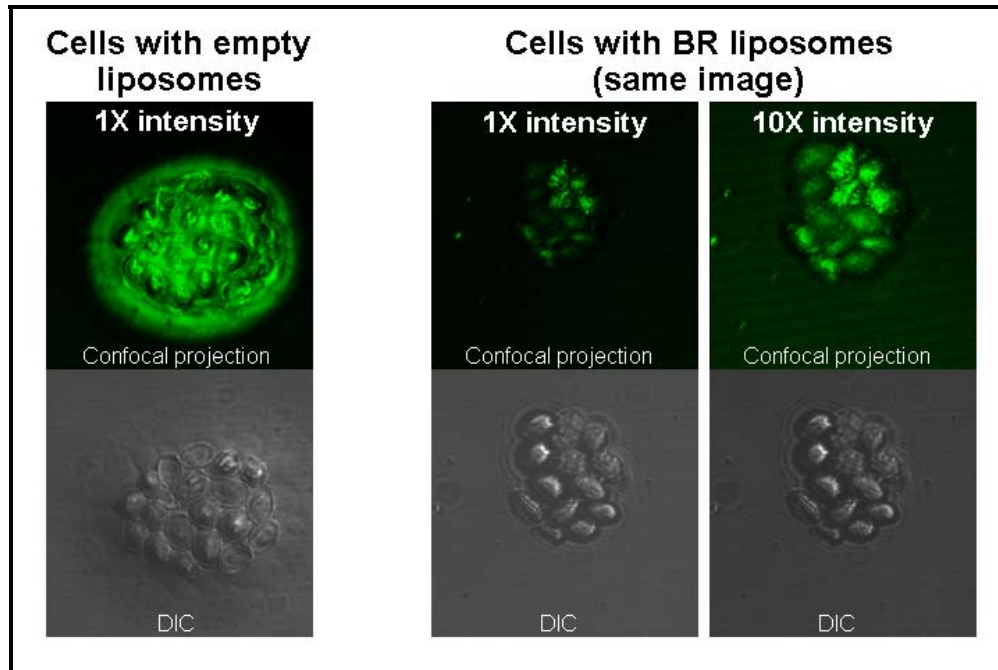


Figure 0-22. BR introduced within DMPC liposomes during CDA retains functionality. (Left) Confocal with pH probe (top) and DIC (bottom) indicate that liposomes alone do not affect pH. (Right) Confocal images with pH probe and different imaging intensities show that BR introduced in liposomes appears to be pumping protons toward the cell region, lowering the pH.

1.1.4.3 Efficient, in-situ genetic modification with exogenous DNA plasmids can be achieved with CDA

Genetic modification is typically accomplished by transforming bacterial cells with plasmids, pieces of extrachromosomal DNA that encode non-native genes. Since these plasmids are cell impermeable under physiological conditions, heat-shock or electroporation are used to make the host cells competent (a state during which plasmids can passively diffuse across the cell membrane). Standard transformation methods can be time consuming, require specialized equipment, and have low transformation efficiencies,

which necessitates the use of high plasmid concentrations. To mediate the limitations of current transformation technologies, we have recently demonstrated that high-efficiency genetic modification can be accomplished during CDA as shown below in Figure 0-23.

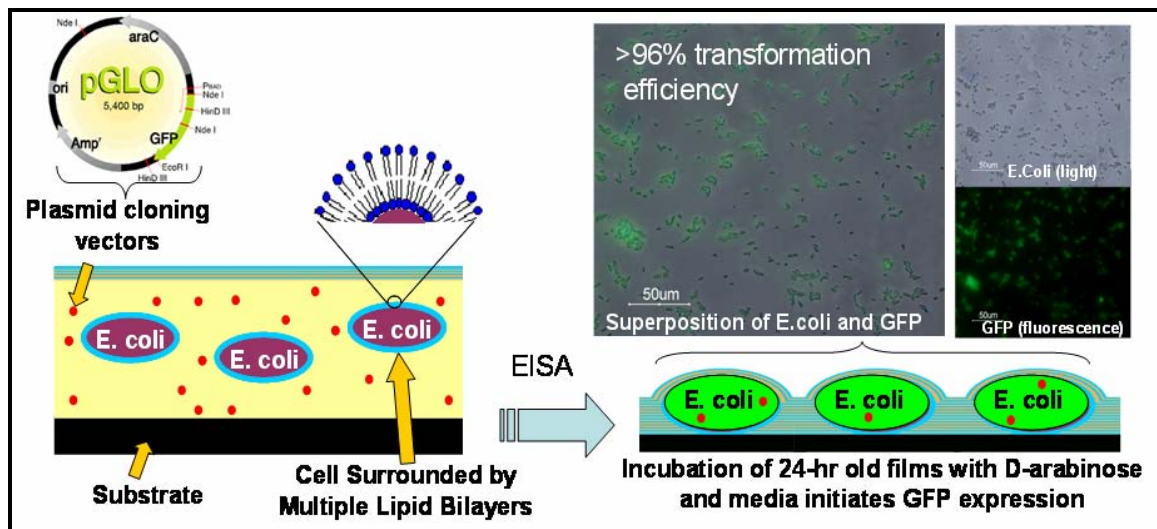


Figure 0-23. High efficiency cell transformation can be achieved via CDA. Schematic illustrates the uptake of DNA plasmids by *E. coli* during CDA with *diC₆PC*. (Right) Fluorescence and optical images show the expression of GFP indicating the uptake of the plasmid DNA following CDA and incubation of cells in films with media and the plasmid promoter, arabinose.

Using *E. coli*, *diC₆PC*, and pGLO plasmids (for introducing D-arabinose dependent GFP expression) introduced during CDA, we find that the plasmids are immediately localized at the cell surface, creating a high effective concentration gradient. Combined with the fluid nature of the bio/nano interface and the gentle permeabilization of the cell membrane by biocompatible short-chained phospholipids, plasmids are able to enter the cell under ambient conditions during the evaporation-induced assembly process. The result is a transformation that approaches 100%, compared to an efficiency of 24%

when transforming cells using the plasmid manufacturer's heat-shock protocol. This amazingly high transformation rate is achieved while using 1/100th of the amount of DNA material as required for the heat-shock method. This simple procedure yields a new method for in-situ genetic modification of immobilized cells that achieves nearly complete cell transformation while using small amounts of genetic material that approach the elusive goal of one transformed cell for each added plasmid.

1.1.4.4 Nutrients can be added while still maintaining cells without liquid

One major detraction of previous applications of cell-directed assembly was the necessity to add exogenous liquid nutrient media in order to allow the cell to undergo useful cycles of transcription and translation. This requirement effectively nullifies the main advantage of traditional CDA – that the cells do not need to be maintained in liquid to ensure viability. Prior to modifications to the CDA process to include media, one would have to take the cells encapsulated in the solid film and immerse them in liquid media along with the analyte of interest in order to elicit the desired response, such as GFP expression. This greatly inhibits the usefulness of the device as a cell-based sensor since the sensor does not actively respond without adding exogenous media. This also nullifies the use of CDA for creating platforms for cell communication, as the addition of liquid changes the transport of signaling molecules and reduces the system back to the standard case of cells in a culture flask or Petri dish. To address these inadequacies, two

strategies have been developed to introduce media while maintaining the ability of the encapsulated cells to function in a solid-state device, as shown below in Figure 0-24.

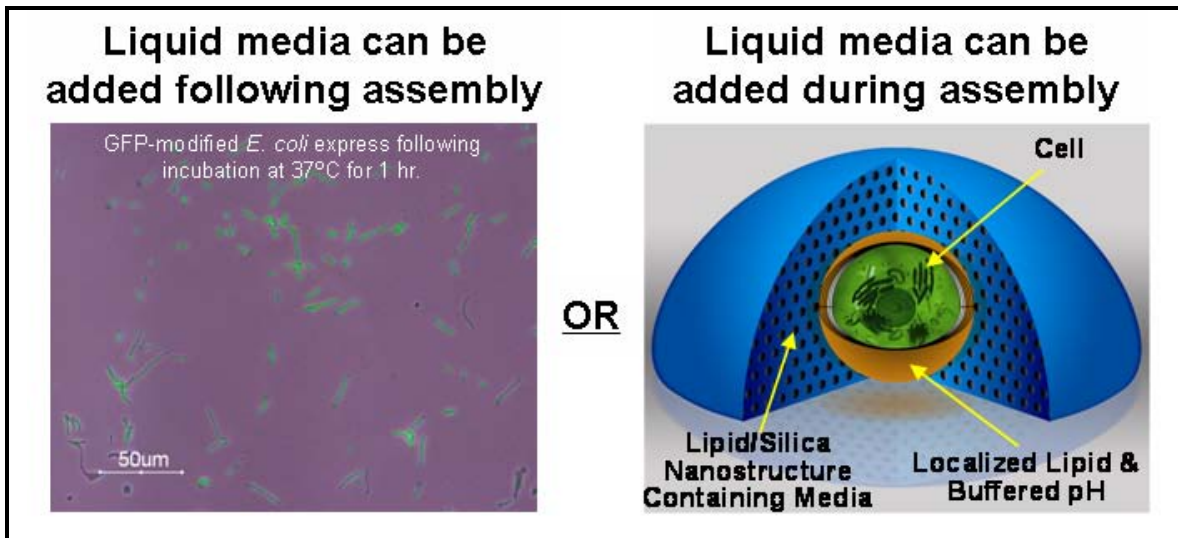


Figure 0-24. Different methods for inclusion of media to matrix compatible with CDA. (Left) Liquid media can be added following the immobilization of GFP-modified *E. coli*, then allowed to dry prior to incubation to induce expression. (Right) Schematic illustrates how media can be included in lipid/silica nanostructure by substitution for water in sol recipe.

In the first and simplest strategy, liquid media can be added following encapsulation of cells via CDA. In this technique, once created, the solid films are immersed in media, allowing exchange of the previously-mentioned water retained within the nanostructure with the aqueous-based media. The cells are then removed from the liquid media and dried with air. This technique has been used to induce GFP expression in genetically-modified *E. coli*, where media containing a plasmid-activating analyte was exchanged with the water in the nanostructure. Following drying, the solid-

state film of encapsulated cells was incubated at 37°C for 1 hour. Fluorescence microscopy confirmed that the media in the nanostructure was available to the cells, allowing them to express GFP.

In the second and more useful strategy, the recipe for the biocompatible silica sol can be modified to include media. This undertaking is not trivial, as the change in pH and electrolytes inherent in adding media affect the kinetics of the biocompatible sol developed previously through much trial and effort. What was found, however, was that, for most types of liquid media, a certain amount of water in the sol recipe could be substituted directly with media without drastically altering the sol-gel kinetics. This technique allows for the inclusion of media during the assembly of the material without compromising the material properties of the film or requiring the encapsulated cells to be re-immersed in liquid media. In order to conduct investigations of communication among immobilized cells, this strategy can be employed in order to avoid altering the transport of molecules by immersing the cells in liquid.

1.1.5 Extension of Cell-Directed Assembly to different cell types

Initial research into cell immobilization in thin films via cell-directed assembly (CDA) centered on using the yeast *Saccharomyces cerevisiae* as a model organism because it is both single-celled and eukaryotic. Continued characterization of immobilized yeast cells has since demonstrated that the number of functional cells present in the device after 3 months far exceeds the requirement for a usable sensor despite exposure to ambient conditions with no added buffer or nutrient media. This data has been independently verified by colleagues working with the US Air Force. In order to extend the CDA approach beyond the well-developed yeast-based system, preliminary studies of other cell types have been performed to determine the feasibility of using CDA as a general cell encapsulation technique.

1.1.5.1 Bacteria can be successfully encapsulated via CDA

Both Gram-positive (*Bacillus subtilis*) and Gram-negative (*Escherichia coli*) bacteria participate in CDA in a manner similar to yeast, as shown below in Figure 0-25 and Figure 0-26, respectively. All types of bacteria that were tested demonstrate a common ability to organize phospholipids (*diC₆PC*, fluorescently labeled green) at the cell surface and to alter the local pH (as observed using a green fluorescent probe, Oregon Green). Although each cell type shares these common traits, each does so in a

slightly different manner or to a different extent, which confirms that each cell type actively participates in the assembly process. Overall, we have recently discovered that many single-celled organisms can be immobilized in nanostructured thin films by utilizing cell-directed assembly. These materials all possess the major qualities of the model yeast-based system, including fluidic connectivity and accessibility, resistance to desiccation, and enhanced viability. More so, CDA systems for immobilizing bacteria can be made using the same lipids and silica sols as with yeast, providing a general encapsulation route for live, single-celled organisms.

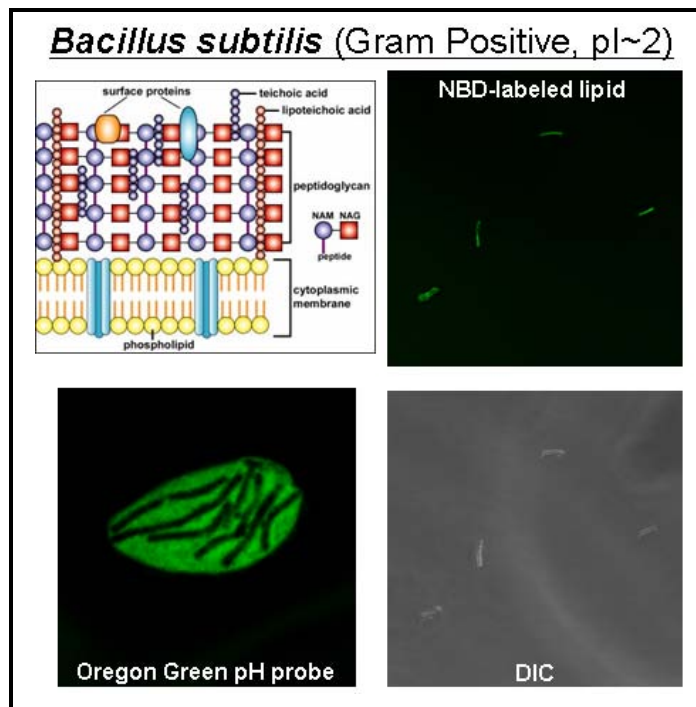


Figure 0-25. Lipid and pH effects of Gram-positive bacterium *B. subtilis* during CDA with *diC*₆PC. (Top, left) Schematic of Gram positive cell wall. (Bottom, left) Fluorescent pH probe indicates that a buffered local pH gradient is formed. (Right) Confocal fluorescence (top) and DIC (bottom) images show localization of NBD-tagged *diC*₆PC around cells.

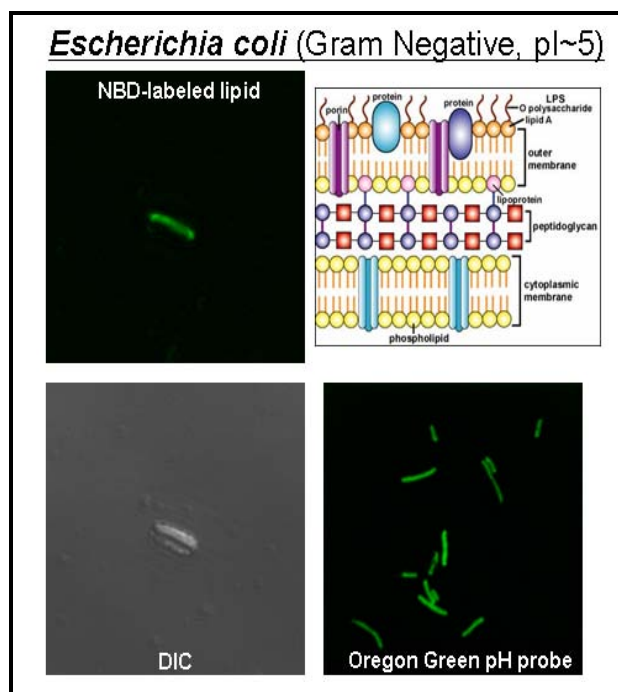


Figure 0-26. Lipid and pH effects of Gram-negative bacterium *E. coli* during CDA with diC_6PC . (Top, right) Schematic of Gram negative cell wall. (Bottom, right) Fluorescent pH probe indicates that a very localized buffered pH gradient is formed. (Left) Confocal fluorescence (top) and DIC (bottom) images show localization of NBD-tagged diC_6PC around cells.

To extend the applicability of our CDA process, we have continued to explore the structure and properties of systems prepared with new organisms and cells - model organisms which provide a baseline to understand the influence of nanostructuring on cellular behavior, unique organisms which may allow the development of unprecedented functions in cell-based devices, and mammalian cells. For example, we have demonstrated CDA with a model eukaryote, *S. cerevisiae*, a model Gram-negative bacterium, *E. coli*, and a model Gram-positive bacterium *S. epidermidis*. We have also

investigated CDA with the anthrax analogue *B. subtilis* for potential biodefense studies, the tuberculosis analogue *M. smegmatis* for potential infectious disease studies, as well as extremophiles like *T. aquaticus*, which lives in high-temperature environments, and *D. radiodurans*, which withstands extraordinary exposures to DNA damaging radiation. We find that all these microorganisms can be successfully immobilized via CDA using identical procedures as yeast. However each organism or cell displays its own unique behavior/interface. We have studied these interactions using GISAXS at the Advanced Photon Source at Argonne National Laboratories as seen below in Figure 0-27. We find that each cell type has a unique ability to localize the lipid surfactant and establish local pH and ion gradients that in turn effect the development of the silica nanostructure probed by GISAXS. In particular, extensive lipid localization at the yeast surface is correlated with the switching of the 2D hexagonal mesophase to a lamellar mesophase during CDA with *diC₆PC*, which is not observed for organisms which exhibit lower extents of lipid localization.

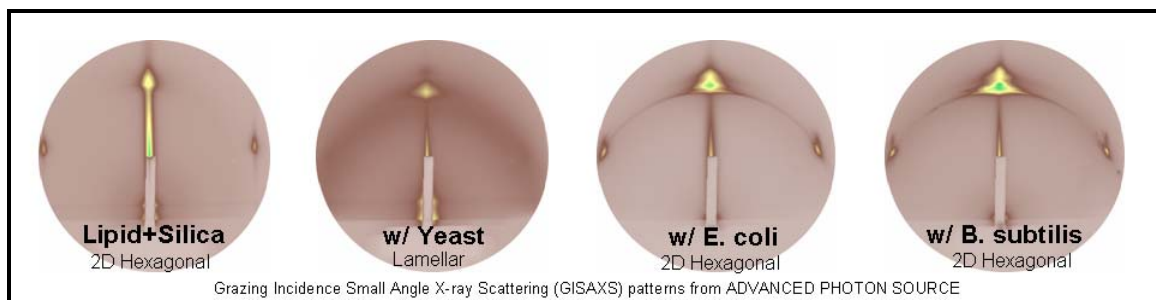


Figure 0-27. GISAXS patterns of various cell types with *diC₆PC* immobilized using CDA. (Far left) Hexagonal nanostructure is formed with 30 mg/mL lipid in sol E. (Near left) When yeast are added, a lamellar nanostructure develops. (Near right) A hexagonal structure forms when *E. coli* and *B.subtilis* (Far right) are used, although some disorder is evident due to localization of the lipid by the cells.

CDA allows each type of organism to interact with its environment during assembly, creating cell-specific assembly that is dictated by each cell's ability to alter pH and localize lipids to differing extents. The most dramatic difference is observed in the development of different nanostructures as mentioned above. The advantage of the CDA system, however, lies in this ability to be widely adaptable by the individual organisms. This flexibility results in remarkably high viability for all of the single-celled organisms that were investigated due to the ability of each cell to be immobilized in a material which it has modified to create a survivable environment. As shown below in Figure 0-28, viability of cells immobilized into a solid-state nanostructured lipid/silica film and incubated at room temperature in air without external fluids or nutrients far exceeds those immobilized in silica alone after just a few hours. After 10 days, we find that no more than 10% of any type of bacteria were viable when immobilized without *diC₆PC* lipid via CDA. However, at that same point in time, no less than 70% of any type of bacteria immobilized using cell-directed assembly were viable. This clearly demonstrates the

utility and flexibility of cell-directed assembly as a technique that is widely-applicable to immobilization of many, and possibly all, types of single-celled organisms.

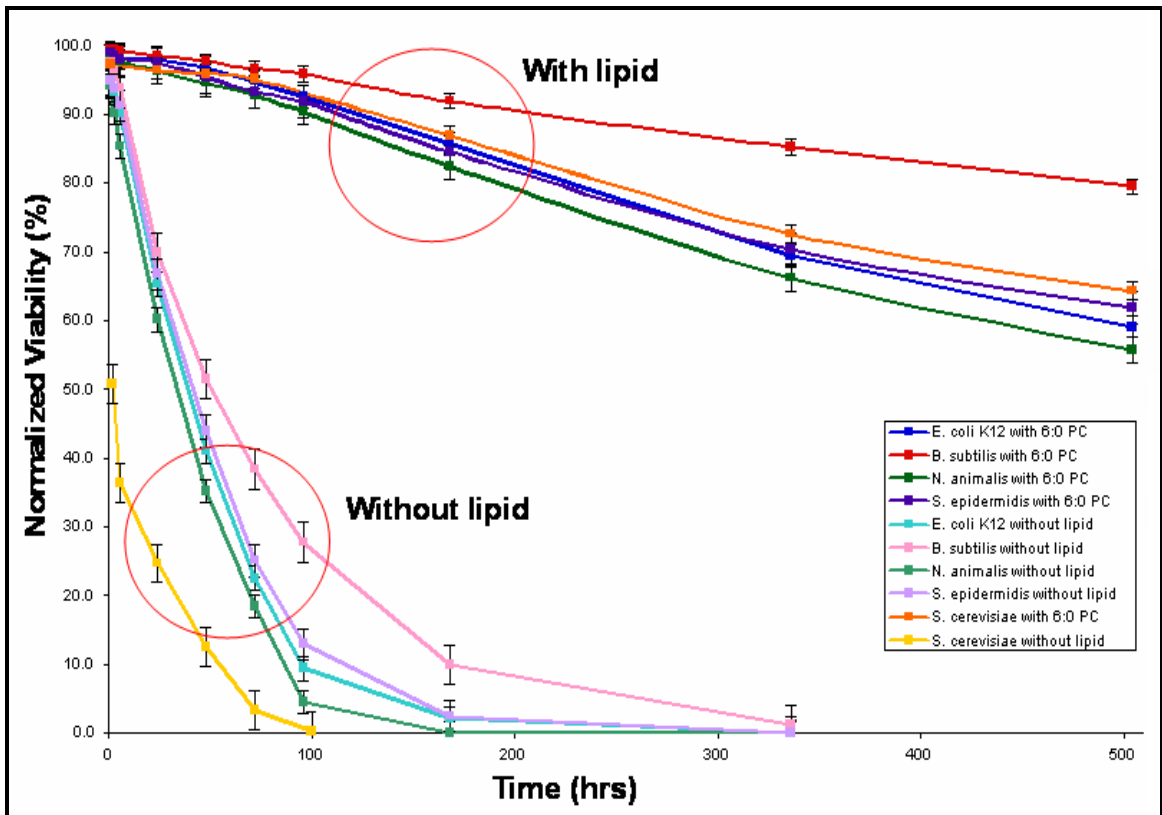


Figure 0-28. Viability of various single-cell organisms encapsulated in via CDA with *diC₆PC*. Viability was evaluated with the standard two-color fluorescent probe for various cells immobilized with (top) and without lipid (bottom). At all times $p < 0.05$ when comparing cells immobilized with lipid versus those without, according to ANOVA Dunn Post-Test. Error bars represent 95% confidence interval.

1.1.5.2 CDA is not highly compatible with mammalian cells

Our previous research has demonstrated CDA as a general immobilization route for various single-celled organisms. To enhance the viability of immobilized cells, we have investigated new media in which to conduct CDA that incorporate essential nutrients and allow the nanostructured silica host to serve as a nutrient reservoir. In this fashion we maintain cellular access to necessary resources and avoid the requirement for constant regeneration of nutrients common to all other cell immobilization techniques to date. Supply of nutrients is especially important for extending CDA to mammalian cell lines. Whereas single-celled organisms can senesce, or pause their metabolic activity until more nutrients are available, mammalian cells quickly expire without constant access to nutrients and other chemical factors. We expect immobilization of mammalian cells to be important for tissue engineering, directing cell differentiation, and studying the onset of disease.

We have used CDA to incorporate model mammalian cells, such as adherent human embryonic kidney (HEK) cells, into our lipid-templated host nanostructures and have found that mammalian cells (stained red) localize and internalize phospholipids (fluorescently-labeled green *diC₆PC*) in a fashion similar to, yet distinct from, single-celled eukaryotes and prokaryotes, as shown below in Figure 0-29. Most notable is the rapid internalization of the *diC₆PC*, reminiscent of CDA with apoptotic yeast. This large influx of lipid could lead to metabolic difficulties, resulting in lower than expected viability.

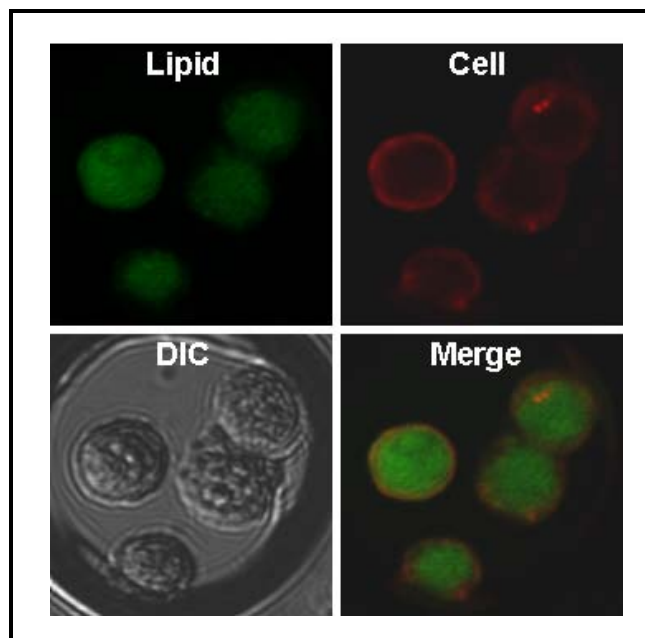


Figure 0-29. Localization and internalization of diC_6PC by HEK cells during CDA. (Bottom left) DIC image shows four cells immobilized in silica nanostructure. Confocal images show the rapid internalization of NBD-tagged lipid (top left) within the red-stained cell (top right), clearly illustrated when the two color images are merged (bottom right).

To assess the viability of the HEK cells immobilized via CDA, fluorescent probes were utilized. Live cells are distinguished by the presence of ubiquitous intracellular esterase activity, determined by the enzymatic conversion of the virtually nonfluorescent cell-permeant calcein AM to the fluorescent calcein, producing an intense uniform green fluorescence in live cells. Ethidium homodimer enters cells with damaged membranes and undergoes a 40-fold enhancement of fluorescence upon binding to nucleic acids, thereby producing a bright red fluorescence in dead cells. The results are shown below in Figure 0-30 for cells that have been encapsulated and allowed to incubate in for 1 hour at 25°F. With the usual CDA protocol, we determined that the number of cells alive after one hour is at least equal to the number of cells alive in buffer, indicating that the CDA

immobilization process does not cause irreversible damage to the cell. Although the viability of mammalian cells immobilized via CDA is equal to that of cells in buffer, the overall viability is not high enough to be useful for most mammalian cell studies. However, this does confirm the ability to use CDA to immobilize intact, mammalian cells, indicating that modifications to the CDA process could be made that would allow incorporation of mammalian cells into solid-state matrices with extended viability.

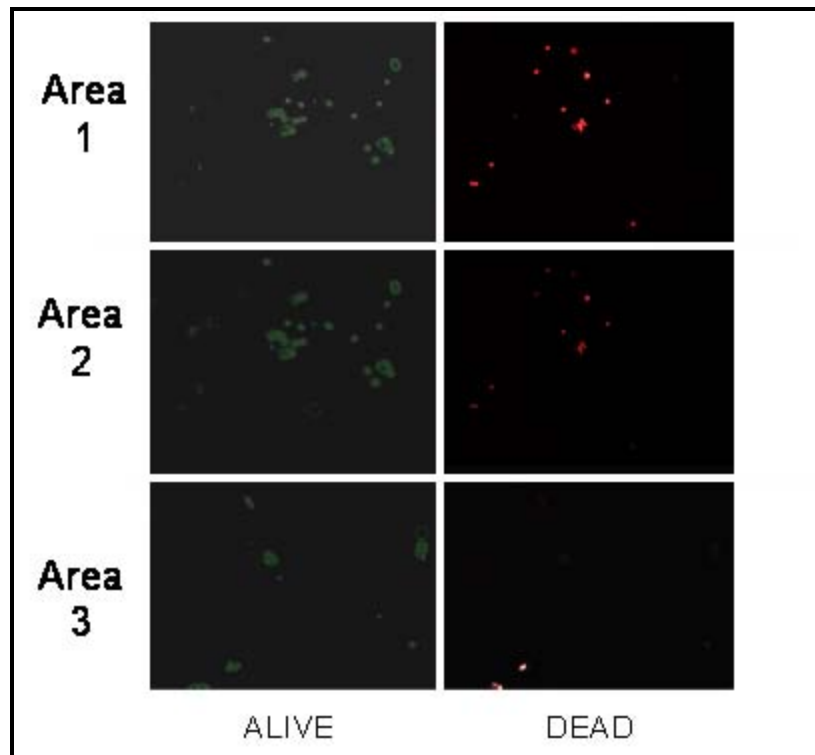


Figure 0-30. Fluorescent viability probe images of HEK cells immobilized via CDA and allowed to incubate for 1 hour at 25°F. Two-color fluorescent viability probe was used to assess 3 areas of immobilized cells within a silica nanostructure. Live cells appear green (left) without any red stain (left) which indicates damaged metabolic activity.

1.1.6 Applications of Cell-Directed Assembly in cell biology

Using a unique self-assembly scheme to isolate individual bacteria (*Staphylococcus aureus*) within a well-defined nanostructure, we prove that so-called ‘quorum sensing’ (QS) and genetic re-programming can be self-induced in a single organism. The QS hypothesis is that bacteria use signaling to detect cellular density. If a quorum exists, bacteria coordinate their gene expression to function as a unit, thereby providing group benefits exceeding those of individual cells. This idea that bacteria act cooperatively for the social good is so appealing that the postulated mechanism and benefits of quorum sensing have become accepted uncritically. No study to date has established the behavior of an individual organism physically and chemically isolated from all others. Using our reduced physical system to simulate the endosomal compartments in which these bacteria become isolated, we show unambiguously for the first time quorum sensing and genetic re-programming to occur at the individual cell level, consistent with evolutionary selection according to ‘survival of the fittest’. This should have profound implications on the interpretation of why QS occurs and how it evolves. Moreover, we establish this discrete quorum sensing for *S. aureus*. In light of the immediate urgency in understanding drug resistance, it is important to note that the community-acquired MRSA strains USA 300 and USA 400 could become isolated within endosomal compartments and activate the discrete QS we describe.

Additionally, we apply an alternative self-assembly scheme to encapsulate *M. tuberculosis* in a physiologically mimicking environment. In order to simulate the lipid-

rich granulomas of the lungs in which these bacteria normally enter latent states, we have immobilized cells within silica nanostructures using phospholipids. We have then investigated the viability of these cells at dramatically extended times. This observed viability, combined with current investigations of the infectious capacity of these cells, could help establish a new model for TB latency that could lead to new drug treatments and vaccines aimed at eradicating this disease which currently affects one-third of the world's population.

1.1.6.1 Creating reduced physical systems for cell biology applications (demonstrated for quorum sensing by individual bacteria)

Nearly all bacteria emit and sense small, diffusible 'signaling' molecules (autoinducers) whose extracellular concentration regulates gene expression through a positive feedback control pathway. The prevailing view of why this signaling takes place is that it allows populations of cells to assess their density- i.e. to quorum sense (QS)¹³. If a quorum exists, bacteria change gene expression and coordinate their behavior, providing group benefits that would be unproductive at lower density¹⁴. However, this interpretation of QS ignores the cell's inability to distinguish between density and other factors influencing autoinducer concentration such as mass transport and degradation. This deficiency led Redfield to propose QS to be diffusion sensing, while Hense et al. proposed the term efficiency sensing: autoinducers would be used as metabolically cheap trial balloons to estimate the value of producing more costly, extracellular products^{15,16}.

These alternative QS motives depend strictly on local autoinducer concentration and should operate at the individual organism level. This is important, as complex group behaviors need to be invoked to account for both QS evolution and maintenance as ‘cheating’ can be common¹⁷. To reconcile these different perspectives, we hypothesized that QS, independent of any group benefit (which may be significant), must also provide benefits to individual bacteria. To verify this hypothesis, we used a nano-structured matrix to control the microenvironment of discrete, isolated bacteria¹⁸. We show self-induction and resultant genetic reprogramming to occur efficiently in individual organisms.

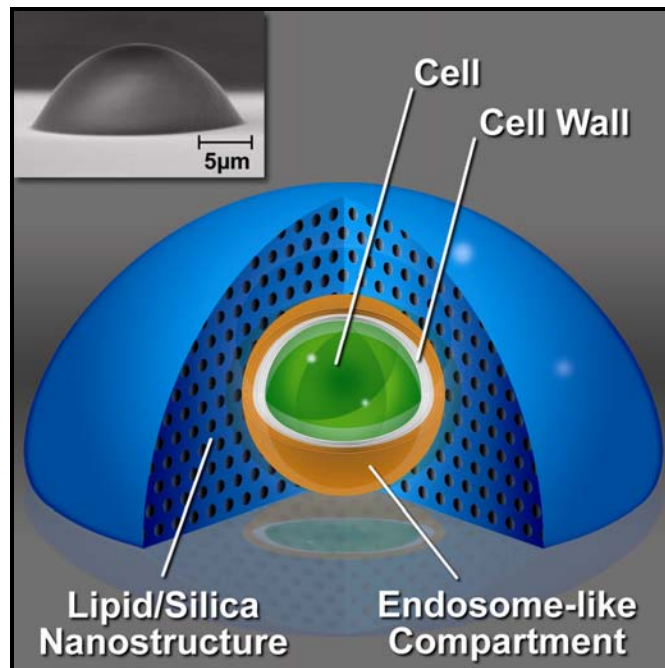


Figure 0-31. Schematic representation of a reduced physical system for individual cell studies. Aerosol is used to generate live cells encapsulated within isolated lipid/silica nanostructures featuring an endosome-like compartment around the cell.

Bacteria were immobilized, individually, within a matrix fabricated at a sufficiently small physical scale ($\sim 20 \mu\text{m}$ diameter, physically isolated hemi-ellipsoids) to ensure that the local cell density (~ 1 cell per $4 \times 10^3 \mu\text{m}^3$, equivalent to $\sim 2 \times 10^9$ cells ml^{-1}) exceeded the reported QS threshold ($10^7 - 10^9$ cells ml^{-1}). The matrix was formed by our cell-directed assembly approach, resulting in cells incorporated within a lipid vesicle surrounded by a silica nanostructure as depicted schematically with an actual SEM image inset in Figure 0-31. Nanostructured ordering of this system was confirmed using x-ray diffraction shown in Figure 0-32.

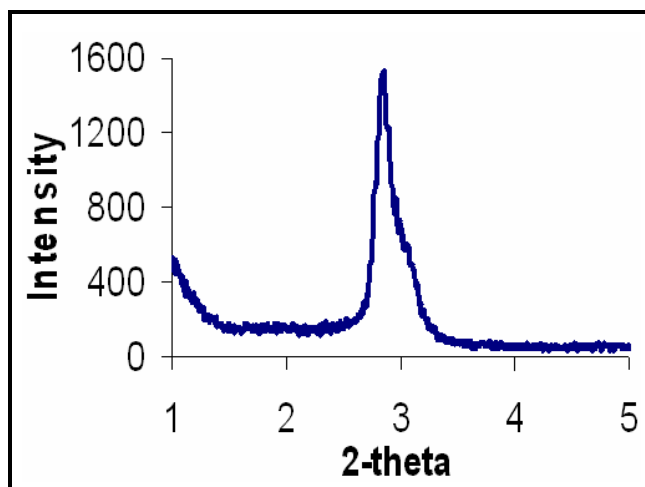


Figure 0-32. X-ray diffraction pattern verifying nanostructure of CDA droplet. XRD of film comprised of cells in lipid/silica droplets show considerable ordering.

Confocal fluorescence microscopy was used to confirm the presence of an endosome-like lipid vesicle surrounding the cell (Figure 0-33) and a physiological pH in

the local cell environment (Figure 0-34). This construct mimics a bacterium entrapped in an intracellular membrane-bound compartment (endosome) and allows individual cells to be maintained in a viable state under externally dry conditions that establish complete physical and chemical isolation of one cell from all others. As a model organism, we used *Staphylococcus aureus* known to become trapped in such intracellular compartments and to employ a QS strategy to switch to a more virulent form¹⁹.

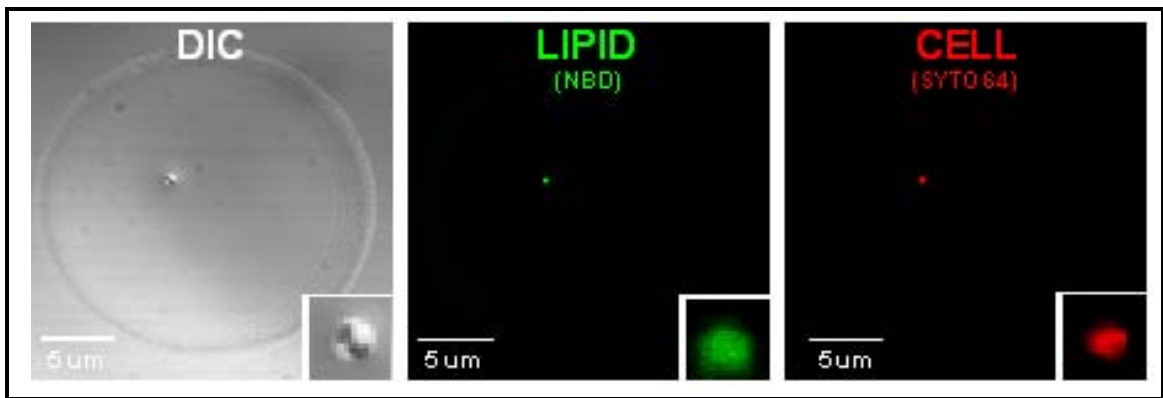


Figure 0-33. Endosome-like compartment is created by localization of lipid within a CDA droplet. (Left) DIC image shows cell entrapped within a lipid/silica droplet. Confocal images indicate NBD-tagged lipid is localized near the surface (middle) of the red-stained cell (right).

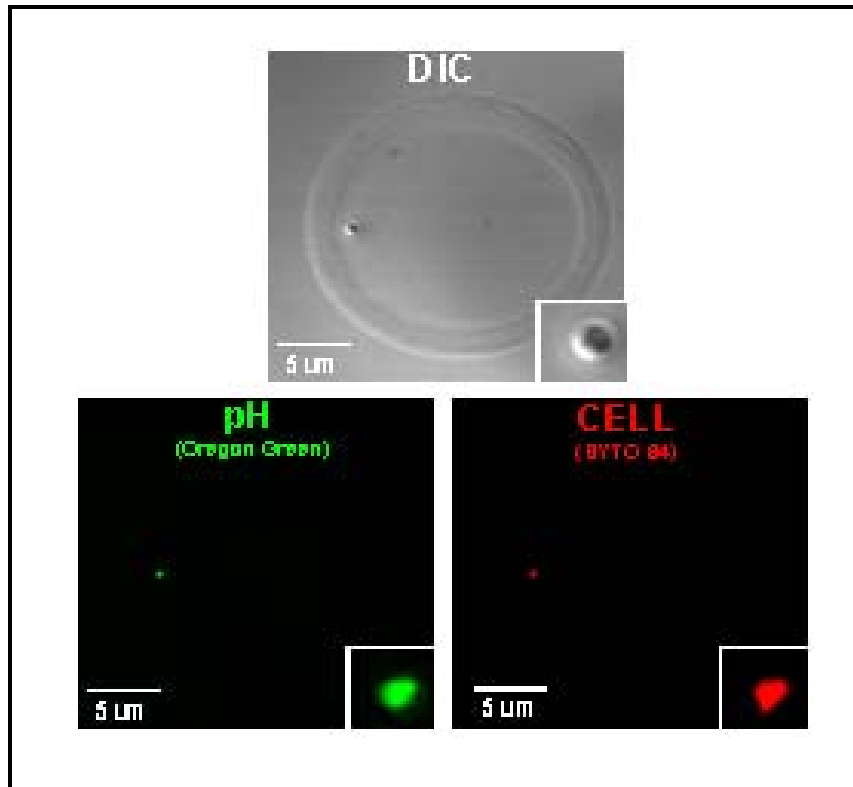


Figure 0-34. Physiological pH is established in endosome-like compartment created using CDA. (Top) DIC image shows cell entrapped within a lipid/silica droplet. Confocal images with fluorescent pH probe (left) indicate that a physiological pH is established near in the local region of the red-stained cell (right).

S. aureus detects and responds to an extracellular autoinducer peptide (AIP). Above a threshold AIP concentration, a phosphorylation cascade activates a regulatory RNA, which represses adhesin expression and induces production of secreted virulence factors like toxins. Phosphorylation also induces signaling by the QS operon responsible for production and export of AIP, exerting positive feedback control on this regulatory system²⁰. This feedback system is described below in Figure 0-35.

To date, quorum sensing in *S. aureus* has been studied exclusively in broth culture systems involving 10^7 - 10^8 bacteria that link growth phase to the genetic program of the entire bacterial population. Therefore, the potential for individual staphylococci to autoinduce is unknown. To observe QS in isolated, individual cells, we immobilized *S. aureus* strains that have been genetically modified to produce GFP at various points in ALC1743 (agr group 1 RN6390 containing reporter agr: P3-gfp, see GFP1 in Figure 0-35) and ALC1740 (RN6390 containing reporter hla-gfp, see GFP2 in Figure 0-35) at an early exponential phase prior to QS induction. Expression of GFP by ALC1743 reports late exponential phase-dependent activation of QS, while in ALC1740 it reports QS-mediated downstream synthesis of a virulence factor (alpha-hemolysin).

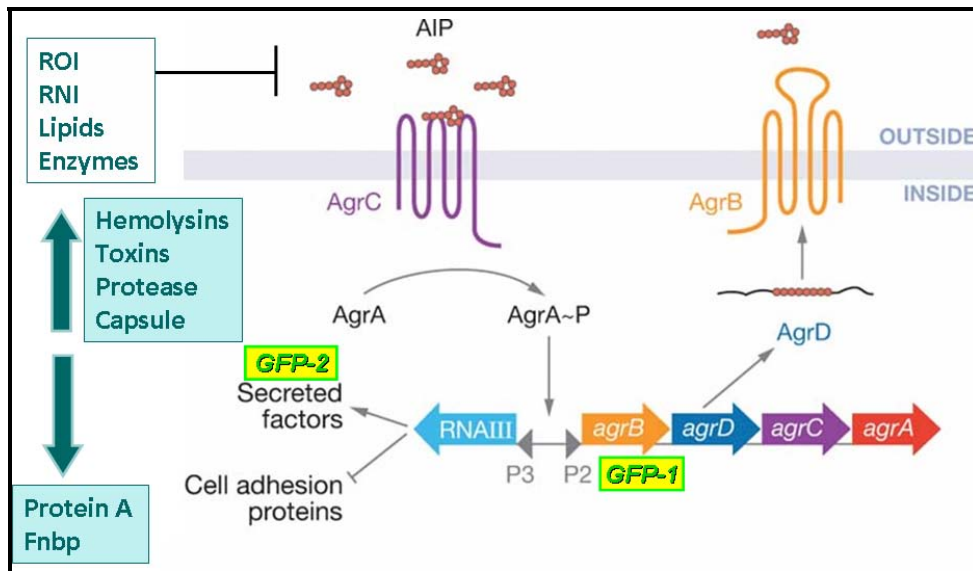


Figure 0-35. Regulation of quorum sensing in *Staph. aureus* (modified from Bassler 2004). Two strains of fluorescently-modified cells were obtained that allow the initiation of the quorum sensing pathway (GFP-1) and the development of virulence factors and toxins (GFP-2) to be visualized.

Figure 0-36 and Figure 0-37 show GFP expression for red stained ALC1743 and ALC1740, respectively. After one hour, no GFP expression was observed. However, after eight hours both ALC1743 and ALC1740 showed strong GFP expression, meaning that both the initial QS pathway as well as pathogenesis are activated. This is the first proof of individual cells exhibiting discrete quorum sensing.

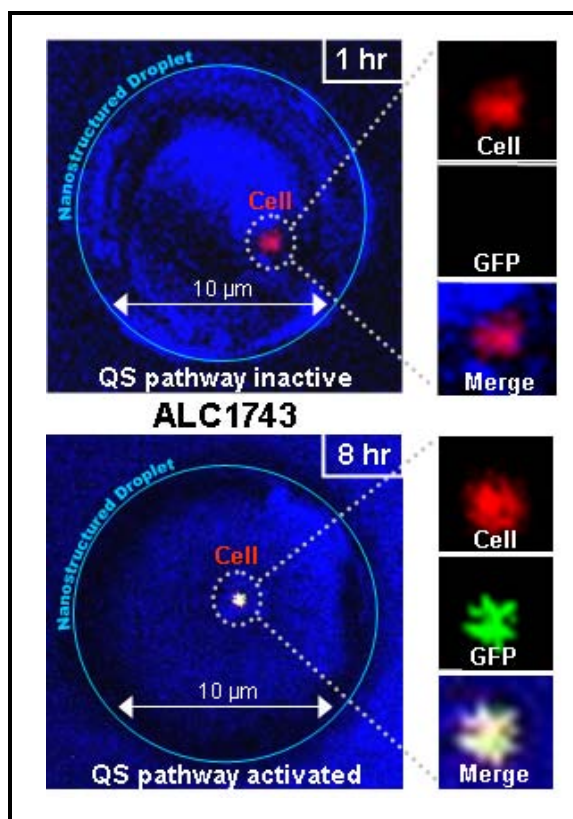


Figure 0-36. Individual, confined cells will initiate quorum sensing when encapsulated in an endosome-like nanostructure. Separated confocal fluorescence channels show that there is initially no GFP production co-localized with the red-stained cell within the blue pseudo-colored droplet (top). After 8 hours of incubation at 37°C, GFP is produced within the individual cell, confirming initiation of the quorum sensing pathway (bottom).

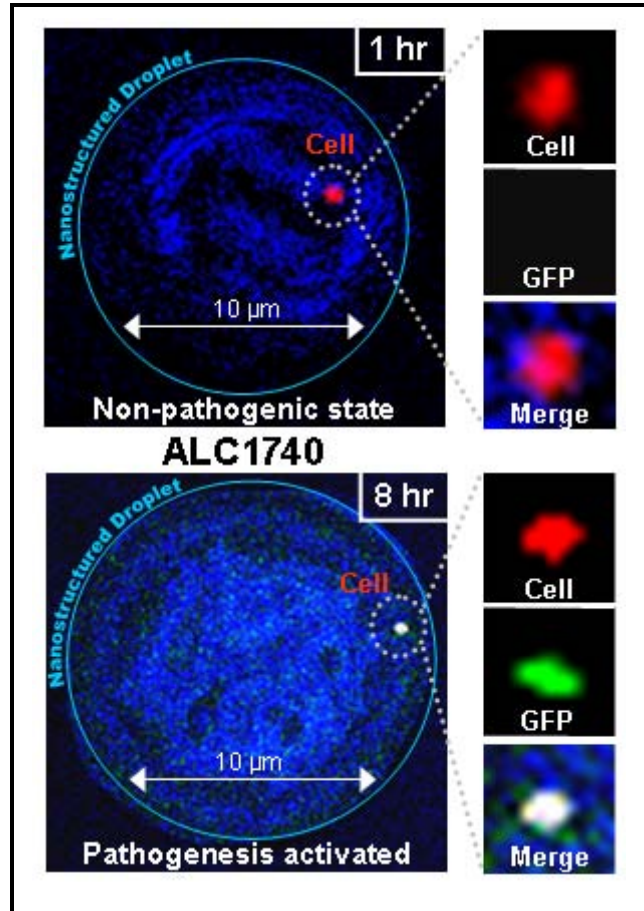


Figure 0-37. Individual, confined cells will become pathogenic when isolated within endosome-like compartments. Separated confocal fluorescence channels show that there is initially no GFP production co-localized with the red-stained cell within the blue pseudo-colored droplet (top). After 8 hours of incubation at 37°C, GFP is produced within the individual cell, confirming the production of the toxin and virulence factor, alpha-hemolysin (bottom).

By use of a reduced physical system, devoid of inter-cellular signaling interference inherent to cultures, we demonstrated unambiguously self-induction for an individual, isolated organism. This ‘discrete’ quorum sensing allows *S. aureus* to sense confinement (through increased extracellular concentration of autoinducer) and to

activate virulence factor pathways needed to survive in such environments (such as pore-forming hemolysins to escape endosomal encapsulation). We also discriminated among multiple possible alternative outcomes including failure of the adherent bacteria to survive in the matrix, failure of an individual bacterium to make sufficient AIP to autoinduce, inactivation of the AIP by oxygen or other byproducts that would prevent its biologic function, or the ability of early exponential phase bacteria to autoinduce. Discrete quorum sensing, and its resultant fitness benefits, provides an alternative model for QS that does not require complex social interactions for its evolution or maintenance, but rather promotes evolutionary selection according to survival of the fittest individuals.

The ability of individual cells to participate in this metabolic pathway that was previously thought to have evolved to benefit large groups of cells raises questions as to the evolutionary advantage of a single cell to upregulate production of the end products of the quorum sensing cascade, such as lipases, proteases, toxins, and growth factors. To assess the advantage to an individual cell of performing quorum sensing, we focused on the viability of individual cells isolated within nanostructured droplets. For this, we used the standard two-dye approach to evaluate the viability of individual cells over an 18-day period. We then compared the viability of individual encapsulated wild-type RN6390 cells, which will initiate quorum sensing after 8 hours of incubation in air at 37°C when immobilized in matrix droplets containing media, to individual encapsulated RN6390 cells that cannot undergo quorum sensing due to a lack of essential nutrients provided in the matrix. Additionally, we compared the viability of the RN6390 cells to individual encapsulated ALC1753 cells (*agr* deletion mutants), which have been genetically modified to be unable to initiate the quorum sensing pathway through deletion.

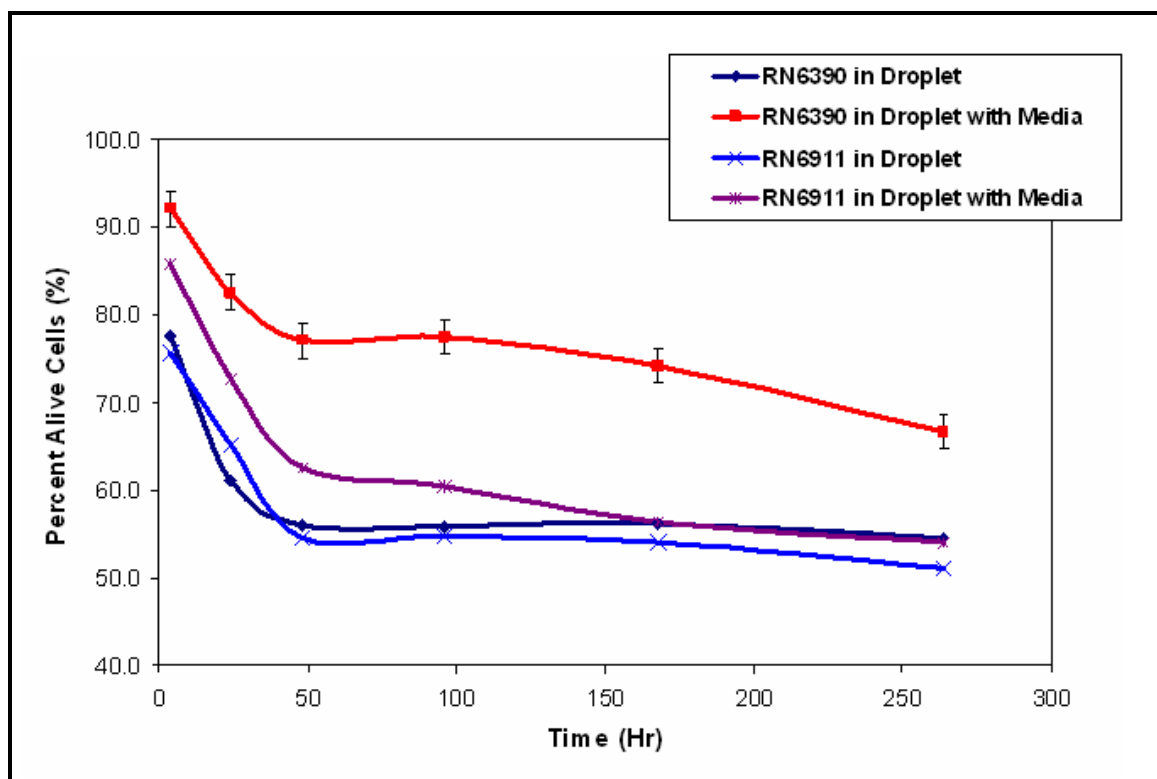


Figure 0-38. Viability of individual *Staph. aureus* cells isolated within endosome-like compartments.. Viability was evaluated with the standard two-color viability probe. Cells which are able to initiate QS pathways and produce associated proteins show increased viability (red) compared to cells that cannot perform QS due to genetic modification (purple) or lack of proper nutrients (dark blue). P=0.046, Gehan-Breslow survival analysis. Error bars represent 95% confidence interval.

A comparison of the viability of individual cells encapsulated within isolated nanostructured droplets is shown in Figure 0-38. We find that the viability of individual cells able to undergo quorum sensing is enhanced over those that cannot initiate the pathway due to genetic or environmental factors. We see that the RN6390 cells that autoinduce the quorum sensing pathway after 8 hours of incubation (those encapsulated

within matrix droplets containing media) do obtain a significant and prolonged viability advantage over the other cells. The rest of the cells tested cannot undergo quorum sensing when confined in the droplets and do not show any advantage in viability. Interestingly, it can also be seen that cells which do not undergo quorum sensing due to lack of nutrients have comparable viability to cells that cannot quorum sense due to genetic modification. This seems to indicate that the ability of a cell to produce the end products of the quorum sensing pathway directly provides a direct physical benefit to individual cells that are drastically confined.

This simple set of experiments demonstrates the validity of using reduced physical systems to study complicated phenomena in the world of biology. By constructing a biomimetic environment using cell-directed assembly, we were able to obtain the first proof of an evolutionarily important mechanism that may have ramifications in the way many bacterial infections are understood and treated. A similar approach could be taken to immobilize and study many complex cellular processes. This concept should prove especially useful when combined with the cell-directed integration process discussed in detail later.

1.1.6.2 CDA may be used to identify a new model for Tuberculosis latency

Approximately 5,000 people will die today due to complications with virulent TB infections²¹. Meanwhile, latent *Mycobacterium tuberculosis* (TB) infections affect almost one-third of the world's population²². Researchers do not currently understand the

mechanisms for triggering latency and the potential deadly reemergence of the disease. Although completely eradicated in the United States, approximately 95% of TB infections are isolated to third world countries. This disparity in basic health care has become some so enraging on the world scale that even the Gates Foundation donated over \$100 million to speed up the search for affordable vaccines, treatments, and cures²³.

While treatment with drug combinations has proven effective, the requirement of 6 months of scheduled treatments is unrealistic for patients in developing countries. A contributing factor to the difficulty in treating TB is the unusually slow growth of the bacterium, allowing cells to live for years in lung granulomas – clusters of cells surrounded by cellular remains and attacking macrophages – until eventually reemerging in a virulent form due to an unknown triggering mechanism. These bacteria are thought to be so resistant to the human immune response due to their unusual cell wall comprised of an extraordinarily high number of hydrophobic lipids and fatty acids, making the cell nearly impermeable to most standard drug treatments²⁴. A representation of the TB cell wall is shown below in Figure 0-39.

The only reasonable accepted theory for TB latency involves a metabolic switch to an anaerobic state and subsequent dormancy induced by gradual apoxia resulting from the formation of granulomas²⁵. This is a difficult argument to understand, based on the assumption of sustainable anaerobic areas within the lungs. Other suggestions for latency and reemergence may also shed light on the importance of phospholipids and iron in latency^{26,27}. The association of dormant TB with lipids, coupled with its unusual metabolism under normally aerobic conditions would make it an ideal choice for encapsulation via cell-directed assembly.

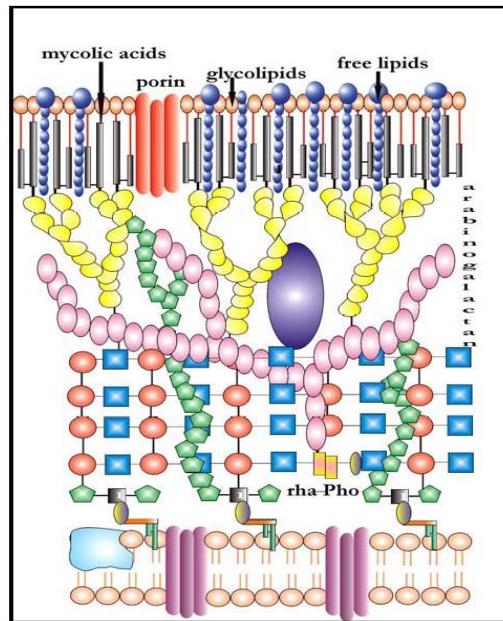


Figure 0-39. Schematic of cell wall of *Mycobacterium tuberculosis*²⁸. Cell wall is comprised of unusually high concentrations of lipids and glycolipids, as well as fatty acids such as mycolic acids.

Features of cells immobilized using CDA include localization of phospholipids, extended viability in air without additional fluids or nutrients, and the observation that many cells enter a viable but not culturable (VBNC) state. These systems appear to share many similarities with observed features of TB, including an unusual affinity for lipids, slow-growth and extended viability despite constant immune attack, and a latent state defined by the bacteria being viable but not culturable²⁹. Thus, it may be possible to develop a new model for TB latency and study the affects of treatments on latent cells by immobilizing TB cells into a nanostructured silica matrix using CDA with phospholipids, mimicking the natural environment of cells in granulomas.

Preliminary studies have been performed using the vaccine strain of *M. tuberculosis*, BCG. Cells were encapsulated in a *diC₆PC*/silica nanostructure and were allowed to incubate at 37° in air without any additional media or fluids. Viability was then assessed using the standard two-color fluorescent probe kit from Invitrogen. After 16 months of aerobic incubation at body temperature, conditions very likely to be found in the lung granuloma environments of TB cells, well over 50% of cells remained viable. These results are shown below in Figure 0-40. This exciting preliminary evidence indicates that TB is able to maintain extended viability under aerobic conditions, suggesting a possible new model for TB latency. Further studies are currently being conducted to assess the metabolic state of these cells, their infectiousness, and their susceptibility to drugs following this prolonged incubation. Additionally, this further demonstrates the ability of the cell-directed assembly process to be used to create reduced physical models of complicated biological systems, allowing investigation of many questions in biology and medicine.

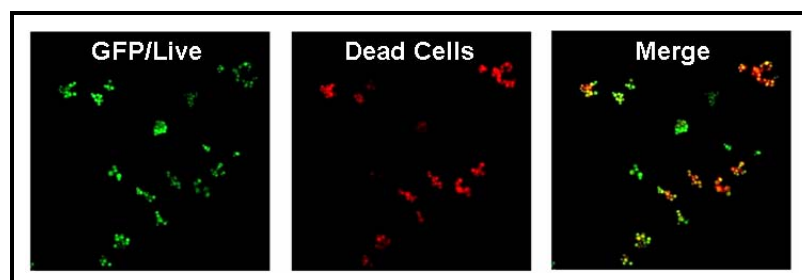


Figure 0-40. Fluorescence viability probe images of BCG cells encapsulated via CDA. Viability was evaluated using the standard two-color fluorescent probe. Live cells are shown as green (left) while dead cells are stained red (middle). Once the two colors have been merged, live cells appear green without any red (right).

1.2 Discovery and Application of Cell-Directed Integration

Cell-directed integration (CDI) is a two part synthesis that separates, to the highest possible extent, the incubation of cells with solvents, precursors and catalysts during the EISA process in order to increase the biocompatibility of the immobilization and address other limitations of traditional CDA. In CDI, a nanostructured film is first created via EISA and then an aqueous suspension of cells are added to the film, as shown below in Figure 0-41.

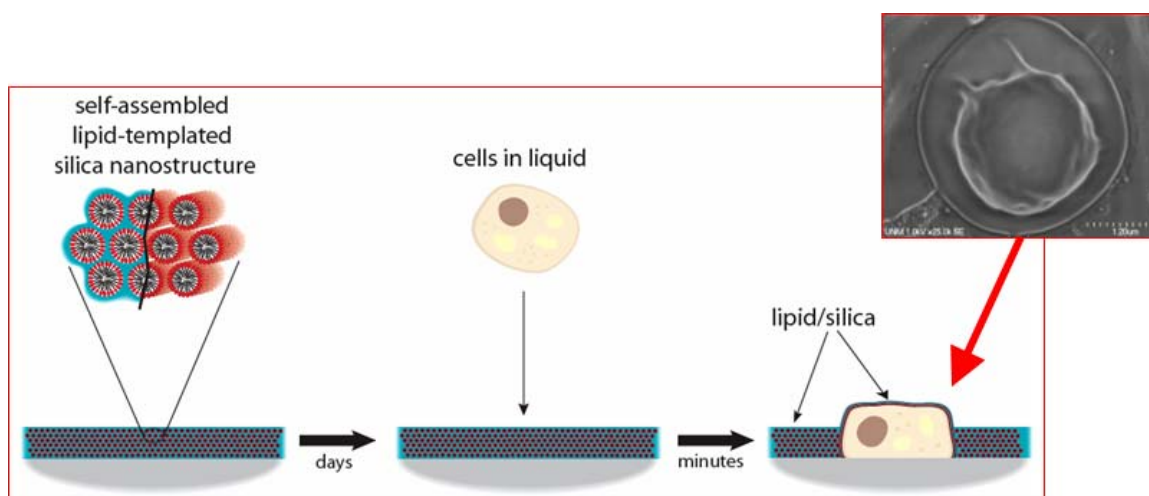


Figure 0-41. Schematic of Cell-Directed Integration. In this process, a lipid/silica nanostructure is first created by EISA. Following creation of these films, live cells can be added in liquid. Within minutes, cells are surrounded by lipid and silica as seen in the inset SEM image.

Since the cells are added following the evaporation of the solvent and towards the end of the silica condensation, exposure of the cells to solvent is minimized, allowing for

the use of more traditional, higher solvent concentration sol recipes while ensuring cell viability. Additionally, the ability to use high-solvent sols enables the use of non-water soluble surfactants, allowing for a dramatic increase in the variety of possible nanostructures that can be developed in the host matrix. Provided the silica is not fully condensed, the cells are able to rearrange a local region of lipid and silica to create a system that is locally similar to CDA, but maintains the desired bulk material properties. Overall, the CDI process creates a very flexible platform for immobilization and encapsulation of all cell types, addressing the limitations of the CDA system, and thereby creating a new technique for development of new bio/nano interfaces, cell-based devices, and cell investigation systems. Furthermore, the CDI process is also easily adaptable and amenable to a wide variety of simple patterning strategies to create a multi-functional cell integration strategy featuring new lithography with life techniques. An overview of key features and components of CDI is shown below in Figure 0-42.

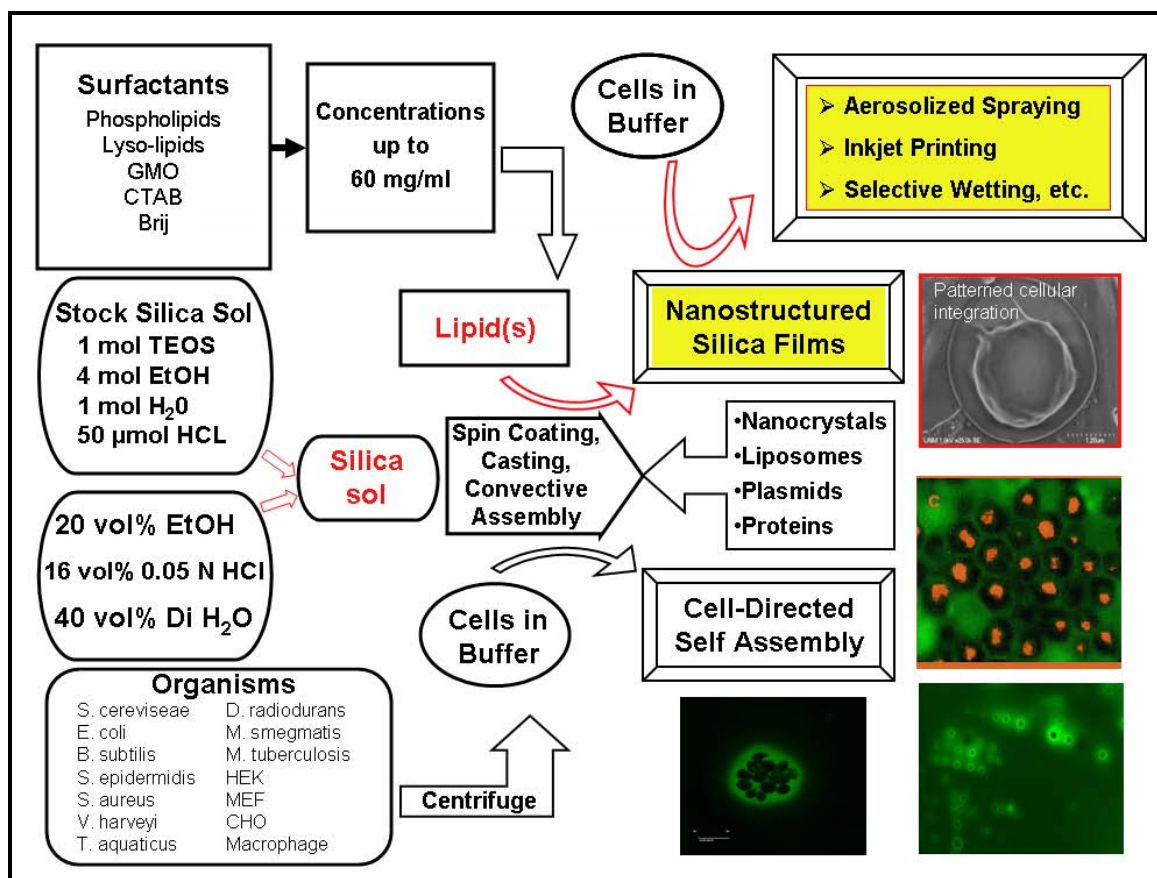


Figure 0-42. Overview of CDI process highlighting pertinent features that can be varied and investigated.

1.2.1 Cells are able to rearrange materials from visibly dry lipid/silica nanostructure

The ability of cells to be encapsulated using the cell-directed integration scheme relies on the ability of cells to rearrange materials from a fluid lipid/silica mesophase that appears dry. Because the lipid/silica system is not fully condensed, it allows the mesophase to be reorganized by the cells in three dimensions, resulting in full encapsulation of cells within a lipid/silica nanostructure. This creates a system in which

cells are able to interact and manipulate their environment, the key feature of the cell-directed assembly process, which is a feature only exploited by our group when immobilizing cells.

To confirm this rearrangement and 3D encapsulation of cells into pre-formed nanostructures, *diC₆PC*/silica films were created using a recipe identical to that of CDA, only without adding the cells in buffer. Following application via spincoating, the lipid/silica nanostructured films were allowed to dry and condense for 24 hours at room temperature and ambient humidity. Following this incubation, presence of the expected hexagonally-arranged nanostructure was confirmed using x-ray diffraction. Then, stationary phase yeast cells and latex beads were applied to the films via aerosolization in either PBS or water. The resulting films were then analyzed using SEM and EDS. The results are shown below in Figure 0-43.

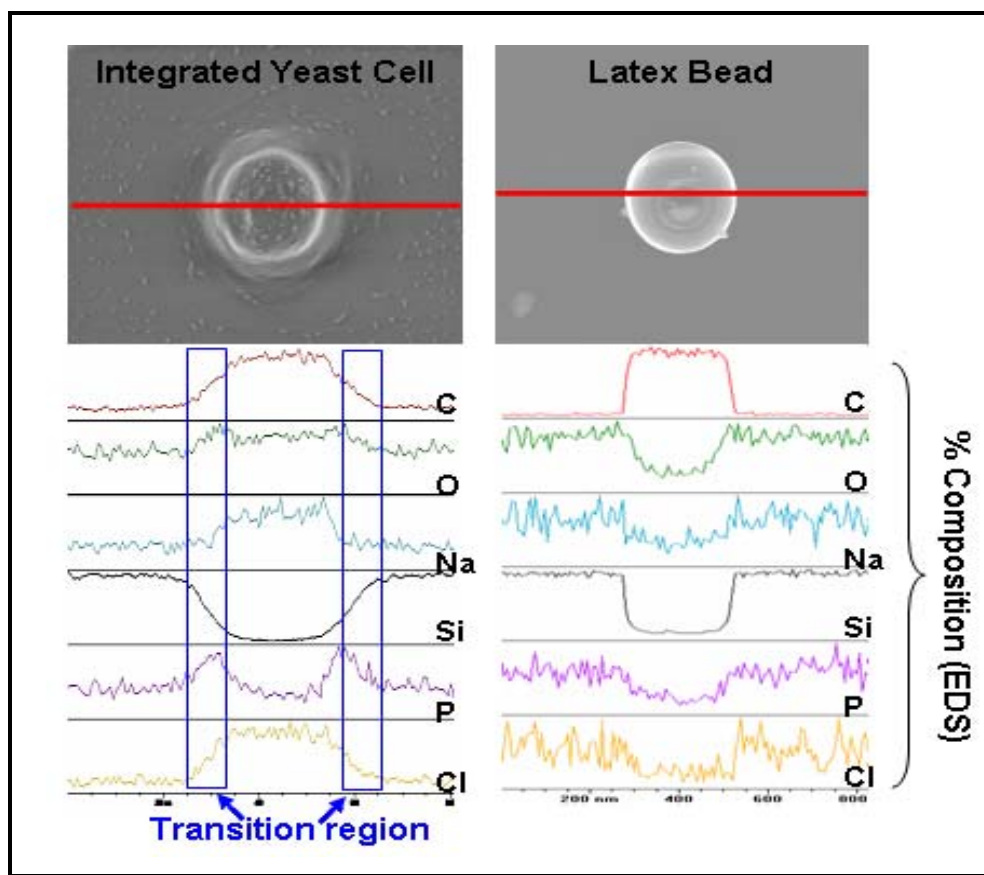


Figure 0-43. SEM and EDS line scans of cell-directed integration for live cells and cell surrogates. SEM (top) of yeast show a region of transient elemental composition in the local vicinity of the cell (blue) as indicated by an EDS line scan (red). When latex beads are introduced (right), no transition between the bulk material and the latex bead is seen.

We see that the yeast cells are able to manipulate a local region of the film, creating a transition region between the cells and the film that appears to contain an intermediate composition of relevant elements. In contrast, latex bead cell surrogates do not create any transition region. Instead, an abrupt change from the lipid/silica film to the latex bead is observed. Additionally, the addition of water or buffer alone only results in localized swelling, as expected for a templated lipid/silica film.

Further evidence of cell integration using the SEM is the ability to image the live cells without any fixation or imaging preparation. Without being encapsulated, cells are quickly vaporized when exposed to the high-voltage electron beam. However, cells that have been integrated using CDI are stable even when the beam power begins to damage the film. This can be contrasted with the system containing negatively-charged latex beads, where the electron beam repels the beads, moving them around like a game of microscopic billiards. The ability of the beads to be moved by the beam demonstrates that they are not able to integrate into the pre-formed nanostructured films.

Confocal microscopy has also been used to investigate the cells' ability to reorganize materials when integrating into pre-formed nanostructures, as shown in Figure 0-44. Using fluorescently-labeled lipid, we find that when yeast are added to *diC₆PC*/silica films, they are able to reorganize the lipid in order to completely surround the cell in three dimensions to form a local, lipid-rich environment similar to that created when immobilizing cells using cell-directed assembly. Similar nanostructured films were also formed with the addition of fluorescently-labeled, biocompatible gold nanocrystals as used previously in investigations of the CDA process. When yeast are added to these films, we find that the cells are able to also rearrange the gold nanocrystals to form a completely new bio/nano interface where gold-covered cells are now encapsulated in an ordered nanocrystal/silica array. This type of hybrid system could lead to the development of novel, electrical and SERS-based detection cell assays.

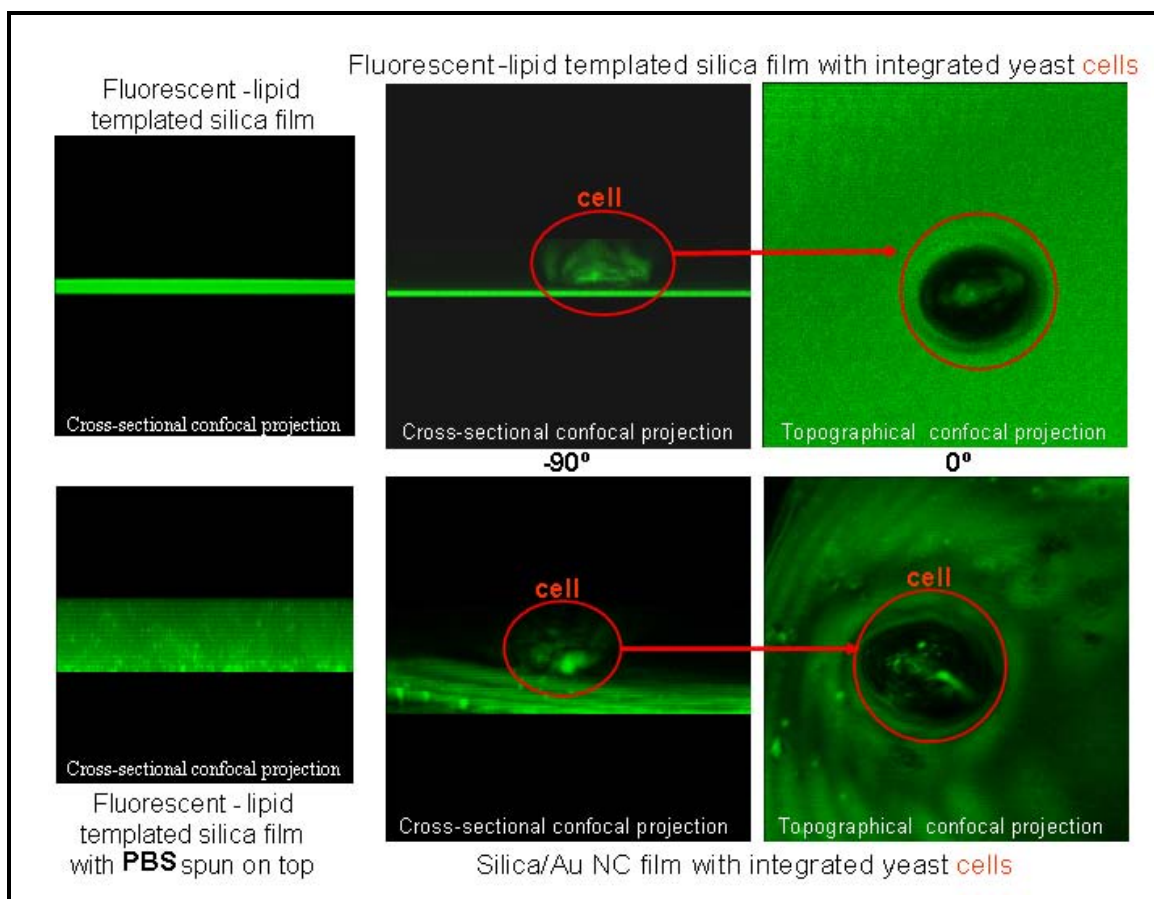


Figure 0-44. Confocal fluorescence images of 3D rearrangement of lipid and other nanocomponents during CDI. Cross-sectional SEM projections of films made with NBD-tagged diC_6PC show a uniform distribution of lipid (top left). Addition of PBS to film simply results in swelling of film (bottom left). Addition of live yeast cells, however, results in 3D rearrangement of the lipid as seen in confocal cross-sectional (top middle) and topographical (top right) projections. If Au nanoparticles solubilized with NBD-lipid are introduced to the system, they are also rearranged, confirmed by confocal cross-sectional (bottom middle) and topographical (bottom right) projections.

1.2.1.1 Live cells are required to reorganize lipid during integration

During integration, cells are able to reorganize and localize lipid to create an environment similar to that found in CDA. To determine whether this rearrangement is accomplished by active process, as in CDA, confocal microscopy was used to investigate

the potential for reorganization of lipid from a pre-formed nanostructure by both live yeast cells and apoptotic yeast cells. Since it was observed that the apoptotic cells did not engage in cell-directed assembly in the same manner as live cells, it was hypothesized that the apoptotic cells would not be able to integrate via the same mechanism, if at all.

We find, when using fluorescently-tagged *diC₆PC* in silica with red stained cells, that the live, integrating yeast do indeed localize a region of lipid to form a bio/nano interface similar to that formed with CDA, as shown below in Figure 0-45. However, when apoptotic cells were used, we find that the cells are unable to interact with the nanostructured material and reorganize the lipid. Instead we find that these cells do not integrate in three-dimensions and as such are easily washed away and are also subject to destruction by the electron beam when attempting to image directly in the SEM.

This data indicates that live cells, capable of performing normal metabolic processes, are required for integration. It is also found that localization of lipid from a pre-formed nanostructured film is a key parameter in the cells' ability to integrate into these types of materials, where cells are able to localize lipid in a manner similar to CDA. Interestingly, we find that cells are not able to integrate into silica films that do not contain any structure-directing agents.

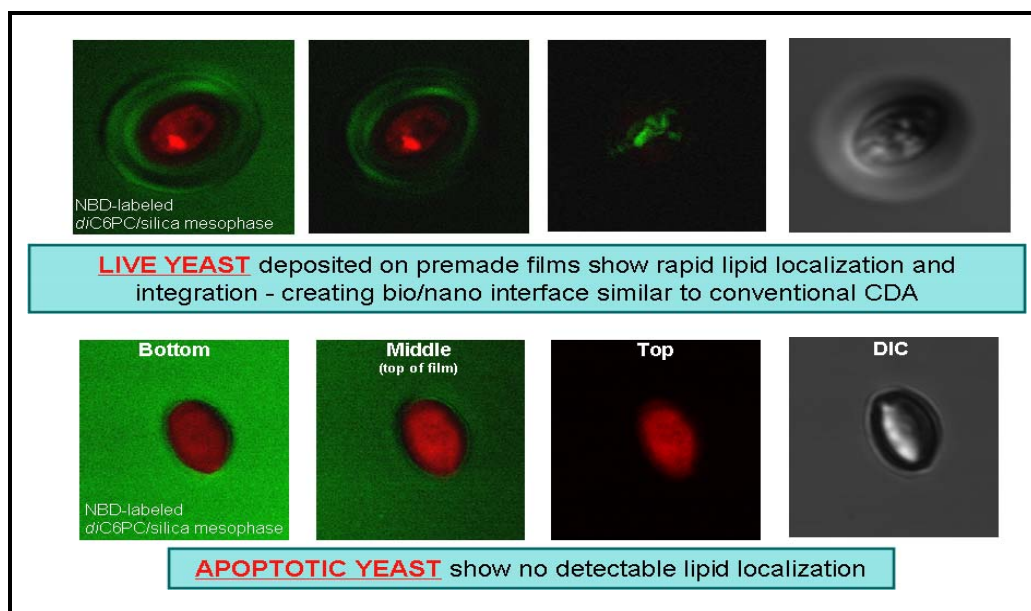


Figure 0-45. Reorganization of lipid during is achieved by live cells but not apoptotic cells. (Top) Confocal slices show movement of NBD-tagged lipid from the film to the top of the red-stained live yeast cell that has been introduced to a premade lipid/silica film via aerosolization. However, no lipid is found to be surrounding the top of an introduced red-stained apoptotic yeast cell, indicating that they are unable to integrate.

1.2.1.2 Live cells establish local pH gradient during integration

Following the observation that live cells will reorganize lipid upon integration within pre-formed silica nanostructures, it was hypothesized that this phenomenon may be linked to the development of a local pH gradient in a process analogous to CDA. During CDA, only live cells are able to establish large external pH gradients when encapsulated in films with lipids.

To verify this hypothesis, nanostructured *diC₆PC*/silica films containing the fluorescent pH indicator Oregon Green were developed. Due to the low pH of approximately 3 in the pre-formed material, the bulk film shows no green fluorescence.

When live yeast (stained red) are added, though, we are able to see the development of a three dimensional pH gradient which is maintained at a near neutral pH near the cell surface, nearly identical to that developed during CDA. However, apoptotic yeast are not able to establish any pH gradient, consistent with the observations of an inability to localize lipid. Because of these similarities between the two major phenomena behind CDA and their discovery in CDI, it suggests that the local environment formed during CDI would be governed by the same forces and yield similar benefits in terms of extended viability for cells maintained without external buffers or nutrients.

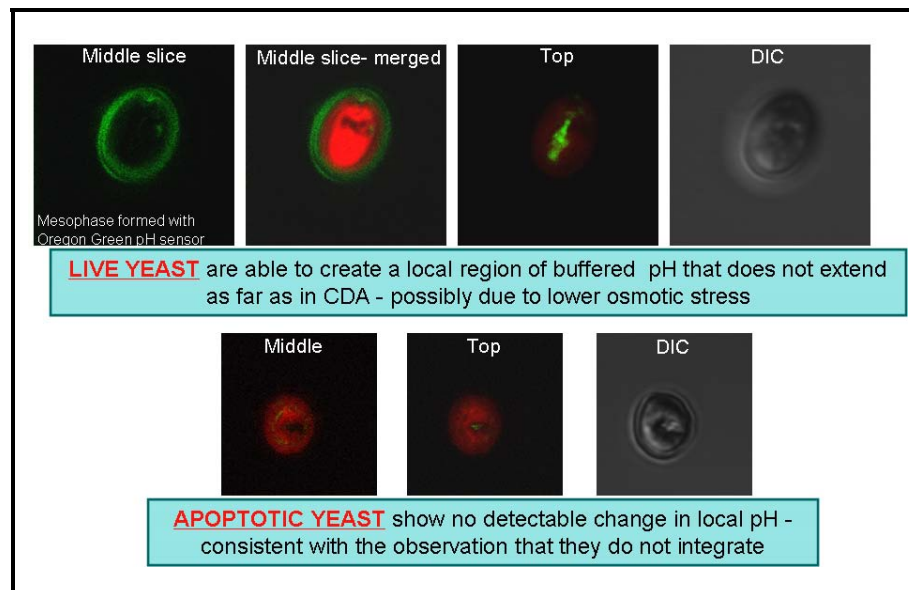


Figure 0-46. Live cells are able to control local pH during integration, unlike apoptotic cells. (Top) Confocal slices show a 3D pH gradient (pH probe, green) of the red-stained live yeast cell that has been introduced to a premade lipid/silica film via aerosolization. However, no pH change is found around an introduced red-stained apoptotic yeast cell.

1.2.1.3 Bulk material properties and nanostructures can now be defined

While the cell-directed integration process seeks to maintain the essential features of CDA that result in increased viability, the process is also designed to address the limitations of CDA. One of these main limitations is the inability to control the development of the nanostructure of the bulk material. During CDA, it was found that live cells irreversibly alter the expected nanostructure through localization of lipid and control of pH. While it is an interesting and useful phenomenon for creating novel bio/nano interfaces, this lack of complete engineering control of the CDA system limits its usefulness in next-generation devices where the controlled transport specifiable by predictable nanostructures and pore geometries will be required. During cell-directed integration, it is observed that the cells only reorganize material in a local region. This should allow the development of systems containing new bio/nano interfaces comprised of cells immobilized in a preferentially-arranged micro-environment that is encapsulated within a definable nanostructured host matrix.

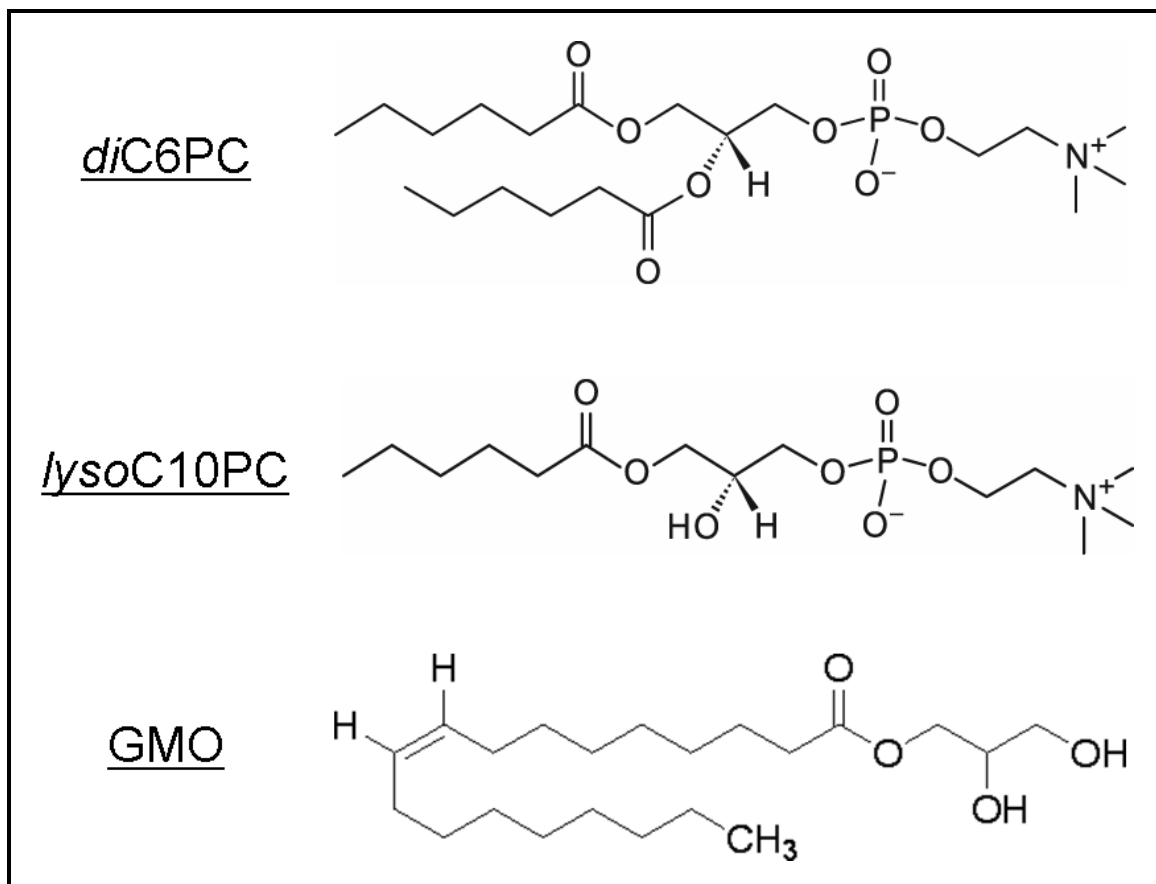


Figure 0-47. Structures of lipids and lipid analogues used to create biocompatible nanostructured films for CDI.

To demonstrate the ability to immobilize cells within defined nanostructures, various ordered films were developed from our standard phospholipid (*diC₆PC*) as well as a modified, longer chain lipid having only one alkyl tail (*lysoC₁₀PC*), and a longer chain lipid analog containing no phosphate or head group (*GMO*), whose structures are shown above in Figure 0-47. Using GISAXS to analyze the nanostructure of the resulting films, we find that we are able to create many different types of structures through the use of different phospholipid analogues in order to create a variety of biocompatible

templated silica nanostructures. As shown below in Figure 0-48, films can be created that display not only hexagonal orientations (*diC₆PC*), but also cubic (*lysoC₁₀PC*) and modified-orthorhombic (GMO) structures with 3D pore connectivity. This represents an important improvement over CDA where simple lamellar structure in Figure 0-49 which was the only structure obtainable through CDA

After order within these various nanostructured films was confirmed, live yeast cells in buffer were added via the aforementioned aerosol application. Full integration of the cells and 3D rearrangement of materials was also verified using confocal microscopy, as well as SEM and EDS analysis as described above. Not surprisingly, the bulk nanostructure of the material was retained, due to the ability of the cells to reorganize materials only in their local micro-environment. The bulk nanostructure remains intact since it is unaffected by the integration process. The slight loss of order of the primary structure in the GISAXS pattern is also accompanied by a development of a minor lamellar structure, similar to the structure normally observed during CDA with yeast. This would be indicative of the cells reorganizing of the material to form a local lamellar structure, while the desired, controllable nanostructure remains in the bulk.

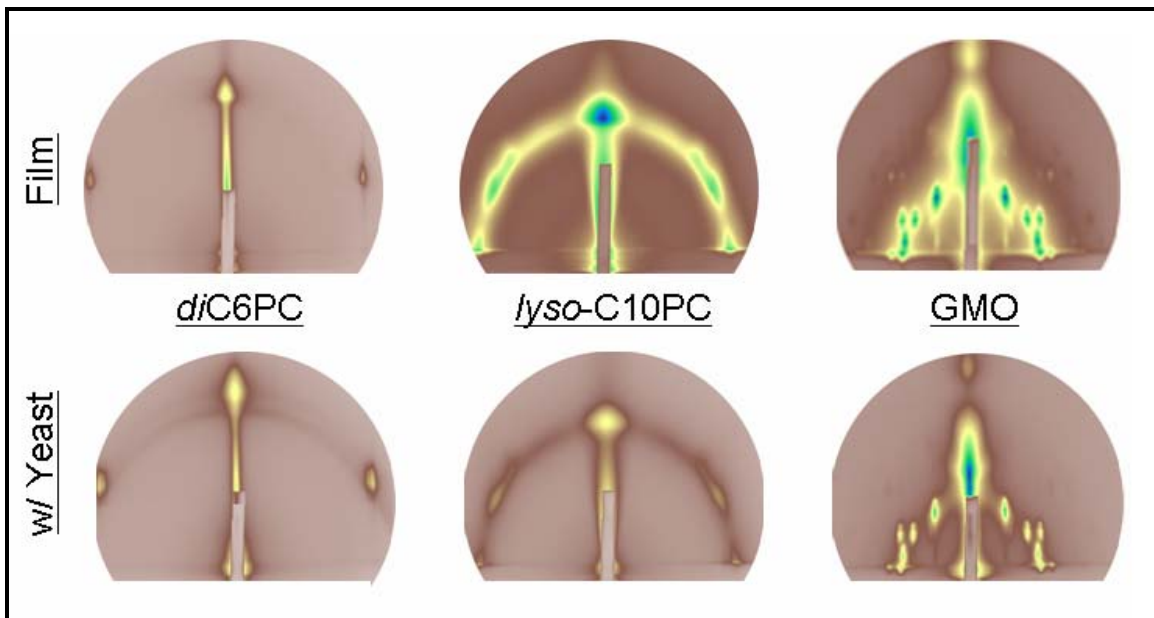


Figure 0-48. GISAXS patterns of different definable nanostructures that can be obtained using CDI. (Top row) Silica nanostructures formed through the use of various biocompatible surfactant templates. (Bottom row) After live yeast were added via aerosolization, the bulk nanostructure of these films was retained.



Figure 0-49. GISAXS of yeast/ diC_6PC /silica nanostructure developed with CDA. This lamellar structure is the only observed nanostructure when live yeast are used in CDA.

1.2.2 Yeast immobilized using CDA demonstrate extended viability

In order to create functional cell-based platforms using CDI, it is essential that the cells remain viable for extended times despite incubation without fluids or nutrients, similar to the enhanced viability observed in CDA. Using the standard two-color fluorescent probe kit, the viability of yeast, immobilized in *diC₆PC*/silica nanostructured films, was determined. As seen below in Figure 0-50, the integrated cells display viability of over 90% after 150 hours of incubation in air at 25°C. Additionally, it was found that over 50% of integrated yeast cells remain alive after 4 months. This sufficiently demonstrates the practicality of CDI to develop solid-state platforms for the use of yeast in various cell-based systems.

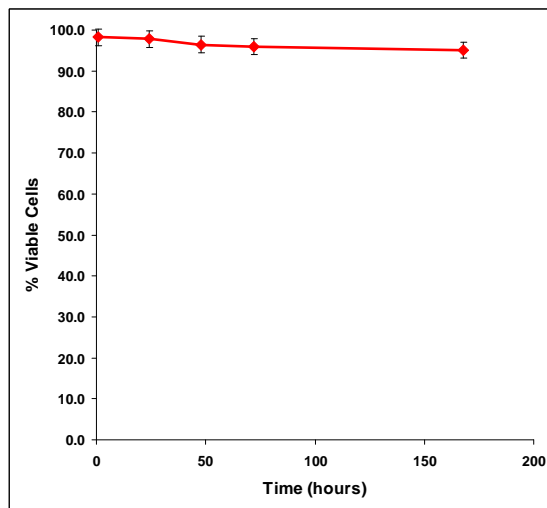


Figure 0-50. Viability of yeast immobilized in *diC₆PC*/silica nanostructures via CDI. Viability was evaluated using the standard two-color fluorescent probe. Cells remain over 90% viability after one week at room temperature without the addition of external buffer or media. Error bars represent 95% confidence interval.

1.2.3 Extension of cell-directed integration to different cell types

In order to demonstrate the ability of the cell-directed assembly platform to be a broad technique applicable for creating new bio/nano interfaces, cell-based devices, and cell interrogation system, it is necessary for the technique to function with a wide variety of cell types. With the understanding that live yeast would integrate into pre-assembled biocompatible nanostructures and form a local region which featured characteristics of CDA, it was hypothesized that CDI would also be applicable for encapsulation of various types of single-celled organisms. Since this new technique separated the cells from the solvent, CDI should also serve as a means of integrating mammalian cells, addressing a limitation of the CDA approach. We find that CDI can be used as a platform for integrating many types of single-cell organisms, as well as functional mammalian cells. This results in a truly diverse technique for encapsulating and immobilizing cells into solid-state matrices for use in a variety of devices and studies.

1.2.3.1 Bacteria can be successfully integrated via CDI

Immediately after characterization of the cell-directed integration process in yeast, it was hypothesized that integration would follow a similar process for each cell type, as in CDA, while also displaying unique, cell-specific, characteristics. Using SEM and EDS as above for yeast and latex beads, we find that live bacteria are able to integrate into pre-

formed lipid/silica nanostructured films. As expected from our understanding of CDA, it was found that each cell type displays a different transition region from the bulk film to the cell surface which is related to the preferential environments formed by the cells during traditional cell-directed assembly. We see with *E. coli*, for example, a distinctly different transition region than observed for yeast, as shown below in Figure 0-51. Integration of the cells was again verified by washing followed by attempted destruction with the high-powered electron beam.

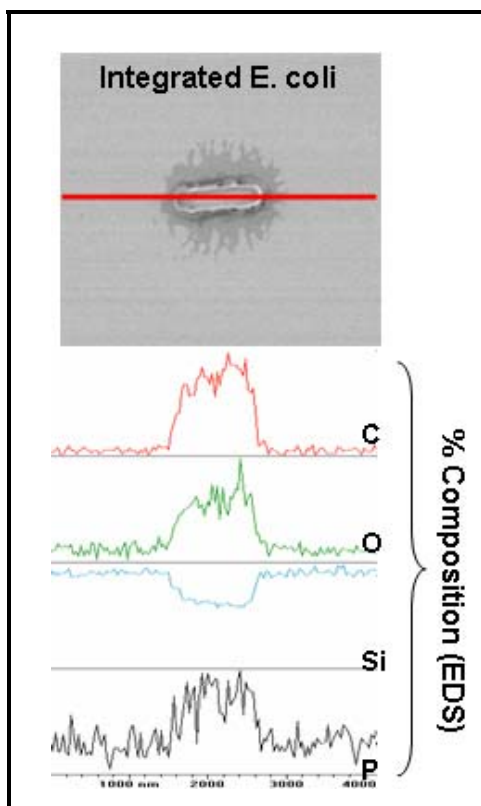


Figure 0-51. SEM and EDS line scan of *E. coli* integrated into a diC_6PC /silica nanostructure via CDI. SEM (top) of an *E. coli* cell shows a region of transient elemental composition in the local vicinity of the cell, as indicated by an EDS line scan (red). This confirms the 3D integration of the cell within the lipid/silica nanostructure.

Upon verification of integration of *E. coli* cells into a *diC₆PC*/silica film, confocal microscopy was used to investigate lipid reorganization/localization and the cell's ability to establish a pH gradient. As seen below in Figure 0-52, *E. coli* cells do reorganize an amount of *diC₆PC* from a pre-formed silica nanostructure and localize the lipid to fully encapsulate the cell in three dimensions. It can also be seen that the cell is able to establish a pH gradient that is maintained at a neutral value near the cell surface. However, both the localized lipid and the pH gradient extend of considerably shorter distances than observed with the yeast. This is also consistent with the observed characteristics of CDA, furthering the concept of the establishment of a cell-specific local region of integration that retains the characteristics of the cell-directed assembly process while allowing the bulk material properties to be retained.

To verify the ability to immobilize bacterial cells in various biocompatible nanostructures, GISAXS was again employed with the results for *E. coli* shown below in Figure 0-53. In these systems, different nanostructured films were created using various lipid analogues as with the aforementioned yeast integration system. Initial ordering was characterized by GISAXS. Then, *E. coli* cells were introduced via aerosolization in buffer. We find, similar to the yeast integration, that we are able to maintain the bulk nanostructure upon integration of bacterial cells. Again we find that a small loss of bulk order is accompanied by the development of a local lamellar region in the cell micro-environment.

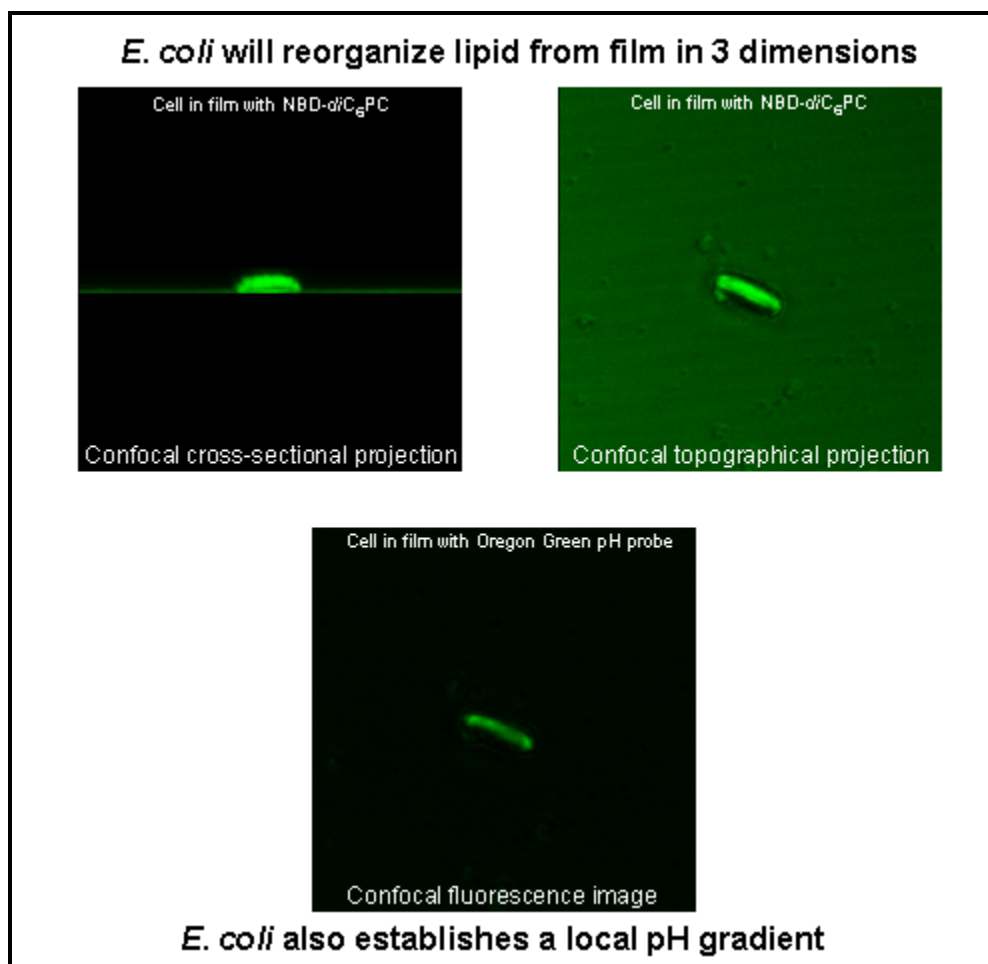


Figure 0-52. Localization of lipid and pH control of *E. coli* during CDI. (Top) When cells are added via aerosolization to an existing lipid/silica film containing NBD-tagged lipid, 3D rearrangement of lipid is confirmed by confocal cross-sectional projections (left) and topographical projections (right). (Bottom) When cells are introduced to films containing a fluorescent pH probe, a local buffered pH gradient can be seen.

Following the observation that bacteria are able to integrate into pre-formed lipid/silica nanostructures in a manner similar to yeast, creating a local environment similar to CDA while retaining the desired bulk nanostructure, it was hypothesized that these conditions would lead to extended viability of cells immobilized using CDI. To verify this, multiple types of bacterial cells were immobilized in *diC₆PC*/silica

nanostructures and incubated in air at 25°C without external fluids or nutrients. Viability was then assessed using the standard two-color fluorescent probe kit. The results, shown below in Figure 0-54, show extended viability, similar to integrated yeast, for all model organisms investigated. This clearly demonstrates the feasibility of using cell-directed integration to immobilize many types of single-cell organisms within silica nanostructures for incorporation into solid-state, cell-based systems.

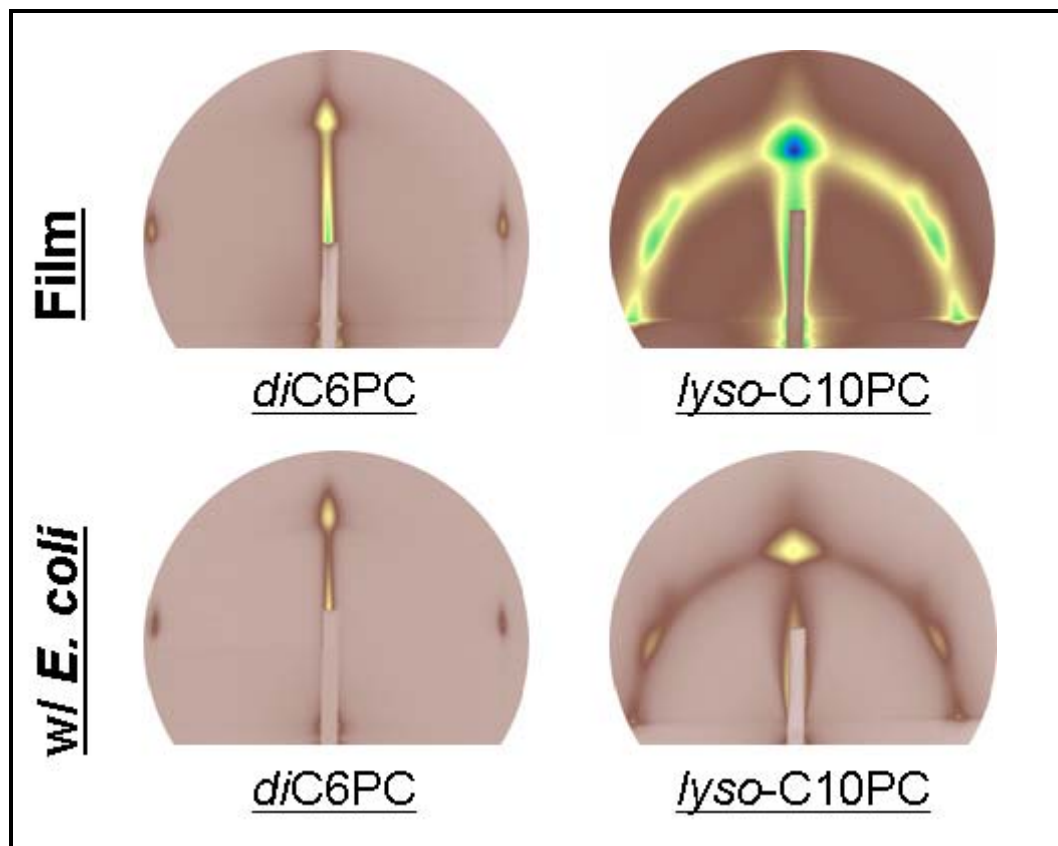


Figure 0-53. GISAXS patterns of different nanostructures maintained during CDI with *E. coli*. (Top row) Silica nanostructures formed through the use of various biocompatible surfactant templates. (Bottom row) After live cells were added via aerosolization, the bulk nanostructure of these films was retained.

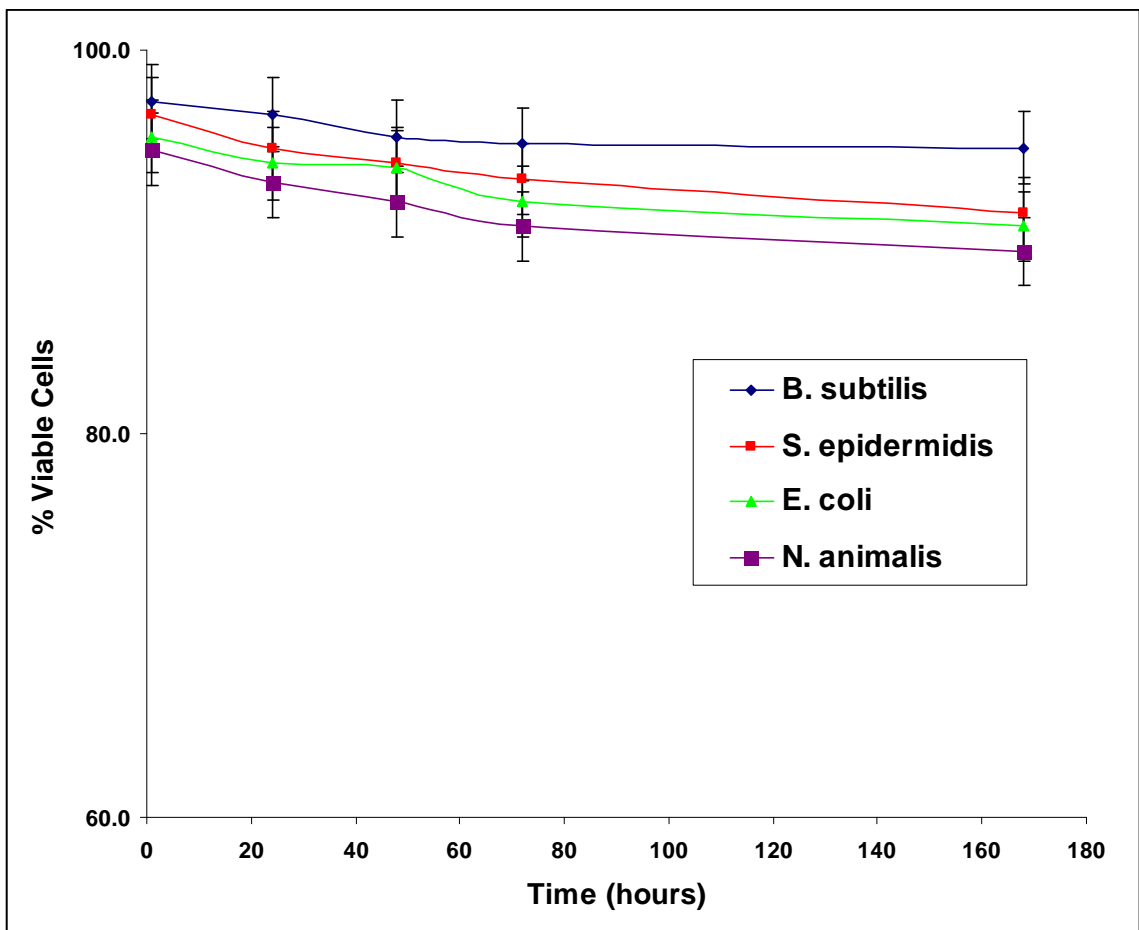


Figure 0-54. Viability of various types of bacterial cells encapsulated via cell-directed integration into diC₆PC/silica nanostructures. Viability was evaluated using the standard two-color fluorescent probe. After one week at ambient conditions, over 85% of all cells remain viable without the addition of external buffer or media. Error bars represent 95% confidence interval.

1.2.4 Comparison of Cell-Directed Assembly to Cell-Directed Integration

Two new cell encapsulation strategies have been demonstrated, with their defining features and characteristics elucidated. Cell-directed assembly allows single-cell organisms to be immobilized while controlling their developing environment. Cell-directed integration separates the CDA process into two steps, allowing greater control over the material while still retaining the interaction between cell and material that is crucial for viability. While differences between the two methods have been mentioned above, they will be described in further detail below.

1.2.4.1 Local environmental effects are similar in both CDA and CDI

The importance of allowing the cell to interact with the developing host matrix has been clearly shown. This feature is crucial to both of the cell-directed processes, allowing each different cell type to create an environment with hospitable conditions for survival. The interaction between the cell and the material have been investigated by monitoring the lipid template added to the systems, as well as by monitoring the pH gradients developed within the systems. These characteristics of the two processes were directly compared by utilizing identical sol and lipid formulations for use in both CDA and CDI. After performing both techniques with identical starting components, both lipid localization and pH development were monitored using the same fluorescence and

confocal techniques as described above. We see that both systems develop a very similar local environment. While both systems display similar behavior, they are also both specific to cell type in identical manners, with yeast affecting a larger environment. Additionally, active processes are required in both techniques, as latex bead cell surrogates are not able to alter their local environment.

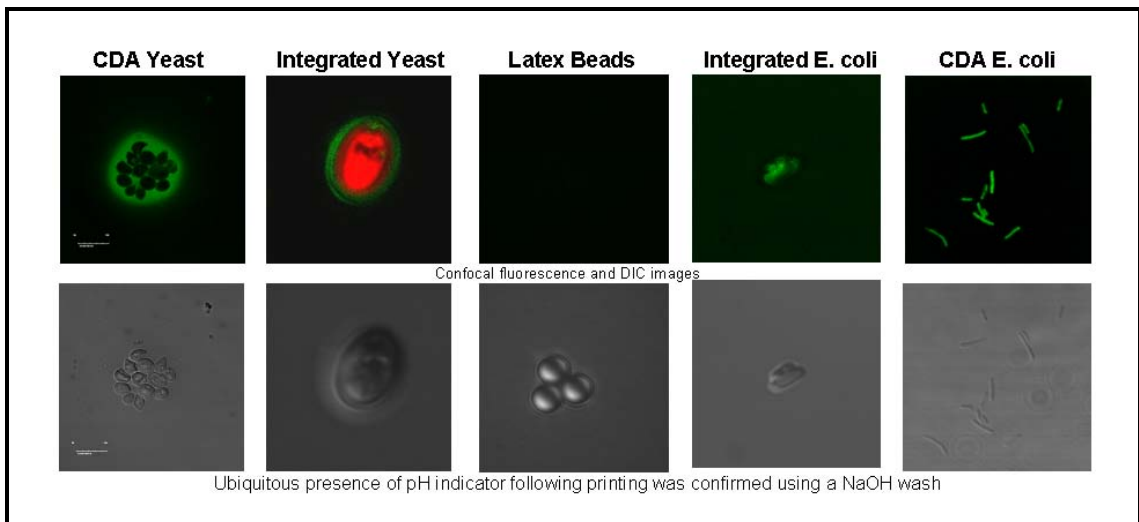


Figure 0-55. Comparison of local pH control during CDA and CDI. Fluorescent pH probe (green) was used to compare the pH gradient that forms around cells during CDA and CDI. Confocal images (top row) and corresponding DIC images (bottom row) show that the pH gradient around yeast extends further throughout films created via CDA.

1.2.4.2 CDI shows comparable viability to CDA among similar systems, but also allows for many more systems that are incompatible with CDA

Extended viability of immobilized single-cell organisms without the need for external buffers and fluids can be achieved using both the cell-directed assembly process as well as the cell-directed integration process. Both systems yield the highest viability when using *diC₆PC*. Similar short chain lipids can also be used with lesser success. Due to the requirements of the CDA process, longer chain surfactants, having lower solubility in water, cannot be used. In CDI, however, high-water sols do not need to be used, allowing for the creation of host matrices from a wider variety of surfactants.

As seen in Figure 0-56, the viability of cells immobilized using *diC₆PC* is very similar with both processes. A slight edge in viability in CDI can be attributed to a higher initial viability since they do not come into contact with the solvents used in CDA. More interesting, though, is the extended viability that can be achieved when a variety of surfactants are introduced via CDI. Very usable viability is achieved for surfactants that cannot be used with CDA, allowing more control and flexibility when creating devices. For example, *diC₁₂PC* can be used to create a host matrix conducive to photo-patterning with PAG, discussed in more detail below. Cells immobilized in this system are over 80% viable after one week. This system is not achievable with CDA. Even more interesting differences appear when using traditional water-soluble surfactants, such as Brij-56. In these systems, the intimate fluid contact of the surfactant and cell during CDA leads to instant cell lysis and zero viable cells. However, when immobilized during CDI, the same surfactant does not only show lower toxicity, but actually reasonable viability. This example clearly demonstrates the dramatic enhancements obtained through CDI, allowing for the use of many different surfactants and materials while also paving the way for mammalian cell integration.

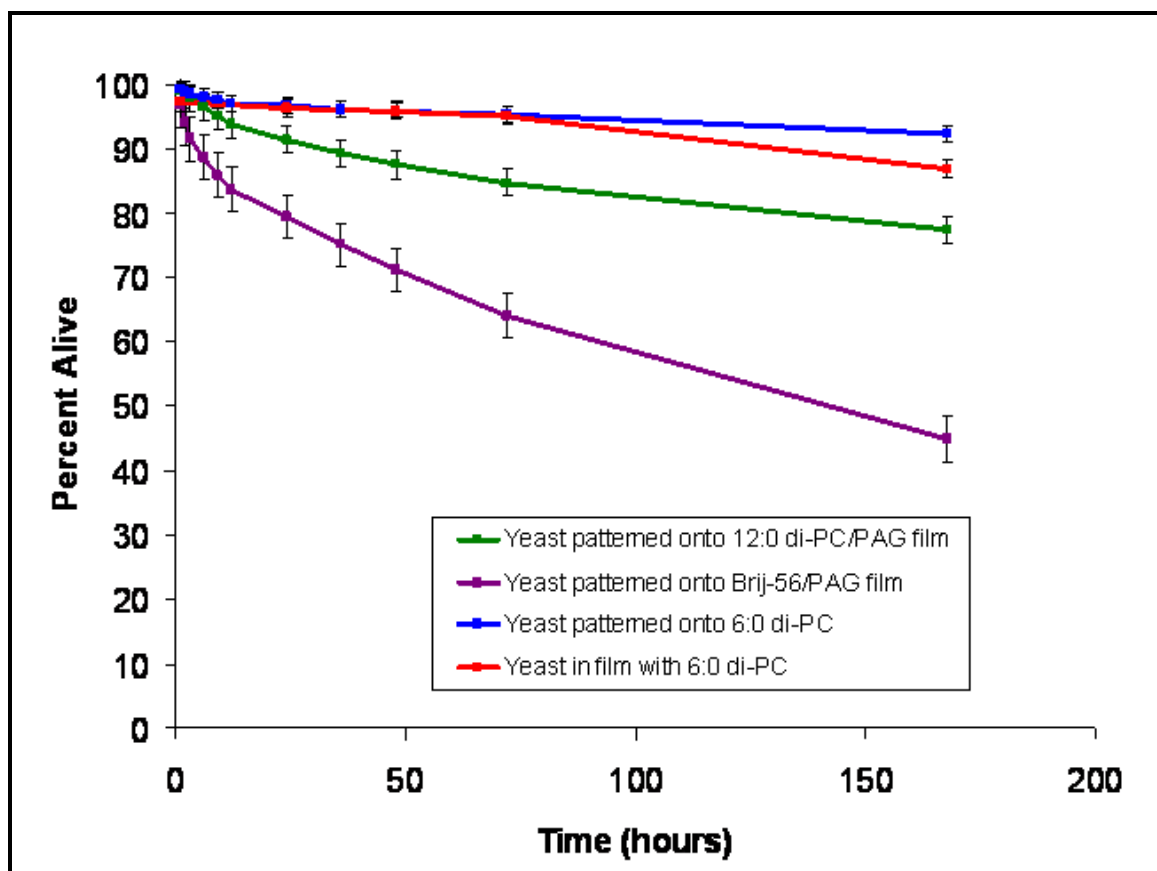


Figure 0-56. Comparison of viability of yeast cells immobilized with CDA versus CDI. Viability was determined using the standard two-color fluorescent probe for cells that have incubated at ambient conditions for the indicated periods of time without external buffers or media. Yeast immobilized in standard CDI system (blue) show slightly higher viability than yeast immobilized using CDA (red). Additionally, viable cells are also obtained using CDI with surfactants that are not compatible with CDA (green, purple). Error bars represent 95% confidence interval.

1.2.5 Functional mammalian cells can be integrated using CDI

One major limitation of the well-studied cell-directed assembly process is the inability to successfully immobilize mammalian cells with retained functionality. The benefits of CDA are not seen with mammalian cells because the exposure to solvent and drying stresses involved in traditional CDA can not be mediated by mammalian cells due to their lack of a cell wall. The cell-directed integration process seeks to minimize cell exposure to these stresses and therefore should be more compatible with mammalian cells.

To investigate the ability to immobilize mammalian cells using CDI, a genetically-modified mouse macrophage (RAW 264.7 Murine Macrophage - available through a collaboration with Sandia National Laboratories) was chosen to allow for simultaneous assessment of viability, accessibility, and functionality. The cells contain a GFP-fusion protein which will undergo ATP-dependent translocation into the cytosol during activation of the toll-like receptor 4 signal pathway by a model antigen, lipopolysaccharide (LPS), as shown below in Figure 0-57. Once these cells have been integrated, LPS can be introduced. If translocation of the GFP is observed, then accessibility of the cells to the surrounding external environment, functionality of cell surface proteins, and ability to conduct normal metabolic process are all confirmed.

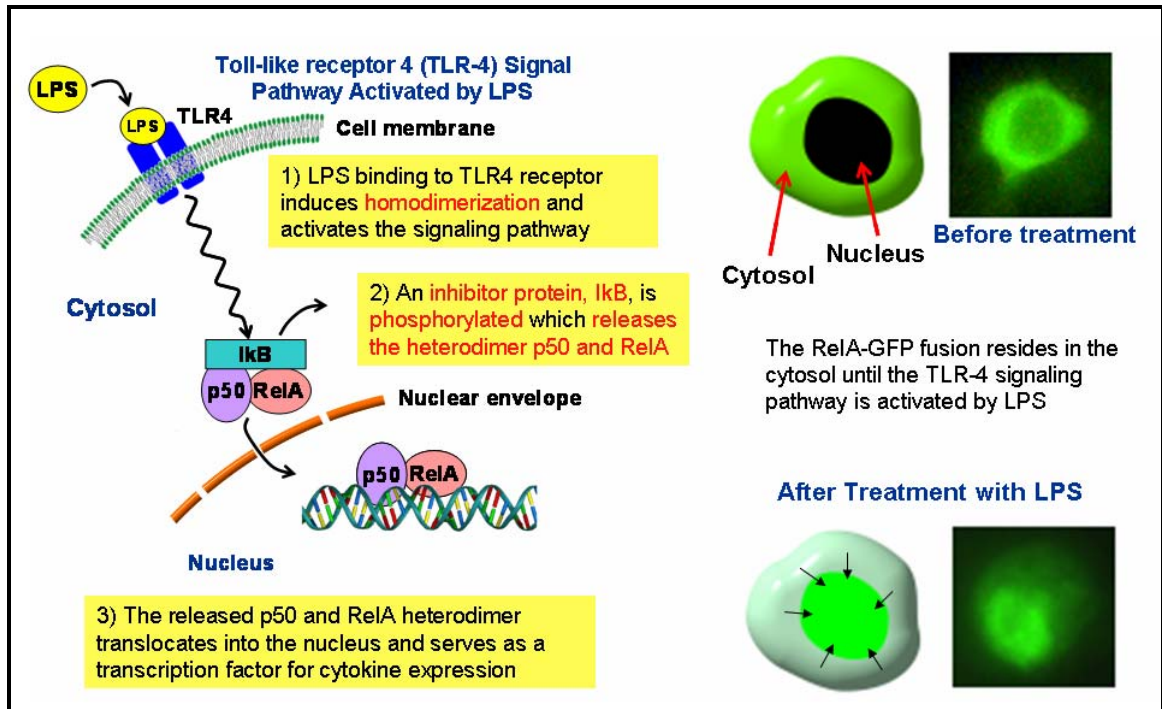


Figure 0-57. Genetic modification of macrophages for verification of accessibility, surface functionality, and viability. In this system, a GFP-fusion protein resides normally in the cytosol of the cell. However, in the presence of the model endotoxin lipopolysaccharide (LPS) and media, an ATP-dependent translocation of the fusion protein to the nucleus is observed.

To prepare macrophages for integration, the cells were removed from their culture dish using trypsin and resuspended in PBS. Nanostructured silica films containing *diC₆PC* were created as for the bacterial cells and yeast integrations. Macrophages in buffer were then added to the film using a pipette and allowed to integrate at room temperature for 2 minutes. Following washing of films with excess buffer, films were visualized using fluorescence microscopy to verify the presence of cells, as shown below in Figure 0-58. It can be seen that many cells remain on the film after washing, indicating the possibility of mammalian cell integration.

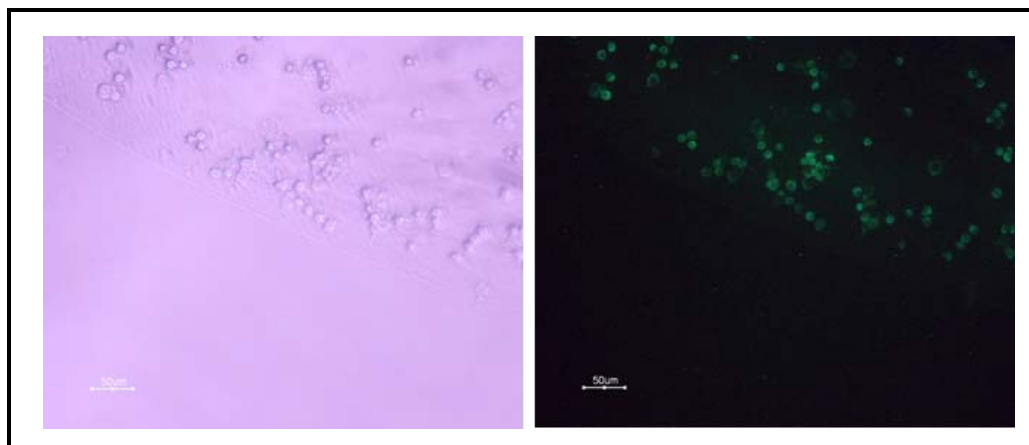


Figure 0-58. Optical and fluorescence images of macrophages integrated into a diC_6PC /silica film. Phase contrast (left) and fluorescence images (right) of the edge of a droplet of concentrated GFP-modified macrophages which have integrated at room temperature for 20 minutes.

To judge immediate interactions of the cells with the material, green fluorescently-labeled lipid was used to prepare additional diC_6PC /silica nanostructured films. Again, macrophages were added in buffer and allowed to incubate for two minutes prior to washing. As can be seen in Figure 0-59, the green lipid is redistributed in the area containing the cells. Although exact determination of lipid localization is difficult due to the ubiquitous presence of GFP in the cells, it can clearly be seen that the cells have some interaction with the film resulting in reorganization of the lipid, indicating that the cells are not simply sitting on top of the film. This is the same observation made with the yeast and the bacterial cells, indicating the localization of lipid around the cells.

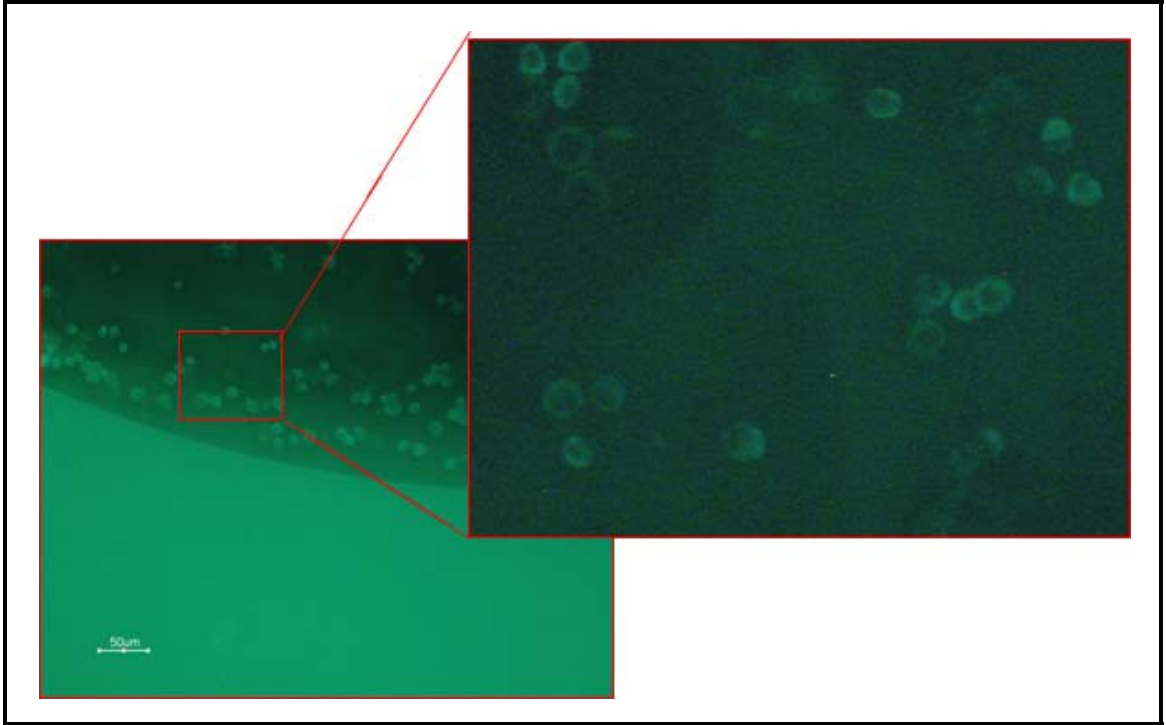


Figure 0-59. Fluorescence image of lipid reorganization by macrophages in an NBD diC_6PC /silica film. (Left) Redistribution of the lipid in the film (bright green) can be seen in a droplet of live GFP-modified macrophages (dull green). (Right) Higher magnification shows local regions of lipid reorganization around various groups of cells.

Verification of full-cell integration was then performed using SEM and EDS as for the yeast and bacteria. It is found that the macrophages can readily be imaged under the high-voltage electron beam after being allowed to incubate on the diC_6PC /silica films, indicating that the cells are protected by an insulating layer of silica as shown below in Figure 0-60. Again a transition region can be observed extending from the bulk film to the cell surface. However, this region appears much smaller due to the much larger size of the macrophage cells compared to the yeast and bacterial cells.

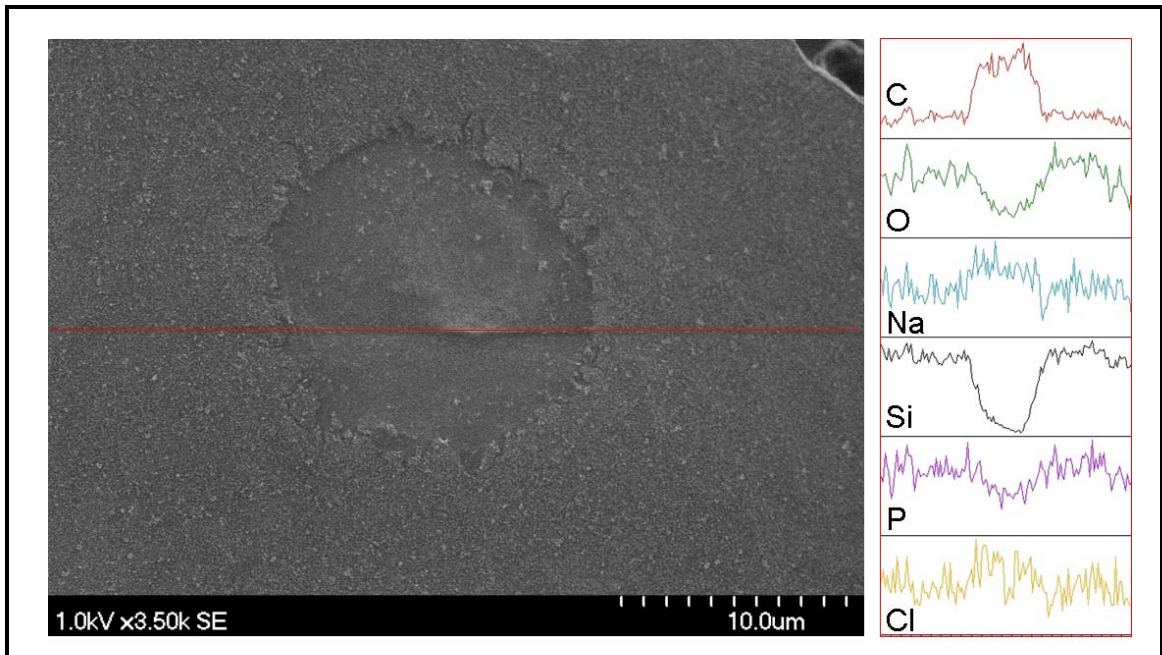


Figure 0-60. SEM image with corresponding EDS line scan of an integrated macrophage cell. SEM (left) of yeast show a region of transient elemental composition in the local vicinity of the cell as indicated by an EDS line scan (red).

Full, three-dimensional integration and encapsulation of the macrophage cells was then confirmed using cross-sectional SEM along with spotlight EDS and spectral elemental verification, as shown below in Figure 0-61. It is seen that cell retains a familiar 3D appearance. In addition to the ability to directly visualize these cells without any preliminary preparation, full encapsulation was confirmed by the spectral elemental analysis identifying the presence of silica on the top of the cell. Collectively, this data indicates that the cell-directed integration process can be used to immobilize and encapsulate mammalian cells in a manner similar to yeast and bacteria encapsulation.

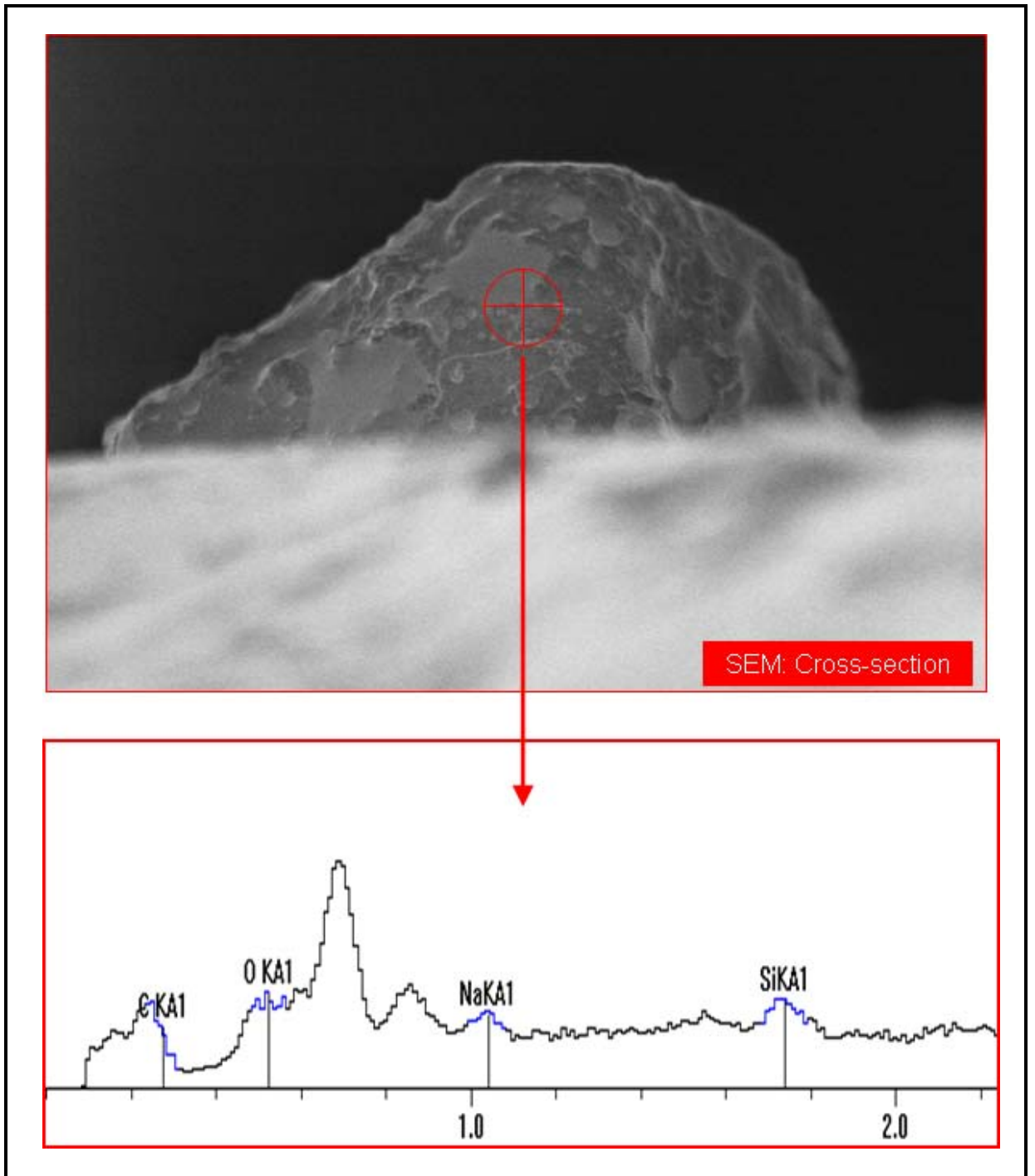


Figure 0-61. SEM cross-section and EDS spotlight confirm full integration of macrophages via CDI. (Top) SEM cross-sectional image of integrated macrophage. Spotlight (red) indicates area where EDS elemental confirmation was collected (bottom). It can be seen that the presence of silica around the cell is confirmed by automatic elemental recognition (blue).

Once the integration of the macrophages was confirmed, viability was assessed by way of the genetic modifications described above. Macrophage cells were integrated into nanostructured *diC₆PC*/silica films as previously discussed. After washing, films were dried and imaged using confocal microscopy to ensure that the integration process did not trigger non-specific translocation of the GFP-fusion protein. This data is shown below in Figure 0-62. After verifying that the integration process did not stimulate an immune response, the integrated cells were allowed to incubate in air at approximately 37°C for 24 hours (actually they sat in my car in the summer). The cells were then incubated at 37°C for 45 minutes in media containing 10 mM LPS. Films containing cells were then washed and imaged using confocal microscopy.

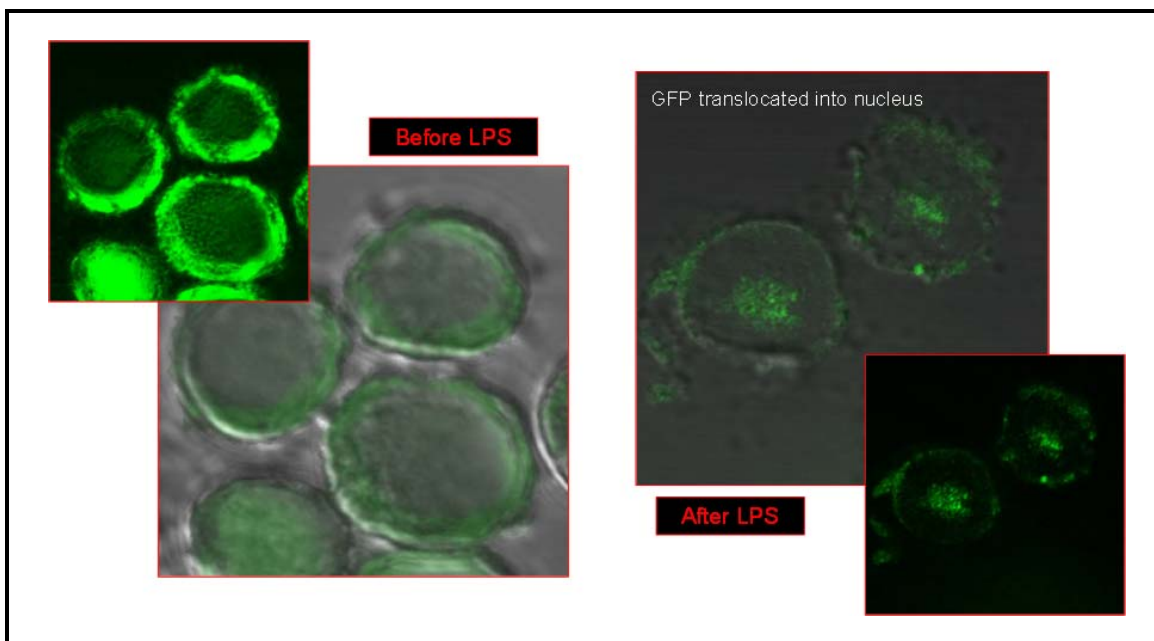


Figure 0-62. Confocal images confirming accessibility and functionality of integrated macrophages. (Left) Confocal and DIC images of macrophages following integration into a *diC₆PC*/silica film show the expected presence of the GFP-fusion protein in the cytosol of the cell, indicating that the integration process does not illicit an immune response. After incubating in air at 37°C for 24 hours, LPS in media is added to the immobilized cells. (Right) Following incubation with LPS and media for 30 minutes at 37°C, immobilized cells show translocation of GFP-fusion protein, confirming viability of the cells, as well as functionality of the cell surface receptors and accessibility of the cell to molecules of LPS and media.

Translocation of GFP to the nucleus can clearly be observed. Presence of GFP in the nucleus, as opposed to the top or bottom of the cell, was also confirmed through the use of confocal optical sectioning. This clearly shows that the integrated cells have remained viable for a much longer time than the cells normally survive even in buffer, where unintegrated cells survive for no more than 3 hours. From this data, we find that mammalian cells can be successfully immobilized using cell-directed integration. Using CDI with mammalian cells results in cells that are fully encapsulated in a nanostructured lipid/silica matrix while remaining accessible to the environment, allowing addition of

nutrients and other molecules of interest. This indicates that cell-directed integration provides the world's first technique for encapsulation of live mammalian cells for use in solid-state cell-based devices and cell interrogation platforms.

1.2.6 Key parameters effecting integration have been elucidated

As with cell-directed assembly, the integration of living cells into pre-formed silica nanostructures is understandably complex. To investigate the influence of both the cells and the nanostructures on the integration process, a standard integration protocol and method for counting the number of cells needed to be developed. To begin, a *diC₆PC*/silica film was created using the standard spincoating procedure and allowed to condense. Then 1 μL of live, stationary-phase yeast cells in DI water at a concentration of 9×10^9 cells/mL, stained with a red-fluorescent marker for easier visualization and counting, were allowed to integrate into the film at ambient conditions for various amounts of time, as shown in Figure 0-63. Following the interaction time, unintegrated cells were removed via washing for 10 seconds. Integration was then confirmed by SEM, EDS, and confocal microscopy as described above. Spots containing integrated cells were visualized using fluorescence microscopy and cells were counted using NIS-Elements microscopy imaging software.

We find that the number of cells that are able to integrate increases linearly for the first 30 minutes. After that time, a saturation level is reached. For this standard protocol, we achieve integration of approximately 1 in 6 cells. This number is likely to be limited by interactions between the cells and silica film relating to the contact angle and subsequent surface area for integration as well as the flocculation of the yeast. These results indicate that the integration process proceeds at a time scale that is similar to the

initial silica condensation time, indicating that silica is re-hydrolyzed resulting in the fluidity of the silica during cell integration.

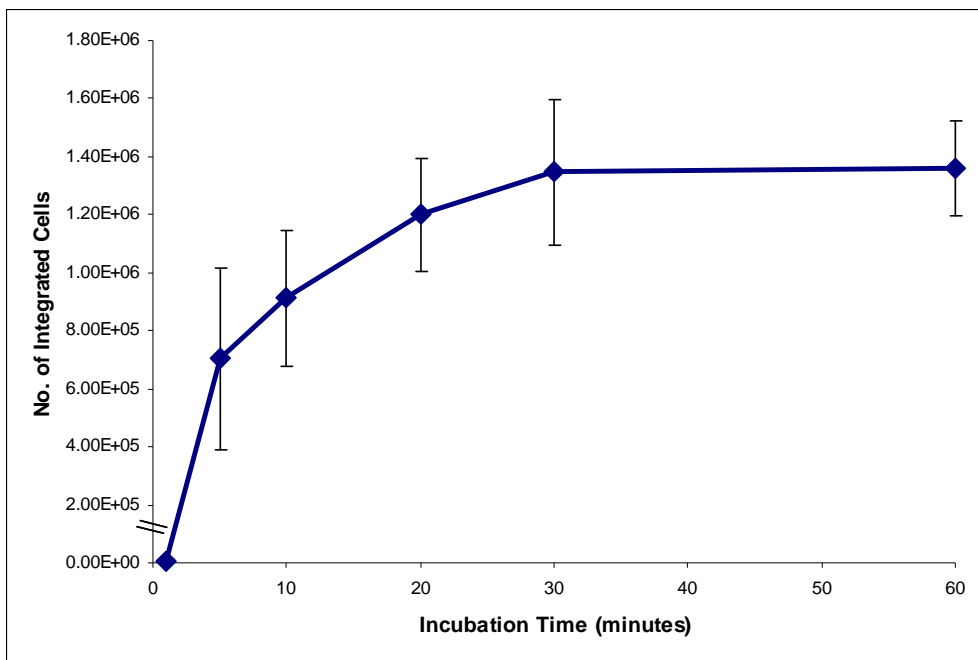


Figure 0-63. Number of integrated cells vs. incubation time. Approximately 10^7 yeast cells stained with SYTO 64 were added in water to premade diC_6PC /silica films and allowed to integrate for the indicated period of time at ambient conditions, after which unintegrated cells were washed off. The number of integrated cells was then counted using NIS-elements microscopy software. At all time points, $n = 12$. Error bars represent 95% confidence interval.

In order to establish this standard integration protocol, it was essential to ensure that the wash process was sufficient to remove all cells that were not integrated to obtain realistic and reliable data. We see in Figure 0-64 that the amount of cells present on a film decreases sharply with washing until a 10 second wash has been performed. After 10

seconds of washing, the number of cells on the film remains constant, indicating that all unintegrated cells have been removed.

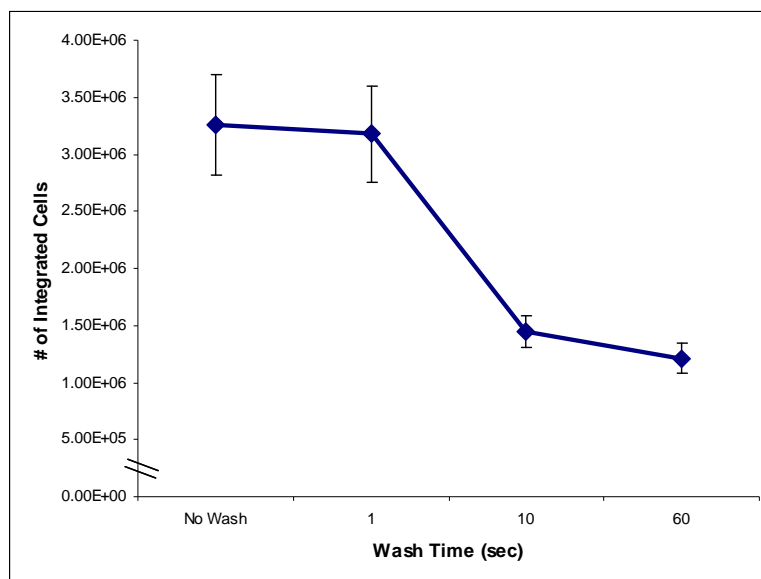


Figure 0-64. Number of cells on nanostructured silica film vs. wash time. Approximately 10^7 yeast cells stained with SYTO 64 were added in water to premade *diC₆PC*/silica films and allowed to integrate for 30 minutes at ambient conditions, after which unintegrated cells were removed by rinsing for the indicated period of time. The number of integrated cells was then counted using NIS-elements microscopy software. At all time points, $n = 12$. Error bars represent 95% confidence interval.

Assuming that intimate contact between the cells and lipid/silica film is required for integration, the competing effect of cell-cell contact may hinder cell integration. To investigate the effects of cell flocculation on the integration process, different initial concentrations of cells were allowed to integrate into a *diC₆PC*/silica film following the

standard procedure developed above. From this data, shown below in Figure 0-65, we find that the number of cells that are able to integrate increases linearly over a physiologically relevant range of concentrations, indicating that cell-cell interactions are not substantially hindering cell-material interactions and integration. However, as the density of the cells increases, we begin to approach a limiting number of integrated cells. At these high densities, flocculation and subsequent stacking of cells prevents interaction of some cells with the film. These cells are not able to integrate and thus removed by washing, confirming the necessity of intimate cell-material contact for integration.

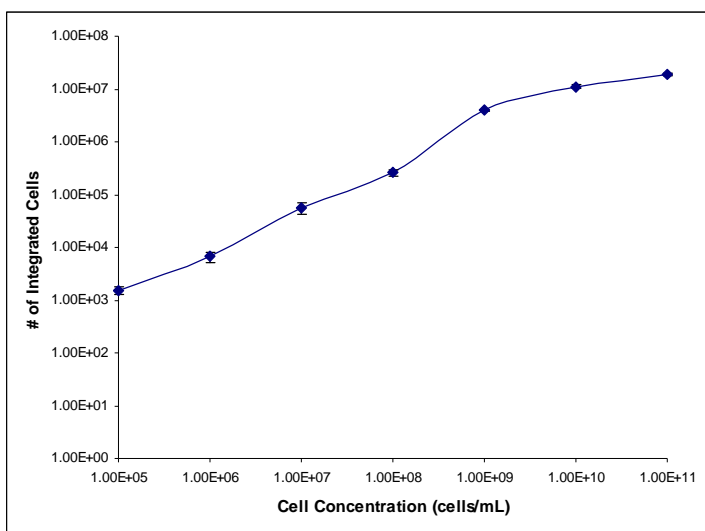


Figure 0-65. Number of integrated cells is linearly proportional to initial cell concentration over physiological values. Various concentrations of yeast cells stained with SYTO 64 were added in water to premade *diC₆PC*/silica films and allowed to integrate for 30 minutes at ambient conditions, after which unintegrated cells were removed by rinsing for 10 seconds. The number of integrated cells was then counted using NIS-elements microscopy software. At all time points, n= 12. Error bars represent 95% confidence interval.

1.2.6.1 Integration is an active process requiring live cells

Because of the observed similarities between integrated cells and cells immobilized using cell-directed assembly, it was assumed that cell-directed integration would also be a complex, active process requiring live cells. It has already been shown above that cell surrogates do not interact with the lipid or the silica and are not able to establish any pH gradients. Cell surrogates should, therefore, be unable to integrate themselves into a nanostructured silica film. To confirm this idea, latex bead cell surrogates were introduced to *diC₆PC*/silica films and counted as per the protocol developed for yeast above. As seen below in Figure 0-66, neither uncharged latex beads nor beads possessing a surface charge were retained after washing. This is a clear confirmation of the necessity of active interactions between live cells and the lipid/silica host to obtain integration.

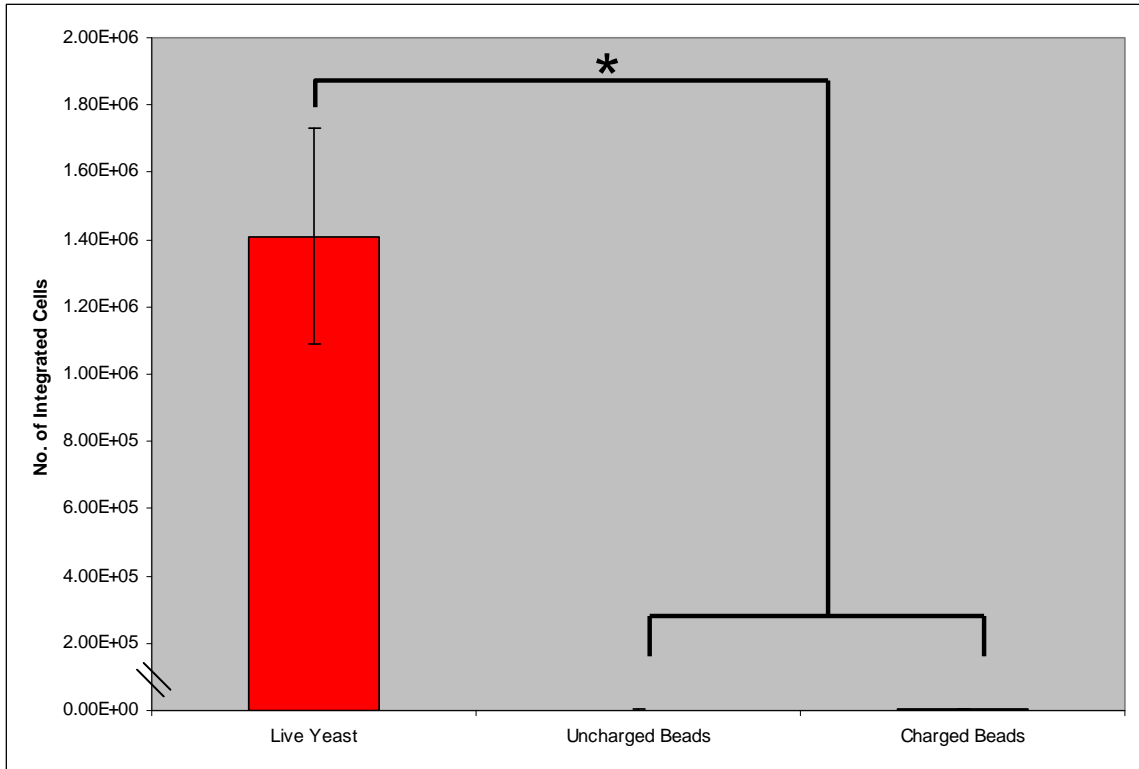


Figure 0-66. Comparison of integration capability of living cells and cell surrogates. Approximately 10^7 yeast cells stained with SYTO 64 or fluorescent latex beads with the indicated surface charge were added in water to premade diC_6PC /silica films and allowed to integrate for 30 minutes at ambient conditions, after which unintegrated cells and beads were removed by rinsing for 10 seconds. The number of integrated cells was then counted using NIS-elements microscopy software. ANOVA with Dunn's Multiple Comparison Post-Test: $n=30$, $*=p<0.05$. Error bars represent 95% confidence interval.

1.2.6.2 Ability of cells to create pH gradient is crucial to integration

One of the many ways in which a cell can interact with its environment is by affecting the pH of the surrounding area through a process of osmosis and ion flux. This ability to control pH has been found to be a key feature in both cell-directed assembly and cell-directed integration. To quantify the effects of establishing a pH gradient during

the integration process, a series of buffers of varying composition, pH, and ionic strength were employed. Yeast cells were introduced to a diC_6PC /silica film as described above, only being suspended in the indicated buffer solution instead of water. After washing, integrated cells were counted, with the results presented below in Figure 0-67.

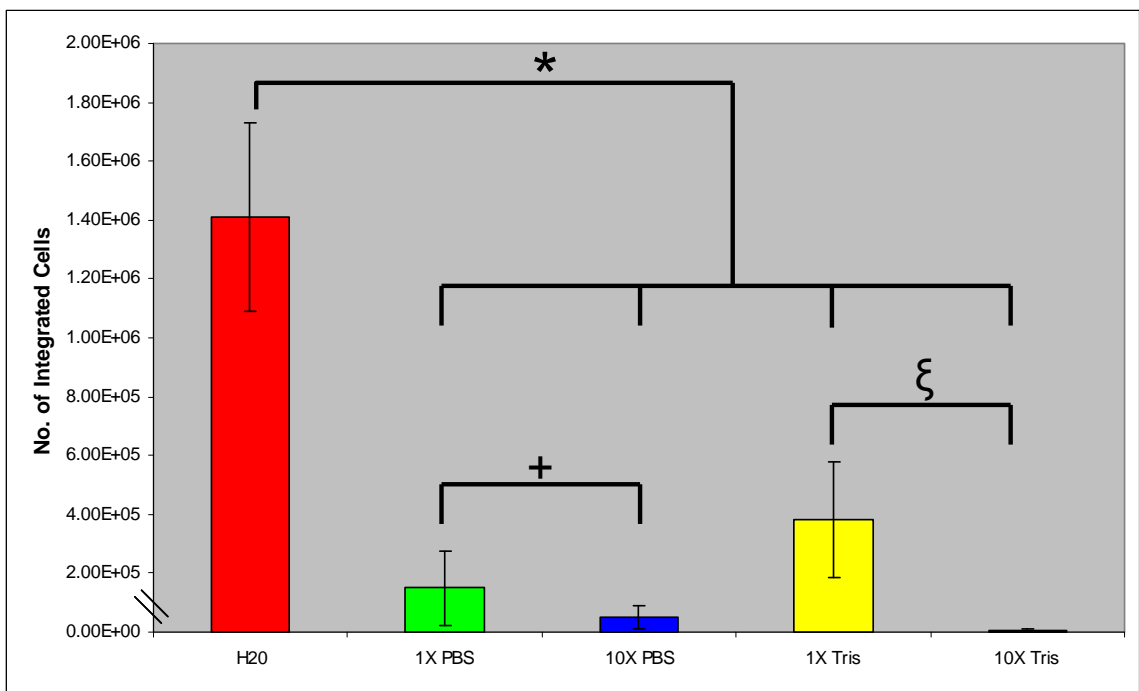


Figure 0-67. Effects of buffers on cell integration. Approximately 10^7 yeast cells stained with SYTO 64 were added in the indicated buffer to premade diC_6PC /silica films and allowed to integrate for 30 minutes at ambient conditions, after which unintegrated cells were removed by rinsing for 10 seconds. The number of integrated cells was then counted using NIS-elements microscopy software. ANOVA with Dunn's Multiple Comparison Post-Test: $n = 30$, $*$ = $p < 0.05$, $+$ = $p < 0.05$, ζ = $p < 0.05$. Error bars represent 95% confidence interval.

We see a dramatic reduction in the number of cells that are able to integrate when introduced in 1X PBS at pH 7. This number is even further reduced when the buffer

capacity is increased to 10X, which effectively prevents the development of any gradients by maintaining the entire system at a neutral pH. This is a clear indication of the necessity of a pH gradient to drive the integration process.

It is also known that phosphates can interact with silicates to hinder silica condensation³⁰. Therefore, integration of cells in the presence of a phosphate buffer such as PBS could be hindered by these interactions. To ensure that this phenomenon was not resulting in the observed decreased number of integrated cells in the presence of PBS, a buffer containing no phosphates, Tris, was used. We find that there is a slight increase in the number of cells that are able to integrate in the presence of a buffer that does not contain phosphates, indicating that the phosphates do contribute a small interference with the interactions of the cell with the silica required for integration. We again find that there is another serious reduction in the number of integrated cells when the buffer strength is increased to 10X. This confirms the requirement of a pH gradient for the rearrangement of lipid and silica during integration to occur.

1.2.6.3 Cell surface composition and metabolic state greatly impact ability to integrate

Since the establishment of a pH gradient is required to drive the integration of cells into lipid/silica nanostructures, it is clear that active metabolic processes from the cell are also needed. With the necessity of intimate interactions between the cell and the material, the surface of the cell must also play a key role in integration. To confirm these

assumptions, various methods were used to alter the cell surface composition as well as the metabolic state of the cell, with the results presented below in Figure 0-68.

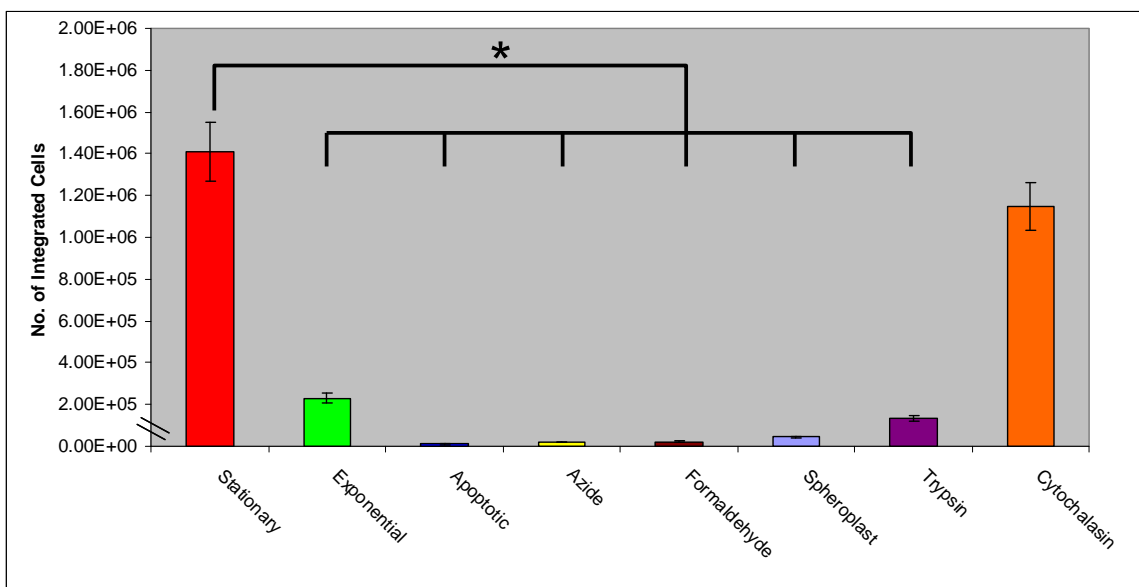


Figure 0-68. Effects of cell surface composition and metabolic state on cell integration. Approximately 10^7 yeast cells, stained with SYTO 64, in the indicated metabolic state or treated with the indicated chemical using the standard microbiology textbook method were added in the indicated buffer to premade diC_6PC /silica films and allowed to integrate for 30 minutes at ambient conditions, after which unintegrated cells were removed by rinsing for 10 seconds. The number of integrated cells was then counted using NIS-elements microscopy software. ANOVA with Dunn's Multiple Comparison Post-Test: $n = 30$, $* = p < 0.05$. Error bars represent 95% confidence interval.

First, yeast were grown out in exponential phase and concentrated to match the stationary-phase standard. After integration and washing, we find that there is a dramatic reduction in the number of exponential-phase cells that are able to integrate compared to stationary phase cells. This is a result of the varying cell metabolism and surface composition found between exponential and stationary growth phases, in which

stationary phase cells display a fully-developed cell wall in contrast with the membrane-like cell wall of cells in an exponential growth phase³¹.

To further characterize the effects of the cells' metabolic state on the integration process, cells that have been induced into apoptosis by heat shock were used. It has been shown above that these cells are not able to establish a large external pH gradient and do not effectively interact with the lipid in the host matrix. We find that these cells integrate at numbers at least two orders of magnitude below the standard, which is at the lower detection limit of our microscopic counting technique. This drastic reduction in the ability of cells to integrate shows that in order for cells to integrate they must be in an active metabolic state capable of interaction with the external environment by controlling the pH.

Additionally, we find that chemically altering the metabolic state of the cell can also limit integration ability. ATP production in the cell can be effectively inhibited by the use of sodium azide to decouple the electron transport within the cell's respiratory cycle. When cells were treated with sodium azide prior to integration, we find that very few of the cells are able to integrate, similar to the apoptotic cells. A similar trend is also observed when cells are fixed with paraformaldehyde. These results confirm the necessity of active metabolic processes to establish a pH gradient and interact with the lipid and silica resulting in integration.

The effects of the cell surface composition can also be investigated by chemically alteration. We have already seen that the change in cell surface between the exponential and stationary growth phases dramatically impacts the integration process. If the cell wall of the stationary phase cell wall is enzymatically removed using zymolase to create

spheroplasts, cells are able to integrate in numbers similar to that of the exponential phase cells. This is not surprising, as it has already been shown above that cells are unable to maintain an effective pH gradient with their cell wall removed. This result displays the influence of the stationary phase cell wall and the corresponding ability to control the pH of the surrounding environment during the integration process. This notion is furthered when similar results were obtained for cells that had been treated with trypsin to damage the cell surface proteins. The impaired ability of the cell to interact with the lipid and silica with damaged surface proteins confirms the importance of the interaction of the cell surface with the lipid and silica in order to achieve integration.

A physical attempt by the cell to “burrow” into the film was also investigated. Cytochelasin was used to destroy the actin composing the yeast cytoskeleton. This destroys the cells’ ability to perform any directed locomotion. When yeast are treated with cytochelasin before attempting integration, we find that this lack of movement does not impact the integration process. This indicates that the interaction of the cell surface with the lipid and silica is dominant during the integration process.

If the integration process truly requires active processes from the cell, then integration should be influenced by the temperature and resulting metabolic rate of the cells. We find, in Figure 0-69 below, that the cell metabolic rate does directly influence the number of cells that integrate. At 32°C, the metabolic rate of the cell is roughly two times the rate at 25°C. Similarly, we found that the number of cells that integrate approximately doubles at 32°C. We also find a corresponding decrease in cell integration at lower temperatures. Additionally, we found that the temperature of the film over this same range was not a factor, as we are already well above the transition temperature for

this lipid. These results indicate that the interaction of the cell surface with the material and the ability to establish pH gradients to drive integration are clearly manifestations of active cell responses.

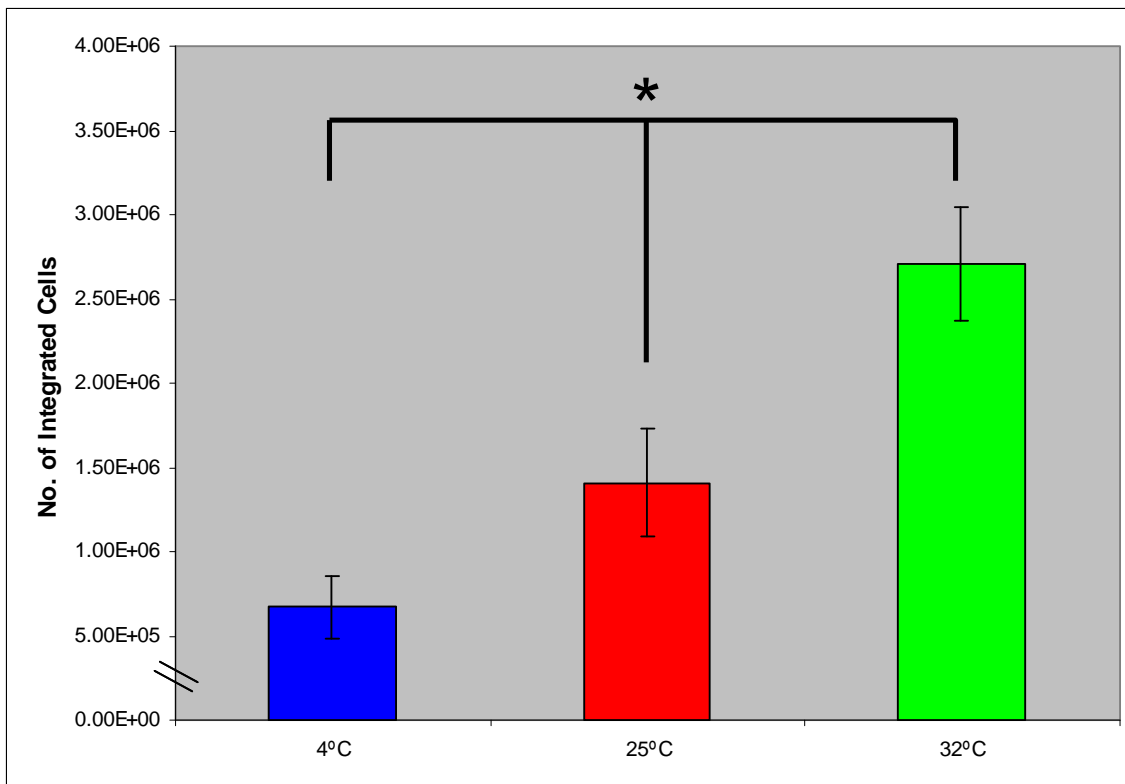


Figure 0-69. Effects of temperature on cell integration. Approximately 10^7 yeast cells stained with SYTO 64 and maintained at the indicated temperature were added in water to premade $diC_6PC/silica$ films and allowed to integrate for 30 minutes at the indicated temperature, after which unintegrated cells were removed by rinsing for 10 seconds. The number of integrated cells was then counted using NIS-elements microscopy software. ANOVA with Dunn's Multiple Comparison Post-Test: $n = 30$, * = $p < 0.05$. Error bars represent 95% confidence interval.

1.2.6.4 All integrated cells establish similar environments

One distinctly interesting observation made during the course of these cell integration experiments is that all cells that were able to integrate appear surprisingly similar. All integrated cells form a distinct pH gradient and a region of localized surfactant, as confirmed by SEM, EDS, and confocal microscopy. This seems to confirm the importance of cellular metabolic behavior and surface interactions with the silica and surfactant in the integration process. Effectively, the only cells that were able to integrate were those that were unaffected by the various treatments.

1.2.6.5 Composition of nanostructure and resulting surface characteristics directly effect integration

The previously mentioned data for cell integration was obtained using a system consisting of *diC*₆PC and partially-hydrolyzed TEOS in a high-water sol displaying a relatively slow condensation rate. One main advantage of the cell-directed integration approach is the ability to integrate cells within various nanostructures by varying the type of surfactant template as well as the sol composition. The effects of differing surfactants and sols on the number of cells that are able to integrate are shown below in Figure 0-70.

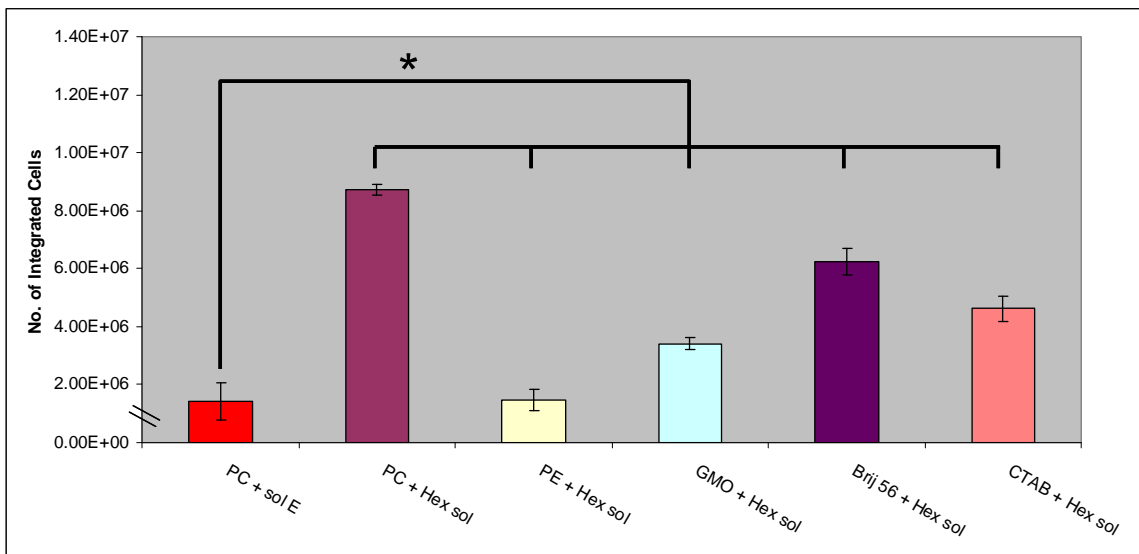


Figure 0-70. Effects of different lipids and sols on cell integration. Approximately 10^7 yeast cells stained with SYTO 64 were added in water to premade films using different surfactants and silica sol compositions, then allowed to integrate for 30 minutes at ambient conditions, after which unintegrated cells were removed by rinsing for 10 seconds. The number of integrated cells was then counted using NIS-elements microscopy software. ANOVA with Dunn's Multiple Comparison Post-Test: $n = 30$, * = $p < 0.05$. Error bars represent 95% confidence interval.

Besides the aforementioned partially-hydrolyzed TEOS sol (sol E), high-quality ordered nanostructures can also be obtained by using diC_6PC with an unhydrolyzed TEOS sol (hex sol). Despite having the same templating molecule and the same nanostructure, these two films do not have similar wetting angles with water. As a result, droplets spread further on the more hydrophilic hex sol system. This effectively increases the surface area of the nanostructure available for interaction with the cells and consequently leads to a higher number of integrated cells.

The hex sol does not contain an abundance of water, and as such can be used to form high quality nanostructures using a variety of surfactant molecules. A variety of

molecules were used, including short-chain lipids with different head groups as well as longer chain lipid analogues and traditional surfactants resulting in hexagonal, rhombohedral, and cubic symmetries to integrate cells as mentioned above. We find that the number of cells that are able to integrate into each film is consistent with the wetting angle of the film surface, further demonstrating the importance of intimate contact between the cell, surfactant, and silica in order for the cell to integrate into the material.

1.2.6.6 Ability of cells to integrate is dependent on the extent of silica condensation

If cell integration is dependent on the ability of silica to be differentially hydrolyzed and condensed due to the pH gradient established by the cell, then the extent of condensation of the film prior to the introduction of cells should be a limiting factor. By using various methods to promote silica condensation, it can be shown that cell integration is hindered by increasing the extent of pre-condensed silica in the film.

Concentrated base vapors can be used to enhance the rate of silica condensation without damaging the surfactant molecules. When standard (*diC₆PC* and sol E) films are exposed to 5N NH_4OH vapors for varying amounts of time, the effects of silica condensation on integration are revealed, as shown below in Figure 0-71. We find that brief exposures can actually increase the number of cells that are able to integrate. This can be attributed to a decreasing contact angle resulting in more accessible surface area, as mentioned above, and a minimal amount of silica condensation at these short times. At longer times, however, the contact angle stabilizes and the number of integrated cells

begins to decrease. This is indicative of the necessity of the cells to interact with uncondensed silica in order to obtain the rearrangement of molecules noted in the integration process.

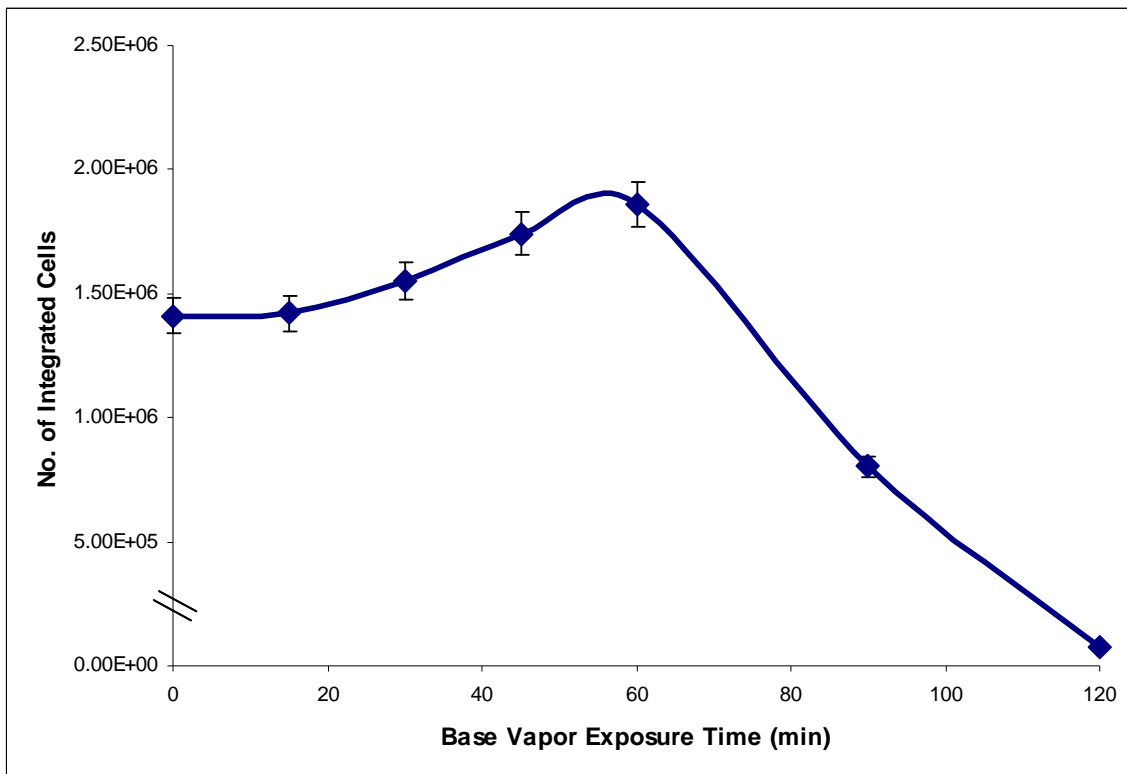


Figure 0-71. Effects of silica condensation by base vapor exposure on cell integration. Approximately 10^7 yeast cells stained with SYTO 64 were added in water to premade diC_6PC /silica films, which had been exposed to saturated ammonium hydroxide vapors for the indicated period of time, and allowed to integrate for 30 minutes at ambient conditions, after which unintegrated cells were removed by rinsing for 10 seconds. The number of integrated cells was then counted using NIS-elements microscopy software. At all time points, $n=12$. Error bars represent 95% confidence interval.

The rate of silica polymerization can be also catalyzed by the presence of UV light. As such, films created using the standard protocol (*diC₆PC* and sol E) were treated in a UV/Ozone reactor (UVO) for varying lengths of time prior to cell integration. The number of cells that were able to integrate into these films is shown below in Figure 0-72. We find, as for the base vapor exposure, initial exposure results in increased hydrophilicity and leads to higher numbers of integrated cells. Again we see an eventual decrease in the number of integrated cells following the stabilization of wetting angle and further condensation. What is interesting to note, however, is that the surfactant is also being broken down and removed by the ozone during this process. By following this process with IR spectroscopy, we find that the contact angle of the film changes as the surfactant is degraded. The stabilization of the contact angle coincides with the destruction of all template molecules. At this point, however, the silica has not been fully condensed. After this time, we see a dramatic decrease in the ability of cells to integrate into these films, demonstrating the importance of the interactions between not only the cell and the silica, but also the interactions of the surfactant with the cell and with the silica.

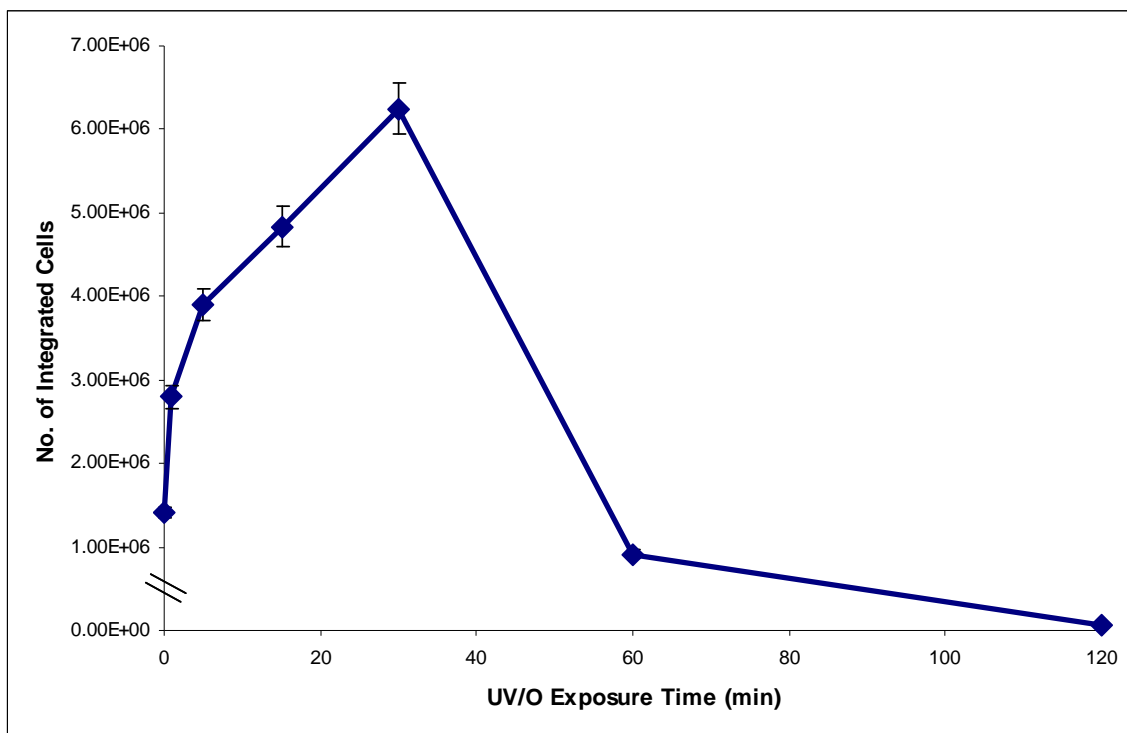


Figure 0-72. Effects of silica condensation by UV/O exposure on cell integration. Approximately 10^7 yeast cells stained with SYTO 64 were added in water to premade diC_6PC /silica films, which had been exposed in a UV/O cleaner to for the indicated period of time, and allowed to integrate for 30 minutes at ambient conditions, after which unintegrated cells were removed by rinsing for 10 seconds. The number of integrated cells was then counted using NIS-elements microscopy software. At all time points, $n=12$. Error bars represent 95% confidence interval.

Humidity is an important, yet often overlooked, factor in creating nanostructured silica materials. Silica condensation is promoted by increasing the humidity, allowing more water, a reactant in this case, to access the developing silica network. The effects of humidity and the resulting silica condensation on cell integration were investigated using the standard films (diC_6PC and sol E). The number of cells that were able to integrate into films which had been exposed to various humidities over time is shown below in Figure 0-73.

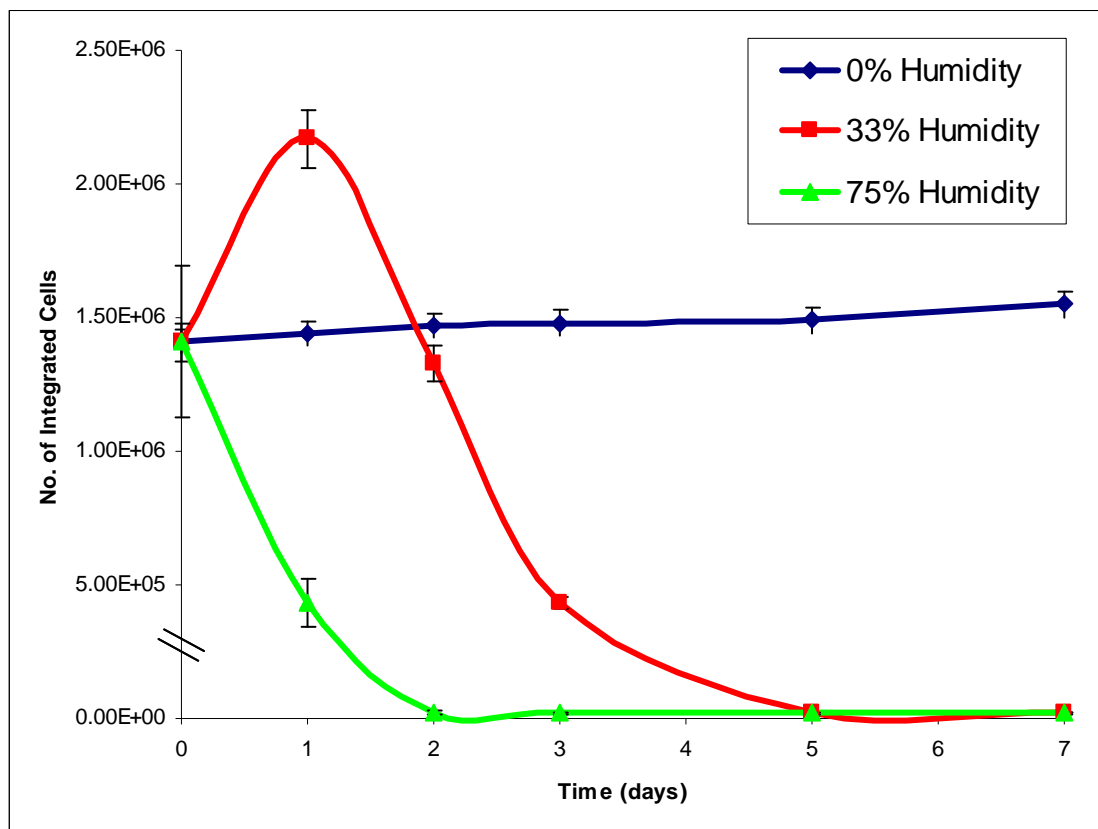


Figure 0-73. Effects of humidity on cell integration. Approximately 10^7 yeast cells stained with SYTO 64 were added in water to premade diC_6PC /silica films, which had been maintained at the indicated humidity for the indicated period of time, and allowed to integrate for 30 minutes at ambient conditions, after which unintegrated cells were removed by rinsing for 10 seconds. The number of integrated cells was then counted using NIS-elements microscopy software. Error bars represent 95% confidence interval.

Again, we find that the amount of cells initially increases due to a decreasing wetting angle. Integration then decreases after stabilization of the contact angle, coinciding with further silica condensation. The time at which the extent of silica condensation begins to hinder the integration process is dependent on the humidity of the environment surrounding the film. By increasing humidity, the rate of silica condensation

also increases, resulting in a dramatic decrease in the number of cells that are able to integrate into the films.

Humidity is of great interest when designing a platform for cell-based systems. The effects of humidity on cell integration give us information related to the shelf-life of the nanostructures. For our nanostructured silica films to serve as platforms for these systems, it is obvious and imperative the cells must be able to integrate into the films. This data shows us that these films could be marketed as platforms for cell immobilization and retain an acceptable shelf-life if stored properly in a low-humidity environment that would minimize the hygroscopic nature of the films.

1.2.7 CDI is amenable to many simple patterning strategies

Another drawback of using cell-directed assembly is the limited ability to create patterned placement of cells. The only practical method involves the aerosol deposition method (as described above for the quorum sensing investigation) combined with some robotic control, such as ink-jet printing. This limits the system to isolated wells of cells surrounded by the matrix. This, however, will not be adequate for investigations of cell-cell communication that are becoming increasingly important. Alternatively, cell-directed integration is conducive to a variety of patterning techniques that would allow for the spatial arrangement of viable cells while retaining connectivity through the nanostructured host.

1.2.7.1 Optical patterning via selective wetting and condensation

Patterned cell-directed integration can be achieved by way of widely available materials needed for conventional optical lithography. Two separate strategies for patterned cell integration have been developed exploiting lithographical control to produce areas of selective wetting and condensation. These simple methods make use of traditional optical lithography with UV light passing through a standard gold-on-quartz mask normally used in conventional semiconductor manufacturing techniques, as represented below in Figure 0-74.

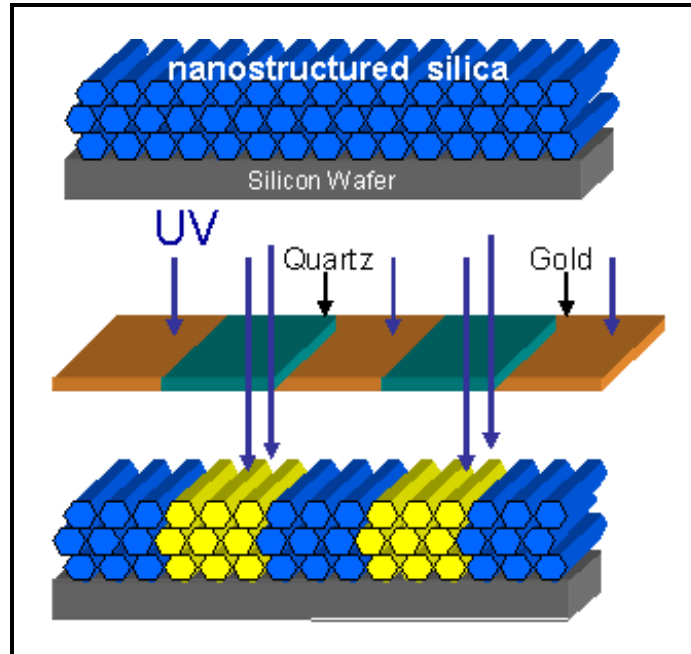


Figure 0-74. Selective wetting/condensation via optical lithography. Areas of different water contact angle can be specified by passing UV light through a gold/quartz mask normally used for traditional optical lithography.

The first cell patterning method makes use of a method previously developed in our group to photo-pattern mesoporous silica films³². In the modified procedure for cell integration, a photoacid generator (PAG) is incorporated into the film which decomposes upon exposure to UV light to form hydrophobic constituents, thereby allowing one to selectively change the wetting angle. This PAG molecule can be incorporated into silica nanostructures formed with various structure-directing agents to obtain different contact angle characteristics. As seen below in Figure 0-75, the behavior in developed contact angle is different when using traditional surfactants, such as Brij 56, versus biocompatible surfactants, such as *diC*₁₂PC.

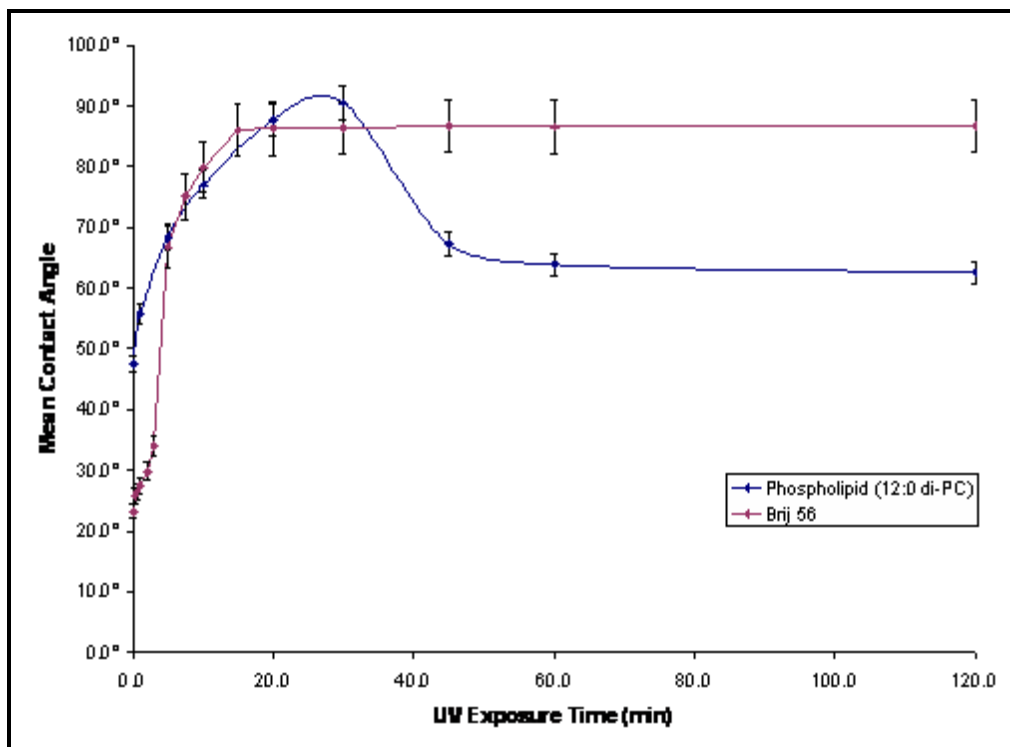


Figure 0-75. Change of contact angle with UV exposure creates selective wetting regions that can be used to immobilize cells via CDI. 5 mol % PAG was added to nanostructured silica films templated with the indicated surfactant and created via EISA. Following exposure to UV light for the indicated periods of time, contact angles were evaluated using a goniometer. . Error bars represent 95% confidence interval.

Initial exposure of these films to UV light results in the expected decomposition of PAG, resulting in an increase in contact angle for the exposed regions. However, an eventual decrease in contact angle with time can be seen for the phospholipid-templated films, attributed to photodecomposition of the phospholipid into hydrophilic components (confirmed with IR spectroscopy) combined with hydrophilic condensation and organic removal from the surface of the silica (as observed for superhydrophobic/philic optical patterning paper that Eric Branson should be writing). Using an optical mask, discrete areas can be created with a defined contact angle. When cells are added, they localize to

the unexposed, hydrophilic regions where they are able to integrate as described above. An example of patternable integration of yeast cells into a lipid/silica nanostructure can be seen below in Figure 0-76. In this system, a mask featuring 10 micron lines on a 20 micron pitch was used to create linear regions of hydrophilic regimes separated by hydrophobic regimes. When a dilute suspension of live yeast cells in PBS is introduced via spincoating on top of the patterned film, the cells localize and integrate in the hydrophilic regions, as expected. This demonstrates one effective method for patterning the integration of live cells into pre-formed silica nanostructures using readily-available materials from the semiconductor manufacturing industry.

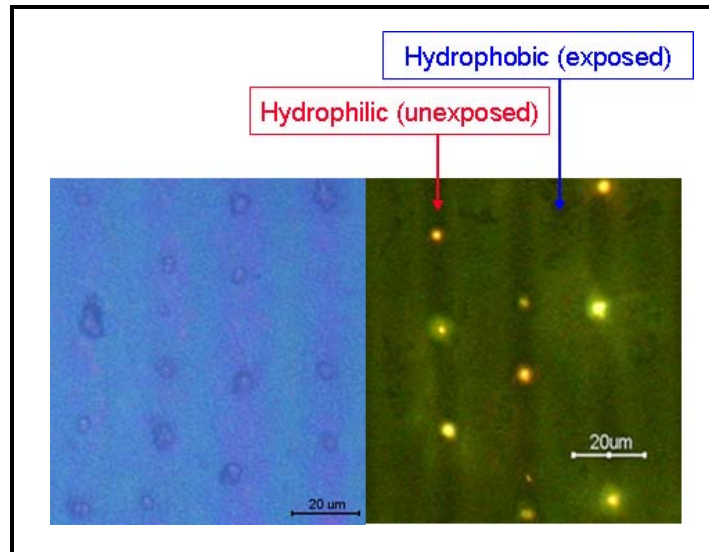


Figure 0-76. Images of integrated yeast patterned via selective wetting. Nanostructured $diC_{12}PC/silica$ films containing 5% PAG were exposed to UV light for 20 minutes under a gold/quartz mask featuring 5 micron lines on a 10 micron pitch to create hydrophilic areas of 50° and hydrophobic areas of 92° . Live yeast cells, stained green and red for visualization, were then added and allowed to incubate for 5 minutes prior to removal via high-speed spinning. It can be seen that the cells preferentially integrate into the uncondensed, hydrophilic areas.

In another related patterning scheme, cells can be immobilized without the use of photoacid generator. Instead of exploiting the ability to pattern regions by selective wetting, this method relies on the ability to promote silica condensation via UV initiation. In this method, a standard optical mask is again used to pattern regions of UV exposure. Using a phospholipid templated silica film, select regions are exposed to UV through the optical mask. The exposed regions undergo rapid condensation of silica. Once the silica has been fully condensed, cells are no longer able to integrate using the cell-directed assembly approach. Cells will, however, integrate into the unexposed, uncondensed regions of the film, creating another technique for localizing cell integration. Live cells can easily be selectively integrated using this patterning method, as seen in Figure 0-77.. In this example, a mask is used that features 100 micron circular spots on a 200 micron pitch. First, live GFP-modified yeast are applied to the lipid/silica film. After incubation at ambient conditions for 5 minutes, the films were washed, leaving only cells that had integrated in the unexposed regions. This demonstrates an alternative method for patterned cell integration using only a standard optical mask and UV light.

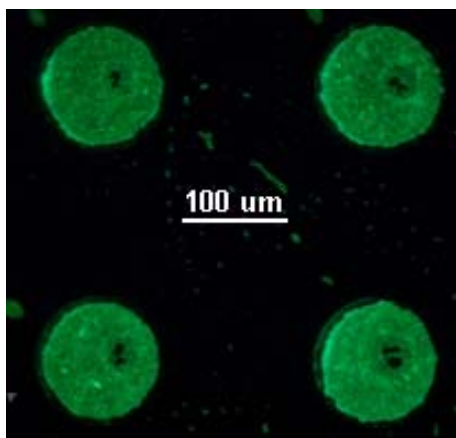


Figure 0-77. Images of integrated yeast patterned via selective condensation. A diC_6PC /silica film was exposed to UV for 5 minutes under a gold/quartz mask featuring 100 micron holes. GFP-modified yeast were then added to the film and allowed to integrate for 5 minutes, after which the unintegrated cells were removed by washing. It can be seen that the majority of cells are only able to integrate into the uncondensed regions of the film.

1.2.7.2 Cells can be directly patterned and integrated

In a different approach to patterning, cells in liquid can simply be placed on a lipid/silica film, allowing integration to occur where the cells are placed. This can be accomplished as simply as placement of cells onto a film using a pipette or syringe. Following a short incubation at room temperature, unintegrated cells can be removed by washing, resulting in cells integrated exactly where they are placed. This direct patterning method can be extended to create arrays of cells at several length scales depending on the method used to introduce the cells. Using hand tools as mentioned above, resolution on the millimeter scale is achievable. To pattern on finer scales, other deposition techniques such as aerosol deposition and ink-jet printing can be used. In this example, yeast cells

were patterned using aerosol deposition through a porous mask, in a manner similar to spray painting with a stencil. This ability of cell-directed integration to be compatible with direct patterning methods could lead to the creation of complex new cell-based devices with precise control of cell placement.

1.2.7.3 Functionality is increased with multi-step UV/O lithography

In order to control the placement of cells along with other materials needed to study spacio-temporal cell-cell interactions, we have developed a novel multi-step optical patterning technique which utilizes several of the patterning strategies previously discussed. This new technique is represented schematically for the integration of yeast in Figure 0-78 below. Nanostructured silica films are created via evaporation induced self-assembly of aqueous silica precursors with a biologically compatible surfactant, glycerol monooleate (GMO) via dip-coating, spin-coating, drop-casting, or aerosol deposition. GISAXS studies show the films to form a highly ordered cubic nanostructure as discussed above. The surfactant can be removed by calcinations or by UV/ozone lithography to yield a porous silica film.

To create patterned regions for cellular integration into the nanostructured silica matrix, we exploit the change in the hydrophobicity and fluidity of the surface of the film upon UV/ozone exposure. When the film is first deposited, it has a relatively low contact angle with water and remains in a semi-solid state. Upon exposure to UV/ozone, the GMO begins to photodecompose and the silanol precursors become more condensed. This yields a pattern where UV/ozone exposed regions are more hydrophobic and

solidified and adjoining unexposed regions are more fluid and hydrophilic. Longer exposure to UV/ ozone removes the surfactant entirely, leaving a porous and extremely hydrophilic film surface. The use of a standard UV lithographic mask on top of the film allows for the definition of hydrophobic/hydrophilic regions when exposed to UV/ozone. The areas that are blocked by the mask remain hydrophilic, while exposed areas are more hydrophobic. Once these regions are defined, living cells introduced in water (or a water-based nutrient media) selectively localize to the defined hydrophilic regions.

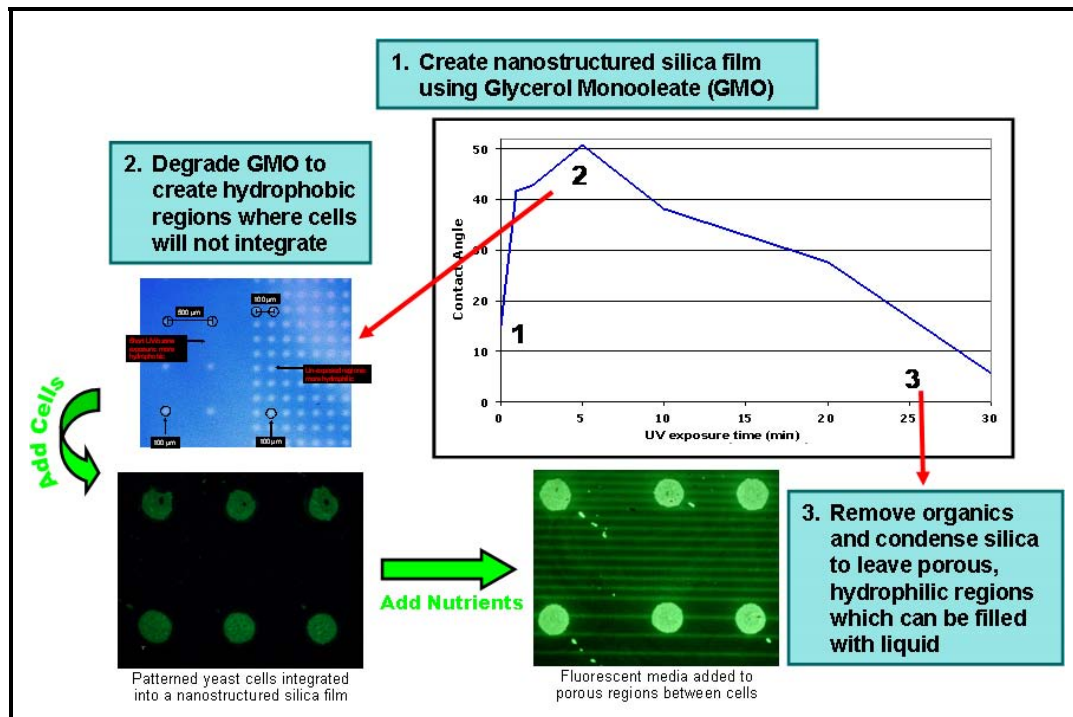


Figure 0-78. Schematic procedure for multi-step UV/O patterning of cells and nutrients. Initially, a GMO/silica film is created having a water contact angle of 18°. Films are then exposed to UV light under the pictured gold/quartz mask for 5 minutes to create regions of defined contact angle difference. GFP-modified yeast cells are then added and allowed to integrate for 5 minutes, after which unintegrated cells are removed by rinsing. Following integration of cells, another exposure to UV light for 30 minutes under a different gold/quartz mask featuring lines is used to create porous regions connecting the integrated cell areas. These porous regions were then filled with fluorescently-tagged media using vacuum-assisted diffusion.

The functionality of this system has also been further extended using the ability to remove the surfactant to regain a hydrophilic film that is now porous. After deposition of the cells onto the hydrophilic/hydrophobic patterned film, the degraded surfactant in the hydrophobic portions can be completely removed using UV light and ozone, leaving porous, hydrophilic portions of the film. With the appropriate pattern on a UV mask, this technique can be used to create porous regions between the localized cells that can be used to introduce nutrient media, growth factors, toxins, or other molecules of interest. These techniques, when used in conjunction, form a new, simple yet powerful way to integrate traditional lithography with living cells.

1.2.7.4 Patternable genetic transformation in conjunction with integration

The characteristics of cell-directed assembly and patternable cell-directed integration can be combined to create a novel technique for the patterned genetic modification of cells. Two schemes have been developed that take advantage the ability to directly place cells for integration along with the formation of the local region surrounding the cells displaying characteristics of cell-directed assembly. It was found previously that CDA could be used to achieve highly efficient cell transformation. It was hypothesized that this feature could be extended to cell-directed integration to create a platform for simultaneously patterning and genetically modifying cells.

In the first scheme, *E. coli* cells are added to a nanostructured lipid/silica film along with a plasmid for arabinose-induced GFP expression, as shown below in Figure 0-79. During integration plasmids are localized to the lipid-rich region which forms near the cell. Plasmid uptake then occurs passively due to membrane permeabilization by short-chain phospholipids as described above for CDA. Following incubation in air at room temperature for 24 hours, the cells are then incubated in media containing arabinose at 37°C for 1 hour. Fluorescence microscopy can then be used to assess transformation efficiency. It is found that approximately 90% of cells are successfully transformed and are capable of transcription and translation of the newly introduced gene.

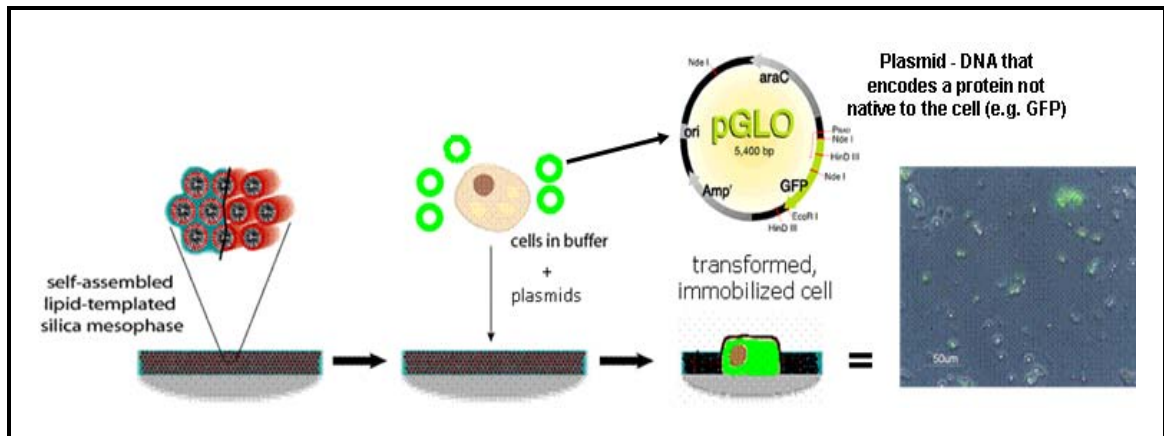


Figure 0-79. Patternable cell transformation scheme #1. Initially a $diC_6PC/silica$ film is created via EISA. Then *E. coli* cells are added in liquid containing GFP plasmid DNA. Integration of cells into films results in competency and efficient uptake of the plasmid. Following integration, cells in films are incubated with media and GFP-promoter for one hour at 37°C. Fluorescence microscopy was then used to assess the number of cells expressing GFP.

A similar scheme in which the plasmid addition is separated from the cell addition can also be used, which is shown below in Figure 0-80. In this process, cells are first introduced on a nanostructured lipid/silica film. Then immediately following addition of the cells, during cell integration, plasmids can be introduced which become localized in the modified region which develops around the integrating cells. Cells are then passively transformed as described above, resulting in integrated, transformed cells. Transformation can be assessed as discussed previously, and has been found to be as high as 80%.

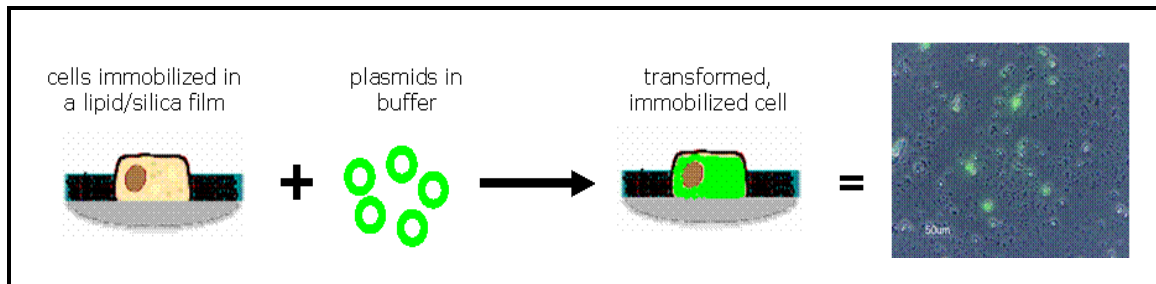


Figure 0-80. Patternable cell transformation scheme #2. Initially a diC_6PC /silica film is created via EISA. Then *E. coli* cells are added in liquid and allowed to integrate into the film. Immediately following integration, GFP plasmid DNA was added. Next, cells in films are incubated with media and GFP-promoter for one hour at 37°C. Fluorescence microscopy was then used to assess the number of cells expressing GFP.

These schemes could also be easily modified to achieve patterned cell transformation by combining this technique with any of the direct patterning methods mentioned above. Application of cells and plasmids to pre-formed nanostructured film using ink-jet printing, for example, would allow for control of the placement of patterned

cells. If patterning is combined with the second scheme, cells could be patterned initially and then modified with introduced plasmids. With this scheme it would be possible to pattern an array of cells, and then introduce different plasmids at different locations to obtain spatially-differentiable cell transformation.

2 Conclusions

The cell-directed assembly process was born out of the necessity of immobilizing live cells for use in a genetically-modified cell-based biosensor. Although the original intent was simply to encapsulate the cells using traditional surfactant-directed self-assembly process that had been modified with biocompatible surfactants, the resulting unanticipated intervention of the cell lead us to a broader understanding of the proactive nature of the cell to maintain homeostasis. By actively localizing available materials and controlling the local pH, cells consistently establish conditions that extend their viability. Not only did the cells alter their local environment, but they also exhibited long range influence by controlling the development of the bulk nanostructure of the material. These observations lead us to understand the importance of allowing cells to have some control over their environment when attempting to maintain their viable in non-native environments. This is the defining characteristic that differentiates CDA from all other immobilization schemes, allowing it to be the preeminent choice for solid-state cell-based devices.

As the cell-directed assembly process was explored in yeast, it was quickly adapted for the immobilization of many different cell types. With each new cell type explored, the same key features of CDA would develop with slight differences that were cell-specific. This flexibility allows for the cell to tailor an environment that is most conducive to its own survival. Immobilization of cells using CDA has presently been expanded to include almost 30 different cell lines of fungi, Gram-positive bacteria, Gram-

negative bacteria, mycobacteria, and extremophile microbes. Single-cell organisms, being able to thrive under a variety of conditions, are well suited to cell-directed assembly. However, cells from multicellular organisms, requiring more specific conditions for growth, do not survive the solvents and stresses associated with CDA well enough to create usable devices.

The cell-directed integration process was developed to address limitations of the cell-directed assembly process while maintaining the key features that allow cells to remain viably encapsulated. By adding cells after forming the nanostructured matrix, exposure to solvents and stresses is minimized, while still allowing the cell to interact with its local environment in a manner similar to CDA. This technique allows for the successful integration of mammalian cells, allowing for innumerable new devices to be made and studies to be performed. Additionally, CDI allows greater control over the bulk material properties and can be easily patterned using a variety of readily-available techniques – important requirements for next-generation cell-based systems.

These two cell encapsulation strategies can both be utilized to immobilize cells while providing extended viability without the need for external buffers or fluids. Additionally, functionality can be enhanced through the introduction of nanoparticles, proteins, and DNA to create not only new cell-based devices, but also novel bio/nano interfaces. These techniques can also be extended to investigate fundamental questions in cell biology and potentially lead to new understandings in disease and infection.

3 References

1. Strathern, J. *The Molecular Biology of Yeast*, 1985, Cold Spring Harbor Laboratories
2. Stevens, M. M.; George, J. H. Exploring and Engineering the Cell Surface Interface. *Science* **2005**, *310*, 1135–1138.
3. Zhang, S. G. Beyond the Petri Dish. *Nat. Biotechnol.* **2004**, *22*, 151–152.
4. Stoodley, P.; Sauer, K.; Davies, D. G.; Costerton, J. W. In *Annual Review of Microbiology*; Ornston, L. N., Balows, A., Gottesman, S., Eds.; Annual Reviews: Palo Alto, CA, 2002; Vol. *56*, pp 187–209.
5. Raghavan, S.; Chen, C. S. Micropatterned Environments in Cell Biology. *Adv. Mater.* **2004**, *16*, 1303–1313.
6. Dohlman HG, Slessareva JE. *Sci STKE*. 2006 Dec 5;2006(364):cm6.
7. Chasse SA, Dohlman HG. *Methods Enzymol.* 2004;389:399-409.
8. Strathern, J. *The Molecular Biology of Yeast*, 1985, Cold Spring Harbor Laboratories
9. Jin, R.C.; Cao, Y.W.; Mirkin, C.A.; Kelly, K.L.; Schatz, G.C.; Zheng, J.G., *Photoinduced conversion of silver nanospheres to nanoprisms*. *Science*, 2001. 294 (5548): p.1901-1903
10. Park, S.J.; Taton, T.A.; Mirkin, C.A., *Array-based electrical detection of DNA with nanoparticle probes*. *Science*, 2002. 295 (5559): p.1503-1506.

-
11. Fan, H.Y., et al., Self-Assembly of Ordered, Robust, Three-Dimensional Gold Nanocrystal/ Silica Arrays. *Science*, 2004. 304: p.567
 12. Imaging Techniques for Biological Specimens
 13. W. C. Fuqua, S. C. Winans, E. P. Greenberg, *Journal of Bacteriology* 176, 269 (Jan, 1994).
 14. P. Diggle, A. S. Griffin, G. S. Campbell, S. A. West, *Nature* 450, 411 (Nov 15, 2007).
 15. J. Redfield, *Trends Microbiol* 10, 365 (Aug, 2002).
 16. B. A. Hense et al., *Nat Rev Microbiol* 5, 230 (Mar, 2007).
 17. K. M. Sandoz, S. M. Mitzimberg, M. Schuster, *Proc Natl Acad Sci U S A* 104, 15876 (Oct 2, 2007).
 18. H. K. Baca et al., *Science* 313, 337 (Jul 21, 2006).
 19. S. Shompole et al., *Mol Microbiol* 49, 919 (Aug, 2003).
 20. R. P. Novick, *Mol Microbiol* 48, 1429 (Jun, 2003).
 21. Doctors without Borders, www.doctorswithoutborders.com
 22. World Health Organization, <http://www.who.int/mediacentre/factsheets/fs104/en/>
 23. Bill and Melinda Gates Foundation, www.gatesfoundation.org/GlobalHealth/Pri_Diseases/Tuberculosis/
 24. Fenton MJ, Vermeulen MW. Immunopathology of tuberculosis: roles of macrophages and monocytes. *Infect Immun.* 1996 Mar;64(3):683-90.

-
25. Kubica GP, Gross WM, Hawkins JE, Sommers HM, Vestal AL, Wayne LG. Laboratory services for mycobacterial diseases. *Am Rev Respir Dis.* 1975 Dec;112(6):773-87.
26. Libraty DH, Byrd TF. Cutaneous miliary tuberculosis in the AIDS era: case report and review. *Clin Infect Dis.* 1996 Oct;23(4):706-10.
27. Cronjé L, Edmondson N, Eisenach KD, Bornman L. Iron and iron chelating agents modulate *Mycobacterium tuberculosis* growth and monocyte-macrophage viability and effector functions. *FEMS Immunol Med Microbiol.* 2005 Aug 1;45(2):103-12. Epub 2005 Mar 30
28. Rieß, F.G., U. Dörner, B. Schiffler and R. Benz, 2001: Study of the properties of a channel-forming protein of the cell wall of the gram-positive bacterium *Mycobacterium phlei*. *J. Membrane Biol.* 182, 147-157
29. Ozçakir O. Viable but non-culturable form of bacteria. *Mikrobiyol Bul.* 2007 Jul;41(3):477-84.
30. Iler, R.K.. *The Chemistry of Silica: Solubility, Polymerization, Colloid and Surface Properties and Biochemistry of Silica*, 1979. Wiley
31. Strathern, J. *The Molecular Biology of Yeast*, 1985, Cold Spring Harbor Laboratories
32. Doshi, D.A., et al., Optically, defined multifunctional patterning of photosensitive thin-film silica mesophases, *Science*, 2000. 290: p.107-111

Confinement-Induced Quorum Sensing of Individual *Staphylococcus aureus* Bacteria

Eric C Carnes¹, DeAnna M Lopez¹, Niles P Donegan², Ambrose Cheung²,
Hattie Gresham³, Graham S Timmins⁴, and CJ Brinker^{1,5,6}

¹Department of Chemical and Nuclear Engineering, University of New Mexico, Albuquerque, NM

²Department of Microbiology, Dartmouth Medical School, Hanover, NH

³New Mexico Veterans Administration Health Care System, Albuquerque, NM

⁴College of Pharmacy, University of New Mexico, Albuquerque, NM

⁵Sandia National Laboratories, Albuquerque, NM

⁶Department of Molecular Genetics and Microbiology, University of New Mexico, Albuquerque, NM

Some bacteria, including medically relevant pathogenic bacteria, emit and sense small diffusible ‘signaling’ molecules (autoinducers) whose extracellular concentrations regulate gene expression and control multiple important functions including virulence and biofilm formation¹. The prevailing view is that this signaling allows populations of cells to assess their density i.e. to quorum sense (QS). If a quorum exists, bacteria alter their gene expression to function as a community, directing coordinated behaviors that provide group benefits exceeding those achievable by individual cells². However it is recognized that, in addition to cell density, other physical and chemical factors, such as the dimensions and diffusional characteristics of the environment, could influence induction of genetic re-programming^{3,4}. Modeling studies^{5,6} predict that QS may potentially operate at the level of a few or even isolated, individual cells, but, due largely to experimental challenges, the potential benefits of quorum sensing at the individual cell level remain virtually unexplored^{7,8,9}. Here we report a physical system that mimics isolation of a bacterium, such as within an endosome or phagosome during infection, and maintains cell viability under conditions of complete chemical and physical isolation. For *Staphylococcus aureus*, we show quorum sensing and genetic re-programming to occur in a single isolated organism. Quorum sensing allows *S. aureus* to sense confinement and to activate virulence and metabolic pathways needed for survival¹⁰. To demonstrate the benefit of confinement-induced quorum sensing to individuals, we showed quorum sensing individual bacteria to have significantly greater viability over non-QS bacteria. These data extend quorum sensing concepts to the individual cell level, and imply that, for this medically important pathogen, QS can contribute significantly to the survival of the isolated individual¹¹.

One method of cell-to-cell bacterial communication involves the ability to produce, secrete, detect and respond to small, hormone-like signaling molecules termed autoinducers¹². Above a threshold extracellular concentration, they alter gene expression, and therefore behavior. The QS hypothesis is that, because the local autoinducer concentration can be cell density dependent, bacteria use signaling to monitor the environment for other like bacteria. When a quorum is detected, genetic reprogramming occurs to coordinate cooperative behaviors at the population level, providing group benefits that would be unproductive at lower density². However as emphasized by Hense et al.⁸ cells are unable to distinguish between density and other factors influencing extracellular autoinducer concentration such as mass transport, confinement, and degradation, since a response is triggered only if the rates of autoinducer production, mass transfer and decay integrated over time reach a threshold concentration at the cell’s location. This led Redfield⁷ to propose QS to be diffusion sensing, while Hense et al. proposed the term efficiency sensing (ES): autoinducers would be used as metabolically cheap proxies to estimate the value to the group of producing more costly, extracellular products. These alternative QS motives depend strictly on local autoinducer concentration and should operate at the individual organism level. This is important, because complex behavior needs to be invoked to account for both QS evolution and maintenance in groups,

as 'cheating' can occur, where individuals exploit secreted group resources without contributing equally to their generation^{2,9}. To reconcile these different perspectives, we hypothesized that QS, independent of its recognized group benefits, could operate also at the single cell level to provide fitness benefits to individual bacteria that could be selected for. To test this hypothesis, we developed a physical system to isolate individual *S. aureus* and examined confinement-induced effects on signaling, gene expression, and viability. Here we show self-induction and resultant genetic reprogramming to occur efficiently in isolated individual organisms, enabling adaptation and survival. It is noteworthy that, while there are data that suggest small numbers of intracellular *S. aureus* can undergo QS¹³ and recent modeling suggests that as few as two cells could induce QS⁶, the ability of a single bacterium to quorum sense in a confined space has not been tested definitively. In fact no study has ever been performed of any physiologic process in bacteria that could examine unambiguously the behavior of a single bacterium in a confined space.

In *S. aureus*, the accessory gene regulator *agr* operon is responsible for QS regulation. It contains two divergent transcripts, RNAII and RNAIII driven by activation of two promoters, P2 and P3, respectively. RNAII encodes four genes, *agrBDCA*, that are required to synthesize, export, and detect an autoinducing cyclic peptide, AIP. AgrC and AgrA form a two-component regulatory pair. AIP binding to its surface receptor, AgrC, activates a phosphorylation cascade inducing expression of RNAIII, a regulatory RNA that represses adhesin expression and up-regulates an array of toxins, hemolysins, degradatory enzymes, and metabolic pathways. Micro-array studies have revealed that 104 genes are up-regulated and 34 are down-regulated as a result of QS, representing ~5% of the genome¹⁴. AgrA-P also induces expression of the RNAII transcript, exerting positive feedback control on this regulatory system¹⁵.

RESULTS

Physical and chemical Isolation of *S. aureus* in a nanostructured matrix

To date, quorum sensing in *S. aureus* has been studied with large numbers of bacteria (1×10^7 - 1×10^9) in either broth suspension cultures or cell cultures of phagocytosed bacteria¹⁶. Therefore, the potential for individual staphylococci to autoinduce in the absence of neighboring bacteria or cell signaling interference inherent to these systems (e.g. through interactions with the phagocytosing host cells) is currently unknown. To observe QS in isolated, individual cells, *S. aureus* were immobilized, individually (or in small groups, see Supplementary Fig. 1 online), within a matrix fabricated at a sufficiently small physical scale (~20 μm diameter, physically isolated hemispherical droplets, see Fig. 1A and B) so that the overall cell density (~1 cell per $2 \times 10^3 \mu\text{m}^3$, equivalent to $\sim 0.5 \times 10^9$ cells mL^{-1}) exceeded the reported QS threshold (10^7 - 10^9 cells mL^{-1}). The matrix was formed by adaptation of our cell-directed assembly approach¹⁷ to an aerosol procedure we developed previously to form ordered porous silica nanospheres¹⁸. It results in cells incorporated within a dihexanoylphosphatidylcholine (*diC₆PC*) lipid vesicle (Fig. 1C) maintained at a pH of ~5.5 (Fig. 1D), approximating that of the early endosome, pH 5.4-6.2, depending on cell type¹⁹, and surrounded by an ordered silicon dioxide nanostructure (Fig. 1A and B) that serves as a reservoir for any added buffer and media. This construct mimics some of the physical and chemical features of a bacterium entrapped within an intracellular membrane-bound compartment (endosome or phagosome), although we note that the shorter chain *diC₆PC* lipid bilayers are expected to be somewhat more permeable than their longer chain counterparts, and that the chemical environment of an endosome or phagosome is more complex than we can achieve in our reduced system. The concentration of the bacterium isolated in a vesicle is approximately 0.5×10^{12} cells mL^{-1} . As discussed below, it is the smaller volume of the vesicle that establishes the effective cell density (\gg QS threshold) and the relevant volume in which AIP can accumulate to trigger a response. Importantly, this architecture, *viz* a vesicle-enveloped cell incorporated in a much larger nanostructured silica bead (Fig. 1A and B), allows individual cells to be maintained in a viable state under externally dry conditions²⁰ that establish complete physical and chemical isolation of one cell from all others. This reduced physical system is biologically relevant, because *Staphylococcus aureus* is known to become trapped in such

intracellular compartments²¹, and it is proposed that they employ a QS strategy to induce new gene expression, promoting intracellular survival and/or escape^{16,21}. However it is presently unknown whether confinement alone can promote QS or whether other factors within the endosomal organelle are required. We use our system to test confinement alone as a mechanism for inducing QS.

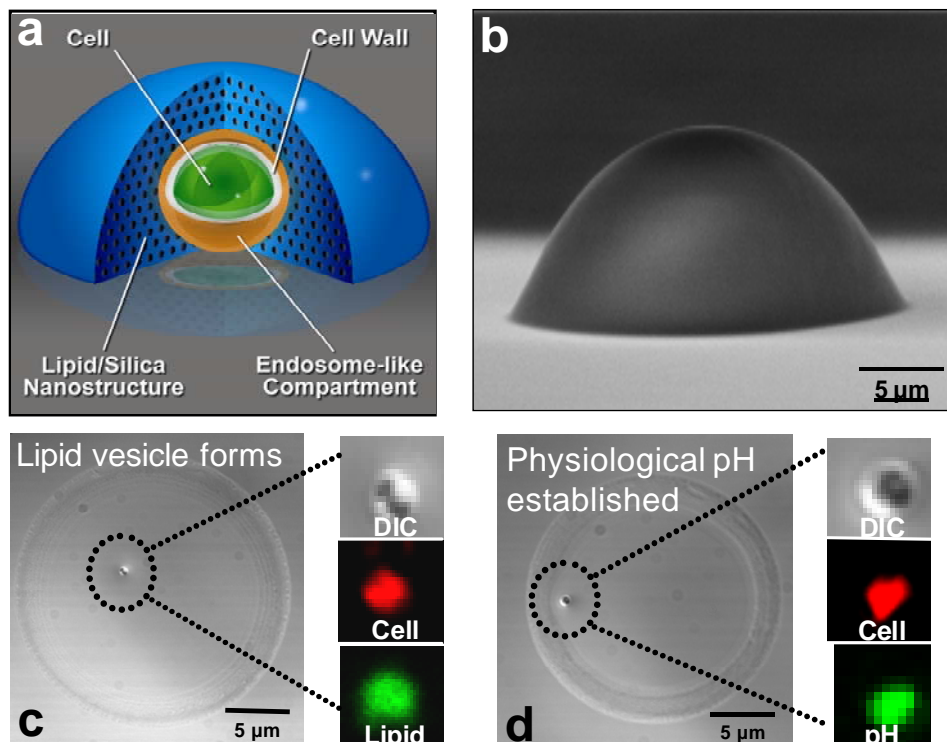


Figure 1. Isolation of individual *S. aureus* within a nanostructured droplet. (A) schematic of physical system (not to scale) showing a cell incorporated in an endosome-like lipid vesicle within a surrounding nanostructured lipid/silica droplet deposited on glass substrate and (B) SEM image of physical system. The nanostructure maintains cell viability under dry external conditions and allows complete chemical and physical isolation of one cell from all others. C and D show plan-view optical microscope images of individual cells in droplets (large outer circular areas). Magnified areas show differential interference contrast image and red fluorescence image of individual stained, isolated cells (both C and D) and green fluorescence image of NBD-labeled lipid localization at cell surface (C) or localized pH (D, using Oregon Green pH-sensitive dye). We find that, within the droplet, the cells become enveloped in an endosome-like lipid vesicle (C), and establish a localized pH consistent with physiological early endosomal conditions (~5.5) (D). For further information regarding aerosol assisted droplet formation and lipid localization and pH establishment, see references 16 and 17.

Monitoring induction of quorum sensing pathways in isolated individual *S. aureus*

To optically monitor the onset and kinetics of auto-induced QS, we used *S. aureus* strains ALC1743 (*agr* group 1 RN6390 containing reporter *agr*: P3-gfp) and ALC1740 (RN6390 containing reporter *hla*-gfp) at an early exponential phase prior to QS induction. Expression of green fluorescent protein (GFP) by ALC1743 reports quorum sensing-dependent *agr* P3-promoter activation (as it would occur in the late exponential phase of growth in broth culture), while in ALC1740 it reports QS-mediated downstream synthesis of the pore-forming toxin, α -hemolysin. As a negative control we used strain ALC6513 (an *agrA*(-) mutant containing reporter *agr*: P3-gfp) – because this strain uses the exact same reporter construct as ALC1743 but lacks AgrA, one component of the two component regulatory pair, it tests for the possibility of non-AIP induced GFP expression. Figure 2 A-B show representative confocal images of isolated, red-stained ALC1743 immediately following encapsulation and after ten hours of incubation at 37°C. As seen in the accompanying kinetic plot (Fig. 3A), GFP expression follows a sigmoidal curve. It initiates over one hour and increases progressively with time to over 90% at ten hours where it begins to level off. (Equivalent QS activation was also obtained for the Newman strain (a clinical isolate) containing reporter *agr*:P3-gfp (see Supplementary Fig. 2 online), confirming that our observations were not unique to the laboratory strain RN6390 that has a

genetic alteration that makes it different from some clinical isolates). The time course of GFP expression in isolated cells is qualitatively similar to but slightly more accelerated than that of the same strains maintained in broth culture at concentrations exceeding the QS threshold²². This is presumably a consequence of localized confinement and restricted transport of extracellular AIP in our nanostructured system compared to that in broth cultures. Over the 24 hour time course we observed no measurable GFP expression from strain ALC6513.

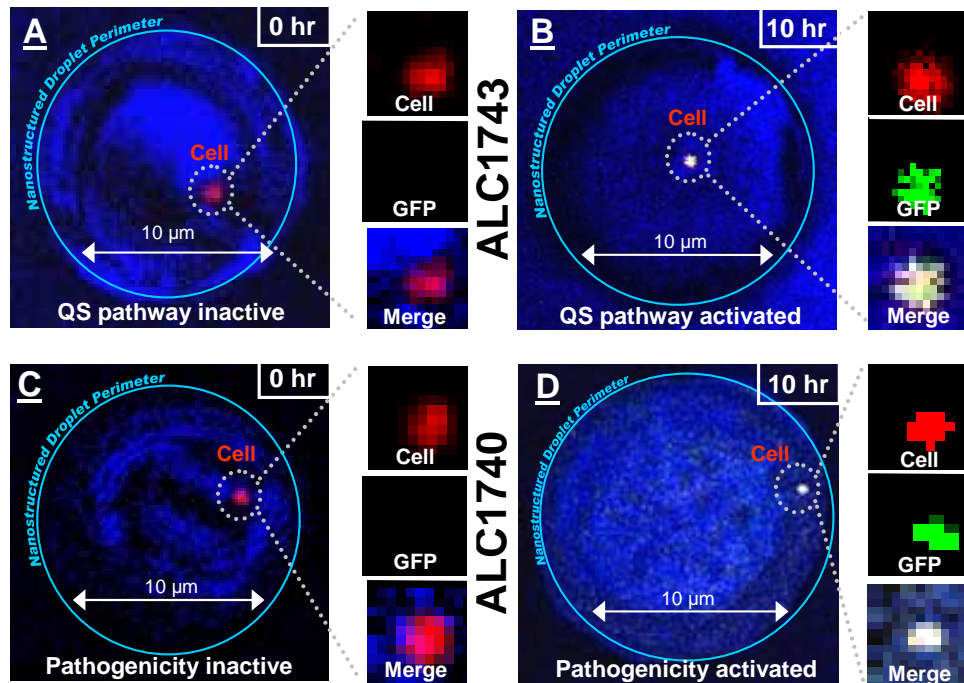


Figure 2. Auto-induction of quorum sensing and pathogenicity in *S. aureus* strains ALC1743 and ALC1740 isolated within nanostructured droplets. All main images show the merged confocal fluorescence image of a *S. aureus* cell (stained red) within a nanostructured droplet (pseudo-colored blue). Enlarged images show discrete fluorescence channels for the red cell stain, green fluorescent protein production, and a merged image for confirming co-localization of any GFP production by the cell. The absence of GFP production by individual cells at 0hr indicates the RNAlII pathway has not been activated (A) and the toxin, α -hemolysin, is not being produced (C). However, after ten hours of incubation in air at 37°C, GFP expression can be observed in individual cells showing activation of the RNAlII-promoted QS pathway (B) as well as expression of secreted virulence factors (D). In (D) we specifically detect activation of the α -hemolysin promoter.

Confinement-induced quorum sensing pathways in isolated individual *S. aureus* are sensitive to exogenous inducers and inhibitors

Figure 3B depicts the time course for GFP expression of ALC1743 isolated in droplets to which exogenous type 1 AIP or the QS inhibitor, very low density lipoprotein (VLDL)²³, was added immediately prior to the aerosol assembly process. We observe cyclic AIP1 to accelerate significantly GFP expression relative to the corresponding ALC1743 sample prepared without exogenous AIP. In contrast VLDL suppresses GFP expression for 10 hours, after which expression kinetics paralleling those of ALC1743 are recovered. As recently reported²³, the mechanism of VLDL inhibition of quorum sensing in *S. aureus* involves binding of the major structural protein of this lipoprotein, apolipoprotein B, to AIP1 preventing binding to the AgrC receptor and antagonizing the QS signaling cascade. For confined cells, GFP expression presumably commences once the local extracellular AIP concentration increases through cellular production and export to become comparable to that of extracellular VLDL. Fig. 3b also plots GFP expression for the *agrA(-)* mutant strain isolated for 24 hours and then dosed with exogenous AIP1. No GFP expression was observed for times up to 24 hours. For all sets of data we observe an insignificant effect of small groups versus individuals on expression kinetics (Chi square analysis). Collectively the data in Figs. 3a and b, showing sensitivity to inducers and inhibitors and no GFP expression for the negative control, indicate that our physical system monitors QS induced by the *agr* encoded two-component regulatory system, as opposed to

other possible confinement-induced outcomes. The similar behavior of individuals and groups suggests that the exogenous AIP or VLDL is incorporated within the vesicles, which surround and isolate cells incorporated individually or in groups, and that it is the vesicle compartment that establishes the volume and effective localized, integrated concentration of cell-secreted plus exogenous AIP activator or inhibitor responsible for regulation of gene expression.

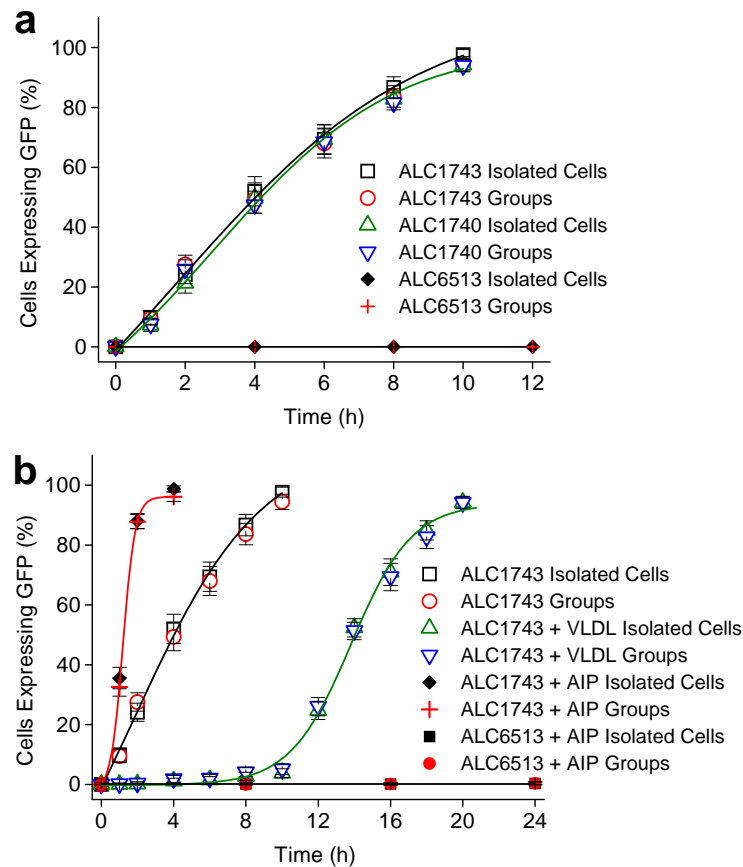


Figure 3. Percentage of individual cells (or small groups of cells, n 2-8, see materials and methods) expressing GFP as function of incubation time at 37°C. (at least 600 cells were counted for each time point). Data are presented as % of cells expressing GFP +/- the 95% confidence interval, with sigmoidal fit only of isolated cell data for clarity. No statistical difference can be seen between individual and small group (2-8 cells) behavior (Chi square analysis). The absence of expression in ALC6513 (an *agrA*(-) mutant containing the same *gfp* reporter, *agr*: P3-*gfp*, as for strains ALC1743, ALC 1740 but lacking *AgrA*, one component of the two component regulatory pair), shows there to be no non-QS induced GFP expression. (B) Percentage of individual cells (or small groups of cells) expressing GFP as function of incubation time at 37°C for samples prepared with exogenous addition of cyclic AIP1 (AIP) or very low density lipoprotein (VLDL), a proven inhibitor of QS in *S. aureus*²¹. For strain ALC6513, the samples were maintained at 37°C for 24 hours prior to addition of exogenous AIP1 to ensure potential effects of confinement not related to AIP1 concentration would not induce GFP expression. The ALC1743 data without exogenous additions are re-plotted for reference.

Confinement induced quorum sensing of isolated individual *S. aureus* up-regulates expression of virulence factors

Figure 2 C and D show representative confocal images of isolated, individual *S. aureus* strain ALC1740 and Fig. 3A shows the corresponding time course of GFP expression. The progressively increasing GFP expression over 10 hours mirrors that of QS (Fig. 3A) and shows activation of the RNAlII-dependent pathway that induces expression of secreted virulence factors. Here we specifically detect activation of the α -hemolysin promoter. Although there are data that suggest that small numbers of intracellular *S. aureus* quorum sense²¹, the combined data in Figures 2 and 3 provide the first proof of auto-induction of an individual, physically and chemically isolated organism. Additionally these data provide the first evaluation of gene expression kinetics for a large population of isolated

individual cells. We postulate that quorum sensing allows isolated *S. aureus* to sense confinement through increased extracellular concentration of autoinducer and to activate virulence factor pathways and initiate new gene expression needed to survive in such confined environments. For both QS and α -hemolysin expression we see no statistical difference between isolated individuals and small groups. This enforces the supposition that our assembly process incorporates cells (individuals or groups) in vesicle compartments that establish the localized extracellular AIP concentration that triggers QS and expression of secreted factors.

Confinement-induced quorum sensing enhances survival of isolated individual *S. aureus*

To demonstrate the benefit of discrete quorum sensing to individuals, we compared the viability of isolated, individual RN6390 to that of RN6911, a RN6390 mutant unable to initiate QS due to deletion of the *agr* operon. RN6390 and RN6911 were isolated in nanostructured lipid/silica droplets prepared with or without incorporation of nutrient (media) in the nanostructured host matrix. Figure 4 shows that, over an 18-day incubation period confined within the media-containing nanostructured lipid/silica droplet at 37°C, the viability of RN6390 (*agr*⁺) was significantly greater than that of the isolated mutant RN6911 (*agr*⁻) ($P = 0.046$, Gehan-Breslow survival analysis, compare Fig. 4 plots A and B). A plausible explanation for the viability difference is that confinement-induced QS and attendant up-regulation of a spectrum of genes affecting virulence and metabolism enhances utilization of external nutrients. Consistent with this idea, the viability of *agr*⁺ isolated in comparable nanostructured lipid/silica droplets self-assembled without nutrients (Fig. 4 plot C) was statistically equivalent to that of the *agr*⁻ mutant isolated in a nutrient containing matrix (Fig. 4 plot B) and that of the additional control, *agr*⁻, immobilized within a matrix fabricated without nutrients (Fig. 4, plot D). These data support the idea that QS poises isolated cells to access and utilize nutrients. The plausibility of this argument is further supported by control experiments with *agr*⁺ and *agr*⁻ performed in broth cultures. Supplementary Figure 3 online shows that, after 47 hours of incubation at 37°C, cells able to quorum sense have significantly greater viability. It is noteworthy that these experiments, prompted by behavior in our reduced system, are the first to show this *agr*⁺ advantage, which is observed for both laboratory strains and recent clinical isolates like MRSA USA300 (data not shown).

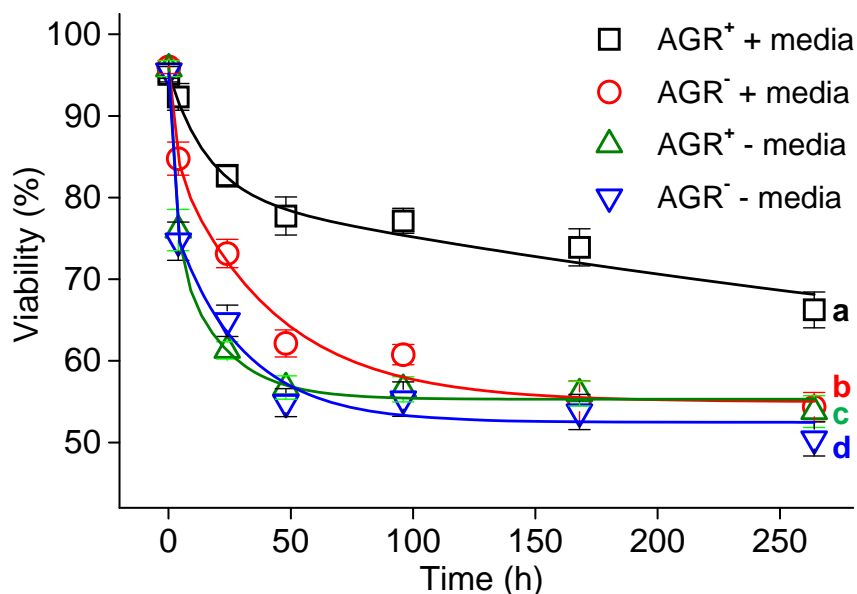


Figure 4. Viability of *agr*⁺ and *agr*⁻ strains of individual *S. aureus* cells isolated within nanostructured lipid/silica droplets (A) wild type (*agr*⁺) in droplet containing Trypticase Soy Broth (TSB) media, (B) RN6911 (*agr*⁻) in droplet containing TSB media, (C) wild type (*agr*⁺) in droplet without media, (D) RN6911 (*agr*⁻) in droplet without media. Viability determined using BacLight™ fluorescent viability probe kit. Error bars represent 95% confidence intervals. At least 600 cells were counted for each time point. A statistical difference can be seen when comparing plots A and B ($P = 0.046$, Gehan-Breslow survival analysis).

DISCUSSION

By use of a reduced physical system, devoid of inter-cellular signaling interference inherent to bulk cultures^{24,25} and previous studies of endosomal entrapment^{13,21} we demonstrated confinement-induced quorum sensing for an individual isolated organism. *S. aureus* entrapped individually within a small volume senses and responds to confinement through accumulation of extracellular AIP and activation of the two-component response regulatory system with its inherent positive-feedback control. We propose that up-regulation of the *agr* effector molecule RNAIII enhances the expression of a diverse array of genes associated with metabolism, transport, and virulence¹⁰. As implied by our viability studies, one benefit derived by autoinduction is the poisoning of isolated cells to be able to scavenge for and utilize external nutrients and thus better survive in isolation. Perhaps more important are the overall implications for bacterial pathogenicity. Unlike in batch cultures, bacteria, certainly pathogens, are often found in small numbers (e.g. in the gut or respiratory track) and in enclosed spaces. Our results imply that, shortly after colonization, individual or small groups of cells initiate virulence factor expression. Therapies aimed at inhibiting quorum sensing are therefore promising strategies for eradication of infection at its outset^{23,26}.

Concerning taxonomy of QS, the confinement-induced QS we report is consistent with the fully articulated QS model and its inherent sensitivity to external factors such as the dimensions and diffusional characteristics of the environment³. However, induction of genetic reprogramming depends on autoinducer concentration exceeding a threshold value at the cell surface, and cells cannot distinguish between the three key determinants of autoinducer concentration, *viz.* cell density, mass-transfer properties, and spatial distribution of cells⁸. Our results clearly illustrate that induction can be independent of both cellular density and spatial distribution. Thus the term quorum sensing, and its implicit definition of 'sensing a quorum', is a misnomer, especially when applied to isolated, individual cells. Furthermore our results confirm one experimental prediction of the diffusion-sensing hypothesis posed by Redfield, "that isolated cells should be able to produce enough autoinducer for self-induction under plausible natural conditions"⁷ But as to whether autoinducer peptide controlled genetic-reprogramming should be classified as QS, DS, or ES, we advocate a systems biology perspective where the underlying two-component regulatory system is inherently sensitive to the combined factors that control the concentration of extracellular autoinducer peptides proximate to the cell surface. This view is consistent with our extension of the QS concept and attendant benefits to the individual cell level, where it is unnecessary to invoke complex social interactions for its evolution and maintenance, allowing selection according to survival of the fittest individuals.

METHODS

Cell lines used. The *Staphylococcus aureus* strains used in this study, ALC1743 (*agr* group 1 RN6390 containing reporter *agr*: P3-gfp), ALC1740 (RN6390 containing reporter *hla*-gfp), ALC1743 (RN6390 *agr* deletion mutant containing reporter *agr*: P3-gfp), wild-type Newman containing reporter *agr*:P3-gfp, wild-type RN6390, and RN6911 (RN6390 *agr* deletion mutant) were generated and grown in trypticase soy broth (TSB, from Becton, Dickinson and Company) broth to early exponential phase before freezing in stock^{27,28}.

Preparation of nanostructured silica droplets containing live cells. Isolated nanostructured droplets containing individual cells (or small groups of cells, see e.g. Supplementary Fig. 1 online) were prepared by an extension of our evaporation-induced self-assembly process where an amphiphilic short chain phospholipid was used as a biocompatible structure directing agent^{17,18,20,29}. Upon evaporation, lipids direct the organization of silica into an ordered lipid/silica nanostructure, which serves in our experiment as a synthetic intracellular milieu in which to incorporate individual cells. To prepare these droplets, stock solutions of soluble silica precursors were prepared by refluxing tetraethylorthosilicate (TEOS, from Sigma), ethanol, de-ionized water and HCl (molar ratios 1: 4: 1: 5x10⁻⁵) for 90 minutes at 60°C. Water, HCl and TSB (a media serving as a nutrient required for GFP expression) were added to the stock solution to achieve a biologically compatible sol with final molar ratios of 1 TEOS: 4 ethanol: 0.01 HCl: 6 water: 6 TSB. 30 mg/mL of the C6 phospholipid, dihexanoylphosphatidylcholine (from Avanti Polar Lipids), was then added to the silica solution along with any exogenous materials - cyclic AIP1 (from Commonwealth, Inc. in Richmond, VA) at a concentration of 100 nM, exceeding the threshold for induction of QS through exogenous cyclic AIP1 addition¹⁵, or VLDL (from US Biological) at 10 µg mL⁻¹. Stocks of the various cell strains (not previously expressing GFP) were centrifuged and immediately resuspended/diluted in water. These cells were added to the silica/lipid solution to yield a final concentration of 10⁶ cells mL⁻¹ << quorum sensing threshold. The sol was immediately aerosol deposited onto glass resulting in physically and

chemically isolated (approximately) hemispherical droplets (Supplementary Fig. 1, A) containing individual or small groups of cells as determined by confocal microscopy (see below). The silica matrix is characterized by a periodic uniform lipid/silica nanostructure as confirmed by small angle x-ray scattering (Supplementary Fig. 1, B). Encapsulated cells prepared with either optically labeled lipid (NBD, from Avanti Polar Lipids) or a fluorescent pH probe (Oregon Green, from Invitrogen) allowed visualization of lipid localization around the cell or maintenance of a localized physiologically buffered pH (Supplementary Fig. 1, I, J), similar to that reported previously for our cell-directed assembly process¹⁷. Individual cell-containing droplets are maintained in air and separated by air gaps with spacings comparable to or exceeding the droplet diameters (10-20 μm), preventing any AIP diffusion between droplets during experiments.

Imaging and determination of GFP induction. Following deposition, droplets were incubated at 37°C for indicated periods of time in air (nanostructure maintains and supplies water and nutrients). No growth or division of the isolated cells was readily observed. Additional samples were also refrigerated for identical periods of time and used to verify the absence of GFP expression in cell stocks. After incubation, samples were stained with 50 μM SYTO 64 for 45 minutes at 37°C for visualization, washed 3 times with DI water, fixed with 4% formaldehyde for 45 minutes, again washed 3 times with DI water, then mounted using DABCO anti-fade reagent. (Due to rapid photobleaching of individual cells, it was not possible to monitor GFP induction in real time using fluorescence microscopy. Therefore fixation and mounting with anti-fade was necessary for confocal imaging). Samples were then imaged on a Zeiss LSM 510-META confocal system mounted on a Zeiss Axiovert 100 inverted microscope. For determination of the time course of GFP expression (Fig. 3), each point represents an average of at least six determinations of approximately one hundred cells each. Fluorescence emission fingerprinting followed by linear unmixing via integrated software was used to separate the fluors from the autofluorescence of the nanostructured silica matrix and confirm the presence of GFP in the cells (Supplementary Fig. 1, C-H). Based on positive and negative control experiments, it was determined that a 100-fold fluorescence intensity increase over non-stimulated cell background constitutes stimulation. Because samples are fixed at individual time points, we cannot discern unambiguously whether replication takes place but suspect that, due to the confined environment, it does not. This is consistent with endosomal entrapment, as in culture studies of *S. aureus* infected MAC-T cells it was concluded, agr-regulated exoproteins appear to be required prior to the release and replication of *S. aureus* within the infected MAC-T cells¹³.

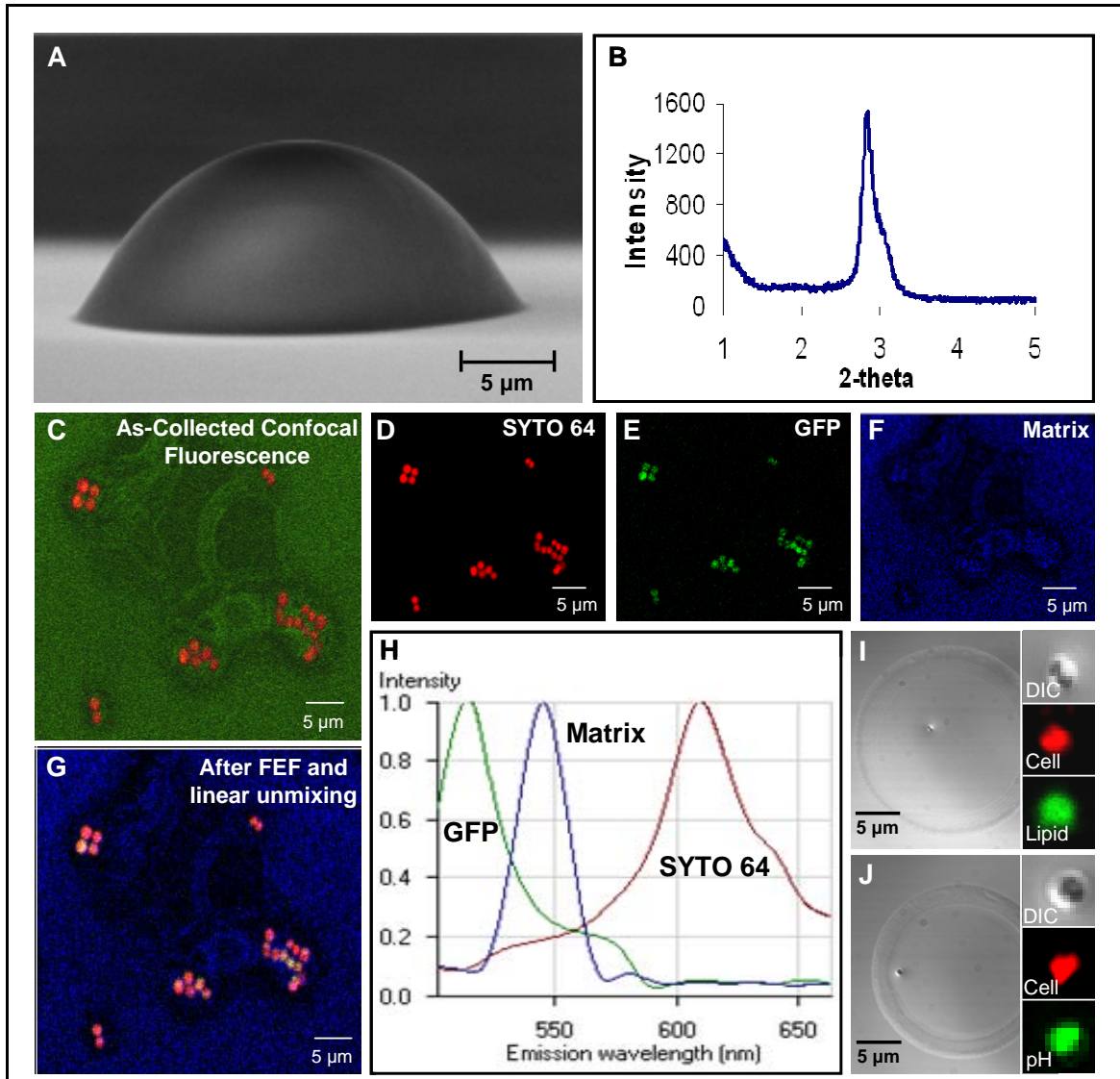
Viability Determination. To evaluate the viability of individual cells encapsulated in the nanostructured droplets, *S. aureus* strains RN6930 and RN6911 were immobilized as described above. The cells in droplets were then incubated in air at 37°C for the indicated periods of time. At the indicated intervals, samples were removed from the incubator and evaluated using the BacLight (Invitrogen) viability dye set according to the product literature to allow labeling and imaging of immobilized cells. Viability was then determined using a Nikon TE2000 inverted fluorescence microscope equipped with a viability dye filter set from Chroma. Each point represents an average of at least six determinations of approximately one hundred cells each.

Acknowledgments: This work is supported by the Air Force Office of Scientific Research grant FA 9550-07-1-0054, DOE Basic Energy Sciences grant DE-FG02-02-ER15368, Sandia National Laboratories' LDRD program, NSF IGERT Fellowship grant DGE-0504276, the Defense Threat Reduction Agency grant B0844671, the NIH/Roadmap for Medical Research under grant PHS 2 PN2 EY016570B, and NIH grants R01 AI-064926, AI-081090, AI-037142, and AI-047441. The authors also acknowledge Linda Kenney and Michael Federle for useful comments. Some images in this paper were generated in the University of New Mexico Cancer Center Fluorescence Microscopy Facility, supported as detailed at: <http://hsc.unm.edu/crtc/microscopy/Facility.html>. Sandia is a multiprogram laboratory operated by Sandia Corporation, a Lockheed Martin Company, for the U.S. Department of Energy's National Nuclear Security Administration under contract DE-AC04-94AL85000.

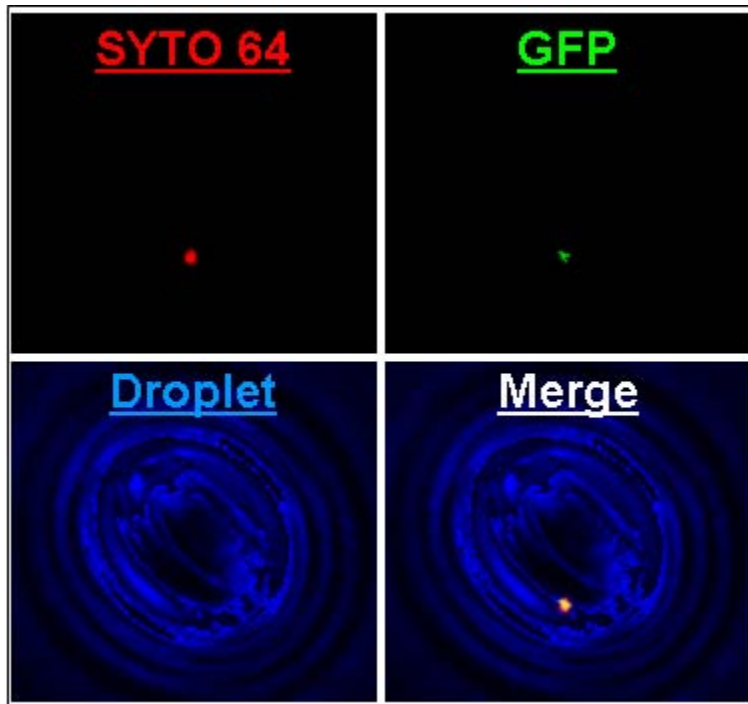
References

1. Fuqua, W., Winans, S. & Greenberg, E. Quorum sensing in bacteria: the LuxR-LuxI family of cell density-responsive transcriptional regulators. *Journal of Bacteriology* **176**, 269-275 (1994).
2. Diggle, S., Griffin, A., Campbell, G. & West, S. Cooperation and conflict in quorum-sensing bacterial populations. *Nature* **450**, 411-414 (2007).
3. Fuqua, C., Parsek, M.R. & Greenberg, E.P. Regulation of gene expression by cell-to-cell communication: Acyl-homoserine lactone quorum sensing. *Annual Review of Genetics* **35**, 439-468 (2001).
4. Horswill, A.R., Stoodley, P., Stewart, P.S. & Parsek, M.R. The effect of the chemical, biological, and physical environment on quorum sensing in structured microbial communities. *Analytical and Bioanalytical Chemistry* **387**, 371-380 (2007).
5. James, S., Nilsson, P., James, G., Kjelleberg, S. & Fagerstrom, T. Luminescence control in the marine bacterium *Vibrio fischeri*: An analysis of the dynamics of lux regulation. *Journal of Molecular Biology* **296**, 1127-1137 (2000).
6. Alberghini, S. et al. Consequences of relative cellular positioning on quorum sensing and bacterial cell-to-cell communication. *Fems Microbiology Letters* **292**, 149-161 (2009).
7. Redfield, R. Is quorum sensing a side effect of diffusion sensing? *TRENDS in Microbiology* **10**, 365-370 (2002).
8. Hense, B. et al. Does efficiency sensing unify diffusion and quorum sensing? *Nature Reviews Microbiology* **5**, 230-239 (2007).
9. Sandoz, K., Mitzimberg, S. & Schuster, M. Social cheating in *Pseudomonas aeruginosa* quorum sensing. *Proceedings of the National Academy of Sciences* **104**, 15876 (2007).
10. Novick, R.P. & Geisinger, E. Quorum Sensing in Staphylococci. *Annual Review of Genetics* **42**, 541-564 (2008).
11. Wang, R. et al. Identification of novel cytolytic peptides as key virulence determinants for community-associated MRSA. *Nature medicine* **13**, 1510-1514 (2007).
12. Waters, C.M. & Bassler, B.L. Quorum sensing: Cell-to-cell communication in bacteria. *Annual Review of Cell and Developmental Biology* **21**, 319-346 (2005).
13. Qazi, S.N.A. et al. agr Expression precedes escape of internalized *Staphylococcus aureus* from the host endosome. *Infection and Immunity* **69**, 7074-7082 (2001).
14. Dunman, P.M. et al. Transcription profiling-based identification of *Staphylococcus aureus* genes regulated by the agr and/or sarA loci. 7341-7353 (2001).
15. Novick, R.P. Autoinduction and signal transduction in the regulation of staphylococcal virulence. *Molecular Microbiology* **48**, 1429-1449 (2003).
16. Shompole, S. et al. Biphasic intracellular expression of *Staphylococcus aureus* virulence factors and evidence for Agr-mediated diffusion sensing. *Molecular Microbiology* **49**, 919-927 (2003).
17. Baca, H.K. et al. Cell-directed assembly of lipid-silica nanostructures providing extended cell viability. *Science* **313**, 337-341 (2006).
18. Lu, Y. et al. Aerosol-assisted self-assembly of mesostructured spherical nanoparticles. *Nature* **398**, 223-226 (1999).
19. Murphy, R.F., Powers, S. & Cantor, C.R. ENDOSOME PH MEASURED IN SINGLE CELLS BY DUAL FLUORESCENCE FLOW-CYTOMETRY - RAPID ACIDIFICATION OF INSULIN TO PH-6. *Journal of Cell Biology* **98**, 1757-1762 (1984).
20. Baca, H.K. et al. Cell-directed assembly of bio/nano interfaces - A new scheme for cell immobilization. *Accounts of Chemical Research* **40**, 836-845 (2007).
21. Jarry, T., Memmi, G. & Cheung, A. The expression of alpha-haemolysin is required for *Staphylococcus aureus* phagosomal escape after internalization in CFT-1 cells. *Cellular Microbiology* **10**, 1801-1814 (2008).
22. Rothfork, J.M., Dessus-Babus, S., Van Wamel, W.J.B., Cheung, A.L. & Gresham, H.D. Fibrinogen depletion attenuates *Staphylococcus aureus* infection by preventing density-dependent virulence gene UP-regulation. *Journal of Immunology* **171**, 5389-5395 (2003).
23. Peterson, M.M. et al. Apolipoprotein B Is an Innate Barrier against Invasive *Staphylococcus aureus* Infection. *Cell Host & Microbe* **4**, 555-566 (2008).
24. Mathesius, U. et al. Extensive and specific responses of a eukaryote to bacterial quorum-sensing signals. *Proceedings of the National Academy of Sciences* **100**, 1444-1449 (2003).
25. Shiner, E.K., Rumbaugh, K.P. & Williams, S.C. Interkingdom signaling: Deciphering the language of acyl homoserine lactones. *Fems Microbiology Reviews* **29**, 935-947 (2005).
26. Balaban, N. et al. Use of the quorum-sensing inhibitor RNAIII-inhibiting peptide to prevent biofilm formation in vivo by drug-resistant *Staphylococcus epidermidis*. Vol. 187 625-630 (2003).
27. Rothfork, J.M. et al. Inactivation of a bacterial virulence pheromone by phagocyte-derived oxidants: New role for the NADPH oxidase in host defense. *Proceedings of the National Academy of Sciences of the United States of America* **101**, 13867-13872 (2004).
28. Kupferwasser, L.I. et al. Salicylic acid attenuates virulence in endovascular infections by targeting global regulatory pathways in *Staphylococcus aureus*. *Journal of Clinical Investigation* **112**, 222-233 (2003).
29. Doshi, D.A. et al. Optically, defined multifunctional patterning of photosensitive thin-film silica mesophases. *Science* **290**, 107-111 (2000).

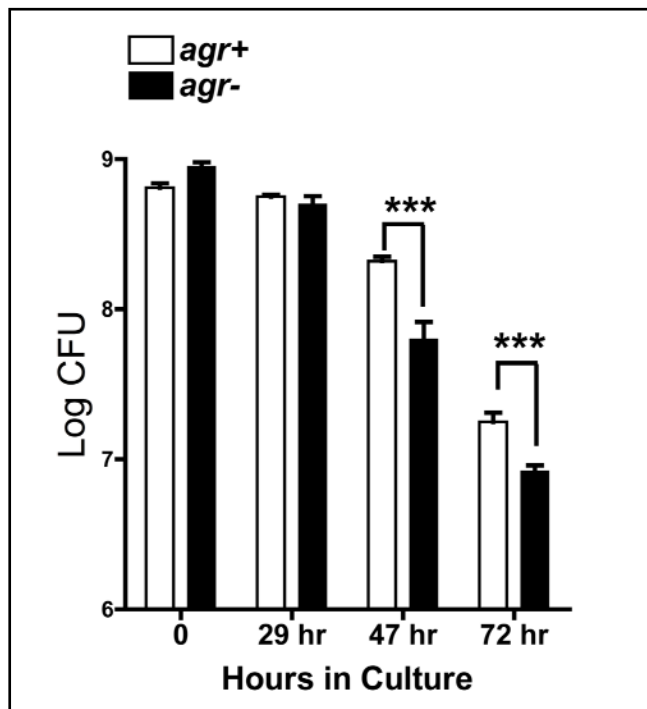
SUPPLEMENTARY FIGURES



Supplementary Figure 1. *S. aureus* cells expressing GFP were stained with SYTO 64 and immobilized in a nanostructured silica matrix. An SEM micrograph shows the general size and shape of the matrix droplets (A), while x-ray diffraction was used to confirm the presence of an ordered nanostructure within the matrix³⁻⁵ (B). The silica matrix displays a large amount of autofluorescence (green), making resolution of the colocalization of GFP (green) and cell stain (red) difficult using standard confocal fluorescent microscopy (C). Following isolation of relevant spectra using control samples (H), fluorescence emission fingerprinting - FEF - can be used to obtain linear unmixed channels for the red cell stain SYTO 64 (D), GFP (E), and the silica matrix (F, pseudo-colored blue for clarity). The unmixed channels can then be merged as in traditional fluorescence microscopy (G). Confocal fluorescence images of NBD-tagged lipid localized around a cell in a droplet (I) and a buffered pH region near a cell visualized with a pH indicator that fluoresces at neutral pH (J) were used to establish the physical characteristics of this system to be similar to those of our previously reported cell-directed assembly process³. All inset images are shown at an additional 5x magnification for clarity.



Supplementary Figure 2. Individual spectral channels of confocal fluorescence images of an individual Newman strain *S. aureus*, containing reporter *agr*:P3-*gfp*, undergoing quorum sensing when confined in an individual lipid/silica droplet containing media and incubated for 10 hours at 37°C. FEF was used to obtain separate spectral channels for the SYTO 64 cell stain (red), the GFP QS marker (green), and the lipid/silica matrix (blue). These images were then merged to confirm the expression of the marker by the isolated cell.



Supplementary Figure 3. Counts of CFUs show that cells able to participate in quorum sensing maintained viability in nutrient depleted media as compared to non-quorum sensing bacteria. Bacteria were grown over night to achieve stationary phase. Cells are then diluted into PBS containing 1% broth at an OD 600 of 1.0. They are maintained at 37°C with shaking for the indicated times. Samples are plated out on agar medium to determine the log CFU. At 47 hours and after, the difference between *agr*⁺ and *agr*⁻ is significant ($p < 0.001$, Student's T Test).

Cell-Directed Localization and Orientation of a Functional Foreign Transmembrane Protein within a Silica Nanostructure

Eric C. Carnes,[†] Jason C. Harper,^{†,§} Carlee E. Ashley,[†] DeAnna M. Lopez,[†] Lina M. Brinker,[†] Juewen Liu,[†] Seema Singh,[†] Susan M. Brozik,^{†,§} and C. Jeffrey Brinker^{*,†,‡,§}

Departments of Chemical and Nuclear Engineering[†] and Molecular Genetics and Microbiology,[‡] University of New Mexico, Albuquerque, NM 87131, and Sandia National Laboratories,[§] Albuquerque, New Mexico 87106.

RECEIVED DATE September 10, 2009; E-mail: cjbrink@sandia.gov

A simple procedure is described for introducing functional exogenous membrane bound proteins to viable cells encapsulated within a lipid templated silica nanostructure. In one method, bR was added directly to a *S. cerevisiae* solution along with short zwitterionic diacylphosphatidylcholines (*diC₆* PC), and mixed with equal volumes of a sol precursor solution. Alternatively, bR was first incorporated into liposomes (bR-proteoliposomes) and then added to a *S. cerevisiae* solution with *diC₆* PC, followed by mixture with sol precursor solution. Films prepared from bR added directly with *diC₆* PC resulted in bR localization near *S. cerevisiae* cells in a disordered and diffuse fashion, while films prepared from bR-proteoliposomes added to the *diC₆* PC/yeast solution resulted in bR preferentially localized near yeast cell surfaces forming bR containing multilayer vesicles. Importantly, bR introduced via proteoliposomes was observed to modulate pH gradients developed at the cell surface, demonstrating both retained functionality and preferential orientation. Localization of liposome lipid or bR did not occur around neutrally charged latex beads acting as cell surrogates, demonstrating that living cells actively organize the multilayered lipid during evaporation-induced self-assembly. We expect this simple procedure for introducing functional and oriented membrane-bound proteins to the surface of cells to be general and adaptable to other membrane-bound proteins. This advance may prove useful in fundamental studies of membrane protein function, cell-cell signaling, microarray development, and in imparting non-native characteristics to arbitrary cells.

The development of new material behaviors based on incorporation of stable and functional biomolecules has attracted considerable interest due to potential applications in biotechnology, biocatalysis, drug delivery, bio-electronic devices, and biological sensing.¹ Recently, the use of sol-gel technology for immobilization of functional soluble proteins in inorganic materials has been widely reported. This success is largely due to advances in sol-gel processing that reduce exposure of biological components to alcohol solvents, toxic by-products, and the highly acidic or basic conditions of hydrolysis.² Similar advances in the development of biocompatible sol-gel processes have also permitted the encapsulation of viable cells.³ The extension of these biologically compatible sol-gel processing techniques to encapsulate more sensitive membrane-bound proteins in sol-gel matrices remains a significant challenge.⁴ The relatively few successful reports of membrane protein encapsulation mostly utilize the photoactive protein-retinal complex, bacteriorhodopsin (bR). This prior work demonstrated that bR retained native photo-induced proton pumping functionality, but that this function was rather inconsequential as the proteins were randomly oriented and therefore could not yield useful ion gradients.⁵ Specific orientation of bR in sol-gel matrices was recently shown, using silica entrapped bR-proteoliposomes (liposome reconstituted bR) to produce proton gradients that facilitated ATP synthesis,⁶ or by intercalation of silica between oriented sheets of intact purple membrane lipid bilayers, which when integrated on an electrode, produced measurable photocurrents.⁷

We recently reported that, using short chain phospholipids to direct the formation of thin film silica nanostructures during evaporation-induced self-assembly⁸ (EISA), the introduction of cells alters profoundly the inorganic self-assembly pathway. Cells actively organize around themselves an ordered, multilayered lipid-membrane that interfaces coherently with a 3D lipid-templated silica nanostructure. This bio/nano interface is unique in that it withstands drying (even evacuation) maintaining cell viability for days to years without external buffer, yet remains accessible to molecules, proteins/antibodies, plasmids, etc. introduced into the 3D silica host.⁹ Herein we report an extension of this cell directed assembly approach where bR is oriented within a multilayered lipid membrane localized at the interface between *S. cerevisiae* and the surrounding lipid-templated silica matrix. To the best of our knowledge this is the first report detailing incorporation of both functional transmembrane bacterial proteins and viable cells in a sol-gel material. Importantly, the bR is observed to modulate pH gradients developed at the cell surface, demonstrating both orientation and retained functionality. Such a simple procedure for introducing functional exogenous membrane bound proteins to immobilized cells may significantly impact

fundamental studies of membrane protein function and cell-cell signaling.

The two methods used by us to introduce bR and yeast cells in a lipid-templated silica matrix are depicted in Figure 1 A. In both methods, equal volumes of sol precursors and yeast cells, suspended in phosphate buffer, were mixed (see Supplemental Information). In one method, bR was added directly to the yeast solution along with short zwitterionic diacylphosphatidylcholines (*diC₆*PC). Alternatively, bR was first incorporated into dimyristoylphosphatidylcholine (DMPC) liposomes (see Supplemental Information) and then added to the yeast solution with *diC₆* PC. Following mixture of the respective yeast solutions with sol precursors the solution was immediately spin-coated onto a glass substrate. Grazing incidence small angle x-ray scattering (GISAXS) and scanning electron microscopy (SEM) were used to characterize the cell-lipid-protein-silica matrix produced from each of the two methods shown in Figure 1 A. Consistent with our previous studies,⁸ films prepared from either method exhibited lamellar structures with repeat distance (d_i) of ~31 Å as a result of the cell-directed assembly process (Figure 1 B). Also consistent with our previous reports, SEM imaging of samples prepared from either method shows *S. cerevisiae* encapsulated in a crack-free silica film with a coherent cell-matrix interface (Figure 1 C).



Figure 1. (A) Encapsulation of yeast and bacteriorhodopsin (bR) in mesoporous silica films by direct addition of bR, or addition of bR incorporated into DMPC liposomes, to the yeast/*diC₆* PC lipid/sol precursor solution. bR added directly with *diC₆* PC was localized in a disordered and diffuse fashion while bR incorporated into DMPC liposomes and added to the *diC₆* PC/yeast solution was preferentially localized near the yeast cell surface forming conformal bR containing multilayer vesicles. (B) Grazing incidence small angle x-ray scattering (GISAXS) pattern of lipid-silica matrix encapsulated yeast-bR film showing lamellar structure. (C) SEM image of lipid-silica matrix encapsulated yeast-bR film.

Localization of the protein and various lipid components was monitored by fluorescent labeling and laser-scanning confocal fluorescence microscopy. Pronounced differences were observed in lipid and protein localization near *S. cerevisiae* cells, when comparing samples prepared by direct addition of bR or addition of bR-proteoliposomes to the yeast/*diC₆* PC solution. Figure 2 A shows that upon addition of bR directly to the yeast/*diC₆* PC solution, bR (red panel) localized near *S. cerevisiae* cells in a diffuse manner that corresponded closely to the region of *diC₆* PC localization (green panel). Localization of *diC₆* PC near yeast cells is consistent with our previous studies which show the formation of a lipid-rich region that interfaces cells with the surrounding nanostructured silica host. Figure 2 B shows that addition of bR-proteoliposomes to the yeast/*diC₆* PC solution resulted in a more conformal localization of bR (red panel) near *S. cerevisiae* cells. The thickness of the protein layer suggests that multiple fusion steps have occurred during cell-directed assembly, forming yeast supported multilayers containing bR. Figures 2B and 3A show that longer chain lipids introduced as liposomes with (Fig 2B) or without (Fig. 3A) bR preferentially localize at the yeast cell surface during cell directed assembly. In Fig. 2B preferential localization of NBD (green) labeled longer chain palmitoylcholine (POPC) (introduced as 1% of the total lipid composition as a marker for DMPC, 99% of lipid, which is unavailable in a labeled form) is clearly shown by the 4-5 cells in which the confocal slice includes the top portion of the cells (Figure 2 B green panel, peripheral cells). Based on additional cell-directed assembly experiments performed with labeled liposomes and labeled *diC₆* PC (e.g. Fig 3A), we propose that bR introduced in proteoliposomes is co-localized with both the longer chain liposomal lipids and the shorter chain lipids in close proximity to the cell surface, but that the bR and liposomal lipids have higher priority to and are more conformal with the cell surface.

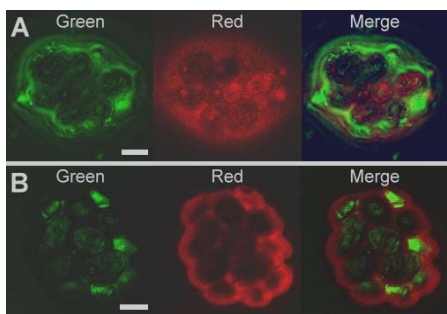


Figure 2. Confocal fluorescence images of Alexa Fluor 594 labeled bR (red emission) localized near yeast cells in the surrounding lipid-silica matrix. (A) bR added with *diC₆* PC only (1% NBD labeled *diC₆* PC, green emission) to yeast. (B) bR incorporated in DMPC liposomes (1% NBD labeled POPC, green emission) added with *diC₆* PC to yeast. Scale bars = 3 μ m.

The importance of evaporation-induced, cell-directed assembly in forming yeast supported bR multilayers is evidenced by the lack of spontaneous liposome fusion or lipid association around yeast cells in buffered solutions. In these control experiments, yeast and POPC liposomes (6% Texas Red labeled DHPE) were mixed, with and without *diC₆* PC, in buffered solutions prepared at various pH values: pH 7, (pH of the initial bR-proteoliposome/yeast/*diC₆* PC solution prior to adding sol precursors), pH 2 (pH of the silica precursor solution), or pH 5 (pH obtained near the lipid/silica encapsulated cells following cell-directed assembly). In each case, no lipid association with yeast cells was observed, showing that neither electrostatic effects under the pH range studied nor the presence of *diC₆* PC, induce liposome fusion with the yeast cells in solution. POPC liposome fusion and multilayer formation around yeast cells was observed, however, when liposomes were added to a yeast/*diC₆* PC/sol precursor solution and spin-coating on a cover glass. As shown in Figure 3A, during evaporation-induced, cell-directed assembly, both the longer chain liposome lipid (6% Texas Red labeled DHPE, red panel) and shorter chain *diC₆* PC lipid (1% NBD labeled green panel) are localized at the

cell surface, but the longer chain lipid is more conformal and has greater priority for the cell surface (merged image). Additionally, it is important to note that viable cells play an active role in formation of yeast supported bR multilayers. In control experiments using neutrally charged latex beads as cell surrogates, neither localization of liposome lipid (Figure 3 B) nor bR (Figure 3 C) occurred upon evaporation.

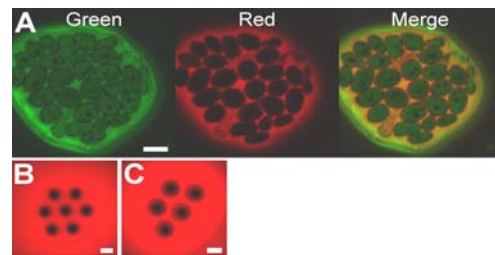


Figure 3. (A) Confocal fluorescence image showing liposome fusion and multilayer formation around yeast cells during cell-directed assembly. POPC liposomes (6% Texas Red labeled DHPE, red emission) were added to a yeast/*diC₆* PC (1% NBD labeled, green emission)/sol precursor solution and spin-coated. (B-C) Confocal projections of cell surrogates (neutrally charged latex beads) added to the *diC₆* PC/sol precursor solution and spin-coated showing (B) POPC liposomes (2.5% Texas Red labeled DHPE) and (C) Alexa Fluor 594 labeled bR in DMPC liposomes are not localized. Scale bars = 3 μ m.

The ability to generate a photo-induced proton gradient in the lipid-protein-cell-silica matrix was investigated using the membrane impermeant pH sensitive fluorescent dye, Oregon Green. As shown in Figure 4 A, the intensity of fluorescent emission decreases as the pH is lowered from approximately pH 6 to 3 with total quenching of fluorescence at highly acidic pH (≤ 2). The pH gradient resulting from exposure of the films to green light¹⁰ is shown using confocal z-axis projections in Figure 4, B-D. As we have previously shown, encapsulated cells form a gradient in pH from approximately pH 3 in the acidic silanol-terminated silica matrix, to pH 5.5 at the encapsulated cell surface, spanning a distance of several micrometers. Figure 4 B shows that a film prepared from addition of DMPC liposomes (without bR) to the yeast/*diC₆* PC lipid solution and exposure of the film to green light (see Supplemental Information) yielded similar pH gradients with pH near 5 at cell surfaces decreasing to approximately pH 3 over a few micrometers. Photo-induced proton pumping was observed in samples prepared from direct addition of bR to the yeast/*diC₆* PC solution (Figure 4 C) which shows a slight decrease in pH to 4.5 at the cell surface, as shown by the reduced intensity of the Oregon Green dye compared to Figure 4 B. This slight decrease in pH is indicative of non-functional and/or randomly oriented bR, as functionality requires a lipid bilayer that can accommodate the hydrophobic domains of the transmembrane protein.

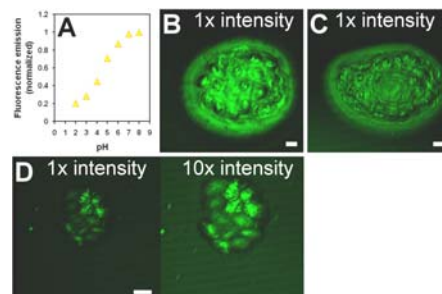


Figure 4. (A) Dependence of the fluorescence emission of the pH sensitive probe, Oregon Green, on pH. (B-D) Confocal projections comparing development of pH gradients using Oregon Green in mesostructured silica encapsulated yeast with: (B) DMPC liposomes without bR, with *diC₆* PC, (C) bR added with *diC₆* PC only, and (D) bR added in DMPC liposomes with *diC₆* PC. Decreasing fluorescence intensity corresponds to decreasing pH. Scale bars = 3 μ m.

Dramatic changes in pH gradient are observed for samples prepared from addition of bR-proteoliposomes to the yeast *diC₆* PC solution. As shown in Figure 4 D, the original several micrometer region of higher pH surrounding encapsulated cells is no longer present. Increasing fluorescence intensity by 10 fold (Fig. 4E) shows that the region surrounding the cells containing bR is now similar in pH to the surrounding silica matrix, ~ pH 3-4, consistent with proton pumping toward the cell. Unfortunately, due to the strongly overlapping spectral windows of Oregon green emission and bR absorption and activation (ref or supplementary) attempts to image the dark pH gradient were unsuccessful – confocal imaging unavoidably stimulates proton pumping eradicating the initial (dark) pH gradient. However, it is clear that the Oregon Green dye penetrates the multilayer vesicle region, retaining its capability to probe pH near the yeast cells, and does not photobleach significantly over the course of these experiments, as shown by the bright green emission in Figure 4 B where bR is absent. (Further addition of exogenous buffer (pH₀) caused immediate uniform green emission throughout the matrix). The decrease in pH of approximately 2 units over the typically 15 minutes required to locate cells and obtain the confocal projection is similar to that previously reported for bR reconstituted in porous silica microsphere supported bilayers.¹¹ In that study, after a 60 minute exposure of the 10 μm diameter microspheres to a UV-filtered xenon lamp, a 1.5 pH unit change was observed and attributed to bR orientation on the microsphere surface driven by fusion of unidirectional aligned bR proteoliposomes with the microsphere.¹¹ For our system, the comparatively smaller volume of the lipid-protein-encapsulated cells (>37x smaller for ~3 μm diameter yeast cells than for microspheres) and higher intensity of the laser light are consistent with a moderately greater pH change over a shorter time period.

These results show that bR retain their native functionality and adopt a preferred orientation to the yeast cellular surface when introduced in proteoliposomes with *diC₆* PC. It has been shown that bR inserts unidirectionally into preformed liposomes under conditions of detergent saturation.¹² *diC₆* PC may act as a detergent that, upon EISA and cell-directed assembly, reaches saturated concentration near the cells. This causes destabilization of the co-localized bR-proteoliposomes, facilitating fusion of liposomes with other liposomes and unidirectional orientation of bR.¹² This thesis is supported by the lack of liposome fusion or bR localization near neutrally charged latex beads (Figure 3 B,C), which we have shown do not localize *diC₆* PC under evaporation-induced cell-directed assembly.⁸ The inside-out orientation of bR reported in this work is identical to the bR orientation reported for bR-proteoliposomes formed in the presence of saturating detergent. Additionally, the proposed mechanism that proteins always insert through the hydrophobic domain of the membrane with the more hydrophobic protein moiety¹³ is followed by this system where the more hydrophobic NH₂-terminal region of bR penetrates the yeast supported multilayers yielding an inside-out orientation of bR.

In summary, we have shown a simple method for interfacing and orienting functional exogenous membrane-bound proteins with cells. We expect that this method is general and can be adapted to other membrane-bound proteins. It may prove useful in fundamental studies of membrane protein function and in imparting non-native characteristics to arbitrary cells.

Acknowledgement. This work was funded by the Air Force Office of Science and Research (AF OSR), the Defense Threat Reduction Agency (DTRA) CB Basic Research Program, and Sandia's LDRD program, and the DOE Office of Science Basic Energy Sciences. We thank Constantine Khripin for measuring the pH dependence of Oregon Green fluorescence emission. Sandia is a multiprogram laboratory operated by Sandia Corporation, a Lockheed Martin Company, for the United States Department of Energy under contract DE-AC04-94AL85000.

Supporting Information Available: Methods. This material is available free of charge via the Internet at <http://pubs.acs.org>.

References

- (1) (a) Avnir, D.; Coradin, T.; Lev, O.; Livage, J. *J. Mater. Chem.* **2006**, *16*, 1013-1030. (b) Hartmann, M. *Chem. Mater.* **2005**, *17*, 4577-4593. (c) Ispas, C.; Sokolov, I.; Andreeescu, S. *Anal. Bioanal. Chem.* **2009**, *393*, 543-554. (d) Lee, M.-Y.; Park, C. B.; Dordick, J. S.; Clark, D. S. *Proc. Natl. Acad. Sci. USA* **2005**, *102*, 983-987.
- (2) (a) Braun, S.; Rappoport, S.; Zusman, R.; Avnir, D.; Ottolenghi, M. *Mater. Lett.* **1990**, *10*, 1-5. (b) Ellerby, L. M.; Nishida, C. R.; Nishida, F.; Yamanaka, S.; Dunn, B.; Valentine, J. S.; Zink, J. I. *Science* **1992**, *255*, 1113-1115. (c) Yi, Y.; Neufeld, R.; Kermasha, S. *J. Sol-Gel Sci Technol.* **2007**, *43*, 161-170.
- (3) (a) Nassif, N.; Bouvet, O.; Rager, M. N.; Roux, C.; Coradin, T.; Livage, J. *Nat. Mater.* **2002**, *1*, 42-44. (b) Carturan, G.; Dal Toso, R.; Boninsegna, S.; Dal Monte, R. *J. Mater. Chem.* **2004**, *14*, 2087-2098. (c) Amoura, M.; Nassif, N.; Roux, C.; Livage, J.; Coradin, T. *Chem. Commun.* **2007**, 4015-4017.
- (4) Brennan, J. D. *Acc. Chem. Res.* **2007**, *40*, 827-835.
- (5) (a) Wu, S.; Ellerby, L. M.; Cohan, J. S.; Dunn, B.; El-Sayed, M. A.; Valentine, J. S.; Zink, J. I. *Chem. Mater.* **1993**, *5*, 115-120. (b) Weetall, H. H.; Roberston, B.; Cullin, D.; Brown, J.; Walch, M. *Biochim. Biophys. Acta* **1993**, *1142*, 211-213. (c) Weetall, H. H. *Biosens. Bioelectron.* **1996**, *11*, 327-333. (d) Shamansky, L. M.; Luong, K. M.; Han, D. H.; Chronister, E. L. *Biosens. Bioelectron.* **2002**, *17*, 227-231.
- (6) Luo, T. J. M.; Soong, R.; Lan, E.; Dunn, B.; Montemango, C. *Nat. Mater.* **2005**, *4*, 220-224.
- (7) Bromley, K. M.; Patil, A. J.; Seddon, A. M.; Booth, P.; Mann, S. *Adv. Mater.* **2007**, *19*, 2433-2438.
- (8) Baca, H. K.; Ashley, C.; Carnes, E.; Lopez, D.; Flemming, J.; Dunphy, D.; Singh, S.; Chen, Z.; Liu, N. G.; Fan, H. Y.; Lopez, G. P.; Brozik, S. M.; Werner-Washburne, M.; Brinker, C. J. *Science* **2006**, *313*, 337-341.
- (9) Baca, H. K.; Carnes, E.; Singh, S.; Ashley, C.; Lopez, D.; Brinker, C. J. *Acc. Chem. Res.* **2007**, *40*, 836-845.
- (10) (a) Birge, R. R. *Biochim. Biophys. Acta* **1990**, *1016*, 293-327. (b) Saaem, I.; Tian, J. *Adv. Mater.* **2007**, *19*, 4268-4271.
- (11) Davis, R. W.; Flores, A.; Barrick, T. A.; Cox, J. M.; Brozik, S. M.; Lopez, G. P.; Brozik, J. A. *Langmuir* **2007**, *23*, 3864-3872.
- (12) Rigaud, J.-L.; Pasternostre, M.-T.; Bluzat, A. *Biochemistry* **1988**, *27*, 2677-2688.
- (13) Eytan, G. D. *Biochim. Biophys. Acta* **1982**, *694*, 185-202.

Characterization of Lipid-Templated Silica and Hybrid Thin Film Mesophases by Grazing Incidence Small-Angle X-ray Scattering

Darren R. Dunphy,[†] Todd M. Alam,[‡] Michael P. Tate,^{§,○} Hugh W. Hillhouse,[§] Bernd Smarsly,^{||} Andrew D. Collord,[‡] Eric Carnes,[†] Helen K. Baca,[†] Ralf Köhn,^{†,⊥} Michael Sprung,^{#,◆} Jin Wang,[#] and C. Jeffrey Brinker^{*,†,▽}

[†]University of New Mexico/NSF Center for Micro-Engineered Materials, Department of Chemical and Nuclear Engineering, Albuquerque, New Mexico 87131, [‡]Department of Electronic and Nanostructured Materials, Sandia National Laboratories, Albuquerque, New Mexico 87185, [§]School of Chemical Engineering, Purdue University, 480 Stadium Mall Drive, West Lafayette, Indiana 47907, ^{||}Physikalisch-Chemisches Institut, Justus-Liebig-University Giessen, Heinrich-Buff-Ring 58, D-35392 Giessen, Germany, [⊥]Department of Chemistry & Biochemistry, University of Munich, Butenandtstr. 5-13 (E), 81377 Munich, Germany, [#]Advanced Photon Source, Argonne National Laboratory, 9700 S Cass Avenue, Argonne, Illinois 60439, and [▽]Advanced Materials Laboratory, Sandia National Laboratories, Albuquerque, New Mexico 87185. [○]Present address: Dow Chemical Company, Midland, Michigan 48674. [◆]Present address: HASYLAB at DESY, D-22607 Hamburg, Germany.

Received March 2, 2009. Revised Manuscript Received April 24, 2009

The nanostructure of silica and hybrid thin film mesophases templated by phospholipids via an evaporation-induced self-assembly (EISA) process was investigated by grazing-incidence small-angle X-ray scattering (GISAXS). Diacyl phosphatidylcholines with two tails of 6 or 8 carbons were found to template 2D hexagonal mesophases, with the removal of lipid from these lipid/silica films by thermal or UV/O₃ processing resulting in a complete collapse of the pore volume. Monoacyl phosphatidylcholines with single tails of 10–14 carbons formed 3D micellar mesophases; the lipid was found to be extractable from these 3D materials, yielding a porous material. In contrast to pure lipid/silica thin film mesophases, films formed from the hybrid bridged silsesquioxane precursor bis(triethoxysilyl)ethane exhibited greater stability toward (both diacyl and monoacyl) lipid removal. Ellipsometric, FTIR, and NMR studies show that the presence of phospholipid suppresses siloxane network formation, while actually promoting condensation reactions in the hybrid material. 1D X-ray scattering and FTIR data were found to be consistent with strong interactions between lipid headgroups and the silica framework.

Introduction

Evaporation-induced self-assembly (EISA),^{1,2} employing amphiphilic surfactants or block copolymers as structure directing agents (SDAs), has been proven to be a versatile route for the synthesis of ordered thin film mesophases characterized by a narrow pore size distribution and a well-defined pore network structure. In this process, a homogeneous alcohol/water solution of a soluble silica precursor, acid catalyst, and surfactant (present at a concentration much less than where bulk mesophases appear) undergoes preferential evaporation of alcohol and then water during film deposition, thus increasing the concentration of silica and surfactants and driving the self-assembly of ordered surfactant/silica mesophases.¹ Subsequent removal of the surfactant template by pyrolysis, UV exposure,³ or solvent extraction leaves a porous silica fossil of the original mesophase. The pore size of these materials, along with the mesophase identity, can be tuned through the size and shape of the surfactant (as understood by the critical packing parameter model)⁴ as well as control of

parameters such as the surfactant/silica and water/silica molar ratios. Common mesophases formed by EISA include lamellar, 2D hexagonal, and various 3D structures including cubic and 3D hexagonal phases.² Importantly, the silica precursor can be replaced with other soluble hydrophilic precursors to form non-silica metal oxide frameworks (TiO₂, SnO₂, etc.)^{2,5,6} as well as with precursors containing carbon–silicon bonds, producing hybrid functional materials.^{2,7} Numerous applications have been proposed for these materials, including separation membranes,⁸ sensors,⁹ and low-*k* dielectrics.¹⁰

Despite over a decade of research on surfactant-directed synthesis of porous or composite materials, one class of amphiphilic SDA that has not been investigated in any great detail is phospholipids. Phospholipids are known as components of cell membranes and liposomes, but their use to direct inorganic mesophases is largely unexplored. Recently, we demonstrated

*To whom correspondence should be addressed. E-mail: cjbrink@sandia.gov.

(1) Lu, Y. F.; Ganguli, R.; Drewien, C. A.; Anderson, M. T.; Brinker, C. J.; Gong, W. L.; Guo, Y. X.; Soye, H.; Dunn, B.; Huang, M. H.; Zink, J. I. *Nature* **1997**, *389*, 364–368.

(2) Sanchez, C.; Boissiere, C.; Grosso, D.; Laberty, C.; Nicole, L. *Chem. Mater.* **2008**, *20*, 682–737.

(3) Clark, T.; Ruiz, R. D.; Fan, H.; Brinker, C. J.; Swanson, B. I.; Parikh, A. N. *Chem. Mater.* **2000**, *12*, 3879–3884.

(4) Israelachvili, J. N. *Intermolecular and Surface Forces*, 2nd ed.; Academic Press: New York, 1991.

(5) Alberius, P. C. A.; Frindell, K. L.; Hayward, R. C.; Kramer, E. J.; Stucky, G. D.; Chmelka, B. F. *Chem. Mater.* **2002**, *14*, 3284–3294.

(6) (a) Crepaldi, E. L.; Soler-Illia, G. J. D. A.; Bouchara, A.; Grosso, D.; Durand, D.; Sanchez, C. *Angew. Chem., Int. Ed.* **2003**, *42*, 347–351. (b) Urade, V.; Hillhouse, H. W. *J. Phys. Chem. B* **2005**, *109*, 10538–10541.

(7) Dunphy, D. R.; Smarsly, B.; Brinker, C. J. In *The Supramolecular Chemistry of Organic-Inorganic Hybrid Materials*; Rurack, K., Ed.; John Wiley & Sons, Inc.: Hoboken, NJ, in press.

(8) Jiang, Y.-B.; Xomertakis, G.; Chen, Z.; Dunphy, D.; Kissel, D. J.; Cecchi, J. L.; Brinker, C. J. *J. Am. Chem. Soc.* **2007**, *129*, 15446–15447.

(9) Innocenzi, P.; Falcaro, P.; Bertolo, J. M.; Bearzotti, A.; Amenitch, H. *J. Non-Cryst. Solids* **2005**, *351*, 1980–1986.

(10) Jiang, Y.-B.; Liu, N.; Gerung, H.; Cecchi, J. L.; Brinker, C. J. *J. Am. Chem. Soc.* **2006**, *128*, 11018–11019.

that, using short chain (C_6) phospholipids, nanostructured films formed via an EISA process can be coassembled with living cells, to create a biocompatible encapsulation matrix for whole-cell biosensor devices¹¹ that preserves cell viability for months under desiccating conditions. Because the surfactants typically used for the EISA process are either nonbiocompatible (e.g., ionic surfactants such as cetyltrimethylammonium bromide) or do not form high quality films and/or mesophases with extended order in the pH range needed for cell viability (block copolymers)⁵, we introduced the use of short-chain zwitterionic phospholipids as templates for nanostructured materials useful for encapsulation of whole cells, specifically *Saccharomyces cerevisiae*. It was hypothesized that the zwitterionic headgroup would minimize electrostatic interactions with the cell membrane (thus increasing cell viability), while shorter acyl chains (6–10 carbons, in comparison to typical cell membrane phospholipids that often contain 18 or more carbons) would increase the template solubility in the alcohol and water media necessary for sol–gel chemistry and because of their reduced packing parameters⁴ promote the formation of higher curvature hexagonal and cubic mesophases. Not only was the biocompatibility of lipid templates confirmed (with cells encapsulated within lipid/silica mesophases actually experiencing increased viability relative to cells encapsulated within films of pure silica)¹¹ but also the presence of cells was found to actively alter the self-assembly pathway of the lipid/silica mesophase, providing a method of localizing lipids plus any added proteins or nanocrystals at the cell/inorganic interface,¹¹ thereby enabling engineering of the cell/nanostructure interface.

For continuation of these studies on cell-directed self-assembly, however, a better understanding of the relationship between the molecular structure of the phospholipid SDA and the resulting lipid/silica mesophase is needed. Although the bulk phase diagrams of short-chain phospholipids in water have not been studied in detail (especially with added soluble silica),¹² a number of analytical techniques have been developed to examine the lyotropic behavior of lipids in general.^{13,14} Of these, small-angle X-ray scattering (SAXS) is perhaps the most widely used method for examining the structure of bulk mesophases of not only lipids but also of surfactants and other types of self-assembling molecules. However, orientation and distortion of mesophases relative to the substrate during EISA generally prevents the unique assignment of the thin-film mesostructure type from 1D diffraction data.¹⁵ Also, the low scattering volume present in a thin film (ca. 250–500 nm thick) complicates standard SAXS analysis. To bypass these issues, we utilized grazing incidence small-angle X-ray scattering (GISAXS), performed at a high-intensity synchrotron source with a 2D detector, to characterize the static phase behavior of various (short-chain) phospholipids in silica films formed via the combination of sol–gel chemistry and EISA. In GISAXS, the X-ray beam is incident upon the sample at an angle greater than the critical angle of the film, but less than that of the substrate, maximizing the scattering volume and enabling the investigation of nanostructure in films as thin as one monolayer. Unlike electron microscopy, a large area of the substrate is

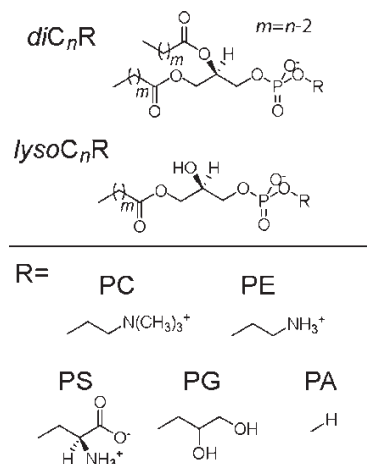


Figure 1. Structures of phospholipids investigated as silica templates in films synthesized via EISA. PC, phosphatidylcholine; PE, phosphatidylethanolamine; PS, phosphatidylserine; PG, phosphatidylglycerol; PA, phosphatidic acid.

interrogated, yielding an overall average (representative) structure of the film.

More specifically, the effect of acyl chain length in diacyl phosphatidylcholines on mesophase structure in lipid/silica films synthesized using EISA, as well as the effect of headgroup identity for diacyl phospholipids of constant tail length (six carbons), was investigated. To increase the range of phases formed by phospholipids to include 3D micellar phases, we examine the templating behavior of monoacyl phosphatidylcholines (so-called lysolipids) in addition to diacyl phospholipids. We also compare lipid-templated silica materials with materials formed using a hybrid precursor (bis(triethoxysilyl)ethane). For these various lipid/silica mesophases, we characterize the pore structure of films obtained after solvent extraction (in 3D mesophases formed from phospholipids) or thermal calcination (for lipid-templated hybrid films). We also examine the effect of phospholipids on framework condensation using vibrational spectroscopy and NMR and find that these lipids suppress the condensation of silica but enhance the reactivity of the hybrid framework. Finally, 1D X-ray scattering and FTIR data are found to be consistent with the presence of strong interactions between lipids and the framework phase.

Experimental Section

In a typical film preparation, 20–50 mg of lipid, 0.122 mL of tetraethyl orthosilicate (TEOS), and 0.16 mL of 0.05 M HCl were added to 0.6 mL of ethanol. This sol was aged for 10 min at room temperature before spin coating at 2000 rpm in a glovebox environment kept at a relative humidity of 15–20% through a flow of dry N_2 . For the synthesis of lipid/bis(triethoxysilyl)ethane (BTESE) films, 69 μ L of BTESE replaced the TEOS in the above formulation, maintaining the same lipid/silicon ratio for both recipes. All lipids were purchased from Avanti Polar Lipids in dry form and were used as received. TEOS (98%), BTESE, and HCl were purchased from Aldrich; absolute ethanol was obtained from Aaper.

The structures of the phospholipid templates investigated in this article are given in Figure 1. We adopt a nomenclature where the prefix *di-* or *lyso-* signifies lipids with one or two acyl tails, respectively, the subscript n in C_n gives the number of carbon atoms in each acyl chain, and the type of headgroup is identified by the suffix (PC = phosphatidylcholines; PE = phosphatidylethanolamine; PS = phosphatidylserine; PG = phosphatidylglycerol; PA = phosphatidic acid).

Because the final mesostructure is largely determined by the surfactant/oxide volume ratio in nanostructure films synthesized

(11) Baca, H. K.; Ashley, C.; Carnes, E.; Lopez, D.; Flemming, J.; Dunphy, D.; Singh, S.; Chen, Z.; Liu, N.; Fan, H.; Lopez, G. P.; Brozik, S. M.; Werner-Washburne, M.; Brinker, C. J. *Science* **2006**, *313*, 337–341.

(12) Koyanova, R.; Caffrey, M. *Chem. Phys. Lipids* **2002**, *115*, 107–219.

(13) Kleinschmidt, J. H.; Tamm, L. K. *Biophys. J.* **2002**, *83*, 994–1003.

(14) (a) Oradd, G.; Gustafsson, J.; Almgren, M. *Langmuir* **2001**, *17*, 3227–3234. (b) Pitzalis, P.; Monduzzi, M.; Krog, N.; Larsson, H.; Ljusberg-Wahren, H.; Nylander, T. *Langmuir* **2000**, *16*, 6358–6365. (c) Qiu, H.; Caffrey, M. *Biomaterials* **2000**, *21*, 223–234.

(15) Tate, M. P.; Urade, V. N.; Kowalski, J. D.; Wei, T.; Hamilton, B. D.; Eggiman, B. W.; Hillhouse, H. W. *J. Phys. Chem. B* **2006**, *110*, 9882–9892.

using an EISA process, we report the amount of lipid added to each formulation relative to the amount of silica present in the sol. For experimental convenience, this ratio is given as mg of lipid per mmol of silica, the latter figure given in molar units to facilitate conversion of the above recipe to sols with different silica precursors (e.g., BTESE).

GISAXS measurements were performed on beamline 8-ID at the Advanced Photon Source at Argonne National Laboratories using a wavelength of 1.6868 Å, a sample-to-detector distance of either 1580 or 1254 mm, and a 2048 × 2048 Marr CCD detector. Reflectivity measurements were used to position the sample angle in the range above the critical angle of the film but below that of the substrate, the criterion for grazing incidence; typical analysis angles were 0.18–0.20°. NANOCELL,¹⁵ a program developed at Purdue University for analysis of SAXS and GISAXS data of nanostructured materials, was used to fit the resulting 2D scattering data.

X-ray diffraction (XRD) was performed on a PANalytical X'pert Pro system equipped with an X'Celerator detector. Refractive index and thickness measurements were made with a J.A. Wollam Co. M44 spectroscopic ellipsometer using a Cauchy dispersion model to determine film optical constants. Refractive index profiles were assumed to be step-index, corresponding to a homogeneous film structure. All refractive index values (reported at a wavelength of 632.5 nm) and thickness measurements were made in triplicate and averaged to obtain the data points reported herein.

Nitrogen adsorption isotherms were collected using an in-house designed 96 MHz surface acoustic wave (SAW) apparatus interfaced with a Micromeritics ASAP 2020 surface area and porosimetry analyzer.¹⁶ Films were deposited on SAW substrates under conditions identical to those used for films made for ellipsometric and X-ray analysis.

TEM was performed on a JEOL 2010, operating at an accelerating voltage of 200 kV and equipped with a Gatan slow scan CCD camera. TEM samples were prepared by scraping the film with a sharp blade and transferring the flakes to a carbon-coated copper grid. Imaging was performed in under-focus conditions. For FTIR studies, films were deposited onto undoped silicon substrates and analyzed in a transmission geometry using a Bruker Vector 22 spectrometer. Confocal and phase contrast images of *diC*₁₀PC/silica films were taken with a BioRad Radiance 2100 confocal microscope using the 488 nm line of a 5 mW Ar laser source.

High resolution solution ²⁹Si NMR spectra were obtained on a Bruker DRX400 instrument at 79.50 MHz using a 10 mm low ²⁹Si background probe, quartz tubes, and an inverse gated pulse sequence. To reduce the spin–lattice relaxation rates, CrAcAc was added to the solution, with a final concentration of 1 mM. The hydrolysis kinetics were followed using 32 to 86 scan averages with a 20 s recycle delay. The ²⁹Si chemical shifts were referenced to external TMS $\delta = 0.0$ ppm. The assignment of the different hydrolysis species was based on previous results.¹⁷

The solid state ²⁹Si and ³¹P magic angle spinning (MAS) NMR spectra were obtained on a Bruker Avance 400 instrument at 79.50 MHz and 171.99 using a 4 mm broad-band probe spinning between 4 and 12.5 kHz. The ²⁹Si cross-polarization (CP) spectra were obtained with a 5 ms contact pulse and a 5 s recycle delay, while the direct single pulse Bloch decay was obtained with a 240 s recycle delay. The ²⁹Si NMR chemical shifts were referenced to the secondary standard Q₈M₈ ($\delta = +11.5$ ppm with respect to TMS $\delta = 0$ ppm). The solid state ³¹P MAS NMR spectra were obtained using a single pulse Bloch decay with a 20 s recycle delay. The ³¹P chemical shifts were referenced to the secondary external standard H₂NH₄PO₄ ($\delta = 0.8$ ppm with

respect to 85% phosphoric acid at $\delta = 0.0$ ppm). All spectra were obtained using high power ¹H TPPM decoupling.¹⁸ The spectral deconvolutions and fitting of the ³¹P chemical shift anisotropy (CSA) tensor and isotropic chemical shift were performed in the DMFIT program.¹⁹

Results and Discussion

Previously, for use in cell-directed assembly, a stock solution containing prehydrolyzed and partially condensed silica oligomers was used to synthesize lipid-templated silica films. This approach can suffer from poor reproducibility of overall film and nanostructure quality, however, because of the difficulty in controlling the degree of condensation during the stock synthesis combined with continuing reaction of the oligomers during stock storage, even at low temperatures.²⁰ Instead, for these studies we use direct addition of the silica precursor, TEOS, to the synthesis solution, followed by hydrolysis at room temperature (20 °C) for 10 min before film coating. Although all experimental data reported here is from films deposited after this 10 min sol aging period, extended aging under ambient conditions for up to 3 h was found to have no effect on macroscopic film quality and nanoscale order, as determined by coating a film every 15 min from a sol maintained at room temperature. Overall film homogeneity was not affected, with the only observable effect on nanostructure being a small increase in lattice spacing with time (an effect of an increase in silica oligomer size during sol aging).²⁰

In addition to silica condensation, lipid degradation under acidic conditions (such as that found in the precursor sol) may impact film quality. We followed the degradation of the headgroup in *diC*₆PC under typical sol conditions (i.e., 0.10 M HCl) using ³¹P and ¹H solution state NMR. After 16 h, only ca. 4% of phosphorus centers had undergone a change in chemical state, with no significant changes in the ¹H spectrum observed after HCl addition.

Diacyl Phosphatidylcholine Templates. Ideally, a lipid/silica mesophase used for cell entrapment will possess an extended, continuous 3D structure such that template removal creates a continuous 3D pore network with long-range pathways for facile mass transport throughout the film. Identifying both a lipid structure and lipid/silica ratio that yields such a mesophase using *a priori* prediction is difficult, however; the critical packing parameter g , defined by $g = v/a_0l_c$ (where v = volume of the lipid tail, a_0 = optimal headgroup area, and l_c = the critical chain length of the lipid tails), is commonly used to describe the aggregation morphology of self-assembling amphiphiles⁴ but is unable to fully predict lipid/water phase diagrams.^{2,21} More advanced (computational) models are also generally limited to qualitative descriptions of lipid/water mesostructure.²² We thus adapt an empirical approach to mapping out the relationships between lipid structure, lipid/silica ratio, and type of mesostructure formed, first investigating mesophase formation as a function of chain length in diacyl phosphatidylcholines, and then, keeping the tail length constant, investigating the effect of headgroup identity.

We first investigated the effect of lipid tail length for the dialkyl phosphatidylcholines *diC*₆PC, *diC*₈PC, and *diC*₁₀PC

(19) Massiot, D.; Fayon, F.; Capron, M.; King, I.; Le Calve, S.; Alonso, B.; Durand, J.-O.; Bujoli, B.; Gan, Z.; Hoatson, G. *Magn. Reson. Chem.* **2002**, *40*, 70–76.

(20) Brinker, C. J.; Scherer, G. W. *Sol-Gel Science: The Physics and Chemistry of Sol-Gel Processing*; Academic Press: San Diego, CA, 1990.

(21) Mezzenga, R.; Schurtenberger, P.; Burbridge, A.; Michel, M. *Nat. Mater.* **2005**, *4*, 729–740.

(22) Mezzenga, R.; Lee, W. B.; Fredrickson, G. H. *Trends Food Sci. Technol.* **2006**, *17*, 220–226.

(16) Ricco, A. J.; Frye, G. C.; Martin, S. J. *Langmuir* **1989**, *5*, 273–276.

(17) Alam, T. M.; Henry, M. *Phys. Chem. Chem. Phys.* **2000**, *2*, 23–28.

(18) Bennett, A. E.; Rienstra, C. M.; Auger, M.; Lakshmi, K. V.; Griffin, R. G. *J. Chem. Phys.* **1995**, *103*, 6951–6958.

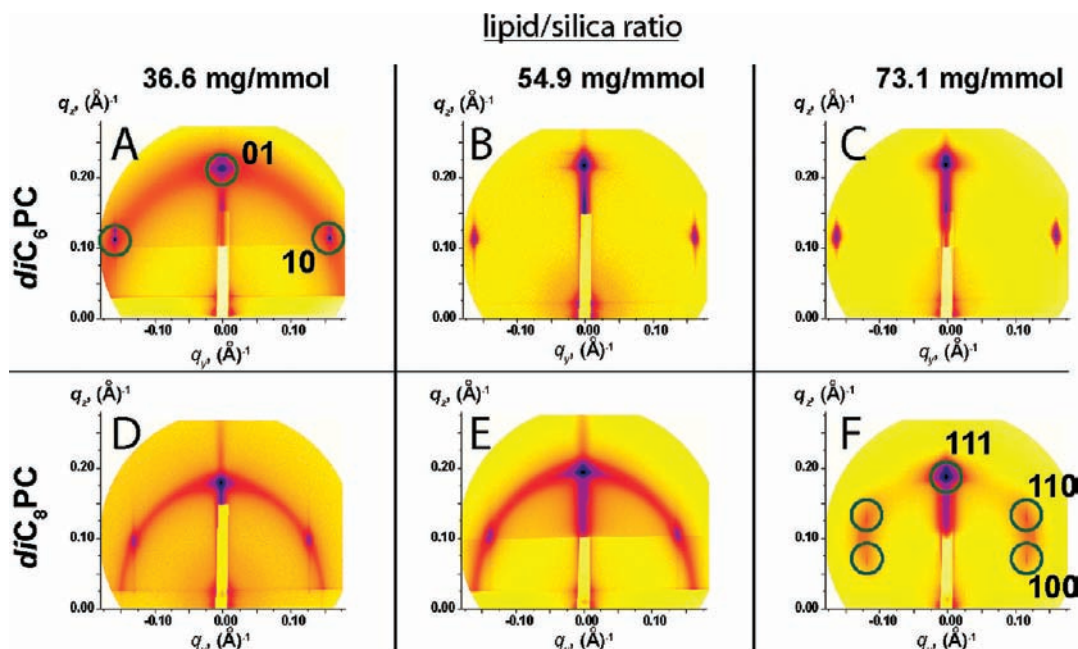


Figure 2. GISAXS patterns for diC_6PC (A–C) and diC_8PC -templated (D–F) silica as a function of the lipid/silica ratio. Data for diC_6PC at a lipid/silica ratio of 36.6 mg/mmol is indexed to a 2D hexagonal mesophase, while the data for diC_8PC at a lipid/silica ratio of 73.1 mg/mmol is indexed to rhombohedral space group $R-3m$.

on lipid/silica film structure over a lipid/silica ratio range of ca. 30–100 mg/mmol. This corresponds to an approximate lipid volume fraction in hydrated, as-deposited films of 30–60% (assuming a density of 1.0 g/mL for the lipid phase).⁵ This range was selected to match the range of surfactant/silica ratios generally used in films templated with synthetic amphiphiles.²

Estimates of g for the diacyl lipids (ca. 0.45 (C_6) to 0.55 (C_{10}))¹³ predict that nonspherical micelles (e.g., hexagonal rods) will dominate the diacyl lipid/ H_2O phase diagram.⁴ This is confirmed for diC_6PC by the GISAXS data given in Figure 2A–C for lipid/silica ratios between 36.6 and 73.1 mg/mmol SiO_2 . However, pure diC_6PC , when cast as a film from an ethanol solution, yields a lamellar phase with interplanar spacing of 25.3 Å; lamellar phases were also observed in diC_6PC /silica films for ratios greater than ca. 80 mg/mmol. Some loss of orientational order can be seen at low lipid/silica ratios, as evidenced by the appearance of a diffuse ring in the GISAXS scattering pattern (Figure 2A). All patterns show uniaxial shrinkage of the nanostructure of ca. 15% in the direction normal to the substrate from silica condensation during film drying (from an undistorted {01} spacing of 35 Å, determined by the position and angle of the (10) reflection relative to the q_y axis).

A 2D hexagonal structure is also observed for diC_8PC -templated silica between lipid/silica ratios of 36.6 and 54.9 mg/mmol (Figure 2D–E), with an undistorted {01} spacing of 40 Å. Compared to diC_6PC , the degree of orientational order of the diC_8PC /silica mesophase is lower, with a diffuse ring present in the GISAXS patterns over the entire compositional range where a 2D hexagonal phase is present. At the lipid/silica ratio for diC_8PC -templated films shown in Figure 2F, a new pattern appears that we fit to a $[111]$ -oriented rhombohedral space group ($R-3m$; $a = 45$ Å; $\alpha = 75^\circ$) using NANOCELL. Although this mesophase could comprise close-packed monodisperse micelles, (the rhombohedral symmetry being derived from distortion of face-centered cubic packing)²³, the size of micellar aggregates

typically formed by diC_8PC (MW $\approx 1-2 \times 10^6$ g/mol,²⁴ $r \approx 7-9$ nm, assuming purely spherical micelles) is not consistent with the fitted unit cell parameters, assuming close-packed micelles. Another potential rhombohedral structure for this film is that of a membrane fusion intermediate whereby hourglass-shaped stalks link adjacent lipid bilayers;²⁵ this phase has been postulated to exist as a transition state in membrane fusion and has been characterized for a methylated analogue of dipalmitoyl phosphatidylcholine. As with diC_6PC , diC_8PC forms lamellar phases with silica at lipid/silica ratios above 80 mg/mmol (pure diC_8PC also adopts a lamellar structure, with an interplanar spacing of 30.4 Å).

For $diC_{10}PC$, complete phase separation between the lipid and silica occurs during the EISA process. X-ray scattering data shows no significant difference in lattice spacing between pure $diC_{10}PC$ (lamellar structure, $d = 34$ Å) and lipid/silica composites ($d =$ ca. 35 Å). Furthermore, confocal microscopy (Figure 3A) of a $diC_{10}PC$ /silica film doped with a polar fluorescein derivative that selectively partitions into the hydrophilic silica framework shows complete macroscopic phase separation between the two components; holes in the fluorescence image correspond to what appear to be globules of lipid in the phase contrast image.

Phase separation of $diC_{10}PC$ is consistent with the trend in critical micelle concentration (cmc) for dialkyl phosphatidylcholines; the cmc for diC_nPC decreases dramatically as n increases, with the cmc for $n = 6, 8,$ and 10 being 15.4, 0.16, and 0.009 mM, respectively.²⁶ This rapid decrease of diC_nPC solubility as the tail is lengthened may also account for the loss of orientational order seen in 2D hexagonal phases for diC_8PC ; during film evaporation, rapid kinetics of mesophase formation will induce the formation of unoriented nanostructures (i.e., favoring precipitation over alignment by the solid/liquid or liquid/air interfaces).

(24) Tausk, R. J. M.; Oudshoorn, C.; Overbeek, J. T. G. *Biophys. Chem.* **1974**, *2*, 53–63.

(25) Yang, L.; Huang, H. W. *Biophys. J.* **2003**, *84*, 1808–1817.

(26) Weshayanwivat, P.; Scamehorn, J. F.; Reilly, P. J. *J. Surfactants Deterg.* **2005**, *8*, 65–72.

(23) Eggiman, B. W.; Tate, M. P.; Hillhouse, H. W. *Chem. Mater.* **2006**, *18*, 723–730.

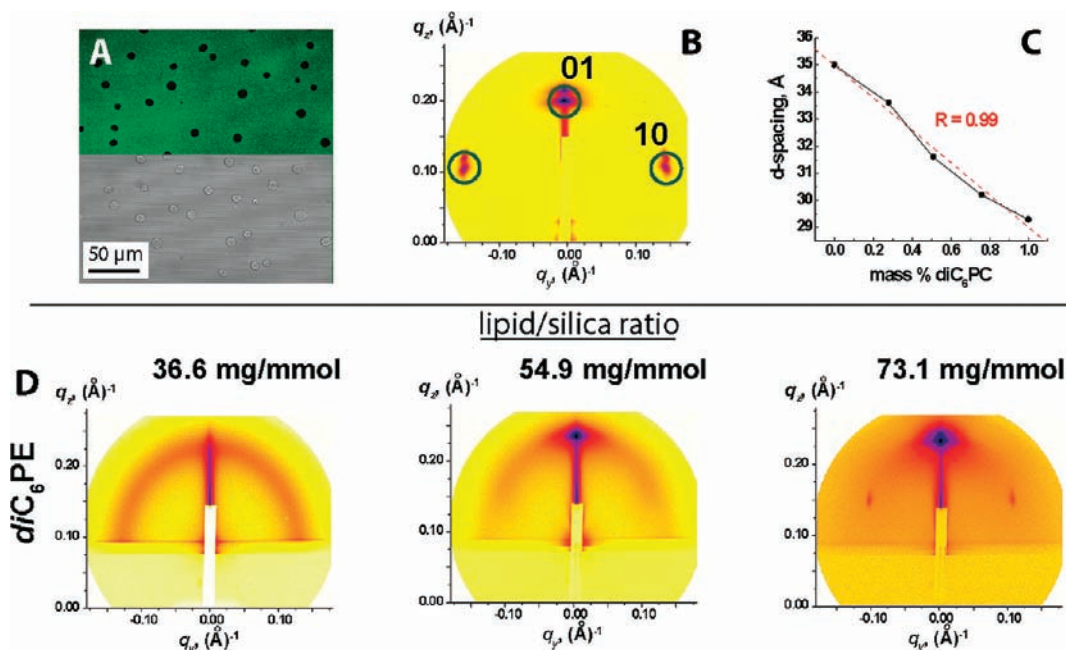


Figure 3. (A) Confocal/phase contrast image of a fluorescein-doped diC_8PC/SiO_2 film, showing phase separation of the lipid. (B) GISAXS image of a 2D hexagonal phase obtained from a mixture of diC_6PC and diC_8PC in SiO_2 . (C) The relationship between interplanar spacing and mass ratio of diC_6PC and diC_8PC in lipid-templated films. (D) GISAXS patterns for diC_6PE -templated silica as a function of the lipid/silica ratio.

Because blends of lipids can be used to modify phase diagrams or the physical properties of particular phases, we examined silica templating by binary mixtures of diC_6PC and diC_8PC . Over the entire range of diC_6PC/diC_8PC ratios, nanostructures with 2D hexagonal symmetry (Figure 3B) were observed, with lattice spacing (as determined by XRD, Figure 3C) being linearly proportional to this ratio.

Removal of the PC lipid template from these nanostructured films was attempted with thermal calcination as well as UV/O_3 treatment. However, complete film collapse was obtained in all experiments, even after film aging, heating, or treatment with NH_3 or HCl vapor to increase the degree of silica condensation. Solvent extraction of the lipid was also ineffective, presumably due to poor accessibility of the lipid mesophase to the surface of the film or strong lipid/silica interactions. TEM analysis of the nanostructured film showed no characteristic structure, likely an effect of damage from the electron beam coupled with the small feature size of the lipid nanostructure.

Effect of the Lipid Headgroup on Mesophase Formation.

Although phosphatidylcholines are prevalent in many biological membranes, a diverse range of headgroup structures are found in nature, each with unique chemical properties (acidity, charge, hydrogen bonding ability, etc.). We investigated the effect of this headgroup chemistry on mesophase formation by synthesizing lipid/ SiO_2 films with diC_6PE , diC_6PG , diC_6PS , and diC_6PA templates under conditions identical to those used for diC_6PC/SiO_2 films. While the templates diC_6PS and diC_6PA produced films of poor macroscopic quality at all lipid/silica ratios, diC_6PE and diC_6PG did yield homogeneous films (for diC_6PG , spin coating at 4000 rpm was used to compensate for an increased solution viscosity due to the glycerol headgroup); the relative degree of nanostructure order was reduced with these two lipid templates in comparison with that of diC_6PC , however. Figure 3D shows GISAXS data for diC_6PE films with lipid/silica ratios of 36.6 to 73.1 mg/mmol SiO_2 . At low lipid concentrations, a diffuse ring indicates a lack of long-range and orientational order. Although this scattering pattern could be interpreted as a

worm-hole-type mesostructure, the possibility of a nonoriented lamellar phase cannot be excluded. As the amount of lipid is increased, a strong reflection from planes parallel to the substrate surface appears, while diffuse scattering is present in the region of the detector where $\{10\}$ reflections would be expected for a 2D hexagonal phase; this diffuse scattering becomes better defined into a $\{10\}$ reflection at a lipid/silica ratio of 73.1 mg/mmol. The relative weakness of these spots, however, compared to the reflection at $q_y = 0$ suggests that a lamellar phase is predominant in comparison to the hexagonal structure. Scattering data for diC_6PG is essentially identical. As was seen for diC_6PC and diC_8PC , removal of diC_6PE or diC_6PG by thermal calcination or UV/O_3 degradation resulted in the collapse of the film, while solvent extraction did not yield any template removal.

Lysophosphatidylcholine Templates. An alternate strategy to using diacyl PCs with short alkyl tails to improve template solubility in polar solvents is to remove one alkyl chain from otherwise insoluble lipids, forming what are termed lysolipids. As an example of the solubility increase attained from this structural modification, the *cmc* of $lysoC_{10}PC$ is 6.0 mM,²⁷ compared to only 0.009 mM for $diC_{10}PC$. Also, elimination of one acyl chain reduces the tail volume by 50%, reducing g to below 0.3, a range where micellar mesophase formation is expected.⁴ Published phase diagrams for these lipids do indeed show the presence of micellar cubic phases that could potentially be used to template 3D porosity in EISA-derived silica films.²⁸

We investigated lysolipids with the general formula $lysoC_nPC$ (Figure 1) for $n = 6, 10, 12, 14,$ and 16 . When $n = 6$, no ordered mesophase is observed for lipid-templated silica (although the pure lipid crystallizes into a 2D hexagonal phase, with the lattice parameter $a = 24.8$ Å). For the other lipids, structured mesophases are obtained over the lipid/silica ratio of 47.8 to 83.9 mg/mmol SiO_2 . GISAXS of these films shows that the phase

(27) Stafford, R. E.; Dennis, E. A. *Colloids Surf.* **1988**, *30*, 47–64.

(28) Arvidson, G.; Brentel, I.; Khan, A.; Lindblom, G.; Fontell, K. *Eur. J. Biochem.* **1985**, *152*, 753–759.

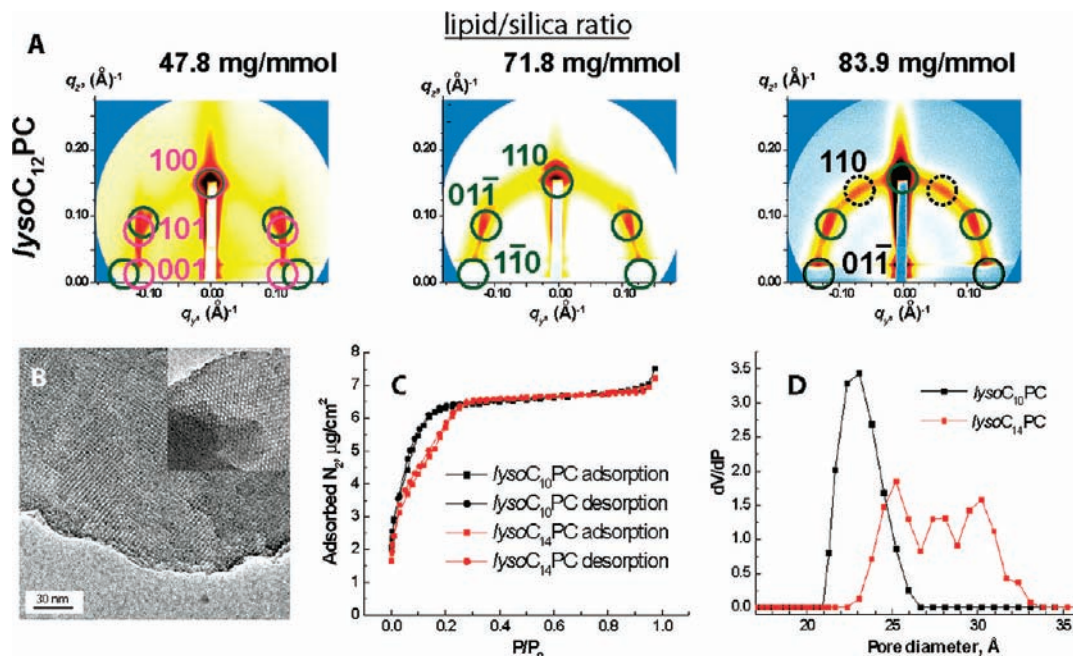


Figure 4. (A) GISAXS patterns for *lysoC*₁₂PC-templated silica as a function of the lipid/silica ratio, indexed as green, [110] oriented *Im*-3m; pink, [100] oriented *P*_{6₃/mmc; black dashed line, [111] oriented *Im*-3m. (B) [001]-oriented TEM image of *Im*-3m *lysoC*₁₄PC-templated silica after solvent extraction. (C) N₂ adsorption isotherms for *lysoC*₁₄PC and *lysoC*₁₀PC-templated SiO₂ films. (D) Pore size distributions calculated from the adsorption branch of these isotherms.}

behavior is similar for all values of n between 10 and 16; Figure 4A contains typical scattering data for *lysoC*₁₄PC at lipid/silica ratios of 47.8, 71.8, and 83.9 mg/mmol SiO₂. At the lowest lipid concentration, a mixture of phases is observed that we fit to two structures obtained from the packing of spherical micelles: [001]-oriented 3D hexagonal (space group *P*_{6₃/mmc, $a = b = 65$ Å, $c = 80$ Å) and another phase consistent with either *Pm*-3n or *Im*-3m symmetry, oriented with the [110] direction orientation parallel to the substrate normal and $a = 65$ Å (but distorted by ca. 30% perpendicular to the substrate surface due to uniaxial shrinkage during film drying). While the 3D hexagonal phase has not been observed previously in any lysolipid/water phase diagram, the *Pm*-3n structure has been well characterized with a body-centered unit cell containing an additional two micelles on each face of the cube.²⁹ However, we tentatively assign the structure to *Im*-3m upon the basis of the unit cell parameter; in the *lysoC*₁₆PC/water system, $a =$ ca. 125 Å for the *Pm*-3n phase,²⁹ while we only measure $a =$ ca. 70 Å in *lysoC*₁₆PC/silica films. Given the lack of higher-order diffraction features in the data from Figure 4, vigorous differentiation between *Pm*-3n and *Im*-3m is not possible at this time.}

As the amount of lipid is raised relative to that of silica, the 3D hexagonal phase becomes less pronounced, eventually disappearing at ca. 71.8 mg lipid/mmol SiO₂, where a loss of orientational order (as evidenced by the appearance of a diffuse ring) is observed, accompanied by the appearance of extra reflections to each side of the (110) diffraction spot. Although a lack of reflections outside the diffuse ring prevents the definitive assignment of these features, these new spots are consistent with the presence of [111]-oriented *Im*-3m domains with the same 30% contraction normal to the substrate found for the [110] orientation. *LysoC*₁₂PC and *lysoC*₁₆PC both feature the same phase behavior as that shown for *lysoC*₁₄PC; *lysoC*₁₀PC, however, differs in that a diffuse ring and the (111) reflections are seen

for all lipid/SiO₂ concentrations, indicating a lack of orientation order relative to that of other lysolipids with longer acyl tails.

As was seen for the diacyl PCs, removal of the lipid template by thermal calcination or UV/O₃ treatment resulted in complete collapse of film porosity. However, solvent extraction in 0.01 M HCl in ethanol for 2 days at 50 °C did yield porous films with total pore volumes of ca. 35–40% (as estimated by spectroscopic ellipsometry). Significant stresses were developed in films during lipid removal, as evidenced by extensive cracking after removal from the extraction solution. N₂ adsorption isotherms for *lysoC*₁₀PC-, *lysoC*₁₂PC-, and *lysoC*₁₄PC-templated films were measured on SAW devices after extraction of the lipid. Figure 4C shows isotherms for *lysoC*₁₀PC/SiO₂ and *lysoC*₁₄PC/SiO₂ films; the former is indicative of a microporous material (using IUPAC terminology, a type I isotherm), while the *lysoC*₁₄PC/SiO₂ film yielded a type IV (mesoporous) isotherm. Both sets of data show a small upturn at high partial pressure from macroporosity created by cracking of the film. Pore size distributions (PSD, Figure 4D) show a narrow (ca. 7 Å wide) pore size distribution for the *lysoC*₁₀PC-templated film centered at 23 Å, while the significantly broader distribution (about 11 Å) for the *lysoC*₁₄PC/SiO₂ film is centered at 27.5 Å; why this lipid shows a wider PSD is unknown at this time. The calculated distribution for a *lysoC*₁₂PC/SiO₂ film (data not shown) is similar to that for the *lysoC*₁₀PC-templated material, with a PSD of 24.5 ± 4 Å.

TEM analysis after lipid extraction (Figure 4B) shows nanostructure consistent with micellar packing, with planes of both 4-fold and 3-fold symmetry. Although the former indicates the presence of a cubic phase, 3-fold symmetry can be obtained from either cubic or 3D hexagonal phases (both of which were identified in *lysoC*₁₄PC/SiO₂ films by GISAXS).

Lipid/Bis(triethoxysilyl)ethane Films. In addition to our investigations of lipid/silica film structure, we also examined the templating behavior of lipids when TEOS was substituted by the hybrid silsesquioxane precursor BTESE. Bridged silsesquioxanes such as BTESE are readily incorporated into the framework of films synthesized using EISA, introducing covalently linked

(29) Eriksson, P.-O.; Lindblom, G. *J. Phys. Chem.* **1987**, *91*, 846–853.

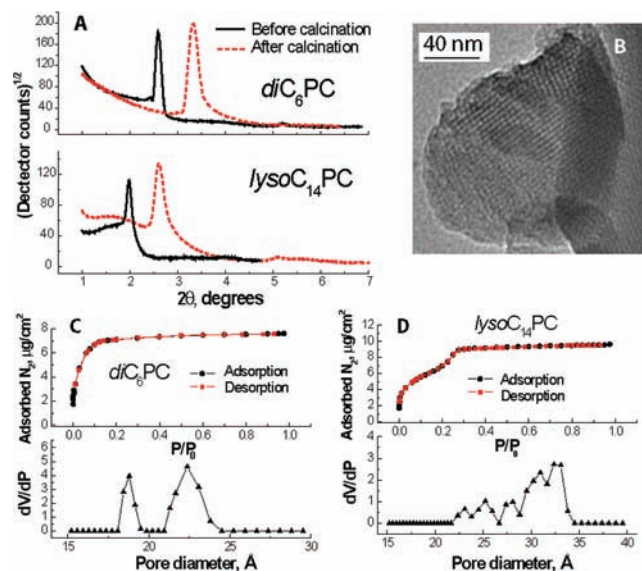


Figure 5. (A) XRD data for *diC*₆PC and *lysoC*₁₄PC-templated BTESE films, before and after thermal calcination. (B) TEM image obtained from a calcined *lysoC*₁₄PC-templated BTESE film. (C) N₂ adsorption isotherm and pore size distribution for a *diC*₆PC-templated BTESE film. (D) N₂ adsorption isotherm and pore size distribution for a *lysoC*₁₄PC-templated BTESE film.

organic functionality into the inorganic network.^{7,30} Porous hybrid materials synthesized with hybrid precursors exhibit new properties, including increased hydrolytic stability relative to materials of pure silica,³¹ a critical property for interfacing lipid-templated films with biological systems at near-neutral pH and high ionic strength.

Lipid-templated BTESE films were synthesized under identical conditions to those used for films made with the purely inorganic precursor TEOS; the EISA precursor solution was only modified by replacing TEOS with BTESE in a 2:1 mol ratio (maintaining a constant Si/lipid ratio in the two systems). Figure 5A shows XRD data for as-deposited *diC*₆PC/BTESE and *lysoC*₁₄PC/BTESE films (using a lipid/Si molar ratio of 71.8 mg/mmol for both cases) and indicates that mesoscale order is maintained when TEOS is replaced with BTESE, with interplanar spacing in each case being similar to those obtained when using the TEOS precursor alone. GISAXS patterns of the *diC*₆PC/BTESE films show that the *p*₆mm 2D hexagonal structure is maintained; for *lysoC*₁₄PC/BTESE, TEM data (Figure 5B) is consistent with the cubic phase seen previously with *lysoC*₁₄PC/SiO₂ films.

Unlike PC/SiO₂ films, however, the nanostructure of these films was preserved during the removal of the lipid template by thermal pyrolysis. Films were placed in a 350 °C oven for 30 min; this temperature was selected to minimize degradation of Si-CH₂CH₂-Si functionality within the hybrid framework. After removal of the lipid, the refractive index at 630 nm of *diC*₆PC- and *lysoC*₁₄PC-templated films was reduced from 1.47 and 1.51 to 1.30 and 1.22, respectively, demonstrating the formation of a porous material. Film thickness was reduced by ca. 15–25% for each film due to uniaxial shrinkage of the film resulting from silica condensation, with the *d*-spacing for the planes of the nanostructure parallel to the substrate surface being reduced by a similar amount (Figure 5A). In addition to stability toward lipid removal by calcination, solvent extraction of *lysoC*₁₄PC/BTESE films

produced porous films with no cracking. UV/O₃ treatment of these films led to complete collapse of porosity, presumably a result of a lack of selectivity for the reaction of O₃ between the lipid template and the integrated organic framework functionality.

*diC*₆PC/BTESE and *lysoC*₁₄PC/BTESE films were prepared on SAW substrates for N₂ adsorption analysis and calcined at 350 °C as described above. Figure 5C and D shows the isotherms obtained from these samples, along with pore size distributions obtained by fitting the data with a DFT-based model.³² The isotherm for the *diC*₆PC/BTESE film is indicative of a microporous material (a type I isotherm), consistent with the expected diameter of cylindrical micelle based upon the thickness of a *diC*₆PC bilayer (ca. 25 Å), after accounting for film shrinkage. Deconvolution of this isotherm yields a bimodal distribution, with ca. 60% of the pores in the expected size range (diameter = 22.5 Å) and the remainder in a narrow range around 18 Å. The source of the secondary porosity is unknown and remains a topic for future investigation. A BET surface area of 319 m²/cm³ of film volume was calculated for this film, typical of that seen for other mesoporous materials (the surface area is given here in units of area per unit film volume as the density of the hybrid silsesquioxane skeleton is not known). A type IV (mesoporous) isotherm was obtained for the *lysoC*₁₄PC film; this isotherm contains a sharper condensation step than that seen for the *lysoC*₁₄/SiO₂ isotherm (Figure 4C), with a similar pore size distribution range but a greater concentration of pores at higher diameter. The BET surface area for this film was determined to be 318 m²/cm³ of film volume. The total N₂ adsorbed at high P/P₀ for both of these isotherms (along with film thickness from ellipsometry) yields porosity levels of 26% (*diC*₆PC) and 31% (*lysoC*₁₄PC), lower than the range obtained from ellipsometric data for films on silicon substrates, 40% and 50% (assuming a similar refractive index for the BTESE wall and surfactant phases), an effect of either porosity that is inaccessible to N₂ adsorption or different thicknesses for films deposited on SAW rather than Si substrates.

Lipid/SiO₂ and Lipid/BTESE Interactions. The inability to remove phosphatidylcholines from silica films by thermal or UV/O₃ degradation, in addition to the apparent stresses in silica formed by extraction of lysophosphatidylcholine as well as the contrary behavior of lipid/BTESE films, suggests the presence of strong interactions between the lipid template and the framework material. We hypothesized that these interactions suppress the condensation of the silica network in lipid/SiO₂ and undertook an *ex-situ* FTIR/ellipsometric study to monitor the removal of the lipid template as well as development of the siloxane framework as a function of temperature. In this study (Figure 6A), a group of *diC*₆PC/SiO₂ films (synthesized with a lipid/silica ratio of 54.9 mg/mmol) as well as CTAB/SiO₂ and pure SiO₂ films (synthesized under conditions identical to those for the lipid/SiO₂ films except for the replacement of CTAB for *diC*₆PC or the omission of any template) were heated at 1 °C/min in a furnace to nearly 400 °C; samples were removed every 50° during this heating ramp for ellipsometric and transmission FTIR analysis. Refractive index data shows no significant changes in *n* for lipid-templated or nontemplated films, whereas a reduction in *n* between 200° and 250° is seen in CTAB-templated samples, corresponding to the removal of the surfactant template to leave a porous film. Thickness data, however, indicates that between

(30) Lu, Y. F.; Fan, H. Y.; Doke, N.; Loy, D. A.; Assink, R. A.; LaVan, D. A.; Brinker, C. J. *J. Am. Chem. Soc.* **2000**, *122*, 5258–5261.

(31) Shylesh, S.; Jha, R. K.; Singh, A. P. *Microporous Mesoporous Mater.* **2006**, *94*, 364–370.

(32) Jaroniec, M.; Kruk, M.; Olivier, J. P.; Kock, S. *Proceedings of the 5th International Symposium on the Characterization of Porous Solids*; Elsevier: Amsterdam, 1999.

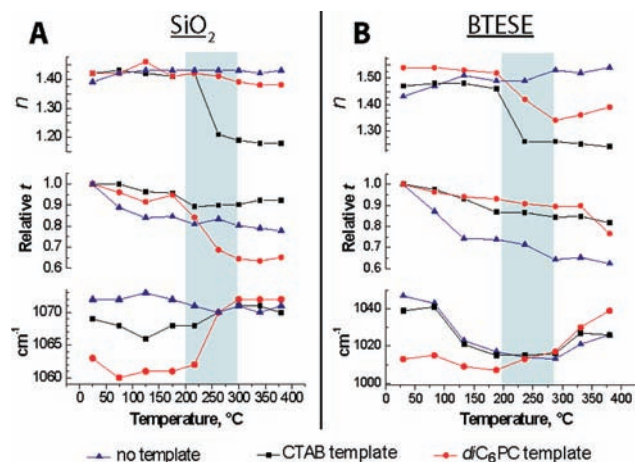


Figure 6. *Ex-situ* ellipsometric data (refractive index, relative thickness) and FTIR band position for the $\nu(\text{Si}-\text{O})$ stretch obtained from films of CTAB-, diC_6PC -, and nontemplated SiO_2 (A) and BTESE (B) during heating at $1^\circ\text{C}/\text{min}$.

175° and ca. 250°C , lipid-templated films collapse as diC_6PC is pyrolyzed (CTAB- and nontemplated films do exhibit some shrinkage, as would be expected from film drying and silanol condensation).

The bottom panel of Figure 6A shows the shift in frequency of the asymmetric $\text{Si}-\text{O}$ stretch ($\nu(\text{Si}-\text{O})$), correlated with the above changes in film refractive index and thickness. In silica sol-gel materials, the energy of this vibration (occurring at ca. 1070 cm^{-1}) has been correlated with the degree of siloxane network connectivity, with the band moving to higher wave numbers with increasing condensation.²⁰ Initially, the position of the $\nu(\text{Si}-\text{O})$ band in the CTAB and diC_6PC templated films indicates suppression of condensation relative to that of the nontemplated material, as has been observed previously for surfactant-templated silica films synthesized through EISA.³³ However, this band appears at a significantly lower energy in the films containing diC_6PC when compared to that of CTAB, a feature we ascribe to a lower degree of condensation in films templated with the former. This relative order in $\nu(\text{Si}-\text{O})$ band energy for the three types of film is reproducible and stable over time; after a period of 10 days, no significant changes in the FTIR spectra are observed, demonstrating that the small differences in sample history (for example, time between film deposition and FTIR data collection) can be ruled out as the source of this observed trend. After diC_6PC removal, above 200° , the frequency of this $\nu(\text{Si}-\text{O})$ stretch for lipid-templated films converges with that of the other films. We interpret this data as confirmation of our hypothesis; siloxane network formation is suppressed by the presence of lipid, preventing structural stabilization of the pore network as the template is being removed thermally. Although this suppression is also seen for CTAB-templated silica, the effect is not as pronounced.

For lysolipid-templated SiO_2 films, we posit that the pore network is stabilized toward collapse during lipid removal by extraction by the presence of an acid condensation catalyst, along with the slow extraction rate from the 3D pore network.

Initial condensation state of the CTAB/silica and lipid/silica films were also compared using ^{29}Si MAS NMR with films scraped from Si wafers. This data, illustrated in Figure 7A, also shows decreased condensation of lipid-templated silica compared to that of the CTAB-templated material, albeit it to a lesser extent. The degree of condensation (DC) for

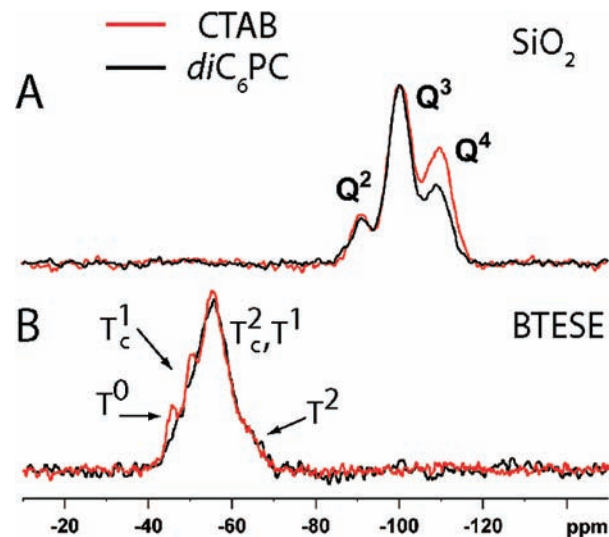


Figure 7. Solid-state ^{29}Si NMR comparing the degree of condensation in CTAB- and diC_6PC -templated SiO_2 (A) and BTESE (B).

TEOS-derived silica can be defined by

$$DC = \left(\sum nQ^n \right) / 4$$

where Q^n is the fraction of the different Q species with connectivity n obtained from fitting the NMR spectra. For the data in Figure 7A, a DC of 0.82 was measured for CTAB/silica, compared to 0.79 for diC_6PC /silica. Although this difference is small, the percentage of Q^4 species in each material supports the interpretation that this difference is significant; % Q^4 for diC_6PC /silica is ca. 25% lower than that for CTAB/silica (27% vs 36%). The smaller differences between lipid- and CTAB-templated materials detected using NMR may reflect a lower sensitivity to long-range network formation when compared with vibrational spectroscopy.

From solution ^{29}Si NMR, the observed disparity in silica condensation state between the two templates appears to arise during or immediately after the self-assembly process as the initial reaction of TEOS in the template solutions are very similar. Comparison of ^{29}Si NMR data (see Supporting Information for spectra and assignments) for TEOS, TEOS/CTAB, and TEOS/ diC_6PC precursor solutions shows that while the hydrolysis and initial condensation rate of TEOS without any added template are rapid (with hydrolysis nearly complete within the first 40 min), inclusion of CTAB or diC_6PC to the TEOS solution reduces the hydrolysis rate by an identical amount (approximately half) while also slowing the initial condensation rate. While this observed reduction in reaction rates may be an effect of specific intermolecular interactions between template molecules and silica precursors, the increase in ionic strength with template present will decrease solution activities, another possible source of the change in reaction rates.

This ellipsometric/FTIR/NMR study was repeated for diC_6PC - CTAB- and nontemplated BTESE films (data in Figures 6B and 7B). Refractive index and thickness changes of films during heating are consistent with the removal of both templates to yield porous films, accompanied by shrinkage of the thickness from silanol condensation inside the film. However, the interpretation of shifts in $\nu(\text{Si}-\text{O})$ bands for BTESE-based films is more complicated than that for SiO_2 . Above 75° , the frequency of this vibration *decreases*, followed by an increase above 200° (for lipid-templated material) and 300° (for CTAB-templated films as well as nontemplated BTESE). This shift in frequency

(33) Doshi, D. A.; Gibaud, A.; Goletto, V.; Lu, M. C.; Gerung, H.; Ocko, B.; Han, S. M.; Brinker, C. J. *J. Am. Chem. Soc.* **2003**, *125*, 11646–11655.

during heating can be explained by a cyclization reaction for BTESE; this monomer forms a bicyclic intermediate during polymerization that is accompanied by a decrease in stretching frequency (from ca. 1100 cm^{-1} for the monomer, dropping to ca. $1000\text{--}1030\text{ cm}^{-1}$ upon cyclization).³⁴ As siloxane network formation proceeds, requiring the opening of the cyclic species, the energy of the $\nu(\text{Si-O})$ band again increases³⁴ to ca. $1040\text{--}1080\text{ cm}^{-1}$.

Comparison of the $\nu(\text{Si-O})$ stretching frequency between diC_6PC and CTAB-templated (as well as nontemplated) BTESE suggests that the presence of the lipid promotes cyclization during film synthesis, as the initial band position before heating is shifted to a lower energy by ca. 30 cm^{-1} to 1012 cm^{-1} , within the region in which cyclized species are expected to occur. Also, the onset of the increase in stretching frequency that is correlated with the formation of acyclic species during network polymerization occurs at a lower temperature for lipid-templated films ($200\text{ }^\circ\text{C}$) than for CTAB-templated or pure BTESE films (ca. $300\text{ }^\circ\text{C}$). This data indicates that, unlike in pure SiO_2 films, diC_6PC promotes condensation in the BTESE material.

Solid state ^{29}Si NMR of as-deposited diC_6PC - and CTAB-templated film material (Figure 7B) is consistent with this model of relative BTESE reactivity. A degree of condensation figure is difficult to calculate for BTESE materials, as cyclic T^2 and acyclic T^1 signals overlap³⁴ (analogous to the nomenclature for TEOS-based materials, T^n is the fraction of the different T species with connectivity n ; the subscript c indicates the signal from a cyclized product). Examination of the NMR data, however, clearly shows that CTAB-templated BTESE contains a higher relative contribution from T^0 and T^1 (cyclized) species than lipid-templated BTESE, consistent with an increase in condensation reactivity when lipid is present.

Further evidence of strong lipid-framework interactions is given by the fitting of low-angle 1D XRD data for lamellar films of SiO_2 , and BTESE templated with diC_6PC to a lamellar model is illustrated in Figure 8.³⁵ Because of the (nonreflectivity) instrumental configuration used to collect this data, the data background is poorly simulated by this procedure. However, for determining the relative thicknesses of the lipid and inorganic layers in the lamellar structure the key parameter is the relative intensities of reflections, a feature in the scattering pattern that is well-reproduced by the simulated data. Our model for this lamellar structure (illustrated in Figure 8A) contains four variables: L and σ_L , the thickness and thickness variance of the lamellar unit cell, respectively, and d_1 and σ_1 , the thickness and thickness variance of one phase in the unit cell, respectively. The assignment of this phase to the inorganic or organic layer is not possible from the data fit. However, it is still clear that extensive interpenetration (and thus interaction) is occurring between the lipid and silica phases in nanostructured diC_6PC/SiO_2 . While one diC_6PC bilayer has a thickness of 25 \AA , an L of 3.16 \AA and a d_1 of 16.0 \AA indicate that the thicknesses of both materials in each lamellae are equal, a structure that is only possible with near complete penetration of the phosphatidylcholine headgroup into the silica framework. For the diC_6PC/BTESE data, L and d_1 (2.92 \AA and 1.00 \AA , respectively) indicate a minimum penetration of the lipid into the BTESE framework of only 0.6 \AA (based on an assignment of d_1 to the BTESE phase). However, the large value of σ_1 (0.7 \AA) signifies the continued presence of significant interactions between lipid headgroups and the BTESE framework.

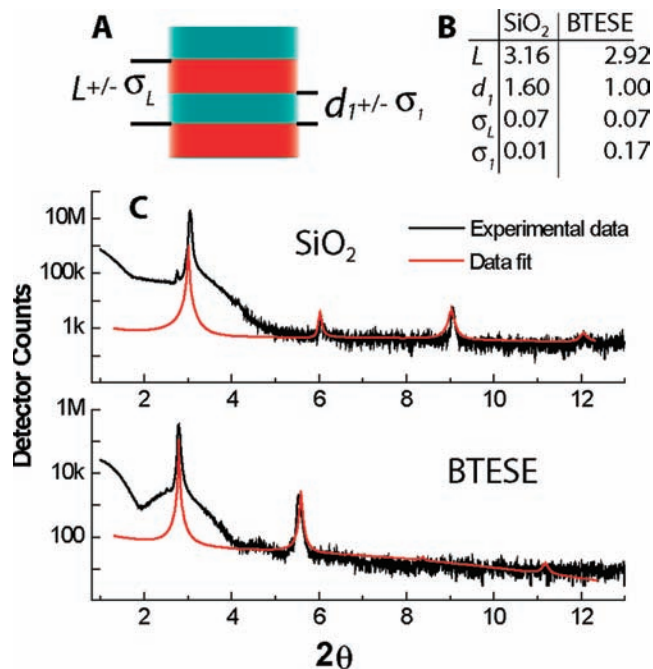


Figure 8. (A) Structural model used to fit 1D diffraction data for lamellar diC_6PC/SiO_2 and diC_6PC/BTESE films, consisting of unit cell thickness L and thickness of phase 1 d_1 . (B) Fit parameters for this model obtained from the data in C. (C) Experimental and simulated data for lamellar diC_6PC/SiO_2 (top panel) and diC_6PC/BTESE (bottom panel) films.

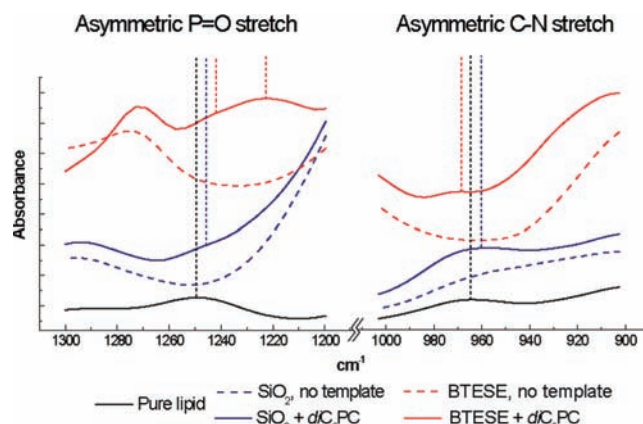


Figure 9. FTIR data for C–N and P=O stretches in diC_6PC headgroup stretches in SiO_2 and BTESE, as well as for pure lipid and nontemplated SiO_2 and BTESE backgrounds.

To examine the chemical interactions between the lipid and framework phases, FTIR was used to probe the chemical environment of the phosphatidylcholine headgroup (Figure 9). Specifically, the vibrational regions for asymmetric C–N and P=O stretches were measured for diC_6PC - and nontemplated SiO_2 and BTESE as well as for pure lipid. The former vibration has been linked to dipolar interactions of the quaternary amine in the phosphatidylcholine headgroup,³⁶ while the frequency of the P=O band has been used as an indicator of hydrogen bonding in the phosphate group.³⁶ Both the diC_6PC/SiO_2 and diC_6PC/BTESE materials show a shift in the P=O band to lower frequencies relative to that of the pure lipid, consistent with an increase in hydrogen bonding with the phosphate center (likely to free silanols at the interface between the lipid and framework

(34) Loy, D. A.; Carpenter, J. P.; Alam, T. M.; Shaltout, R.; Dorhout, P. K.; Greaves, J.; Small, J. H.; Shea, K. J. *J. Am. Chem. Soc.* **1999**, *121*, 5413–5425.

(35) Ruland, W.; Smarsly, B. *J. Appl. Crystallogr.* **2004**, *37*, 575–584.

(36) Popova, A. V.; Hinch, D. K. *Biophys. J.* **2003**, *85*, 1682–1690.

phases), with the BTESE-based material exhibiting more hydrogen bonding relative to that of silica. Also, this band is split into two peaks for *diC₆PC*/BTESE films, suggesting the presence of more than one chemical environment. The C–N stretch can be interpreted as reflecting a more polar environment for the headgroup in the hybrid material relative to the material containing only silica in the framework.

As another means of examining the environment of the lipid headgroup, ³¹P NMR chemical shifts for *diC₆PC*/SiO₂ and *diC₆PC*/BTESE materials were measured, yielding $\delta = 5.3$ and 5.0 ppm, respectively. Although this small shift may be insignificant, the slightly larger chemical shift seen in the silica material could result from either small differences in the pH of the headgroup environment or by an increase in the relative negative charge on the *diC₆PC* headgroup as a result of stronger hydrogen bonds. Again, FTIR proved to be a more sensitive probe for the comparison of chemical environment between the two types of templated material; future experiments should enable a better understanding of the discrepancies in material structure/chemical environment depicted by each analytical technique.

Conclusions

We have characterized the nanostructure of silica- and hybrid-thin films synthesized using EISA with phospholipid templates and found that a variety of phases (1D, 2D, and 3D) can be formed by proper selection of the lipid structure. Also, lipid-framework interactions in these materials appear to be very

strong, with suppression or enhancement of siloxane framework reactivity. Other types of nanostructures (e.g., those based on bicontinuous minimal surfaces) may, in the future, be accessible using other biologically derived lipid types (for example, glycerates or bile salts) and will be explored in future research.

Acknowledgment. Use of the APS is supported by the Department of Energy under contract DE-AC02-06CH11357. Sandia is a multiprogram laboratory operated by Sandia Corporation, a Lockheed Martin Company, for the United States Department of Energy's National Nuclear Security Administration under contract DE-AC04-94AL85000. Partial support of this work (TMA) was through the DOE BES funding to Sandia, Sandia's Laboratory Directed Research and Development (LDRD) Programs, as well as through Air Force Office of Scientific Research Grant FA 9550-07-1-0054 and the National Institutes of Health through the HHH Roadmap for Medical Research Award number PHS 2 PN2 EY016570B. Images in this article were generated in the University of New Mexico Cancer Center Fluorescence Microscopy Facility, supported as detailed on the webpage <http://hsc.unm.edu/crtc/microscopy/Facility.html>.

Supporting Information Available: NMR characterization of the initial hydrolysis and condensation kinetics for TEOS solutions with *diC₆PC*, CTAB, and no template. This material is available free of charge via the Internet at <http://pubs.acs.org>.

Appendix A -- Publications, Presentations, Patents, and Awards (2006-2009):

Refereed Journal Articles, Submitted or Accepted:

1. Carnes, EC; Lopez, DM; Gresham, H; Cheung, A; Timmins, GS; and Brinker, CJ. *Confinement-Induced Quorum Sensing of Individual Staphylococcus aureus Bacteria*. Nature Chemical Biology, Accepted for publication September 4, 2009.

Refereed Journal Articles, Published 2006 to 2009:

1. Carnes, EC; Harper, JC; Ashley, CE; Lopez, DM; Brozik, SM; Brinker, CJ. *Cell-Directed Localization and Orientation of a Functional Foreign Transmembrane Protein with a Silica Nanostructure*. Journal of the American Chemical Society, Published online, September 18, 2009, <http://pubs.acs.org>.
2. Dunphy, DR; Alam, TM.; Tate, MP.; Hillhouse, HW.; Smarsly, B; Collord, AD.; Carnes, EC; Baca, HK.; Kohn, R; Wang, J.; Brinker, CJ. *Characterization of Lipid-Templated Silica and Hybrid Thin Film Mesophases by Grazing Incidence Small-Angle X-ray Scattering*. Langmuir, 2009. **25**(16): p. 9500-9509.
3. Liu, J.; Stace-Naughton, A.; Brinker, CJ. *Silica Nanoparticle Supported Lipid Bilayers for Gene Delivery*. Chemical Communications, 2009. **34**, p. 510-+.
4. Liu, J; Jiang, XM; Ashley, CE; and Brinker CJ. *Electrostatically Mediated Liposome Fusion and Lipid Exchange with a Nanoparticle Supported Bilayer for Control of Surface Charge, Drug Containment, and Delivery*. Journal of the American Chemical Society, 2009. **22**, p. 7567-7569
5. Liu, J.; Stace-Naughton, A.; Jiang, XM.; Brinker, CJ. *Porous Nanoparticle Supported Lipid Bilayers (Protocells) as Delivery Vehicles*. Journal of the American Chemical Society, 2009. **131**(4): p. 1354-1355.
6. Zhang, L; Singh, S; Tian, C; Shen YR, Wu, Y; Shannon, MA; and Brinker, CJ. *Nanoporous Silica-Water Interfaces Studied by Sum Frequency Vibrational Spectroscopy*. Journal of Chemical Physics, 2009. **130**(15), p. 154702-154702-10.
7. Pang, J.B., et al., *Free-standing, patternable nanoparticle/polymer monolayer arrays formed by evaporation induced self-assembly at a fluid interface*. Journal of the American Chemical Society, 2008. **130**(11): p. 3284-+.
8. Pang, J.B., et al., *Directed aerosol writing of ordered silica nanostructures on arbitrary surfaces with self-assembling inks*. Small, 2008. **4**(7): p. 982-989.
9. Dovgolevsky, E., et al., *Self-assembled conjugated polymer-surfactant-silica mesostructures and their integration into light-emitting diodes*. Journal of Materials Chemistry, 2008. **18**(4): p. 423-436.
10. Fan, H.Y., et al., *Modulus-density scaling behaviour and framework architecture of nanoporous self-assembled silicas*. Nature Materials, 2007. **6**(6): p. 418-423.
11. De, G., et al., *Nanocrystalline mesoporous palladium activated tin oxide thin films as room-temperature hydrogen gas sensors*. Chemical Communications, 2007(18): p. 1840-1842.
12. Baca, H.K., Carnes, E.C., Singh, S., Ashley, C.E., Lopez, D., Brinker, C.J., *Cell-directed assembly of bio/nano interfaces - A new scheme for cell immobilization*. Accounts of

- Chemical Research, 2007. **40**(9): p. 836-845.
13. Wright, A., et al., *Hierarchically organized nanoparticle mesostructure arrays formed through hydrothermal self-assembly*. Chemistry of Materials, 2006. **18**(13): p. 3034-3038.
 14. Truesdell, R., et al., *Drag reduction on a patterned superhydrophobic surface*. Physical Review Letters, 2006. **97**(4): p. 4.
 15. Singh, S., et al., *Superhydrophobicity - Drying transition of confined water*. Nature, 2006. **442**(7102): p. 526-526.
 16. Rodriguez, A.T., et al., *Nanoporous carbon nanotubes synthesized through confined hydrogen-bonding self-assembly*. Journal of the American Chemical Society, 2006. **128**(29): p. 9276-9277.
 17. Jiang, Y.B., et al., *Nanometer-thick conformal pore sealing of self-assembled mesoporous silica by plasma-assisted atomic layer deposition*. Journal of the American Chemical Society, 2006. **128**(34): p. 11018-11019.
 18. Jiang, X.M. and C.J. Brinker, *Aerosol-assisted self-assembly of single-crystal core/nanoporous shell particles as model controlled release capsules*. Journal of the American Chemical Society, 2006. **128**(14): p. 4512-4513.
 19. Fan, H.Y., et al., *Three-dimensionally ordered gold nanocrystal/silica superlattice thin films synthesized via sol-gel self-assembly*. Advanced Functional Materials, 2006. **16**(7): p. 891-895.
 20. Fan, H.Y., et al., *Ordered nanocrystal/silica particles self-assembled from nanocrystal micelles and silicate*. Chemical Communications, 2006(22): p. 2323-2325.
 21. Brinker, C.J. and D.R. Dunphy, *Morphological control of surfactant-templated metal oxide films*. Current Opinion in Colloid & Interface Science, 2006. **11**(2-3): p. 126-132.
 22. Baca, H.K., et al., *Cell-directed assembly of lipid-silica nanostructures providing extended cell viability*. Science, 2006. **313**(5785): p. 337-341.

Books Edited (2006 to 2009):

1. Annual Review of Nano Research – Volume 2
Cao, Guozhong and Brinker, C. Jeffrey, editors
World Scientific Publishing Co. Ltd., Singapore/London, 2008
2. Annual Review of Nano Research – Volume 1
Cao, Guozhong and Brinker, C. Jeffrey, editors
World Scientific Publishing Co. Ltd., Singapore/London, 2006

Books Chapters Edited (2006 to 2009):

1. Control of Morphology in Mesoporous and Mesostructured Hybrid Materials
Darren R. Dunphy, Bernd Smarsly, C. Jeffrey Brinker
in The Supramolecular Chemistry of Organic-Inorganic Hybrid Materials, Knut Rurack, ed,
John Wiley & Sons, Inc., Hoboken, NJ. (in press, Sept 2009).
2. Photoresponsive Nanocomposite Materials Including Axobenzene-Containing Polysilsesquixane Films and Photoswitched Nanovalves
Nanguo Liu and C. Jeffrey Brinker

in Smart Light-Responsive Materials: Azobenzene Containing Polymers and Liquid Crystals, Yue Zhao and Tomiki Ikeda, eds., John Wiley & Sons, Inc., Hoboken, NJ. April 2009.

Presentations at Professional Meetings

1. Carnes, EC and Brinker CJ. *Metabolically and Optically Defined Lithography Using Living Cells*. 13th International Conference on Surface and Colloid Science/83rd ACS Colloid and Surface Science Symposium, Columbia University, New York, NY, June 14-19, 2009.
2. Johnson, P; Carnes, EC; Ashley, CE; Lopez, DM; Timmins, G; and Brinker, CJ. *Lithography with Life: A New Means of Patterned Cellular Integration into Self-Assembled Nanostructures*, Materials Research Society Spring Meeting, San Francisco, CA. April 12-17, 2009.
3. Carnes, EC; Harper, JC; Ashley, CE; Lopez, DM; Douthit, CM; Karlin, S; Pelowitz, J; Khripin, C; and Brinker, CJ. *Metabolically and Optically Controlled 3D Cellular Integration - Lithography with Life*. Materials Research Society Spring Meeting, San Francisco, CA. April 12-17, 2009.
4. Ashley, CE; Carnes, EC; Dunphy, DR; Petsev, D; Atanassov, P; Peabody, D; and Brinker, CJ. *In-Situ Grazing Incidence Small Angle X-ray Scattering (GISAXS) Characterization of 2D Bacteriophage Arrays Deposited via Convective Assembly*. Materials Research Society Fall Meeting, December 1-5, 2008. Boston, MA.
5. Capecehatro, A.; Carnes, EC; Karlin, S.; Douthit, C; Ashley, CE; Dunphy, DR; Harper, JC; Jeff Brinker, CJ. *Patternable Cell Directed Integration*, Materials Research Society Spring Meeting, March 24-28, 2008. San Francisco, CA.
6. Jiang, YB; Chen, Z; Kissel, DJ; Xiong, S; Liu, J.; Ashley, CE; Carnes, EC; Dunphy, DR; Sewell, RM., Cecchi, JL; and Brinker, CJ. *Atomic Layer Deposition of Hybrid or Microporous Low-k Materials*. Materials Research Society Spring Meeting, March 24-28, 2008. San Francisco, CA.
7. Carnes, EC; Ashley, CE; Lopez, DM; Douthit, C; Karlin, S; Pelowitz, J; Capecehatro, A; Harper, JC; Dunphy, DR; Gresham, H; Timmins, G; and Brinker, CJ. *Lithography with Life: A New Means of Patterned Cellular Integration into Self-Assembled Nanostructures*. Bioscience and Technology Forum, Sandia National Laboratories, February 6, 2008, Albuquerque, NM.
8. Carnes, EC; Ashley, CE; Lopez, D; Douthit, C; Pelowitz, J; Karlin, S; Capecehatro, A; Dunphy, D; Timmins, G; and Brinker, CJ. *Lithography with Life: A New Means of Patterned Cellular Integration into Self-Assembled Nanostructures*. HK IAS – US ICMR Workshop on Advanced Materials, September 12-15, 2007. HKUST, Hong Kong.
9. Douthit, CM, Carnes, EC; Ashley, CE; Lopez, D; Karlin, S; Pelowitz, J; Capecehatro, A; Dunphy, D; Gresham, H; Timmins, G; and Brinker, CJ. *Integrating Living Yeast Cells into Self-Assembled Nanostructures*. 19th Annual Rio Grande Symposium on Advanced Materials – RGSAM, October 9, 2007. Albuquerque, NM.
10. Brinker, CJ ; Baca, HK ; Carnes, EC ; Singh, S ; Ashley, CE ; Lopez, DM. *Directing the Self-Assembly of Nanostructured Sol-Gel Films with Living Cells*. XIVth International Sol-Gel Conference, September 2-7, 2007, Montpellier, France.
11. Carnes, EC ; Ashley, CE ; Lopez, DM ; Douthit, CM ; Karlin, S ; Pelowitz, J ; Singh, S ; Dunphy, DR ; Gresham, H. ; Timmins, G. ; Brinker, CJ. *Integration of Living Cells in Self-*

- Assembled Nanostructures : A Platform for Single-Cell Interrogation*. 2007 Joint ACS AIChE Rocky Mountain Regional Meeting, August 29th – September 1, 2007. Denver, CO.
12. Carnes, EC ; Ashley, CE ; Lopez, DM ; Douthit, CM ; Singh, S ; Dunphy, DR ; Brinker, CJ. *Integration of Living Cells within Self-Assembled Nanostructures*, 1st Annual Symposium on Integrating Nanotechnology with Cell Biology and Neuroscience, August 15, 2007. Albuquerque, NM.
 13. Carnes, EC ; Ashley, CE ; Lopez, DM ; Douthit, CM ; Singh, S ; Dunphy, DR ; Brinker, CJ. *Integration of Living Cells within Self-Assembled Nanostructures*, 43rd Annual Symposium New Mexico Chapter of the American Vacuum Society, May 21-22, 2007, Albuquerque, NM. (undergraduate student poster competition 1st prize)
 14. Carnes, EC ; Ashley, CE ; Lopez, DM ; Baca, H ; Singh, S ; Dunphy, DR ; Brinker, CJ. *Cell-Directed Assembly : A New Means of Bio/Nano Integration*, Center for Integrated Nanotechnologies (CINT) Annual Program Review, April 18-20, 2007, Sandia National Laboratories, Albuquerque, NM.
 15. Carnes, EC ; Ashley, CE ; Lopez, DM ; Douthid, CM ; Karlin, SA ; Pelowitz, J ; Gresham, H ; Timmins, G ; Brinker, CJ. *Patternable Integration of Living Cells with Self-Assembled Nanomaterials*, Materials Research Society Spring Meeting, Symposium N: Printing Methods for Electronics, Photonics, and Biomaterials, April 9-13, 2007, San Francisco, CA.
 16. Brinker, CJ. Self-Assembly of Bio-Inspired and Bio-Directed Nanostructures. *2007 AFOSR Biomimetic, Biomaterials and Biointerfacial Sciences Program Review*, Duck Key, FL, January 8-12, 2007.
 17. Carnes, E., Ashley, C., Lopez, D., Douthit, C., Karlin, S., Pelowitz, J., Wise, A., Singh, S., Brinker, C.J., *Creation of Integrated Platforms for Engineered Cell-Cell Communication via Cell Directed Assembly*, Materials Research Society Fall 2006 Meeting, November 27-December 1, 2006, Boston, MA.
 18. Brinker, C.J., Carnes, E., Ashley, C., Singh, S., *Engineered Bio/Nano Interfaces via Cell-directed Assembly*, Materials Research Society Fall 2006 Meeting, November 27-December 1, 2006, Boston, MA.
 19. Douthit, C.M., Carnes, E.C., Ashley, C.E., Lopez, D., Pelowitz, J., Karlin, S.A., Brinker, L.M., and Brinker, C.J., *In-Situ Genetic Modification through Cell-Directed Assembly*, 18th Annual Rio Grande Symposium on Advanced Materials – RGSAM, October 10, 2006, Albuquerque, NM.

Patents Issued and Applications Filed (2006 to 2009):

Relevant patents issued / allowed

1. Preparation of Hydrophobic Coatings. **U.S. Patent No. 7,485,343 B1, Issued February 3, 2009.**

Relevant patent applications and disclosures filed (2006-2009)

1. **C. Jeffrey Brinker**, Carlee Ashley, Juewen Liu. Porous Nanoparticle Supported Lipid Bilayer Nanostructure. UNM-936; Provisional Appl. 61/142,495 filed 1/5/2009

2. **C. Jeffrey Brinker** and Xingmao Jiang. An Aerosol Method for Nano Silver-Silica Composite Anti-microbial Agent. UNM-847; Appl. 12/324,318 filed 11/26/2008
3. **Eric Carnes**, Vojo Deretic, DeAnna Lopez, Sharon Master, Graham Timmins, Brinker, C. Jeffrey . Extended Viability Live Vaccine for TB. MC-401; Provisional Appl. 61/132,4000 filed 6/18/2008
4. C. Jeffrey Brinker and Helen K Baca. Cell-Directed Assembly. SD-10664/S-112562, March 26, 2007.

Awards and Honors (2006-2009):

PI Awards, C. Jeffrey Brinker

2006 Directeur de Recherche Universite Pierre et Marie Curie, Paris VI
 2006 Rutgers University Distinguished Alumnus Award
 2007 R&D 100 Award: Self-Assembling Process for Fabricating Tailored Thin Films
 2008 R&D100 Award: Patterned Superhydrophobic Surfaces
 2008 Edward R. Orton Jr. Memorial Award, American Ceramic Society and ASM
 2009 IBM Distinguished Lecturer in Materials Science and Engineering
 2009 Named Fellow of the Materials Research Society

Major National and International Graduate Student Awards and Fellowships:

1. Carlee Ashley (PhD est 2010), Materials Research Society Fall Meeting, Top Poster Award, 2008, *Targeted in-vitro Drug Delivery*.
2. Carlee Ashley, NSF Interdisciplinary Graduate Research Trainee (IGERT) Fellowship, 2007-2009
3. Eric Carnes (PhD 2008), NSF Interdisciplinary Graduate Research Trainee (IGERT) Fellowship, 2006-2008
4. Eric Carnes, Carlee Ashley, NSF Engineering Ethics Pilot Fellowship, 2007-2008
5. Carlee Ashley, Darren Dunphy, Eric Carnes, C. Jeffrey Brinker, Materials Research Society Fall Meeting, Top Poster Award Finalist, 2008, *Self-assembly of Well-Ordered, Close-Packed 2D Arrays of Recombinant Virus-Like Particles that Nucleate the Growth of Inorganic Nanomaterials*.
6. Shisheng Xiong (PhD 2010), Y. Gao, J. Pang, J. Grey, C. Jeffrey Brinker, Materials Research Society Fall Meeting, Top Poster Award Finalist, 2008, *Functional Monolayer Nanoparticle/polymer Composites Formed by EISA at a Fluid Interface*.
7. Carlee Ashley, First Prize, Graduate student Oral Competition, *GISAXS Characterization of 2D Bacteriophage Arrays Deposited via Convective Assembly*, NM Chapter of the American Vacuum Society, May 22, 2007, Albuquerque, NM (paid trip to AVS International Symposium, Seattle, WA, October 2007).
8. Carlee Ashley, Eric Carnes (PhD 2008), Helen Baca, Jeff Brinker. First Prize, Graduate student poster competition *Cell-Directed Assembly of 3-D Bio-Nano Interfaces*. Industrial Advisory Board Meeting of the UNM/RUTGERS/PENN STATE Ceramic and Composite Materials Center (CCMC), March 13, 2007, Albuquerque, NM

Undergraduate Student Awards

1. DeAnna Lopez, First prize, Spectral Image category, Confocal microscope image “Cells Take the Lead”, Microscopy Facility Image Competition, Cancer Center Fluorescence Microscopy Facility, University of New Mexico, February 2008, Albuquerque, NM. Published in Life in Print, Science News Online, Jan 26, 2008, vol. 173, no. 4, p. 56.
2. Cynthia Douthit, Second Prize, Undergraduate student poster competition, Examining Integration Techniques using Living Yeast Cells into Self-Assembled Nanostructures, AIChE 2008 Annual Meeting, November 16-21, 2008, Philadelphia, PA.
3. Cynthia M. Douthit, First Prize, Undergraduate student poster competition *Integrating Living Yeast Cells into Patterned Self-Assembled Nanostructures*, Rio Grande Symposium on Advanced Materials -- RGSAM, October 9, 2007, Albuquerque, NM
4. Andrew Collord, Third Prize, Undergraduate student poster competition, *Structure and Aqueous Stability of Surfactant-Templated Porous Films Synthesized using a Hybrid Inorganic/Organic Sol-Gel Precursor*, Rio Grande Symposium on Advanced Materials -- RGSAM, October 9, 2007, Albuquerque, NM
5. DeAnna Lopez, First Prize, Undergraduate Student Poster Competition, *Cell-to-cell communication among nano-confined cells in self-assembled matrices*. Sandia National Laboratories’ Student Symposium, Albuquerque, NM , Aug 2, 2007
6. Patrick Johnson, First Prize, Undergraduate Student Poster Competition, *Gecko-Inspired Superadhesives*, Sandia National Laboratories’ Student Symposium, Albuquerque, NM , Aug 2, 2007.
7. DeAnna Lopez, First Prize, Undergraduate Student Poster Competition, *Integration of Living Cells within Self-Assembled Nanostructures*, NM Chapter of the American Vacuum Society, May 22, 2007, Albuquerque, NM

Distribution

1	MS1349	Eric C. Carnes, 1815
1	MS1349	Carlee E. Ashley, 1815
1	MS0892	DeAnna M. Lopez, 1714
1	MS1349	Darren R. Dunphy, 1815
2	MS1349	C. Jeffrey Brinker, 1002
4	MS1349	Carol S. Ashley, 1815
2	MS9018	Central Technical Files, 8944
2	MS0899	Technical Library, 4536
1	MS0123	D. Chavez, LDRD Office, 1011
1	MS0161	Patent and Licensing, 11500

